Dissertation

submitted to the

Combined Faculty of Mathematics, Engineering and Natural Sciences

of Heidelberg University, Germany

for the degree of

Doctor of Natural Sciences

Put forward by

Benjamin Weyland (formerly Schreiner)

born in: Charleston, SC, USA

Oral examination: 16.01.2024

Detection of nitrous acid in the lower, middle, and upper troposphere: potential formation mechanisms of excess HONO

Referees:

Prof. Dr. Klaus Pfeilsticker

Prof. Dr. Thomas Wagner

Zusammenfassung

Salpetrige Säure wurde in der unteren, mittleren und oberen Troposphäre während 25 Forschungsflügen des HALO-Flugzeugs im Rahmen der beiden Messkampagnen EMeRGe und CAFE-Africa in den Jahren 2017 und 2018 gemessen. Diese Kampagnen wurden bei einer Vielzahl unterschiedlicher atmosphärischer Bedingungen durchgeführt, von Reinluft mit niedrigem NO_x-Gehalt über dem Atlantischen Ozean während der CAFE-Africa-Kampagne bis hin zu stark verschmutzter Luft mit hohem NO_x-Gehalt während der EMeRGe-EU und -Asia Kampagnen. Mithilfe des Fernerkundungs-Mini-DOAS Instruments wurden anschließend aus der DOAS-Analyse ermittelte Schrägsäulendichten mit der Skalierungsmethode O_3/O_4 in Volumenmischungsverhältnisse umgewandelt. Ergänzt werden diese Beobachtungen durch gleichzeitige Messungen von Formaldehyd und Stickstoffdioxid mit dem mini-DOAS Instrument. Es wird gezeigt, dass die O_3/O_4-Skalierungsmethode hinsichtlich der Wahl des jeweiligen spektralen Intervals und des Skalierungsgases robust ist. Weiterhin wurden diese Messungen mit Beobachtungen von Spurengaskonzentrationen und atmosphärischen Parametern einer Vielzahl anderer Instrumente an Bord des HALO-Flugzeugs sowie mit Modellsimulationen kombiniert. Obwohl sich die mit dem Mini-DOAS Instrument gemessenen HCHO und NO_2 Konzentrationen gut mit Modellen und In-situ-Instrumenten übereinstimmen, liegen die ermittelten HONO Konzentrationen oft über dem, was man von der bekannten Bildung durch Gasphasereaktionen erwarten würde, oder was durch die chemischen Transportmodelle EMAC und MECO(n) vorhergesagt wird. Mit den gemeinsam gemessenen Spezies werden potenzielle heterogene und gasförmige Quellen dieser überschüssigen salpetrigen Säure für die untersuchten Schichten der Atmosphäre, insbesondere die untere und obere Troposphäre untersucht. In der marinen Grenzschicht mit niedrigem NO_x-Gehalt wird die beobachtete HONO Konzentrationen durch frühere Studien in derselben Region bestätigt und kann durch die Photolyse von partikulärem Nitrat erklärt werden. Die erhöhten HONO Konzentrationen in der verschmutzten unteren Atmosphäre wurden schon bei früheren Messungen beobachtet und die wahrscheinlichste Erklärung ist die heterogene Umwandlung von NO_2 an unterschiedlichen Oberflächen oder atmosphärischen Aerosolen unterschiedlicher Zusammensetzung, obwohl ein genauer Mechanismus mit der verfügbaren Instrumentierung nicht bestimmt werden kann. Für die gegenüber den Modellen erhöhte HONO Konzentrationen in der oberen Troposphäre wird eine neuartige Gasphasenquelle von HONO, die Oxidation von Peroxysalpetriger Säure untersucht und vorgeschlagen. Insgesamt legen die Messungen eine größere Rolle von HONO bei der Bildung des wichtigen Oxidationsmittel OH und damit für die Oxidationskapazität der Atmosphäre als bisher nahe.

Abstract

Nitrous acid was measured in the lower, middle, and upper troposphere during 25 research flights of the HALO aircraft across two research missions, EMeRGe and CAFE-Africa in 2017 and 2018. These missions represent a variety of atmospheric conditions, from pristine low-NO_x air over the Atlantic Ocean during the CAFE-Africa mission to polluted high-NO_x air during the EMeRGe-EU and -Asia missions. Using the remote sensing mini-DOAS instrument, slant column densities retrieved from DOAS analysis are converted to volume mixing ratios with the O_3/O_4 scaling method. These observations are complemented by coincident measurements of formaldehyde and nitrogen dioxide from the mini-DOAS instrument. It is demonstrated that the O_3/O_4 scaling method is robust with respect to choice of the spectral interval as well as scaling gas. These measurements are combined with observations of trace gas concentrations and atmospheric parameters from a host of other instruments onboard the HALO aircraft, as well as model simulations. While the HCHO and NO_2 measured by the mini-DOAS instrument compare well with photochemical model predictions and with measurements of complementary in situ instruments, the retrieved HONO is often in excess of what would be expected from the known gas phase formation mechanisms of nitrous acid, or what is predicted by the atmospheric chemistry models EMAC and MECO(n). With the co-measured species, potential heterogeneous and gas phase sources of this excess nitrous acid are investigated for the probed layers of the atmosphere, specifically the lower and upper troposphere. In the low-NO_x marine boundary layer, the observed HONO is corroborated by previous studies in the same region, and may be formed by the photolysis of particulate nitrate. In the polluted lower troposphere, the heterogeneous conversion of NO_2 on the surface or in the bulk of atmospheric aerosol is the most likely source of the observed HONO, though a precise mechanism cannot be determined with the information provided by the measurements of the available instrumentation. In the cold upper troposphere, a novel gas phase source of HONO, the oxidation of peroxynitrous acid is suggested and investigated. Overall, our measurements indicate a larger role of HONO than hitherto considered for the formation of OH, which is the major oxidant in the Earth's atmosphere.

Contents

Acronyms

AENEAS AtmosphEric Nitrogen oxides mEAsuring System. 42, 57, 69, 111, 113

AMF Air Mass Factor. 26, 32

AMTEX AtMospheric Trace EXperiment. 42, 111

AQD Air Quality Design NOx Chemiluminescence Analyzer. 33, 49, 50

ARINC Aeronautical Radio, Incorporated. 36, 45, 97

ATD Arizona Test Dust. 13

BAHAMAS Basic Halo Measurement and Sensor System. vii, 36, 44, 111

BIRA-IASB Royal Belgian Institute for Space Aeronomy. 10, 12

C-ToF-AMS Compact Time-of-Flight Aerosol Mass Spectrometer. vii, 37, 63, 65, 67, 68, 80, 81, 107–111, 137

CAFE-Africa Chemistry of the Atmosphere: Field Experiment in Africa. v, vii, viii, 2, 3, 19, 34, 36–39, 42–45, 47–49, 54–59, 61, 63–68, 75–79, 81–83, 85, 88–92, 95, 96, 103–107, 110–113, 115, 128–131, 137

CARIBIC Civil Aircraft for the Regular Investigation of the atmosphere Based on an Instrument Container. 51

CIMS Chemical Ionization Mass Spectrometer. 2, 42, 44, 45, 65–68, 82, 111

CMAQ Community Multiscale Air Quality. 82

COSMO Consortium for Small-scale Modeling. 38

CTM Chemical Transport Model. 37, 49

DLR Deutsches Zentrum fuer Luft and Raumfahrt. 2, 19, 36, 137

DOAS Differential Optical Absorption Spectroscopy. v, vii, viii, 2, 3, 9, 19–22, 25, 32, 33, 49, 51, 53, 83, 95, 97, 99, 100

DOASIS DOAS Intelligent System. 20

ECHAM ECMWF Hamburg. 37

ECMWF European Centre for Medium-Range Weather Forecasts. 38

EMAC ECHAM/MESSy Atmospheric Chemistry. v, vii, 2, 19, 27, 28, 30, 35, 37, 39, 49, 54–57, 68, 81–83, 95

EMeRGe Effect of Megacities on the Transport and Transformation of Pollutants on the Regional to Global Scales. v, vii, viii, 2, 3, 19, 29, 33–42, 44, 45, 47–52, 54–59, 61, 63, 68–75, 79–82, 95, 96, 103–109, 111–113, 115, 118–127, 137

FAAM Facility for Airborne Atmospheric Measurements. 33, 49, 50, 95

FAIRO Fast AIRborne Ozone. vii, 37, 42, 57, 111

FLEXPART FLEXible PARTicle. 39

FOV Field of View. 19

FWHM Full Width Half Maximum. 19

FZJ Forschungszentrum Juelich. 37

HALO High Altitude Long-range research aircraft. v, vii, 2, 3, 19, 21, 33, 36, 37, 39, 41–43, 45, 49–52, 55, 57, 64, 65, 69, 70, 72, 73, 75–77, 79–83, 95–97, 111, 118, 119, 122–124, 128, 129

HKMS Proton transfer reaction mass spectrometer. 33, 40–42, 45, 49–52, 111, 137

HORUS HydrOxyl Radical measurement Unit based on fluorescence Spectroscopy. 44, 57, 75, 111

HYSPLIT Hybrid Single-Particle Lagrangian Integrated Trajectory. 39

IDS Image Development Systems. 19, 44

IMK Institute for Meterology and Climate Research. 37, 42, 137

IPA Institute of Atmospheric Physics. 42

ISRF Instrumental Spectral Response Function. 97

ISS International Space Station. 28

ITCZ Intertropical Convergence Zone. 42

IUP Institut fur Umweltphysik. 42

IUPAC International Union for Pure and Applied Chemistry. 85, 88–90

JPL Jet Propulsion Laboratory. 6

KIT Karlsruhe Institute of Technology. 42, 137

KORUS-AQ Korea-United States Air Quality. 13

LIDAR light detection and ranging. 28

LIVAS LIdar climatology of Vertical Aerosol Structure for space-based lidar simulation studies. 28

MBL Marine Boundary Layer. 3, 48, 49, 51, 56, 63, 67, 82, 95

MECO(n) MESSy-fied ECHAM and COSMO/MESSy models nested n times. v, vii, 2, 19, 28, 35, 37–39, 49, 54–56, 68, 81, 95

MMS Proton transfer reaction time-of-Flight mass spectrometer. 43, 44, 77, 78, 111, 128–131

MPC Major Population Centers. 9, 39

MPIC Max Planck Institute for Chemistry. 37, 43, 44, 83, 137

NASA National Aeronautics and Space Administration. 6

NCAR National Center for Atmospheric Research. 13

NOAA National Oceanic and Atmospheric Administration. 51

NOAH Nitrogen Oxides Analyser on HALO. 43, 44, 57, 111, 113

NSF National Science Foundation. 13

OD Optical Depth. 20, 24, 27

OMPS Ozone Mapping and Profiler Suite. 28

PBL Planetary Boundary Layer. 2, 12, 50, 51, 54

PCA Principle Component Analysis. 33

PeRCEAS Peroxy Radical Chemical Enhancement and Absorption Spectrometer. 42, 45, 57, 111

PSS PhotoStationary State. 1, 16, 57, 63, 75, 83, 96

RMS Root Mean Square. 21, 22, 100

SAGE Stratospheric Aerosol and Gas Experiment. 28

SCD Slant Column Density. 19, 20, 22, 24–27, 29–33, 35, 100

SKY-OPC Optical Particle Counter in C-ToF-AMS. vii, 37, 42, 59, 68, 111

SOA Secondary Organic Aerosol. 8, 82

SP2 Single Particle Soot Photometer. vii, 37, 68, 111

SSA Single Scattering Albedo. 28

SZA Solar Zenith Angle. 13, 16

TROPOMI Tropospheric Monitoring Instrument. 9, 10, 12

UTC Coordinated Universal Time. 112

UV ultraviolet. vii, viii, 5–7, 13, 16, 19, 21, 23–25, 28, 32, 33, 35, 37, 47, 49, 50, 57, 99, 103, 105, 106, 113

VCD Vertical Column Density. 10–12

VMR Volume Mixing Ratio. 1, 5, 7–10, 19, 26–28, 31, 33, 35–37, 41–43, 47–50, 52–55, 57, 58, 63–66, 68–83, 85, 95, 96, 103–106, 113, 114, 118–131

VOC Volatile Organic Compound. vii, viii, 6–8, 10–13, 15, 17, 41, 42, 45, 47, 72, 80–82, 97, 113–115

WMO World Meteorological Organisation. 5

Chapter 1

Introduction

> We put everything, everything in doubt... What we find today, tomorrow we will erase from the blackboard and we will not write any more, at least until we find it again the day after that. If some discoveries follow our predictions, we will look on them with particular distrust... And only when we have failed, when beaten and without hope we are reduced to licking our wounds, then with iron in our souls we will begin to ask ourselves if we might not be right after all.
>
> Bertolt Brecht

In the Anthropocene, the effects of air pollution on human health are of increasing concern [Lelieveld et al., 2015]. In polluted environments, one of the key species in the production of photochemical smog is the hydroxyl radical (OH). Sources of the hydroxyl radical need to be well quantified in order to understand the ozone production and oxidation capacity within polluted air masses. One such source of the hydroxyl radical is the photolysis of nitrous acid.

For some time it has been known that nitrous acid (HONO) is a key species in atmospheric photochemistry, in particular in the polluted environment, due to its effects on the formation of hydroxyl radicals (OH) and its potential to recycle reactive nitrogen (e.g., Perner and Platt [1979]; Platt et al. [1980]; Jacob [2000]; Zhou et al. [2001]; Alicke et al. [2003]; Kleffmann et al. [2005]; Acker et al. [2006]; Zhang et al. [2009]; Li et al. [2014]; Ye et al. [2016b, 2017, 2018], and others). Near the ground, OH produced by the photolysis of HONO may outpace OH production from the reaction of $O(^1D)$ with H_2O, especially in the morning.

However, past studies — mainly performed at the ground — revealed much larger HONO Volume Mixing Ratio (VMR)s (up to some ppb) and source strengths (up to several ppb h^{-1}) than the well known gas phase formation reaction (1.1), and destruction by photolysis (1.2) and reaction with the OH radical (1.3) can explain (e.g., Kleffmann et al. [2005]; Acker et al. [2006]; Villena et al. [2011]; Wang et al. [2015]; Tong et al. [2016], and many others).

$$\mathrm{NO + OH + M \longrightarrow HONO + M} \tag{1.1}$$

$$\mathrm{HONO} + \mathrm{h}\nu(\lambda < 579\ \mathrm{nm}) \longrightarrow \mathrm{OH + NO} \tag{1.2}$$

$$\mathrm{HONO + OH \longrightarrow NO_2 + H_2O} \tag{1.3}$$

In consequence of reactions 1.1 to 1.3, in a PhotoStationary State (PSS) the HONO concentration can be calculated from

$$[\mathrm{HONO}] = \frac{\mathrm{k}_{1.1}[\mathrm{NO}][\mathrm{OH}]}{\mathrm{J_{HONO}} + \mathrm{k}_{1.3}[\mathrm{OH}]} \tag{1.4}$$

which can serve as a benchmark against which HONO measurements should be compared to quantify HONO sources in excess of predictions of equation 1.4. Since in near surface measurements in the polluted environment reaction 1.1 was often found to be insufficient to explain measured HONO, a large set of homogeneous and heterogeneous reactions were investigated, mostly in laboratory studies which are discussed in the following and tabulated in table 2.1.

It is now generally accepted that in the polluted boundary layer and lower atmosphere, in addition to reaction 1.1, HONO is mainly produced by heterogeneous reactions involving NO_x on macroscopic surfaces (e.g., infrastructure and vegetation), and/or on the surface and/or in the bulk of atmospheric aerosols (e.g., Lammel and Cape [1996]; Ammann et al. [1998]; Reisinger [2000]; Kleffmann et al. [2003]; Monge et al. [2010]; Ma et al. [2013a]; Cheng et al. [2016]; Tong et al. [2016]; Lu et al. [2018], and many others). It also has been recognized that its production can be greatly enhanced by the presence of organics tied to surfaces and potentially within the aerosol when exposed to sunlight (e.g., George et al. [2005]; Stemmler et al. [2006]; Scharko et al. [2014]; Wang et al. [2015]; Laufs and Kleffmann [2016]; Benedict et al. [2017]; Ye et al. [2017], and others). In addition, photolysis of HNO_3 tied to surfaces including those of vegetation [Zhou et al., 2003, 2007] and snow pack [Zhou et al., 2001] has also been suggested as a major daytime HONO source in low-NO_x environments. Moreover, different HONO sources in the topsoil have also recently been identified, which are mostly mediated by nitrate to nitrite reducing soil bacteria (e.g., Su et al. [2011]; Oswald et al. [2013]; Wu et al. [2019]). The photolysis of particulate nitrate (pNO_3) has also been frequently discussed in the literature [Ye et al., 2016a; Reed et al., 2017; Andersen et al., 2023]. These HONO formation mechanisms have been summarized in several review papers [Kleffmann, 2007; Ma et al., 2013b; Spataro and Ianniello, 2014].

While previous investigations mostly addressed HONO in near surface air, where the formation of HONO in the gas phase (reactions 1.1 to 1.3), by heterogeneous reactions on and within the aerosol, on macroscopic surfaces and within the topsoil may simultaneously act and therefore can hardly be distinguished, to date only few studies addressed HONO in air of the upper Planetary Boundary Layer (PBL) and in the free troposphere. There, the contribution from the ground and thus from the soil and macroscopic surfaces can largely be excluded, at least during the day when the HONO lifetime ($\sim$ 10 min) (equations 1.2 and 1.3) is significantly shorter than the timescale for vertical transport (e.g., Ye et al. [2018]). Previous airborne studies of HONO include those of Zhang et al. [2009]; Li et al. [2014]; Neuman et al. [2016]; Ye et al. [2016b, 2018] and Andersen et al. [2023].

In airborne investigations, most commonly used to measure HONO are wet chemical techniques such as long-path absorption photometry (often abbreviated LOPAP) (e.g., by Li et al. [2014]; Ye et al. [2016b, 2018])). It is based on ambient air sampling and collection of HONO in a stripping coil by a fast chemical reaction and converted into an azo dye, which is photometrically detected in long path absorption in a special Teflon tubing [Heland et al., 2001]. Other wet chemical techniques such as HPLC described in Huang et al. [2002] have also been employed to detect HONO [Zhang et al., 2009].

Recently, CIMS (e.g. Neuman et al. [2016]), DOAS (e.g. Heue et al. [2014], and here, see below) have also been employed in airborne HONO studies. Evidently, each technique comes with specific strengths and weaknesses, but recent comparison studies indicated a reasonable agreement among the various instruments for the detection of HONO, at least in comparison exercises of large HONO mixing ratios (in the ppb range) such as those met in the polluted environment [Crilley et al., 2019].

Despite decades of research, the formation and presence of HONO in the real atmosphere remains poorly quantified. This work attempts to reconcile observed HONO with the proposed HONO formation mechanisms. It accomplishes this with airborne measurements of a variety of species necessary for the formation of HONO. Because of the short lifetime of HONO in the atmosphere ($\sim$ 10 min at noon), airborne observations are less influenced by direct HONO emissions at the surface and can therefore be used to quantify in situ production. An overview of the heretofore proposed HONO formation mechanisms potentially relevant for the present thesis (i.e. excluding ground processes) is given in table 2.1. A more detailed description can be found in section 2.1. Some mechanisms (in particular mechanisms 1, 2, 3, 4, and 6) have been shown to be insufficient to explain daytime observations of HONO (for details see the comments at the bottom of table 2.1).

This thesis investigates the presence and potential formation mechanisms of HONO throughout the troposphere in different photochemical environments probed by the German High Altitude Long-range research aircraft (HALO) over Europe, East Asia, and the tropical Atlantic. Using a novel airborne DOAS instrument [Hüneke et al., 2017; Stutz et al., 2017], remote sensing measurements of nitrous acid, formaldehyde, and nitrogen dioxide, are reported from twenty five scientific flights of the HALO aircraft operated by the Deutsches Zentrum fuer Luft and Raumfahrt (DLR). Our limb Differential Optical Absorption Spectroscopy (DOAS) measurements are complemented by simultaneous in situ measurements of photo-chemically related trace gases, as well as measurements of relevant atmospheric parameters performed by other instruments on board the HALO aircraft. For the studied research missions, Effect of Megacities on the Transport and Transformation of Pollutants on the Regional to Global Scales (EMeRGe) (2017/2018) and Chemistry of the Atmosphere: Field Experiment in Africa (CAFE-Africa) (2018), ECHAM/MESSy Atmospheric Chemistry (EMAC) and MESSy-fied ECHAM and COSMO/MESSy models nested n times (MECO(n)) model data is also available for comparison. In these comparisons it is found that while the retrieved HCHO and NO_2 compare well with those models' predictions (and with in situ instruments), the observed concentrations of nitrous acid are in excess of those predictions in the polluted boundary layer and adjacent lower troposphere. Further, measured HONO in the low-NO_x Marine Boundary Layer (MBL) compares well with previous studies [Andersen et al., 2023]. Surprisingly, our measured HONO in the upper troposphere is also larger than predicted, which due to the low rate for uptake of precursor gases (e.g. HNO_3) onto aerosol particles suggests the existence of a hitherto unknown gas phase source of HONO at cold temperatures. The co-measured trace gas species and atmospheric parameters are combined with the remote sensing limb observations to investigate potential sources of this excess nitrous acid in the various seasons, regions of the globe, and layers of the troposphere. Specifically: within the low-NO_x MBL, observed HONO may be formed by the photolysis of particulate nitrate. In more polluted air of the lower troposphere, heterogeneous formation mechanisms may explain the observed excess HONO, but cannot be attributed to a precise mechanism with the instrumentation available. Finally, within the cold upper troposphere, observed HONO may potentially be explained by gas phase oxidation of peroxynitrous acid, for which suitable formation mechanisms exist [Amedro et al., 2020], since loss by thermal decomposition at low temperatures is slow. The formation and destruction of peroxynitrous acid in the upper troposphere may explain our HONO observations as well as the yet unexplained Leighton ratio observations at those altitudes [Silvern et al., 2018], without perturbing the HO_x budget [Roland, 2022].

Outline of this thesis

The thesis is organized as follows: chapter 2 describes the relevant photochemical context of the studied trace gases in the troposphere. Chapter 3 describes the mini-DOAS instrument, the DOAS measurement technique and the scaling method, as well as the additional instrumentation on board the HALO aircraft and the features of the photochemical transport models described above. Chapter 4 describes the research missions of the HALO aircraft on which the mini-DOAS was deployed: EMeRGe-EU in summer 2017, EMeRGe-Asia in spring 2018 and CAFE-Africa in fall 2018. Chapter 5 presents the measurements of formaldehyde, nitrogen dioxide, and nitrous acid observed by the mini-DOAS instrument. These measurements are compared with measurements by in situ instrumentation, with model predictions, and combined with other measurements to investigate the oxidation capacity in the observed air masses. Chapter 6 investigates and discusses the potential formation mechanism(s) of excess nitrous acid in the lower and upper troposphere. Chapter 7 summarizes and concludes the study.

Chapter 2

Background

The earth's atmosphere is divided into layers, which can be categorized according to their thermal structure. This thesis is concerned primarily with the lower atmosphere: i.e. the troposphere and the lowermost stratosphere. The troposphere is the lowest layer of the atmosphere, which is prone to convection driven by solar heating at the surface and the release of latent heat. It is also the layer into which most natural and anthropogenic pollutants are emitted, and is therefore the focus of the present thesis. Within the troposphere, temperature and pressure — and thereby the total number density[1] — decrease with increasing altitude from the earth's surface. This negative lapse rate (-6 to -7 K km^{-1}) promotes vertical mixing when warmer air rises and latent heat is released, causing the troposphere to be well mixed and turbulent. The troposphere is separated from the layer above it, the stratosphere, by the tropopause, where the vertical temperature structure is primarily dominated by radiative processes [Gettelman et al., 2011].

There are various definitions for the tropopause, but here we will use the World Meteorological Organisation (WMO) definition [WMO and OMM, 1966]: the tropopause is where the lapse rate has increased to -2 K km^{-1}. The height of the tropopause varies with season and decreases with increasing latitude, from 18 km in the tropics to only 6 km near the poles. The stratosphere, in contrast to the troposphere, is stratified due to radiative heating and cooling, and contains very little water. The stratosphere extends from the top of the tropopause to ≈ 60 km and is characterized by the increasing influence of downward short wave solar radiation and upward long wave radiation. The increasing temperature with altitude — or positive lapse rate — inhibits vertical mixing, leading to the stratification.

It is the mixing of trace gases within the troposphere — and the influence of solar radiation — which initiates tropospheric photochemistry. Within the troposphere, atmospheric trace gases have vertical gradients driven by natural and anthropogenic emissions at the surface as well as production of intermediates within the troposphere. The residence time of a trace gas in the atmosphere is determined by atmospheric chemistry, driven by the presence of sunlight, as well as by uptake on aerosols by dry and wet deposition. Air pollutants emitted in the troposphere often have diurnal cycles driven by daylight, while the long life time of some trace gases lead to their presence in extended spatial scales; they may be carried thousands of kilometers before being removed from the atmosphere (see figure 2.1).

This chapter introduces the key concepts in tropospheric photochemistry relevant to this thesis. A more comprehensive overview of the photochemistry of the troposphere is beyond the scope of this thesis, as tropospheric photochemistry is multifaceted, but there are several excellent text books and reviews available [Crutzen, 1988; Finlayson-Pitts and Pitts Jr, 1999; Seinfeld and Pandis, 2016]. Rather, the objective here is to introduce the relevant concepts, species, and reactions, to provide the appropriate background and context. The photo-chemically active trace gases common to the troposphere are described in section 2.1. Special attention is given to those trace gases accessible to ultraviolet (UV)/visible limb spectroscopy and to those which contribute to the oxidative capacity of the atmosphere. The Leighton relationship is defined in section 2.2, and the oxidation capacity of the atmosphere is defined in section 2.3. The reactions

---

[1] When comparing concentrations of gases within different layers of the atmosphere, the exponentially decreasing (with altitude) total number density of the atmosphere can cause confusion. Therefore, VMRs (ppm = 10^{-6}, ppb = 10^{-9}, ppt = 10^{-12}) are preferred, and will be used instead of concentrations throughout this study unless otherwise specified.

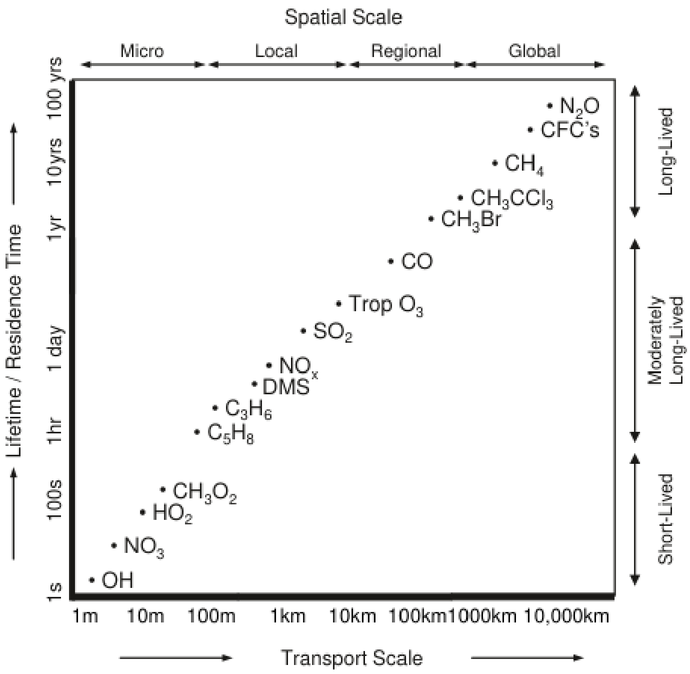

Figure 2.1: The lifetime of a trace gas in the atmosphere can range from seconds to centuries. The consequent scale of transport of those gases ranges from meters to global distribution. Adapted from Seinfeld and Pandis [1998].

listed as well as the photolysis threshold wavelengths are taken from the most recent evaluation of National Aeronautics and Space Administration (NASA)'s Jet Propulsion Laboratory (JPL) [Burkholder et al., 2020] unless otherwise indicated.

2.1 Tropospheric photochemistry

Visible and UV light in the atmosphere carry enough energy (a few eV) to break molecular bonds. This photo-dissociation or photolysis is one of the primary loss mechanisms for atmospheric trace gases, air pollutants, and greenhouse gases. Together with oxidation, photolysis catalyzes the photochemistry of the atmosphere, by e.g. converting nitrogen oxides into ozone. This photochemistry is relevant to the conversion and production of air pollutants, and particularly concerns (but is not limited to) the following families of trace gases: ozone (O_3), hydrogen oxide radicals ($HO_x = OH + HO_2$), nitrogen oxides ($NO_x = NO + NO_2$), nitrous acid (HONO), Volatile Organic Compound (VOC)s, and others.

2.1.1 Formation and loss of ozone

Ozone (O_3) is a toxic oxidant, a greenhouse gas and a respiratory pollutant. A pale blue gas, it is named for its pungent odor. Most (90 %) of the ozone column in the atmosphere is found in the stratosphere, in the aptly named ozone layer, located between 20 and 30 km altitude. Ozone formation in the stratosphere and part of the troposphere is governed by the Chapman cycle [Salawitch et al., 2019]:

$$\mathrm{O_2 + h\nu(\lambda < 242\ nm) \longrightarrow 2O(^3P)} \tag{2.1}$$

$$\mathrm{O(^3P) + O_2 + M \longrightarrow O_3 + M} \tag{2.2}$$

$$\mathrm{O_3 + h\nu(\lambda < 411\ nm) \longrightarrow O_2 + O(^1D)} \tag{2.3}$$

$$\mathrm{O(^3P) + O_3 \longrightarrow 2O_2} \tag{2.4}$$

i.e. the photolysis of molecular oxygen by UV-C and ozone by UV and visible light. Here M represents a molecule which is necessary for the energy conservation of the reaction but otherwise unaffected by it, h is the Planck constant, ν is the frequency of the photon, and λ is the wavelength. The distinction between $O(^1D)$ and $O(^3P)$ indicates the electronic state of atomic oxygen, where $O(^3P)$ is the ground state, and $O(^1D)$ is an excited state. Ozone is formed when molecular oxygen is photolyzed, leading to combinations of atomic and molecular oxygen. The ozone then goes on to absorb UV radiation, and is itself photolyzed, reproducing molecular oxygen. The Chapman cycle overestimates ozone; there are additional catalytic loss processes of ozone. Figure 2.2 shows the relative distribution of ozone within the lower and middle atmosphere.

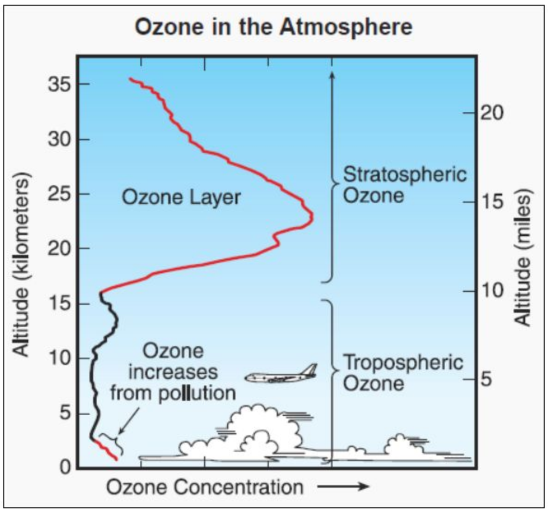

Figure 2.2: The relative concentration profile of ozone in the lower and middle atmosphere. Adapted from Salawitch et al. [2019].

While stratospheric ozone shields the earth from harmful UV-B and UV-C radiation, in the troposphere it acts as an air pollutant and respiratory irritant. In the troposphere, ozone is one of the major components affecting air quality. It is produced primarily by the photolysis of nitrogen dioxide:

$$NO_2 + h\nu(\lambda < 398 \text{ nm}) \longrightarrow NO + O(^3P) \tag{2.5}$$

$$O(^3P) + O_2 + M \longrightarrow O_3 + M. \tag{2.6}$$

Ozone is also formed indirectly by VOCs, e.g. the oxidation of methane (CH_4) in the presence of nitrogen oxides:

$$CH_4 + 4O_2 \longrightarrow HCHO + H_2O + 2O_3 \tag{2.7}$$

For more details see below.

Tropospheric ozone is then produced by nitrogen oxides as well as in a coupled cycle by VOCs in the presence of nitrogen oxides. Which production dominates depends on their relative mixing ratios. Figure 2.3 quantifies tropospheric ozone production as a function of the concentrations of VOCs and nitrogen oxides.

Ozone loss is primarily due to photolysis (eq. 2.3) or reaction with atomic oxygen, odd hydrogen, nitric oxide, halogens, and unsaturated VOCs [Brasseur and Solomon, 2005].

$$O(^3P) + O_3 \longrightarrow 2O_2 \tag{2.8}$$

or by reaction with nitric oxide:

$$O_3 + NO \longrightarrow NO_2 + O_2. \tag{2.9}$$

Otherwise, ozone in the troposphere is also removed by reaction with OH and HO_2:

$$OH + O_3 \longrightarrow HO_2 + O_2 \tag{2.10}$$

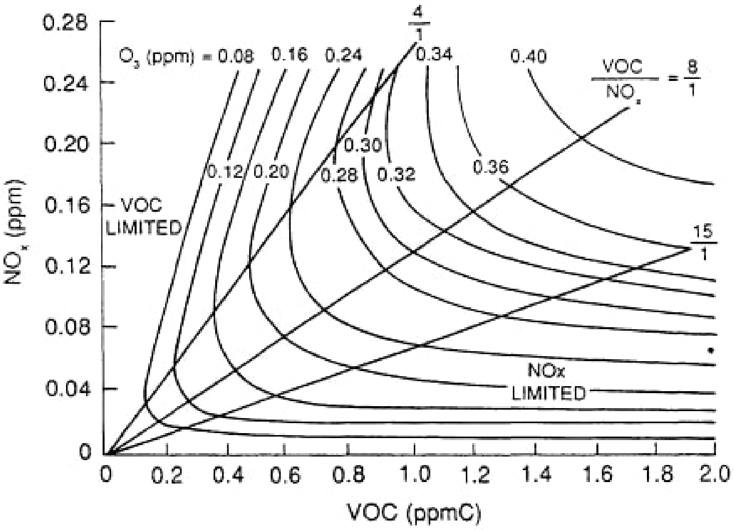

Figure 2.3: Ozone production in polluted air masses can be characterized as NO_x-limited or VOC-limited. Here the isopleths represent ozone VMRs, for a given [VOC]/[NO_x] ratio. Ozone production is typically VOC-limited where [VOC]/[NO_x] $<$ 4:1, and NO_x-limited where [VOC]/[NO_x] $>$ 15:1. The figure is from Council et al. [1991].

$$HO_2 + O_3 \longrightarrow OH + 2O_2 \tag{2.11}$$

Ozone is moderately long-lived in the troposphere (see figure 2.1). Local ozone VMRs in the troposphere are measured in the parts per billion. Ozone concentrations in the atmosphere are generally monitored from satellites to for example detect the recovery of the stratospheric ozone hole or to measure air pollution in the troposphere.

2.1.2 Hydrogen oxide radicals

The hydrogen oxide radicals ($HO_x = OH + HO_2$) are critical species for the oxidation capacity of the atmosphere. Both species are short-lived (see figure 2.1).

The hydroyxl radical

OH rapidly reacts with most species, which is the primary loss mechanism for most trace gases in the atmosphere. The primary oxidant of the atmosphere, the hydroxyl radical is present only in the parts per trillion and lower. It is extremely short-lived with a typical lifetime of < 1 s. Commonly referred to as the atmospheric detergent, it converts NO_x to NO_y, destroys most VOCs, and contributes to the formation of Secondary Organic Aerosol (SOA) via the oxidation of VOCs. It is produced by the photolysis of ozone (equation 2.3) in the presence of water vapor. The photolysis of ozone produces excited atomic oxygen, and its consequent reaction with water vapor is the primary source of OH in the atmosphere.

$$O_3 + h\nu(\lambda < 411 \text{ nm}) \longrightarrow O_2 + O(^1D) \tag{2.12}$$

$$O(^1D) + H_2O \longrightarrow 2OH. \tag{2.13}$$

OH is also produced by the photolysis of HONO.

$$HONO + h\nu(\lambda < 579 \text{ nm}) \longrightarrow OH + NO \tag{2.14}$$

and by the ozonolysis of alkenes. Which photolytic production term dominates the OH budget depends on the local VMRs of the respective trace gases.

Hydroperoxyl radical

HO_2 acts as a reservoir for OH and is produced by the oxidation of VOCs, as well as by the oxidation of hydrogen peroxide:

$$\mathrm{OH} + \mathrm{H_2O_2} \longrightarrow \mathrm{HO_2} + \mathrm{H_2O} \tag{2.15}$$

which is in turn produced by OH and HO_2:

$$\mathrm{OH} + \mathrm{OH} + \mathrm{M} \longrightarrow \mathrm{H_2O_2} + \mathrm{M} \tag{2.16}$$
$$\mathrm{HO_2} + \mathrm{HO_2} \longrightarrow \mathrm{H_2O_2} + \mathrm{O_2}. \tag{2.17}$$

HO_2 reacts with NO to produce NO_2 and OH.

$$\mathrm{NO} + \mathrm{HO_2} \longrightarrow \mathrm{NO_2} + \mathrm{OH}. \tag{2.18}$$

Local VMRs of HO_2 are about 10–50 times more abundant than OH and are measured in the parts per trillion. Because of the reactions between the HO_x and NO_x species, the HO_x budget is largely dependent on the NO_x budget [Jaeglé et al., 2001].

2.1.3 Nitrogen oxides

Nitrogen oxides ($NO_x = NO + NO_2$) are reactive radicals which affect the oxidation capacity of the atmosphere. While NO_x is produced naturally by biomass burning, lightning, and soil emissions, more than half of global NO_x emissions are anthropogenic (fossil fuel combustion, industrial activity, etc.) [Logan et al., 1981; Delmas et al., 1997].

Nitric oxide

NO is a colorless gas which is formed by combustion and by lightning, and is the primary component of most NO_x. It is also produced by the photolysis of NO_2 (equation 2.5). NO in the stratosphere is also produced by the oxidation of of the long-lived greenhouse gas, nitrous oxide (N_2O):

$$\mathrm{N_2O} + \mathrm{O(^1D)} \longrightarrow 2\mathrm{NO}. \tag{2.19}$$

Its reaction with ozone forms NO_2:

$$\mathrm{NO} + \mathrm{O_3} \longrightarrow \mathrm{NO_2} + \mathrm{O_2} \tag{2.20}$$

as does its reaction with HO_2:

$$\mathrm{NO} + \mathrm{HO_2} \longrightarrow \mathrm{OH} + \mathrm{NO_2} \tag{2.21}$$

(see section 2.2). A moderately long-lived species, local VMRs of NO are typically measured in the parts per billion.

Nitrogen dioxide

NO_2 is an atmospheric pollutant. It is short lived, with a lifetime against photolysis of approximately two minutes at noon. Brownish, with a chlorine-like scent, it can be fatal if inhaled in large quantities. A respiratory irritant, it is one of the primary components affecting air quality. While a significant amount of NO_2 is found in the stratosphere [Noxon, 1979], the relative fraction of the total NO_2 column found in the troposphere depends on local NO_x emissions. It is a weak greenhouse gas, and a precursor to acid rain. NO_2 is produced in the atmosphere by the reaction of NO with O_3 or HO_2 (see above).

Besides photolysis:

$$\mathrm{NO_2} + \mathrm{h}\nu(\lambda < 398\ \mathrm{nm}) \longrightarrow \mathrm{NO} + \mathrm{O(^3P)} \tag{2.22}$$

NO_2 is also removed from the atmosphere by oxidation, producing nitric acid.

$$\mathrm{NO_2} + \mathrm{OH} + \mathrm{M} \longrightarrow \mathrm{HNO_3} + \mathrm{M}. \tag{2.23}$$

Because rapid photolysis is a primary loss mechanism of NO_2, the concentration of NO_2 in the atmosphere has a diurnal cycle. The NO_2 produced builds up over night in the absence of sunlight, and is quickly photolyzed in the morning.

Because of its relevance to air quality, NO_2 is often observed from space borne instruments to monitor its concentration [Beirle et al., 2004, 2011]. Figure 2.4 shows the global column densities of NO_2 as measured by the Tropospheric Monitoring Instrument (TROPOMI) instrument. Enhanced column amounts are highly localized to densely populated areas, such as Major Population Centers (MPC)s and megacities. Airborne DOAS retrievals of NO_2 offer a high-resolution alternative to satellites and models for the monitoring of local NO_2 concentrations [Lamsal et al., 2017].

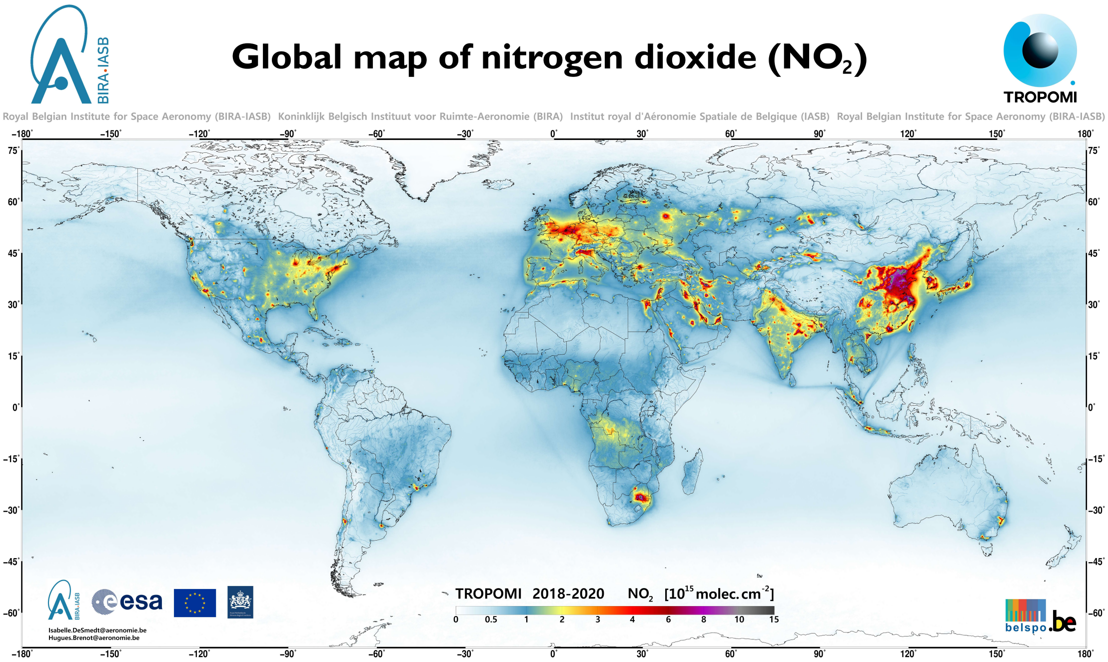

Figure 2.4: Global NO_2 Vertical Column Density (VCD)s [molec. cm^{-2}] from TROPOMI from 2018–2020. The figure is from `https://uv-vis.aeronomie.be/data/tropomi_posters/posterTROPOMI_NO2_2018_2020.pdf`, last access: November 2022. Copyright: Contains modified Copernicus Sentinel data processed by Royal Belgian Institute for Space Aeronomy (BIRA-IASB).

Nitric acid HNO_3 is a colorless, corrosive acid. It is considered the terminal product for most reactive nitrogen in the atmosphere, and is a major component of total reactive nitrogen (NO_y). It forms via the reaction of HO_x and NO_x species:

$$\mathrm{OH} + \mathrm{NO_2} + \mathrm{M} \longrightarrow \mathrm{HNO_3} + \mathrm{M} \tag{2.24}$$

$$\mathrm{NO} + \mathrm{HO_2} + \mathrm{M} \longrightarrow \mathrm{HNO_3} + \mathrm{M}. \tag{2.25}$$

It is removed from the atmosphere by deposition in acid rain, or otherwise photolyzed in a process called renoxification [Reed et al., 2017]:

$$\mathrm{HNO_3} + \mathrm{h}\nu(\lambda < 581\ \mathrm{nm}) \longrightarrow OH + NO_2. \tag{2.26}$$

$$\mathrm{HNO_3} + \mathrm{h}\nu(\lambda < 392\ \mathrm{nm}) \longrightarrow HONO + O(^3P) \tag{2.27}$$

This renoxification recycles reactive nitrogen in the atmosphere, albeit very slowly. Local VMRs of HNO_3 are usually measured in the parts per billion.

2.1.4 VOCs

The family of volatile organic compounds is a broad class of molecules with high vapor pressure at room temperature, including alkanes, alkenes, alkines, aromatics, and oxygenated VOCs.

Formaldehyde

HCHO is a colorless, noxious gas with a pungent odor, a respiratory irritant, and a VOC. It is produced naturally by the oxidation of methane and non-methane VOCs such as isoprene, as well as anthropogenically by combustion and biomass burning. The production from methane oxidation also produces ozone in the presence of NO_x:

$$\begin{aligned}
CH_4 + OH &\longrightarrow CH_3 + H_2O && (2.28)\\
CH_3 + O_2 + M &\longrightarrow CH_3O_2 + M && (2.29)\\
CH_3O_2 + NO &\longrightarrow CH_3O + NO_2 && (2.30)\\
CH_3O + O_2 &\longrightarrow HCHO + HO_2 && (2.31)\\
HO_2 + NO &\longrightarrow OH + NO_2 && (2.32)\\
2(NO_2 + h\nu) &\longrightarrow 2(NO + O(^3P)) && (2.33)\\
2(O(^3P) + O_2 + M) &\longrightarrow 2(O_3 + M) && (2.34)\\
\hline
CH_4 + 4O_2 &\longrightarrow HCHO + H_2O + 2O_3 && (2.35)
\end{aligned}$$

In the absence of NO_x, HCHO is produced without ozone formation:

$$\begin{aligned}
CH_4 + OH &\longrightarrow CH_3 + H_2O && (2.36)\\
CH_3 + O_2 + M &\longrightarrow CH_3O_2 + M && (2.37)\\
CH_3O_2 + HO_2 &\longrightarrow CH_3O_2H + O_2 && (2.38)\\
CH_3O_2H + h\nu &\longrightarrow CH_3O + OH && (2.39)\\
CH_3O + O_2 &\longrightarrow HCHO + HO_2 && (2.40)\\
\hline
CH_4 + O_2 &\longrightarrow HCHO + H_2O && (2.41)
\end{aligned}$$

In these reaction chains, reaction 2.30 leads to the production of ozone, (reactions 2.33 and 2.34), while reactions 2.39 and 2.40 are major sources of HO_x.

The presence of HCHO is generally indicative of the presence of other VOCs. Because of the terrestrial sources of formaldehyde, the altitude profile of HCHO in the atmosphere generally decays exponentially with altitude from the surface. The lifetime of HCHO in the atmosphere is several hours (a moderately long-lived species), as the primary removal by photolysis is slow.

$$\begin{aligned}
HCHO + h\nu(\lambda < 361\ \text{nm}) &\longrightarrow H_2 + CO && (2.42)\\
HCHO + h\nu(\lambda < 330\ \text{nm}) &\longrightarrow H + HCO. && (2.43)
\end{aligned}$$

Otherwise, HCHO is itself oxidized by OH.

$$HCHO + OH \longrightarrow HCO + H_2O. \qquad (2.44)$$

The HCO radical produced by the photolysis or oxidation of HCHO, reacts with O_2 and produces HO_2

$$HCO + O_2 \longrightarrow HO_2 + CO \qquad (2.45)$$

while CO is slowly converted to CO_2 by oxidation with OH. The photolysis of HCHO is therefore another source of HO_x in the troposphere.

Formaldehyde is often detected from space borne instruments to monitor its concentration in the atmosphere [Wittrock et al., 2006]. Figure 2.5 shows the global HCHO VCDs as measured by the TROPOMI instrument. The production from isoprene emissions in tropical forests drives the enhancements in those regions.

2.1.5 Formation and loss of nitrous acid

Nitrous acid (HONO) is an important source of the OH radical in the troposphere. The formation of HONO is not well understood, and measurements of its concentration in the troposphere are often in excess of model predictions based on gas phase formation alone. The gas phase formation of HONO is determined by the concentrations of OH and NO:

$$OH + NO + M \longrightarrow HONO + M \qquad (2.46)$$

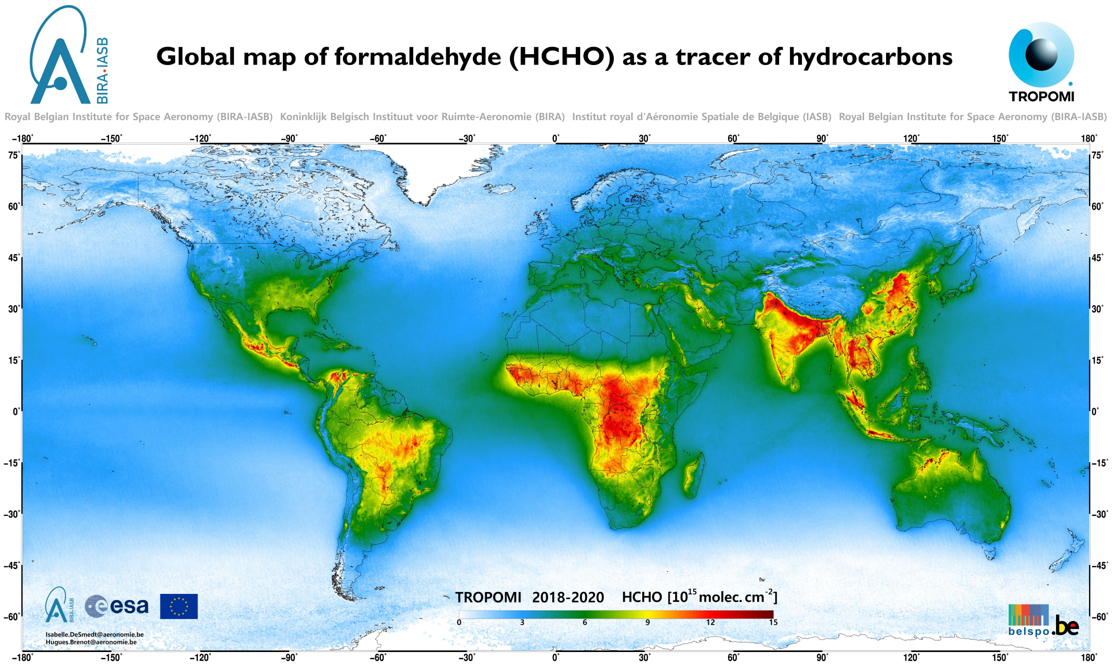

Figure 2.5: Global HCHO VCDs [molec. cm^{-2}] measured from TROPOMI from 2018–2020. The figure is from `https://uv-vis.aeronomie.be/data/tropomi_posters/posterTROPOMI_HCHO_2018_2020.pdf`, last access: November 2022. Copyright: Contains modified Copernicus Sentinel data processed by BIRA-IASB.

as well as by the disproportionation of NO_2, which at large NO_2 concentrations may lead to the buildup of HONO overnight:

$$2NO_2 + H_2O \longrightarrow HONO + HNO_3. \tag{2.47}$$

The loss of HONO is primarily due to its photolysis.

$$HONO + h\nu(\lambda < 579\ \text{nm}) \longrightarrow OH + NO. \tag{2.48}$$

The lifetime of HONO against photolysis is approximately ten minutes at solar noon. Loss by reaction with OH also removes HONO from the atmosphere:

$$HONO + OH \longrightarrow H_2O + NO_2. \tag{2.49}$$

but is typically much slower because of low OH concentrations. Because HONO produces OH upon photolysis, its concentration in the lower atmosphere is critical to the oxidation capacity of the troposphere, particularly around noon.

Numerous studies have attempted to elucidate the formation of HONO in recent decades. The hydrolysis of NO_2 on aerosol surfaces is a well-known HONO source [Finlayson-Pitts et al., 2003] (mechanism 6 in table 2.1). However, measured uptake coefficients are too small to explain HONO formation in the atmosphere. Othere heterogeneous reacitons may thus be of higher importance, see below.

A gas phase source of HONO potentially non-negligible in the polluted environment has also been proposed by Bejan et al. [2006], i.e. the photolysis of ortho-nitrophenols (mechanism 2 in table 2.1). Another gas phase mechanism, the photo-excitation of NO_2, was proposed by Li et al. [2008] (mechanism 4 in table 2.1). However, the rate coefficient is too low to render HONO produced by photo-excitation efficient [Crowley and Carl, 1997; Amedro et al., 2011]. The reaction of nitric acid and VOCs in diesel exhaust [Rutter et al., 2014] (mechanism 9 in table 2.1) may be either a gas phase or heterogeneous HONO formation mechanism [Spataro and Ianniello, 2014].

Ammann et al. [1998]; Kalberer et al. [1999]; Kirchner et al. [2000] and later Monge et al. [2010] investigated the formation of HONO on soot (mechanism 5 in table 2.1). It was found that the uptake coefficients of NO_2 varied over 7 orders of magnitude from 10^{-1} to 10^{-8} with HONO yields ranging from a few percent to about 100 % [Ammann et al., 1998]. Soon thereafter it was determined that the NO_2 to HONO reaction on soot rapidly saturates due to a deactivation of reactive sites and thus it cannot be the main source of HONO in the PBL [Kalberer et al., 1999]. Later Monge et al. [2010] found that the efficiency of the reaction with NO_2 drastically increases in the presence of artificial solar radiation, presumably due to photolytic activation of polycyclic aromatic hydrocarbons (PAH) such as pyrene, which is ubiquitous in soot. However, it was found to decline over short time as well as with increasing relative humidity in the dark. Since in the polluted atmosphere all ingredients are available in sufficient quantities, they concluded that soot photo-chemistry of HONO may be a key player in urban air pollution at least during daytime. Further, the study of George et al. [2005] indicated that uptake of NO_2 on phenolic species is significantly enhanced with an uptake coefficient in the range of 10^{-6} or higher, when irradiated with light of 300 – 420 nm, and that HONO is formed with a high yield (50 – 100 %) when the gas is humidified (mechanism 12 in table 2.1). See also [Stemmler et al., 2007].

The reaction of NO_2 on hydrated mineral Arizona Test Dust (ATD) and the formation of HONO was studied by Ndour et al. [2008]; Dupart et al. [2014] and others (mechanism 7 in table 2.1). The general observation was that in the dark, the uptake on dust aerosols is rather negligible (e.g., Goodman et al. [1999], and others), while a strong enhancement of the NO_2 uptake is observed under UV irradiation ($<$ 400 nm) with similar observations made for grounded Saharan sand and ATD. Measured uptake coefficients ranged from $0.12 \cdot 10^{-6}$ to $1.9 \cdot 10^{-6}$ [Ndour et al., 2008] and $(0.6 \pm 0.3) \cdot 10^{-8}$ to $(2.4 \pm 0.4) \cdot 10^{-8}$ with a HONO yield of 30 % for dust particles [Dupart et al., 2014]. Taking these numbers, this process can potentially be important in the polluted dust-loaded atmosphere (e.g. in the North Chain plain), depending on the prevailing mineral dust concentration and possibly dust type.

The photolysis of adsorbed HNO_3 on quartz glass surfaces was studied by Laufs and Kleffmann [2016]. Due to its small photolysis frequency $J(HNO_3 \rightarrow HONO)$ ($2.4 \cdot 10^{-7}$ s^{-1} at SZA $=$ 0° for a relative humidity of 50 %), they concluded that renoxification by photolysis of adsorbed HNO_3 on non-reactive surfaces is likely a minor process in the atmosphere (mechanism 8 in table 2.1). In the laboratory, the photolysis of pNO_3 has been investigated by Mark et al. [1996]; Scharko et al. [2014]; Ye et al. [2017] and others (mechanism 13 in table 2.1). Mark et al. [1996] photolyzed aqueous nitrate solutions at 254 nm in the absence of oxidizable additives, but in the presence of methanol or propan-2-ol and oxygen as well as cyclopentane under anaerobic conditions. For acid solutions, i.e. pH values in the 4–7 range, they found that the major products were $NO_2 + O^-$ (quantum yield 0.09 – 0.1) and not ${NO_2}^- + O$ (quantum yield $<$ 0.001), the latter of which could result in HONO. In their photolysis study of pNO_3, Scharko et al. [2014] focused on the formation of HONO (rather than on the direct photolysis products NO_2 and ${NO_2}^-$), and they found that nitrous acid is formed in higher quantities at pH 2 – 4 (a factor of 4) than expected based on consideration of primary photochemical channels alone. Both experimental and modeled results indicated that the additional HONO is not due to an enhanced ${NO_3}^-$ absorption cross-sections or effective quantum yields, but rather to secondary reactions of NO_2 in solution. They further concluded that NO_2 might be more efficiently hydrolyzed in solution when it is generated in situ during ${NO_3}^-$ photolysis than for the heterogeneous systems where mass transfer of gaseous NO_2 into bulk solution is prohibitively slow. Further, the presence of non-chromophoric OH scavengers (they alternatively used ethylene glycol or sodium benzoate) that are often in aerosols increased HONO production 4-fold, therefore they may play an important role in enhancing daytime HONO formation from ${NO_3}^-$ photochemistry.

More recently Benedict et al. [2017] determined the quantum yield ($\phi({NO_2}^-)$) of the photolysis of ${NO_3}^-$ to 1.1 ± 0.2 % (at 313 nm, 50 μM nitrate, pH $\geq$ 5) and noted that it is of similar size as the NO_2 channel. They convincingly demonstrated that the larger $\phi({NO_2}^-)$ yield than previously estimated is primarily due to the presence of an OH scavenger. They also argued that the apparent decrease in $\phi({NO_2}^-)$ for pH $<$ 4.5 is due to release of HONO into the gas phase rather than a change in scavenging. Next, Ye et al. [2017] sampled filters on the National Science Foundation (NSF)-National Center for Atmospheric Research (NCAR) C-130 aircraft and studied the photolysis frequency of pNO_3 ($J(HNO_3(l))$) later measured in the laboratory (median of $8.3 \cdot 10^{-5}$ /s, range $6.2 \cdot 10^{-6}$ /s – $5.9 \cdot 10^{-4}$ /s). In agreement with the studies mentioned above, they further noted that chemical compositions, specifically nitrate loading and organic matter, may affect the rate of photolysis. Somewhat in contrast to the findings of the above-mentioned studies, based on in situ observations of NO_x and HNO_3 collected during the

Korea-United States Air Quality (KORUS-AQ) (and other) research mission, Romer et al. [2018] constrained the aerosol NO_3^- photolysis frequency to $J(HNO_3(l)) = EF \cdot J(HNO_3(g))$ where EF < 30, or $\sim 6 \cdot 10^{-6}$ s^{-1} in the studied air masses.

Field measurements of the photolysis of particulate nitrate conducted by Andersen et al. [2023] in low-NO_x environment of the marine boundary layer found that the enhancement factor depends on the nitrate load as well as on relative humidity. From these studies, it became clear that the efficiency of the pNO_3 photolysis may largely depend on the chemical environment, in particular on the aerosol composition and pH, as well as the presence of non-chromophoric OH scavengers (cf. solvable VOC, etc). Therefore, without detailed knowledge of the chemical composition of the aerosol, individual studies on HONO formation can hardly be compared.

More recently, studies conducted in China provide evidence for ammonium promoted hydrolysis of NO_2 [Li et al., 2018a; Xu et al., 2019] as well as the oxidation of sulfates Cheng et al. [2016]; Li et al. [2018b] by NO_2 producing HONO during haze events (mechanisms 10 and 11 in table 2.1). Which of the many proposed heterogeneous formation mechanisms of HONO are relevant in the atmosphere may thus depend on the specific character of the investigated air masses.

Table 2.1: Homogeneous (gas phase) and heterogeneous (mixed phase) HONO formation mechanisms investigated in past studies.

No.	Reactants		Products	Reference	Comment
		Gas phase reactions			
1	$NO + OH + M$	$\longrightarrow$	$HONO + M$	Sander et al. [2011]	(i)
2	ortho-nitrophenols + hν	$\longrightarrow$	HONO + products	Bejan et al. [2006]	(ii)
3	$HO_2 \cdot H_2O + NO_2$	$\longrightarrow$	$HONO + O_2 + H_2O$	Li et al. [2014]	(iii)
				Ye et al. [2015]	
4	$NO_2 + h\nu$	$\longrightarrow$	$NO_2{}^*$	Crowley and Carl [1997]	(iv)
	$NO_2{}^* + H_2O$	$\longrightarrow$	$HONO + OH$	Amedro et al. [2011]	
		Mixed phase reactions			
5	$NO_2 + HC_{red}$	$\longrightarrow$	$HONO + HC_{ox}$	Ammann et al. [1998]	(v)
				Kalberer et al. [1999]	
				Monge et al. [2010]	
6	$2NO_{2(g)}$	$\longleftrightarrow$	$N_2O_{4(g)}$	Goodman et al. [1999]	(vi)
	$N_2O_{4(g)}$	$\longleftrightarrow$	$N_2O_{4(surface)}$	Finlayson-Pitts et al. [2003]	
	$N_2O_{4(surface)}$	$\longrightarrow$	$ONONO_{2(surface)}$	Yabushita et al. [2009]	
	$ONONO_{2(surface)} + NO_{2(g)}$	$\longrightarrow$	$N_2O_{4(surface)} + NO_{2(g)}$	Martins-Costa et al. [2020]	
	$ONONO_{2(surface)} + H_2O_{(surface)}$	$\longrightarrow$	$HONO_{(g,surface)} + HNO_{3(surface)}$		
7	Dust + hν	$\longrightarrow$	$h^+ + e^-$	Ndour et al. [2008]	(vii)
	$e^- + O_2$		$O_2{}^-$	Dupart et al. [2014]	
	$NO_2 + O_2{}^-$ (or e^-)	$\longrightarrow$	$NO_2{}^- + O_2$	Dyson et al. [2021]	
8	$HNO_{3(ads)} + h\nu$	$\longrightarrow$	$HONO + O(^3P)$	Zhou et al. [2003]	(viii)
				Ziemba et al. [2010]	
				Laufs and Kleffmann [2016]	
9	HNO_3 + VOC	$\longrightarrow$	$HONO + VOC_{ox}$	Rutter et al. [2014]	(ix)
10	$NH_3 + ONONO_2 + nH_2O_{(l)}$	$\longrightarrow$	$HONO + HNO_3 + NH_3 + (n\text{-}1)\,H_2O_{(l)}$	Li et al. [2018a]	(x)
				Xu et al. [2019]	
11	$2\,NO_{2(a)} + HSO_3{}^-{}_{(a)} + H_2O_{(l)}$	$\longrightarrow$	$3\,H^+_{(a)} + 2\,NO_2{}^-{}_{(a)} + SO_4{}^{2-}{}_{(a)}$	Cheng et al. [2016]	(xi)
				Li et al. [2018b]	
12	$HA + h\nu$	$\longrightarrow$	$A_{red} + X$	George et al. [2005]	(xii)
	$A_{red} + NO_2$	$\longrightarrow$	$A'' + HONO$	Stemmler et al. [2006]	
13	$NO_3{}^- + h\nu$	$\longrightarrow$	$NO_2 + O^-$	Warneck and Wurzinger [1988]	(xiii)
			$(\Phi=0.01)$	Mark et al. [1996]	
	$NO_3{}^- + h\nu$	$\longrightarrow$	$NO_2{}^- + O$	Scharko et al. [2014]	
			$(\Phi = 0.011 \pm 0.002)$	Benedict et al. [2017]	

(i) Included in atmospheric chemistry models.

(ii) Ortho-nitrophenols are not measured in this work.

(iii) Refuted by Ye et al. [2015] due to a small HONO yield (< 0.03), though Li et al. [2015] maintains that a gas phase source of HONO consumes nitrogen oxides in the troposphere.

(iv) In the atmosphere, the rate is too small [Crowley and Carl, 1997; Amedro et al., 2011].

(v) A rapid HONO formation (but not of HNO_3) is observed from reactions of NO_2 on fresh soot, but soot becomes deactivated after a few seconds [Kalberer et al., 1999]. UV radiation increases the reactivity of the soot [Monge et al., 2010].

(vi) Finlayson-Pitts et al. [2003] finds that the reaction is first order with respect to NO_2 due to its chemical equilibrium with N_2O_4. The equilibrium constant of N_2O_4 is too small for atmospheric concentrations of NO_2, even though it may increase with decreasing temperature. See also Yabushita et al. [2009] and Martins-Costa et al. [2020].

(vii) Under UV-A irradiation, Dupart et al. [2014] found $\gamma = (0.6 \pm 0.3)$ to $(2.4 \pm 0.4) \cdot 10^{-8}$ and a HONO yield of 30 %. Goodman et al. [1999] performs their experiment on hydrated silica particles, though the reaction applies to surfaces generally.

(viii) Laufs and Kleffmann [2016] found $J(HNO_3 \rightarrow HONO) = 2.4 \cdot 10^{-7}\ s^{-1}$ and for the secondary produced NO_2 a $J(HNO_3 \rightarrow NO_2) = 1.1 \cdot 10^{-6}\ s^{-1}$ both at (Solar Zenith Angle (SZA) = 0 °, and 50 % r.h.). Sullivan et al. [2018] noted the strong dependence of the absorption cross-section of adsorbed HNO_3 on relative humidity. See also Zhou et al. [2003] and Ziemba et al. [2010].

(ix) This mechanism was studied in the context of diesel exhaust. The gas phase or heterogeneous phase nature is disputed [Spataro and Ianniello, 2014].

(x) NH_3 mediation reduces the energy barrier for the reaction to 0.5 kJ/mol.

(xi) This reaction may be pH dependent; aerosol pH was not measured in this work.

(xii) HA: humic acid; A_{red}: reductive centers; X: oxidant. George et al. [2005] finds a humidity and irradiation dependence. See also Yang et al. [2018].

(xiii) Warneck and Wurzinger [1988] measured the quantum yield (ϕ(O)) of the photolysis of $NO_3{}^-$ into $NO_2{}^-$ + O to be (0.0011 ± 0.0001) which was also measured by Mark et al. [1996] at 254 nm when excluding an oxidizable additives in the solution. Scharko et al. [2014] finds that the addition of an organic OH scavenger largely increased (a factor of 4) the HONO formation. More recently Benedict et al. [2017] determined the quantum yield ($\phi\ (NO_2{}^-)$) in the photolysis of $NO_3{}^-$ to 1.1 ± 0.2 % (at 313 nm, 50 μM nitrate, pH ≥ 5). They convincingly demonstrated that the larger $\phi(NO_2{}^-)$ than previously assumed is primarily due to the presence of an OH scavenger.

2.2 The Leighton relationship

The Leighton ratio predicts the concentration of tropospheric ozone, given the concentrations of nitrogen oxides [Finlayson-Pitts and Pitts Jr, 1999]. Combining equations 2.20 and 2.22 yields an expression which should equal unity under conditions of a PSS:

$$\Phi = \frac{k_{2.20}[NO][O_3]}{J_{NO_2}[NO_2]} \tag{2.50}$$

i.e. the photolysis of NO_2 (J_{NO_2}), which produces NO and O_3 is in a PSS with the reaction of O_3 and NO which produces NO_2. Here $k_{2.20}$ is the reaction rate coefficient of the NO + O_3

reaction (cm^3 molec.$^{-1}$ s^{-1}). Rearranging equation 2.50 yields measurable ratios:

$$\frac{[\mathrm{NO}]}{[\mathrm{NO_2}]} = \frac{\mathrm{J_{NO_2}}}{\mathrm{k_{2.20}}[\mathrm{O_3}]}. \tag{2.51}$$

Determining Φ reveals whether the photochemistry in an observed air mass is well captured by this simple approximation. The quantity Φ can be used as a proxy for the atmospheric oxidation capacity: $\Phi > 1$ suggests fresh NO emissions, while $\Phi < 1$ reveals that NO is being transformed into NO_2 without ozone. Hydroperoxy radicals may also react with NO to produce NO_2 without loss of ozone (equation 2.18). Therefore, the expression for Φ needs to be expanded to include this correction:

$$\Phi = \frac{\mathrm{k_{2.20}}[\mathrm{NO}][\mathrm{O_3}] + \mathrm{k_{2.18}}[\mathrm{NO}][\mathrm{HO_2}]}{\mathrm{J_{NO_2}}[\mathrm{NO_2}]} \tag{2.52}$$

Again, rearranging 2.52 yields measurable quantities:

$$\frac{[\mathrm{NO}]}{[\mathrm{NO_2}]} = \frac{\mathrm{J_{NO_2}}}{\mathrm{k_{2.20}}[\mathrm{O_3}] + \mathrm{k_{2.18}}[\mathrm{HO_2}]} \tag{2.53}$$

Any other oxidant which converts NO to NO_2 without ozone (e.g. RO_2) may be added to the expression. Therefore, measured Φ provides a proxy for the quantification of the oxidation capacity of the atmosphere. Recent observations of the $[NO]/[NO_2]$ ratio in the upper troposphere reveal inconsistencies between observation and expectation, suggesting the presence of an unknown NO_x reservoir in that part of the atmosphere [Silvern et al., 2018].

2.3 Oxidation capacity

The described interaction of air pollutants (NO_x, VOCs) leads to the efficient formation of ozone (see equations 2.5 and 2.7 in section 2.1 above), and thereby photochemical smog, which is hazardous to human health and the environment. The oxidation capacity of the atmosphere describes its ability to remove air pollutants from this reaction cycle. A primary removal mechanism of most air pollutants is reaction with the OH radical, known as the detergent of the atmosphere. Oxidation by O_3 and NO_3 also remove air pollutants [Elshorbany et al., 2009]. Therefore the formation of HONO from any formation mechanism other than the well known gas-phase is of utmost interest, since the photolysis of HONO may significantly increase OH, thereby modulating the lifetime of air pollutants, as well as of greenhouse gases, and their consequent effects on human health and radiative forcing, respectively.

Chapter 3

Instrumentation & Methods

This thesis employs the measurements of several instruments operated on board the HALO aircraft, including the remote sensing mini-DOAS instrument, as well as several in situ instruments. It also utilizes simulations of the EMAC and MECO(n) models for comparison and interpretation. This chapter describes the mini-DOAS instrument, the DOAS technique, the scaling method, introduces the supplemental instrumentation which augments the mini-DOAS observations, and describes the models used for construction of a priori profiles as well as post-analysis comparison. All these instruments, as well as the methods of analysis, are described in the following sections: the mini-DOAS instrument in section 3.1, the DOAS retrievals in section 3.2, the scaling method in section 3.3, the additional instrumentation in section 3.4, and the models in section 3.5. For the mini-DOAS instrument, the error budget of the DOAS analysis and the scaling method is explored in detail.

3.1 The mini-DOAS instrument

The mini-DOAS instrument records scattered skylight in the ultraviolet/visible/near-infrared wavelength ranges in the nadir and limb viewing geometries Stutz et al. [2017]; Hüneke et al. [2017]; Werner et al. [2017]; Rotermund et al. [2021]; Kluge et al. [2020, 2023]. In this study, absorbing species including (but not limited to) O_3, O_4, NO_2, HCHO, and HONO, are detected in the limb geometry with the UV and visible spectrometers. The interpretation of the mini-DOAS observations requires the DOAS analysis of the measured skylight spectra [Platt and Stutz, 2008], radiative transfer modeling of the observation conditions with a Monte Carlo model such as McArtim [Deutschmann et al., 2011], and the conversion of the Slant Column Density (SCD)s retrieved with the DOAS technique into VMRs using the novel scaling method [Stutz et al., 2017; Hüneke et al., 2017]. In this study, the focus is on limb geometry measurements of NO_2, HCHO and HONO performed during twenty five scientific flights of the EMeRGe (e.g. `https://acp.copernicus.org/articles/special_issue1074.html`, Andrés Hernández et al. [2022]; Lin et al. [2023]; Förster et al. [2023]) and CAFE-Africa (e.g. Tadic et al. [2021]; Nussbaumer et al. [2021b]; Hamryszczak et al. [2023]) missions during 2017 and 2018.

The airborne mini-DOAS instrument is an optical spectrometer with six channels which is regularly installed into the German research aircraft HALO operated by the DLR. It detects scattered sunlight in the UV-A (310–440 nm, Full Width Half Maximum (FWHM) = 0.5 nm), visible (420–640 nm, FWHM = 1 nm) and near-infrared (1100–1680 nm, FWHM = 10 nm) wavelength ranges. The six telescopes (Field of View (FOV): 0.4 ° x 3.2 °) collect skylight from the nadir and limb viewing geometries (one telescope per wavelength range per geometry), the latter at varying elevation angles (+5° to −90°) when commanded. During normal operation, the limb telescopes are motor controlled to align with the horizon against the roll of the HALO aircraft at 1 Hz, with a standard error of 0.10 °. The collected skylight is conducted to six optical spectrometers by glass fiber bundles, while the spectrometers are assembled in an evacuated ($P \approx 10^{-5}$ mbar) and cooled ($T \approx 1$ °C) housing in the boiler room of the aircraft, which is otherwise unpressurized and uninsulated. The mini-DOAS instrument probes air masses on the starboard side of the aircraft, perpendicular to the direction of travel — in the limb geometry — typical photon path lengths in the UV wavelength range between ≈ 5 km (near the surface) and ≈ 75 km at the maximum flight altitude of the aircraft (≈ 15 km), depending on the wavelength, aerosol concentration and cloud cover (cf., Fig. 2 in Kluge et al. [2020] as well as below). An Image Development Systems (IDS) uEye camera (FOV: 46 °) is aligned with the limb telescopes (but not motor controlled to align with the horizon) and provides images of the sampled atmosphere at 1 Hz. More detailed descriptions of the instrument, its design and characterization, and a history of deployments and scientific studies can be found in Großmann [2014]; Hüneke [2016] and/or Hüneke et al. [2017], while more recent studies utilizing the instrument can be found in Kluge et al. [2020]; Rotermund et al. [2021]; Rotermund [2021]; Kluge et al. [2023]; Kluge [2023].

3.2 DOAS retrievals of O_3, O_4, NO_2, HCHO, and HONO

The DOAS technique exploits the Beer-Lambert law:

$$\mathrm{I}(\lambda) = \mathrm{I}_0(\lambda) \cdot \exp\left(-\sum_{\mathrm{i}}^{\mathrm{n}} \sigma_{\mathrm{i}}(\lambda) \cdot \int_0^{\mathrm{L}} \rho_{\mathrm{i}}(\mathrm{l})\mathrm{dl}\right) \tag{3.1}$$

which describes the wavelength dependent absorption of light by trace gases and other absorbing species along a light path. Here I_0 is the radiance at emission (or down-welling solar radiation at the top of the atmosphere), I is the radiance at observation, σ is the wavelength specific absorption cross section [cm^2/molecule] of some absorber, and ρ is the concentration of that absorber [molecules/cm^3]. DOAS analysis retrieves SCDs [molecules/cm^2]:

$$\mathrm{SCD}_{\mathrm{i}} = \int_0^{\mathrm{L}} \rho_{\mathrm{i}}(\mathrm{l})\mathrm{dl} \tag{3.2}$$

whereby any information about the variability in the concentration of the absorber along the light path is lost. The measured optical depth τ

$$\ln\left(\frac{\mathrm{I}_0}{\mathrm{I}}\right) = \tau \tag{3.3}$$

is then equal to the sum of the products of cross sections (σ) and SCDs of all absorbers in the light path. DOAS retrieval algorithms determine SCDs by minimizing the difference between the observed optical depth and the retrieval parameters.

$$\chi^2 = (\tau - \sum_{\mathrm{i}}^{\mathrm{n}} \sigma_{\mathrm{i}} \cdot \mathrm{SCD}_{\mathrm{i}})^2. \tag{3.4}$$

In practice, additional wavelength dependent broadband scattering and absorption is also accounted for.

While the Beer-Lambert law is only strictly relevant for individual wavelengths, the DOAS technique generalizes this approach to wavelength ranges. The recorded skylight spectra are analyzed for the absorption structures of weakly absorbing (Optical Depth (OD) < 0.01) trace gases (e.g. O_3, O_4, NO_2, HCHO, and HONO) using a Levenberg-Marquardt algorithm. The DOAS retrievals in this study are performed with the software DOAS Intelligent System (DOASIS) [Kraus, 2006; Peters et al., 2017], which corrects each spectrum for offset, dark current, and performs a wavelength calibration according to measured emission lines of mercury and krypton lamps. The absorption cross sections of the absorbing species are convolved by the instrument's spectral response function before being fit against the observed signal. Several other parameters must be considered in the DOAS retrieval scenarios:

- The retrieval range is chosen such that the target gas has a distinct absorption within the wavelength range.
- The retrieval range is kept narrow to minimize the difference in radiative transfer at opposite ends of the wavelength range.
- All gases absorbing light in this wavelength range must be included in the retrieval if they are present in the light path.

- The absorption cross sections are often temperature dependent. Commonly, two orthogonalized ozone parameters are included to account for stratospheric and tropospheric absorption.
- The Ring effect, which describes the filing in of Fraunhofer lines with rotational Raman scattering [Vountas et al., 1998], is included, with a secondary orthogonalized wavelength dependent effect.
- The I_0 effect, as described in Aliwell et al. [2002], is accounted for among stratospheric absorbers (e.g. O_3 & NO_2).
- The order of the DOAS polynomial is fixed at 2, since higher orders are found to destabilize the retrieval.
- The absorption cross sections are shifted and squeezed, to account for the tilt effect [Lampel et al., 2017b] or any other minor changes in the optical imaging of the spectrometer during the measurements.

In this work, the Root Mean Square (RMS) of the DOAS retrieval residual is generally small enough to ignore additional effects, such as vibrational Raman scattering [Lampel et al., 2015]. The specific retrieval scenario settings for the retrieval of each target gas can be found in tables 3.1 and 3.2 and in the following sections. Given the ambient temperatures of the sampled atmosphere (200–300 K), the Ring spectrum is calculated at 250 K. Sample DOAS retrievals from the UV wavelength range are shown below. Sample retrievals from the visible wavelength range for can be found in appendix A. A more rigorous treatment of the principles of DOAS analysis can be found in Platt and Stutz [2008].

Table 3.1: For each absorbing gas, the absorption cross sections used for the spectral retrievals, their temperatures and uncertainties are given.

No.	Absorber	Temperature [K]	Reference	Uncertainty
1	O_3	223, 293	Serdyuchenko et al. [2014]	3 %
2	O_4	293	Thalman and Volkamer [2013]	4 %
3	NO_2	223, 293	Bogumil et al. [2003]	3 %
4	H_2O	296	Polyansky et al. [2018]	1 %
4b	H_2O	293	Rothman et al. [2009]	8 %
5	HCHO	293	Chance and Orphal [2011]	10 %
6	HONO	298	Stutz et al. [2000]	5 %

Table 3.2: For each target trace gas retrieved with DOAS analysis, the following retrieval scenario parameters including wavelength range, included absorbers, I_0 effect, Ring effect (R), DOAS polynomial order, and offset polynomial order are specified.

Target	Interval [nm]	Fitted absorbers	Parameters	Polynomial	Offset
O_3	335–362	1, 2, 3, 4	I_0, R, R·λ^4	2	1
	435–490	1, 2, 3, 4b	I_0, R, R·λ^4	2	1
O_4	338–370	1, 2, 3, 4	I_0, R, R·λ^4	2	1
	434–486	1, 2, 3, 4b	I_0, R, R·λ^4	2	1
NO_2	333–379	1, 2, 3, 4, 5, 6	I_0, R, R·λ^4	2	1
	445–491	1, 2, 3, 4b	I_0, R, R·λ^4	2	1
HCHO	323–357	1, 2, 3, 4, 5, 6	I_0, R, R·λ^4	2	1
HONO	337–373	1, 2, 3, 4, 5, 6,	I_0, R, R·λ^4	2	1

3.2.1 O_3

Ozone absorbs light throughout the UV and visible wavelength ranges. Here the focus is on the Huggins and Chappuis bands (300–370 and 400–700 nm, respectively). The absorption cross-section used is taken from Serdyuchenko et al. [2014], and is defined between 213 and 1100 nm.

The maximum absorption of 1.1 $\cdot 10^{-17}$ [cm^2/molec.] is found at 255 nm. For ozone, the I_0 effect is calculated for a maximum ozone column of 1 $\cdot 10^{19}$ molec./cm^2. Two cross-sections (T = 223 & 293 K) are orthogonalized against each other to account separately for stratospheric and tropospheric O_3 absorption. Since it is often measured in situ on board the HALO aircraft, ozone is also used as a scaling gas. An exemplary retrieval is shown in figure 3.1.

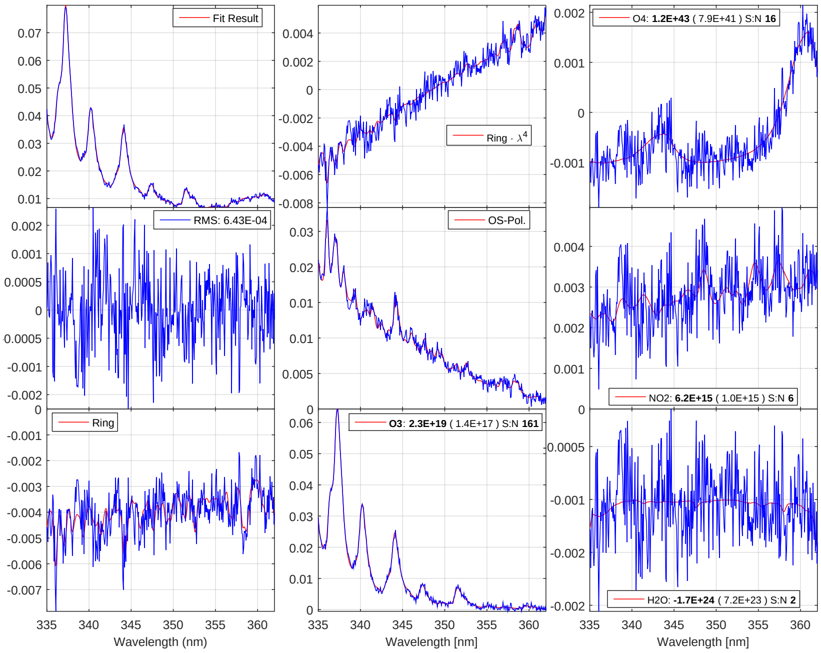

O3-Fit | MeasSpec: M000776 | RefSpec: 1082 | Recording Time: 08:30:40 -- 08:31:28 UTC | Lat./Long.: 16.756/-29.5052 | Alt: 10.6925 km
NScans: 100 | ExpTime: 385.34 ms | Temp: 0.75 °C | EA: 0° | SZA: 79.579° | SRAA: 134.8856°
S/N: 160.76 | χ^2: 1.59E-04 | DOAS-Polynom. deg: 2 | OffSet-Polynom. deg: 1
RefRingShift: 0.0015948 (0.00014183) | RefRingSqueeze: 1 (8.8914e-06)
GasShift: 0.11606 (0.0034491) | GasSqueeze: 0.99602 (0.00070829)

Figure 3.1: An exemplary O_3 spectral retrieval in the UV wavelength range. From top to bottom, left to right, the panels show: the optical depth τ in blue with the retrieval result overlaid in red, the retrieval residual with the RMS in the legend, the fitted parameters for the Ring effect, the wavelength dependent Ring effect, the offset polynomial, and the included absorbing trace gas species. For each absorbing trace gas the legend contains the retrieved SCD, the associated error, and the consequent signal to noise ratio. The text box lists associated information such as the spectrum number, reference spectrum number, integration time, latitude, longitude, altitude, number of scans, exposure time, detector temperature, elevation angle, solar zenith angle, solar relative azimuth angle, signal to noise ratio, cost parameter, DOAS polynomial order, offset polynomial order, ring shift and squeeze, and gas shift and squeeze.

3.2.2 O_4

O_4 does not refer to a stable molecule under atmospheric conditions but rather is a shorthand used to refer to the collisional complex $O_2{-}O_2$:

$$2O_2 \longrightarrow O_4. \tag{3.5}$$

The equilibrium constant (k_{eq}) for this reaction is not known. Rather, atmospheric concentrations of O_4 are determined in proportion to the square of the O_2 concentration:

$$[O_4] = k_{eq} \cdot \left(\frac{0.21 \cdot p \cdot N_A}{R \cdot T}\right)^2. \tag{3.6}$$

The oxygen collisional complex O_4 describes the simultaneous excitation of two oxygen molecules. The absorption cross-section is taken from Thalman and Volkamer [2013] (@ 293 K) and is defined from 336–600 nm. The maximum absorption of 1.1 $\cdot 10^{-45}$ [cm^5/molec^2] is located at 578 nm. The units of cm^5 molecules^{-2} betray that the equilibrium constant $k_{eq} = [O_4]/[O_2]^2$ is not known. Rather, what is known is the collisional (binary) absorption cross section.

$$k_{eq}\sigma = \frac{OD}{[O_2]^2 L}. \tag{3.7}$$

This distinction is suppressed in the notation for simplicity, but is accounted for mathematically when using O_4 as a scaling gas. The absorption of light by O_4 is highly predictable, with a sensitive dependence on the light-path, while the concentration of oxygen in the atmosphere is easily determined according to the ideal gas law. This motivates the usage of O_4 as a scaling gas in the UV and visible wavelength ranges. The first atmospheric O_4 extinction profile measurements were performed by Pfeilsticker et al. [2001]. An exemplary retrieval is shown in figure 3.2.

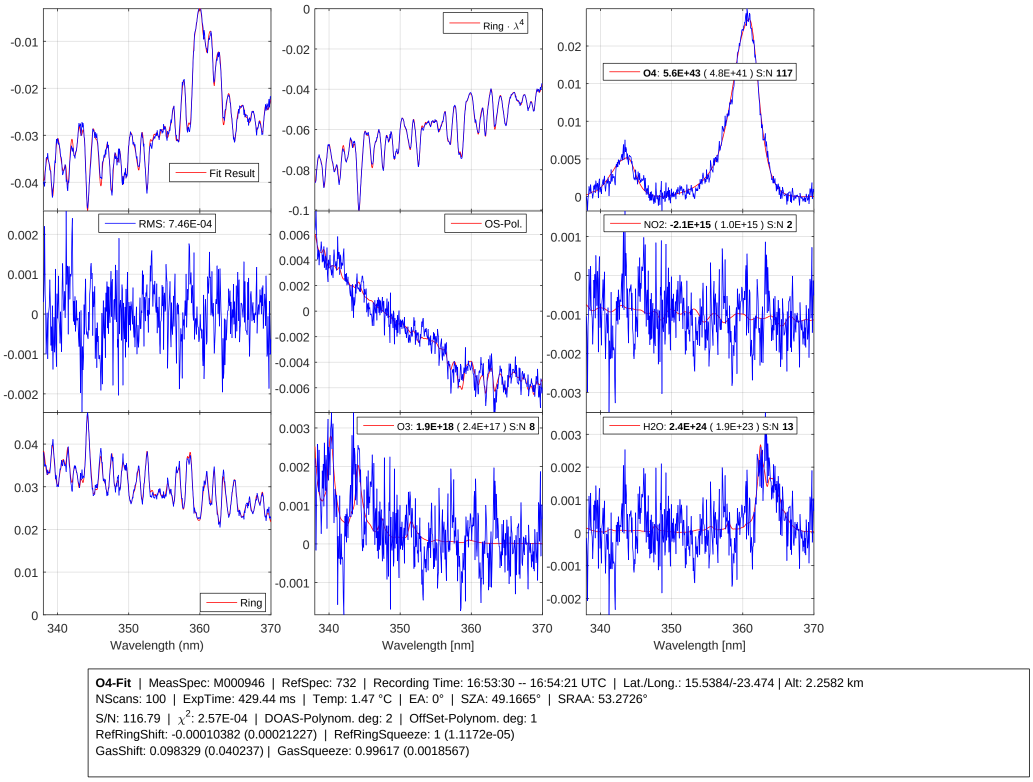

```
O4-Fit  |  MeasSpec: M000946  |  RefSpec: 732  |  Recording Time: 16:53:30 -- 16:54:21 UTC  |  Lat./Long.: 15.5384/-23.474 | Alt: 2.2582 km
NScans: 100  |  ExpTime: 429.44 ms  |  Temp: 1.47 °C  |  EA: 0°  |  SZA: 49.1665°  |  SRAA: 53.2726°
S/N: 116.79  |  χ²: 2.57E-04  |  DOAS-Polynom. deg: 2  |  OffSet-Polynom. deg: 1
RefRingShift: -0.00010382 (0.00021227)  |  RefRingSqueeze: 1 (1.1172e-05)
GasShift: 0.098329 (0.040237) |  GasSqueeze: 0.99617 (0.0018567)
```

Figure 3.2: An exemplary O_4 spectral retrieval in the UV wavelength range. The panels are as described in figure 3.1.

3.2.3 NO_2

NO_2 absorbs light in the UV and visible wavelength ranges. The absorption cross section is taken from Bogumil et al. [2003] and is defined from 230 – 930 nm. The broad B-X and A-X bands reach a maximum absorption of 7.4 $\cdot 10^{-19}$ [cm^2/molec] which occurs at 414 nm. For NO_2, the I_0 effect is calculated for an overhead column of 1 $\cdot 10^{16}$ molec./cm^2. Two cross sections (@ 223 & 293 K) are orthogonalized against each other to account separately for stratospheric and tropospheric NO_2 absorption. An exemplary retrieval is shown in figure 3.3.

3.2.4 HCHO

Absorption of light by HCHO is defined by vibrational excitations in the A^1A_2-X^1A_1 system between 240 and 380 nm. HCHO is retrieved in the UV wavelength range with settings adapted

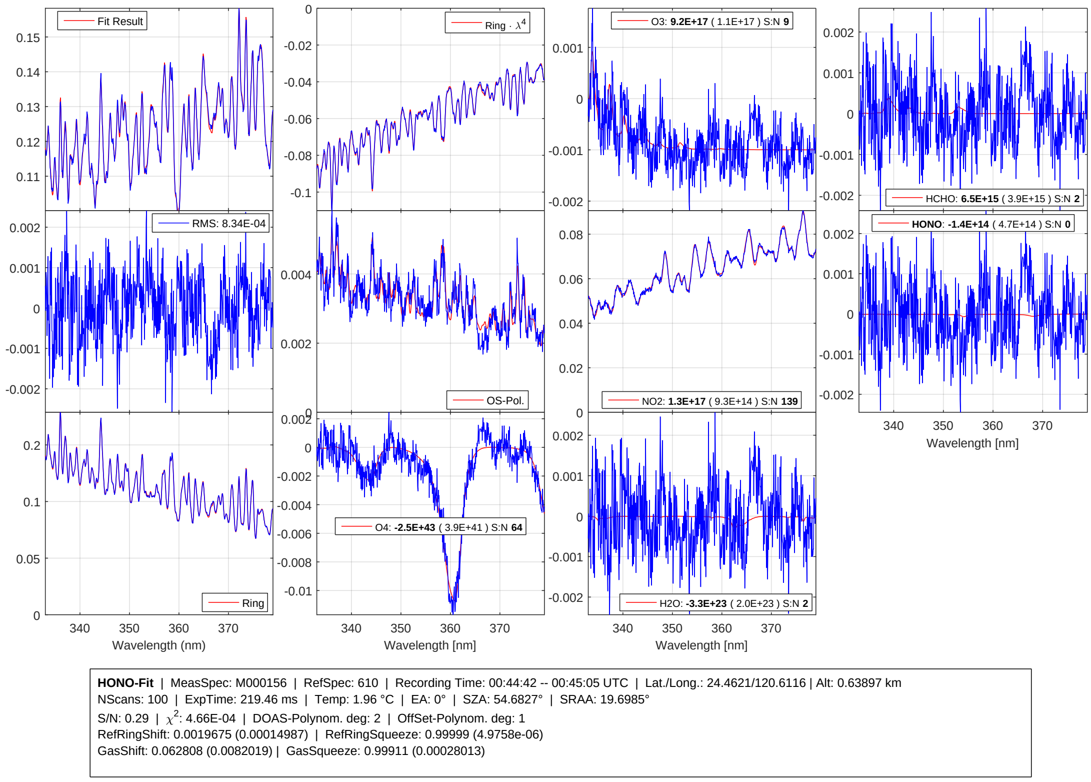

HONO-Fit | MeasSpec: M000156 | RefSpec: 610 | Recording Time: 00:44:42 -- 00:45:05 UTC | Lat./Long.: 24.4621/120.6116 | Alt: 0.63897 km
NScans: 100 | ExpTime: 219.46 ms | Temp: 1.96 °C | EA: 0° | SZA: 54.6827° | SRAA: 19.6985°
S/N: 0.29 | χ^2: 4.66E-04 | DOAS-Polynom. deg: 2 | OffSet-Polynom. deg: 1
RefRingShift: 0.0019675 (0.00014987) | RefRingSqueeze: 0.99999 (4.9758e-06)
GasShift: 0.062808 (0.0082019) | GasSqueeze: 0.99911 (0.00028013)

Figure 3.3: An exemplary NO_2 spectral retrieval in the UV wavelength range. The panels are as described in figure 3.1.

from De Smedt et al. [2008] and Kluge et al. [2020]. The absorption cross section (@ 293 K) is taken from Chance and Orphal [2011] and is defined from 300–360 nm. The maximum absorption of 2.4 $\cdot 10^{-19}$ [cm^2/molec] is located at 326 nm. An exemplary retrieval is shown in figure 3.4.

3.2.5 HONO

The absorption cross section of HONO is highly structured between 300 and 400 nm. Vibrations in the $A^1A'' \leftarrow X^1A'$ transition reach a maximum of 5.2 $\cdot 10^{-19}$ [cm^2/molec] near 354 nm. HONO is retrieved in the UV-A range 337–373 nm according to the recommendations of Wang et al. [2017, 2019], with slight modifications. For example the Taylor terms for NO_2 at 298 K as described by Puķīte et al. [2010] and recommended by Wang et al. [2017, 2019] are not included. While they are recommended for limb observations and UV retrievals, the ODs from NO_2 absorption observed with the mini-DOAS instrument do not necessitate including these terms (see figure 3.3). Including the Taylor terms only has a minor effect on the retrieved HONO dSCDs, ≈ 1–2 %.

The HONO cross section from Stutz et al. [2000] is used because Brust et al. [2000] is underestimated by 22 % [Sander et al., 2011]. Meanwhile, no lower temperature cross sections have been published to date. The absorption cross section (@ 298 K) is defined from 292 to 404 nm. An exemplary retrieval is shown in figure 3.5.

3.2.6 H_2O

The absorption of light by gaseous water vapor must be accounted for in most DOAS retrievals [Lampel et al., 2017a], since water vapor is ubiquitous in the troposphere and causes considerable light absorption in the considered wavelength intervals. Absorption cross sections from Polyansky et al. [2018] and Rothman et al. [2003] are used in the UV and visible wavelength ranges, respectively. The Rothman et al. [2003] cross section (@ 293 K) is defined from 397 to 650 nm, with a maximum absorption of 9 $\cdot 10^{-24}$ [cm^2/molec] found at 648 nm. The Polyansky et al.

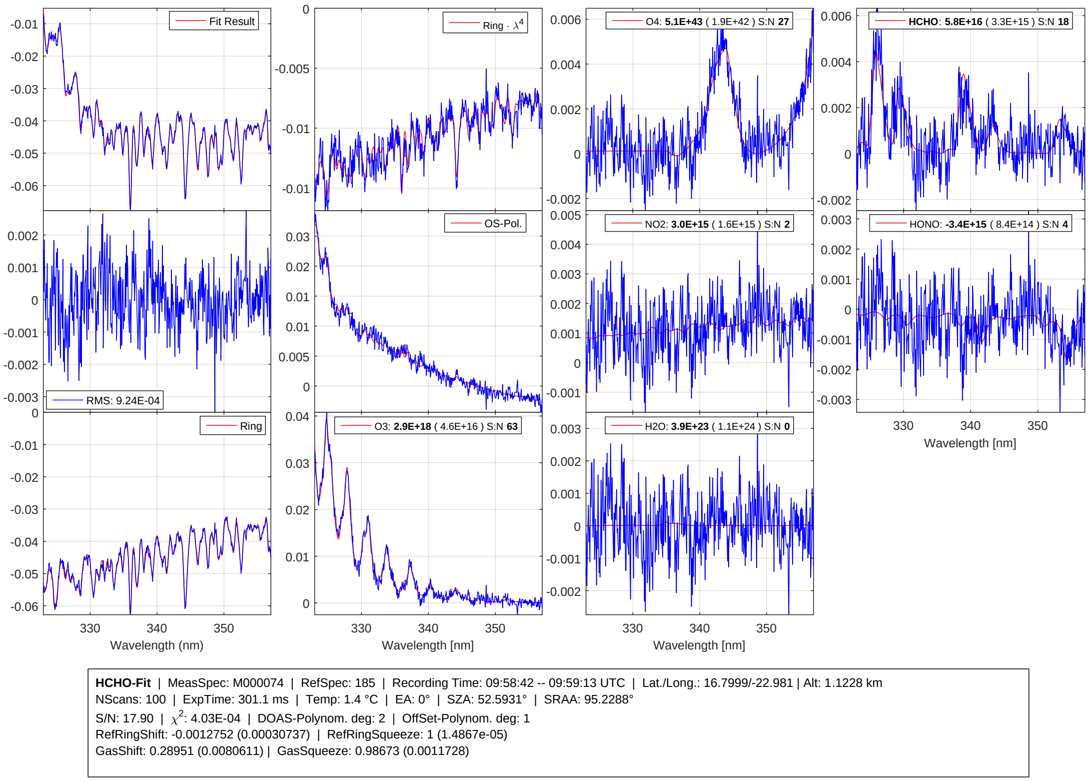

```
HCHO-Fit | MeasSpec: M000074 | RefSpec: 185 | Recording Time: 09:58:42 -- 09:59:13 UTC | Lat./Long.: 16.7999/-22.981 | Alt: 1.1228 km
NScans: 100 | ExpTime: 301.1 ms | Temp: 1.4 °C | EA: 0° | SZA: 52.5931° | SRAA: 95.2288°
S/N: 17.90 | χ²: 4.03E-04 | DOAS-Polynom. deg: 2 | OffSet-Polynom. deg: 1
RefRingShift: -0.0012752 (0.00030737) | RefRingSqueeze: 1 (1.4867e-05)
GasShift: 0.28951 (0.0080611) | GasSqueeze: 0.98673 (0.0011728)
```

Figure 3.4: An exemplary HCHO spectral retrieval in the UV wavelength range. The panels are as described in figure 3.1.

[2018] cross section (@ 296 K) is defined from 242 to 1000 nm with a maximum absorption of $5.8 \cdot 10^{-21}$ [cm^2/molec] at 943 nm. While H_2O absorption is accounted for in DOAS retrievals, the SCDs are not to be interpreted like other trace gases. The mixing ratio of water vapor in the troposphere varies by several orders of magnitude, so assigning observed limb absorption to a particular layer of the atmosphere is made untenable by the presence of multiple scattering.

3.2.7 Fraunhofer reference

For measurements from inside the atmosphere, DOAS spectral retrievals only determine the differential slant column density (dSCD) relative to a reference spectrum. For total SCDs, the absorption present in the so called Fraunhofer reference spectrum $\mathrm{SCD}_{\mathrm{ref}}$ must also be determined:

$$\mathrm{SCD} = \mathrm{SCD}_{\mathrm{ref}} + \mathrm{dSCD}. \tag{3.8}$$

For stronger absorbers (e.g. O_3), the reference $\mathrm{SCD}_{\mathrm{ref}}$ can be obtained from a spectral retrieval of the Fraunhofer spectrum against a high resolution external solar spectrum (i.e. from the 'Kurucz', [Chance and Kurucz, 2010]), while for weaker absorbers it can be determined either from a measurement at high altitude (above which the concentration of — and thereby the light absorption by — the target absorber is low or even negligible) where $\mathrm{SCD}_{\mathrm{ref}}$ can reasonably be assumed to be zero (e.g. HCHO, HONO), or calculated with a radiative transfer model (such as McArtim) which simulates absorption given an a priori profile of the targeted absorber(e.g. O_3, O_4, NO_2, HCHO). In practice, a retrieval of the measured spectrum against the extraterrestrial spectrum of Chance and Kurucz [2010] (called a Kurucz fit) is only robust for certain gases (e.g. O_4) and certain wavelength ranges, so simulated $\mathrm{SCD}_{\mathrm{ref}}$ are preferred. The two methods can be compared to determine whether the atmospheric conditions are well captured by the radiative transfer model.

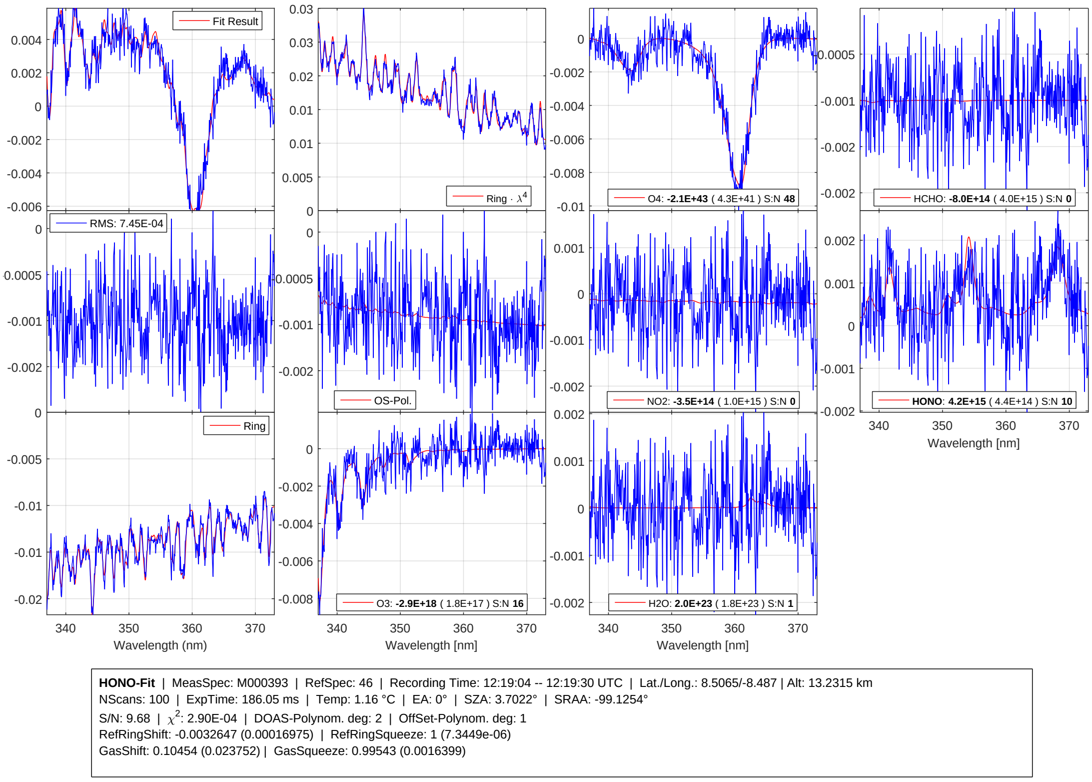

HONO-Fit | MeasSpec: M000393 | RefSpec: 46 | Recording Time: 12:19:04 -- 12:19:30 UTC | Lat./Long.: 8.5065/-8.487 | Alt: 13.2315 km
NScans: 100 | ExpTime: 186.05 ms | Temp: 1.16 °C | EA: 0° | SZA: 3.7022° | SRAA: -99.1254°
S/N: 9.68 | χ^2: 2.90E-04 | DOAS-Polynom. deg: 2 | OffSet-Polynom. deg: 1
RefRingShift: -0.0032647 (0.00016975) | RefRingSqueeze: 1 (7.3449e-06)
GasShift: 0.10454 (0.023752) | GasSqueeze: 0.99543 (0.0016399)

Figure 3.5: An exemplary HONO spectral retrieval in the UV wavelength range. The panels are as described in figure 3.1.

3.3 The scaling method

The attribution of the determined SCDs to VMRs of the targeted gases in space and time in the atmosphere is performed using the novel scaling method (e.g. Hüneke [2016]; Hüneke et al. [2017]; Stutz et al. [2017]; Kluge et al. [2020]; Rotermund et al. [2021]; Rotermund [2021]; Kluge et al. [2023]; Kluge [2023]). The scaling method relies on information about the radiative transfer inferred from co-measured or calculated absorption of a gas with a known concentration or extinction $[\mathrm{P}]_i$ in an atmospheric layer i. The concentration of a target gas $[\mathrm{X}]_i$ is then given by:

$$[\mathrm{X}]_\mathrm{i} = \frac{\alpha_{\mathrm{X_i}}}{\alpha_{\mathrm{P_i}}} \cdot \frac{\mathrm{SCD_X}}{\mathrm{SCD_P}} \cdot [\mathrm{P}]_\mathrm{i} \tag{3.9}$$

where SCD_P is the slant column density of the scaling gas O_3 or the optical depth of the scaling gas O_4, $[\mathrm{P}]_i$ is the calculated clear sky extinction of O_4 or the in situ concentration of O_3, and SCD_X is the measured SCD of the target gas X. Figure 3.6 displays the various components going into eq. 3.9 for an exemplary HONO retrieval for a research flight on 13.07.2017.

The α-factors represent a ratio of absorption from a trace gas in layer i relative to the total atmospheric absorption, a quantity that depends on the relative shape of the a priori profile (see e.g. Knecht [2015] and for details the supplement in Hüneke et al. [2017]). The α factors and their ratio $\frac{\alpha_{X_i}}{\alpha_{P_i}}$ are products of the the box air mass factors (Box Air Mass Factor (AMF)s) calculated by the radiative transfer model McArtim [Deutschmann et al., 2011] and the chosen a priori profiles. McArtim requires parameterization of atmospheric conditions such as temperature and pressure, and can calculate the radiative transfer in up to three dimensions. The radiative transfer mostly depends on aerosol scattering and surface albedo [Perliski and Solomon, 1993]. Aerosol profiles are determined from the Stratospheric Aerosol and Gas Experiment (SAGE) (384 nm and 520 nm) instrument from the International Space Station (ISS) and LIdar climatology of Vertical Aerosol Structure for space-based lidar simulation studies (LIVAS) (355 nm and 532 nm) light detection and ranging (LIDAR) instrument, while parameterization

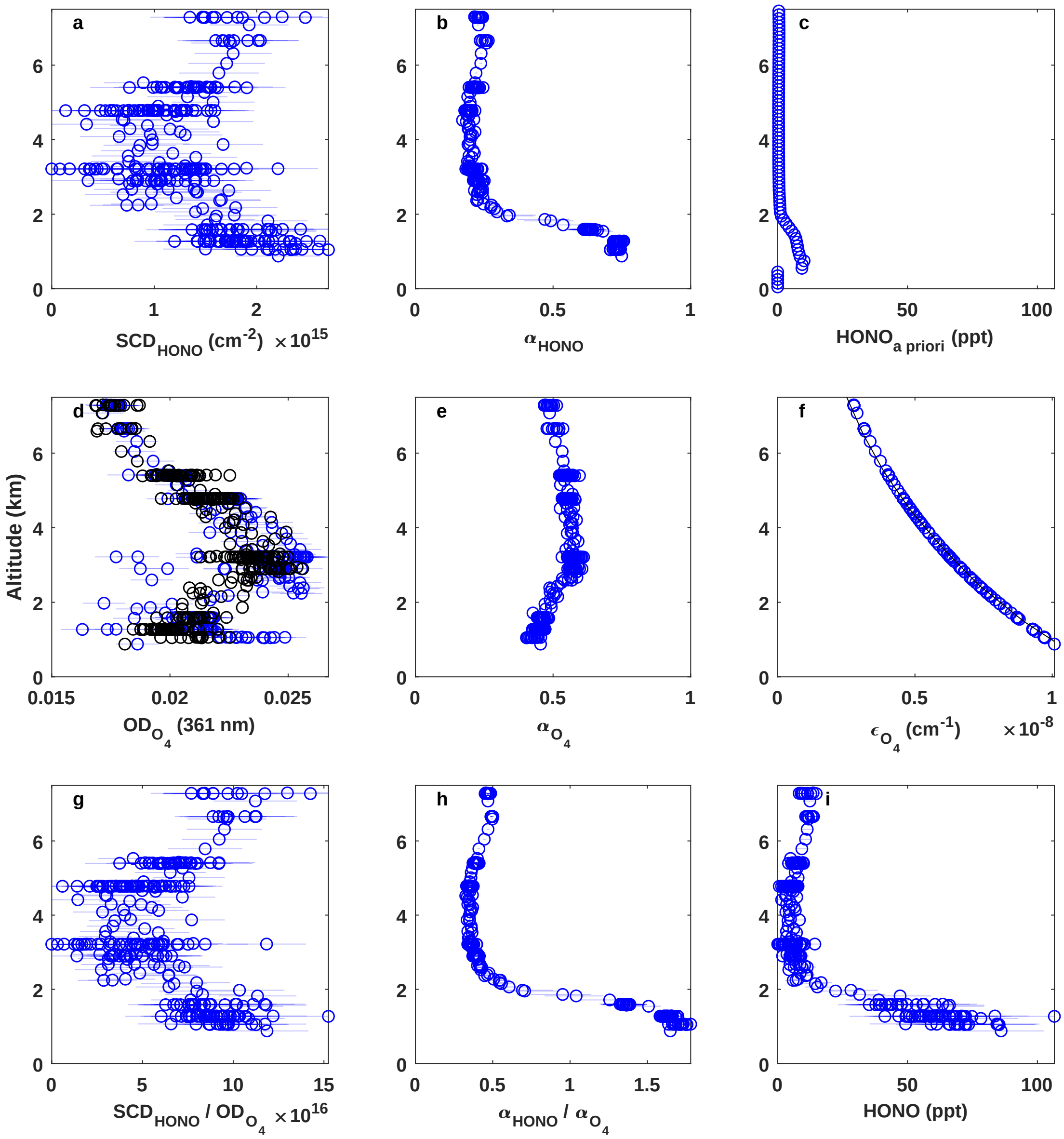

Figure 3.6: All the relevant components of the scaling method for an exemplary HONO retrieval on 13.07.2017. Panel a is the retrieved SCD of HONO, panel b the calculated α factors of HONO, and panel c the a priori profile of HONO (from the EMAC model). Panel d is the retrieved optical depth of O_4 in blue (with the OD simulated by McArtim — at 361 nm — overlaid in black), panel e the calculated α factors of O_4, and panel f the a priori extinction profile of O_4. Panel g is the ratio of HONO SCD and O_4 OD, panel h the ratio of α factors, and finally panel i represents the retrieved HONO VMRs obtained by multiplying the contents of panels f, g and h (as in equation 3.9). All are plotted as altitude profiles.

of the Single Scattering Albedo (SSA) [Heintzenberg et al., 1997] and Henyey-Greenstein phase function [Toublanc, 1996] are also included.

Concentration weighted box air mass factors are simulated and summed to calculate the α-factors [Stutz et al., 2017; Hüneke et al., 2017]. The a priori extinction profiles of the O_4 collisional complex are calculated from the oxygen concentration and the collisional absorption cross section. The a priori profile of ozone is determined from in situ ozone measurements and Ozone Mapping and Profiler Suite (OMPS) satellite data. The a priori profiles of the target gases are taken from the EMAC or MECO(n) models, where available. The a priori profiles of the target gas are also iterated, i.e. the a posteriori of the scaling retrieval is used as a priori in the next iteration until the results converge (only for the sampled altitudes, the profile above the maximum altitude of the sampled atmospheric volume is unchanged — see also Kluge et al. [2023], figure 1). Given the similarities of the a priori profile shapes with those of the a posteriori, in practice the convergence is generally achieved in one iteration.

3.3.1 Averaging volume

The mean of the photon path length distribution in the limb direction may vary significantly over the course of a flight, mainly due to the presence of aerosols and clouds (which affect Mie scattering) and by the air density (i.e. flight altitude) which mostly affects Rayleigh scattering (further details can be found in figure 3 and the discussion in Kluge et al. [2020]). However, the equivalence theorem in optics [Irvine, 1964; Partain et al., 2000] as well as extensive radiative transfer simulations (see e.g. Knecht [2015]) suggest that for weak absorbers, the photon path length distributions and therefore the mean photon path lengths are the same at a given wavelength, provided that they share the same spatial distribution in the atmosphere. For all trace gases with sources and sinks at the surface and in the lower troposphere, this criterium is reasonably well approximated when using O_4 as scaling gas [Kluge et al., 2020]. The α-factor ratios (see equation 3.9) account for remaining differences in the profile shapes of the target gas (X) and scaling gas (P) and their center wavelengths of absorption. The α-factors express the fraction of the line-of-sight absorption at the measurement altitude relative to the total atmospheric absorption. These may may differ for the target gas compared to the scaling gas, because of their different profile shapes. For the limb measurements in this study, the average path length (approximately) determines the spatial resolution of the measurements perpendicular to the flight direction. For a wavelength of 477 nm, the photon path lengths range from 10 km near the ground up to 100 km at maximum altitude ($\approx$ 15 km). In the UV wavelength range, mean photon path lengths range from 5–70 km across the same altitude range (see figure 3.7).

In the flight direction, the spatial resolution is a product of the (variable) aircraft speed and the spectrum integration time, which ranges from 7–60 seconds in the visible and 20–80 seconds in the ultraviolet spectral range depending on the available light (the exposure time is adjusted automatically), as well as the $\approx 0.4\,^\circ$ vertical viewing angle of the telescopes. The retrieved VMRs from the scaling method then represent averages over a volume determined by the product of the average photon path length (perpendicular to the flight direction), and the distance traveled by the aircraft during the spectral integration, as well as the height of the sampled atmospheric layer (e.g. 350 m for a photon path length of 50 km). This horizontal averaging is relevant when comparing the remote sensing observations of the mini-DOAS instrument with those of in situ instruments, or in comparisons with model simulations. Cloud cover modulates the limb radiances observed during flights, and hence the integration times of the spectra recorded by the mini-DOAS instrument vary from several seconds to a few minutes depending on wavelength and atmospheric conditions. Therefore, the spatial resolution of each recorded spectrum is modulated not only by average light path length perpendicular to the direction of flight (see above), but also along the flight track (the product of spectral integration time and aircraft speed). In consequence, when the remotely sensed mini-DOAS data are compared with in situ measured data and/or modeled data, the different temporal and spatial resolutions have to be handled with caution as they may not strictly correlate. In the analysis that follows, the measurements of in situ instruments are brought into coincident time series by averaging any reported values over the integration time of the mini-DOAS spectra.

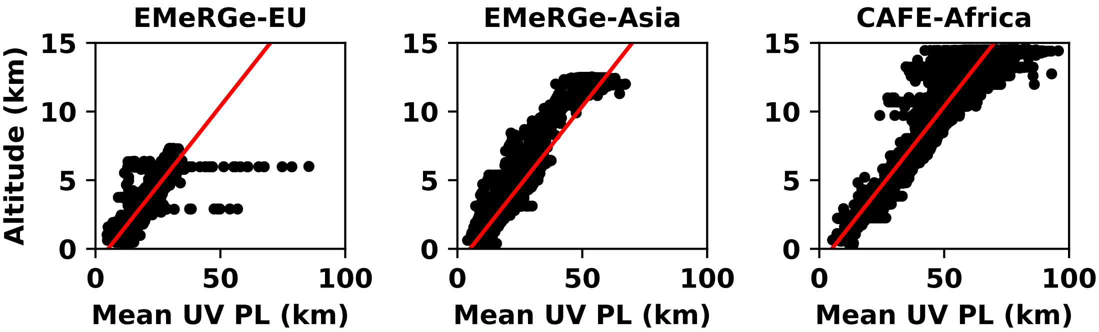

Figure 3.7: The mean of the light path length distribution at 360 nm for the three missions as altitude profiles, both in kilometers. Mean photon path lengths are determined from the measured O_4 absorption, the calculated O_4 a priori extinction profile, and the simulated O_4 α factors. The mean photon path length generally increases with altitude (as indicated by the red lines), and is modulated by the presence of clouds and/or aerosols.

3.3.2 Attribution of the measured absorption to different atmospheric layers

The concept of the α-factors allows us to attribute the measured atmospheric absorption to fractional contributions from (a) the line-of-sight (expressed by the α-factor itself), (b) the absorption from the overhead column and (c) the absorption from below the aircraft due to multiple scattering (see section 2 in Kluge et al. [2020]). Evidently, this partitioning of the total measured absorption to the different layers of the atmosphere is a function of the vertical profile of the investigated trace gas, the aerosol concentration, cloud cover, and measurement altitude. Ideally, for the retrieval of target gases, the scaling gas would trace this optical situation perfectly if both gases share the same spatial distribution. In reality, however, this is often not the case, in particular for gases with a sharp gradient in the residual layer of the boundary layer towards the free troposphere, such as for example expected of HONO. Therefore, as a consequence of multiple photon scattering, HONO absorption observed in the limb direction above a polluted boundary layer may be partially misattributed to line-of-sight absorption above the boundary layer rather than to absorption carried by the back-scattered photons of the HONO loaded boundary layer. The scaling equation mostly accounts for this misinterpretation by design, since the measured O_4 absorption would similarly be affected by upwelling photons from the boundary layer, but some uncertainty remains in the α-factor calculations due to the different profile shapes of the target and scaling gases. For example, while observations of HONO within the free troposphere are partly attributable to multiple scattering from the boundary layer, it is precisely the weighting of the observed SCD by the α-factors that removes this influence, since $\mathrm{SCD}_{\mathrm{limb}} = \alpha \cdot \mathrm{SCD}_{(\mathrm{limb+oh+ms})}$ (see figure 3.8) Then, provided that the observed profile shape resembles the assumed profile shape, contributions to the observed absorption from above or below the aircraft are largely divided out.

For sensitivity simulations (see figure 3.9), we assume a priori HONO profiles such as (a) a Heaviside function with an edge at the top of the boundary layer (i.e. non-zero HONO in the boundary layer and zero HONO above) and (b) from model simulations, where the column amount of HONO within the boundary layer is normalized to equal the integral of profile (a) and (c) where we apply the a priori to the HONO measurements from the EMeRGe intercomparison flight on 13.07.2017 [Schumann, 2021]. In the worst case, HONO would only be present within the boundary layer, such as reflected by a Heaviside function. As a consequence of the radiative transfer, HONO is then underestimated up to 400 m below and overestimated up to 400 m above such a sharp boundary, respectively. However, only 10 (2) % of the HONO within the boundary layer is attributed to 100 (400) m above the layer, respectively. A more reasonable test profile, e.g. one taken from the EMAC model and enhanced to contain the same column amount of HONO within the boundary layer as the Heaviside case, does not suffer from this attribution uncertainty. HONO observed above the boundary layer, therefore, can hardly be explained by backscatter from a polluted boundary layer (irrespective of aerosol loading), since any observation above this layer is diluted by the α-factors, necessarily, and scaled by a gas which shares its radiative transfer. Nor can the HONO observed at higher altitudes be attributed to overhead or multiple scattering contributions. Only when the a priori profile includes HONO at the altitudes where it is observed in the limb, can simulated SCDs reproduce the observations at flight altitude.

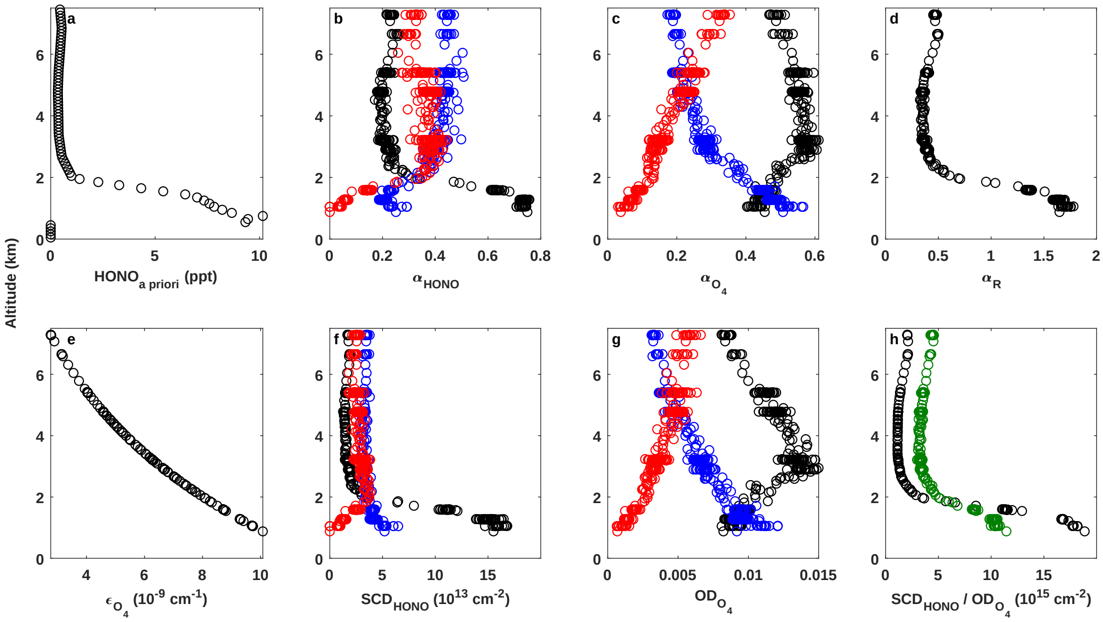

Figure 3.8: The robustness of the scaling method with respect to multiple scattering, as determined by the α factors, for the same retrieval as figure 3.6. Panel a is the a priori profile of HONO from the EMAC model, panel b the consequent α factors (in black), panel c the α factors of O_4 (in black), and their ratio is panel d. In panels b, c, f and g, contributions to the observed absorption from above and below the aircraft are also shown in blue and red, respectively. Panel e is the a priori profile of O_4 extinction, the simulated SCD of HONO in panel f, the simulated optical depth of O_4 in panel g and the ratio of the two is panel h. In panel h, the black data represents the ratio of limb contributions, while the green data represents the ratio of total absorption, whereby the difference between the two is accounted for by the α factors, by construction, i.e. $\alpha \cdot \mathrm{SCD} = \mathrm{SCD}_{\mathrm{limb}}$. All components are plotted as altitude profiles.

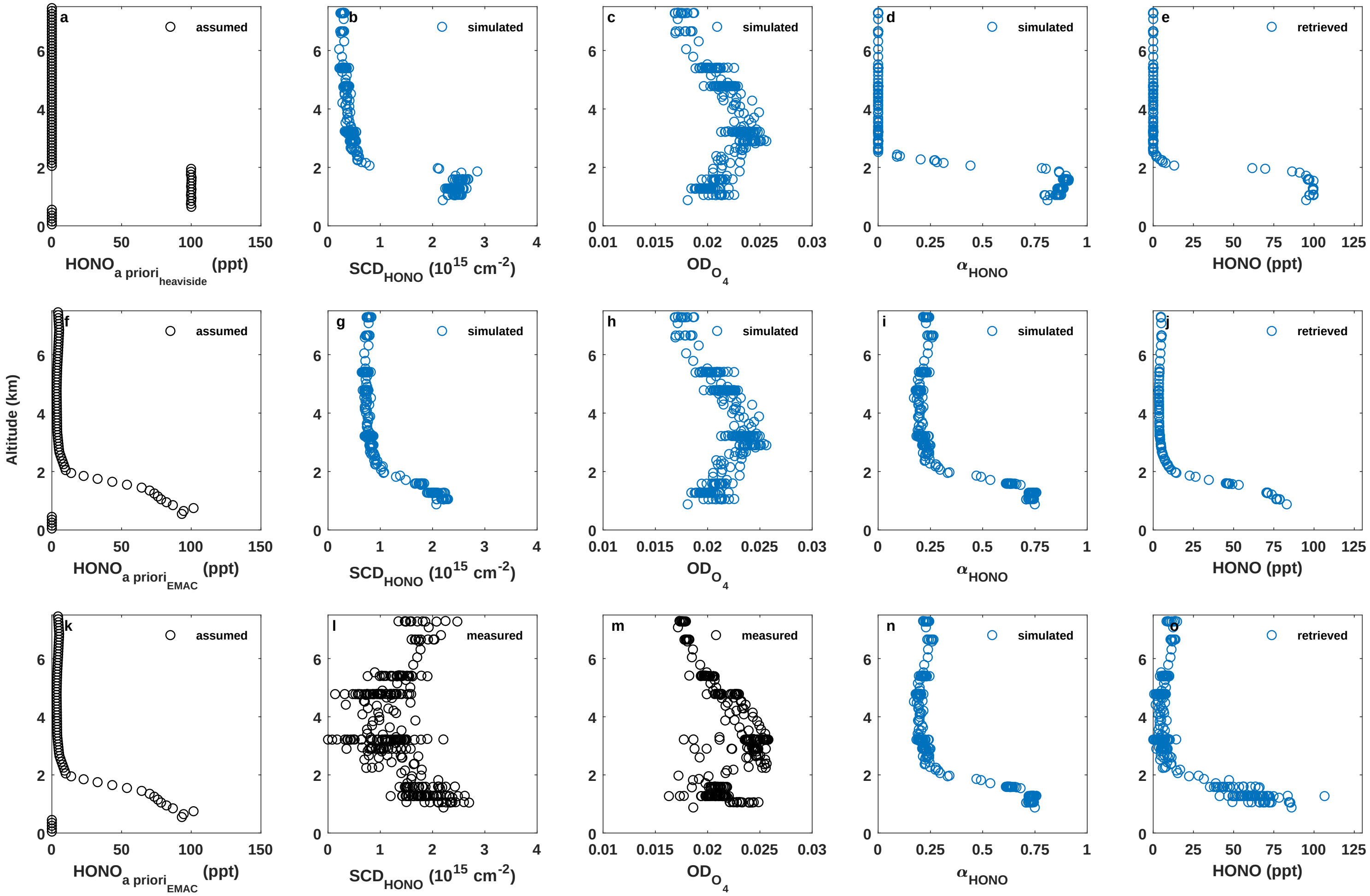

Figure 3.9: The robustness of the scaling method with respect to a priori information, for the same retrieval as in figures 3.6 and 3.8. In each row, from left to right: the first panel is an a priori profile of HONO, the second panel contains the simulated (blue) or measured (black) SCD of HONO, and the third panel is the simulated or measured optical depth of O_4. The fourth panel contains the simulated α factors of HONO, and the last panel contains the consequent retrieved HONO VMRs. The simulated α factors of O_4 are not shown, since they are identical in all three cases. All components are plotted as altitude profiles.

3.3.3 Error budget

The errors and uncertainties of the scaling retrievals are composed of both random and systematic elements. Their magnitudes and sources are discussed below.

Random errors

The random error contributions follow a Gaussian distribution and can be determined from the terms of equation 3.9 according to

$$\Delta[\mathrm{X}]_\mathrm{i} = [\mathrm{X}]_\mathrm{i} \cdot \sqrt{\left(\frac{\Delta\alpha_{\mathrm{R,i}}}{\alpha_{\mathrm{R,i}}}\right)^2 + \left(\frac{\Delta\mathrm{SCD}_{\mathrm{X,i}}}{\mathrm{SCD}_{\mathrm{X,i}}}\right)^2 + \left(\frac{\Delta\mathrm{SCD}_{\mathrm{P,i}}}{\mathrm{SCD}_{\mathrm{P,i}}}\right)^2 + \left(\frac{\Delta[\mathrm{P}]_i}{[\mathrm{P}]_\mathrm{i}}\right)^2}. \tag{3.10}$$

The calculated temperature and altitude dependent O_4 extinction used in the scaling equation as $[\mathrm{P}]_i$ has an uncertainty of < 1 % [Thalman and Volkamer, 2013; Greenblatt et al., 1990]. Error in the SCDs stems from error in the dSCD and error in the reference SCD, which are also summed in quadrature

$$\Delta\mathrm{SCD}_i = \mathrm{SCD}_i \cdot \sqrt{\left(\frac{\Delta\mathrm{dSCD}_\mathrm{i}}{\mathrm{dSCD}_\mathrm{i}}\right)^2 + \left(\frac{\Delta\mathrm{SCD}_{\mathrm{ref,i}}}{\mathrm{SCD}_{\mathrm{ref,i}}}\right)^2} \tag{3.11}$$

The ΔdSCD is determined by the DOAS retrieval [Platt and Stutz, 2008] for each spectrum, and it is limited by the accuracy of the absorption cross sections as listed in table 3.1. ΔdSCD is typically low (1 %) for the scaling gases O_3 and O_4 and some target gases (e.g. NO_2) but is at least 10 % for all HONO retrievals analyzed here, and can reach 100 % in the worst cases. $\Delta\mathrm{SCD}_\mathrm{ref}$ depends on the method used to retrieve it (the error is 3 % when simulated with 10k photons, the error for Kurucz retrievals is variable and depends on the wavelength region and trace gas). As discussed in Hüneke et al. [2017] and Stutz et al. [2017], the detection limit for most target gases is largely determined by $\Delta\mathrm{SCD}_\mathrm{X}$, specifically $\Delta\mathrm{dSCD}_\mathrm{X}$. Random errors in α_X or α_{O_4} and therefore α_R from Mie extinction due to aerosols and clouds were extensively investigated by Knecht [2015] for worst case cloud conditions. A maximum α_R error of 15 % was found in α_R, with a typical error of 10 %. Additional errors due to ground albedo and/or pointing error of the telescopes were also determined to be minor (see the supplements of Stutz et al. [2017] and Hüneke et al. [2017]). Error from the noise of the radiative transfer model is a function of the number of photons used in the simulations, and can be reduced at the cost of computation time. The 10,000 photons used per spectrum for the radiative transfer simulations in this thesis return a random error of 3 %, which propagates into $\Delta\alpha_X$ and $\Delta\alpha_{O_4}$ via the AMFs and also into $\Delta\mathrm{SCD}_\mathrm{ref}$ (if simulated, see above). The random error contributions to the scaling retrievals are summarized in table 3.3.

Systematic errors

Potential sources of systematic error are a) if the true profile shape of a target gas deviates significantly from the a priori (when it is not iterated), b) vertical sampling error due to pointing error of the telescopes, and c) differences in the wavelength dependent radiative transfer between the target and scaling gases.

Systematic errors in α_R are due to uncertainties in the relative profile shape of X and pointing error due to misalignment of the telescopes. The uncertainty in the profile shape of the target gas X is reduced by iterating the a priori profile of the target gas, whereby the a posteriori from the scaling retrieval is used as a priori for the next iteration until they converge. This procedure reduces uncertainty but may introduce systematic errors should the true profile shape differ significantly from both the model prediction and retrieval results. In practice the successive outputs agree within the margin of random errors. Meanwhile $\mathrm{SCD}_\mathrm{ref}$ calculated from these profiles carries an uncertainty, which is typically smaller than the random error in dSCD_X. The uncertainty in α_{O_4} is comparatively small (< 1 %) because of the predictable nature of the O_4 profile shape.

Errors from vertical sampling are investigated by shifting the target and scaling gas profiles up and down, since in the worst cases a 0.2 degree angle error (as determined in post flight analysis) along a photon path of 100 km would mean a 300 m vertical sampling error in the target and scaling gas profiles [Hüneke et al., 2017]. This is an overestimation of the vertical sampling error in most cases, given the shorter photon path lengths at lower altitudes, especially in the UV, as well as the fact that the plane turns as little as possible during flight. Even under these worst case assumptions, the error due to vertical sampling is generally less than the random error. Other vertical sampling errors near (very) sharp concentration gradients (e.g. near the tropopause, polar vortex, or stratified layers) are not of concern in this thesis given the altitude ranges sampled, the scaling gas used, and the convection-prone regions and seasons during which the measurements were performed.

Changing concentrations of the target or scaling gas in the line of sight may also introduce errors to the extent that the concentration of the target gas [X] may be under/over-estimated near plumes. With O_4 as a scaling gas, local horizontal variability is not expected, but the concentration of the target gas may vary at scales below the spatial resolution of the scaling method. Here it is not useful to refer to a systematic error, rather to understand that as a remote sensing instrument, the mini-DOAS instrument retrieves an average VMR over a volume within which small scale variability is smoothed out.

Finally, systematic errors due to differences in wavelength dependent radiative transfer is minimized by retrieving the target and scaling gases in narrow, overlapping wavelength ranges (see table 3.2).

In summary, the total error $\Delta[\mathrm{X}]_i$ varies with altitude (see e.g. figure 3.10) and is limited primarily by $\Delta\mathrm{SCD}_\mathrm{X}$ and to a lesser extent $\Delta\alpha_\mathrm{X}$ (which can be reduced with iteration). Minimum errors vary between gases and mission. For NO_2, relative errors are generally at least 10 %, for HCHO at least 10 % and for HONO at least 20 %. Retrievals with greater than 100 % error are excluded from further analysis.

Table 3.3: Random error contributions to the VMRs from the scaling retrieval

Parameter	Source	Typical value	Maximum value
$\Delta\alpha_\mathrm{R}$	model noise	3 %	3 %
	Mie scattering	10 %	15 %
$\Delta\mathrm{SCD}_\mathrm{R}$	DOAS retrieval error	1–10 %	100 %
	Cross section	3 %	6 %
	$\mathrm{SCD}_\mathrm{ref}$	5–10 %	20 %
$\Delta[\mathrm{P}]$	O_4 calculation	1 %	1 %
	O_3 in situ	2 %	2.5 %

These error estimates are well supported by the findings of the intercomparison study during the EMeRGe-EU mission [Schumann, 2021]. For example, a reasonable agreement is found between HCHO and NO_2 retrieved by the mini-DOAS with the scaling method (in the UV, using O_4 as a scaling gas) and HCHO and NO_2 measured in situ by the Proton transfer reaction mass spectrometer (HKMS) instrument on board the HALO aircraft and the Air Quality Design NOx Chemiluminescence Analyzer (AQD) instrument on board the Facility for Airborne Atmospheric Measurements (FAAM) aircraft, respectively (see Schumann [2021] and section 5.2.1). Moreover, it is found that NO_2 retrieved and scaled in the UV wavelength range is consistent with NO_2 retrieved and scaled in the visible wavelength range. This suggests that any error in the HONO retrieved should be specific to its SCD error or a priori profile uncertainty, rather than a systematic error of the scaling method itself.

Recent upgrades to the mini-DOAS computer also allow more rapid alignment of the telescopes with the horizon against the roll of the aircraft. This reduces the telescope angle error and thereby one of the larger sources of systematic error. The instrument's spectral response function may also be parameterized as a super Gaussian as described in Beirle et al. [2017] in order to better account for its temperature dependence, which is the primary source of the DOAS retrieval residual, according to a Principle Component Analysis (PCA). Including Taylor terms in the DOAS retrieval as described in Puķīte et al. [2010] may also further reduce retrieval errors.

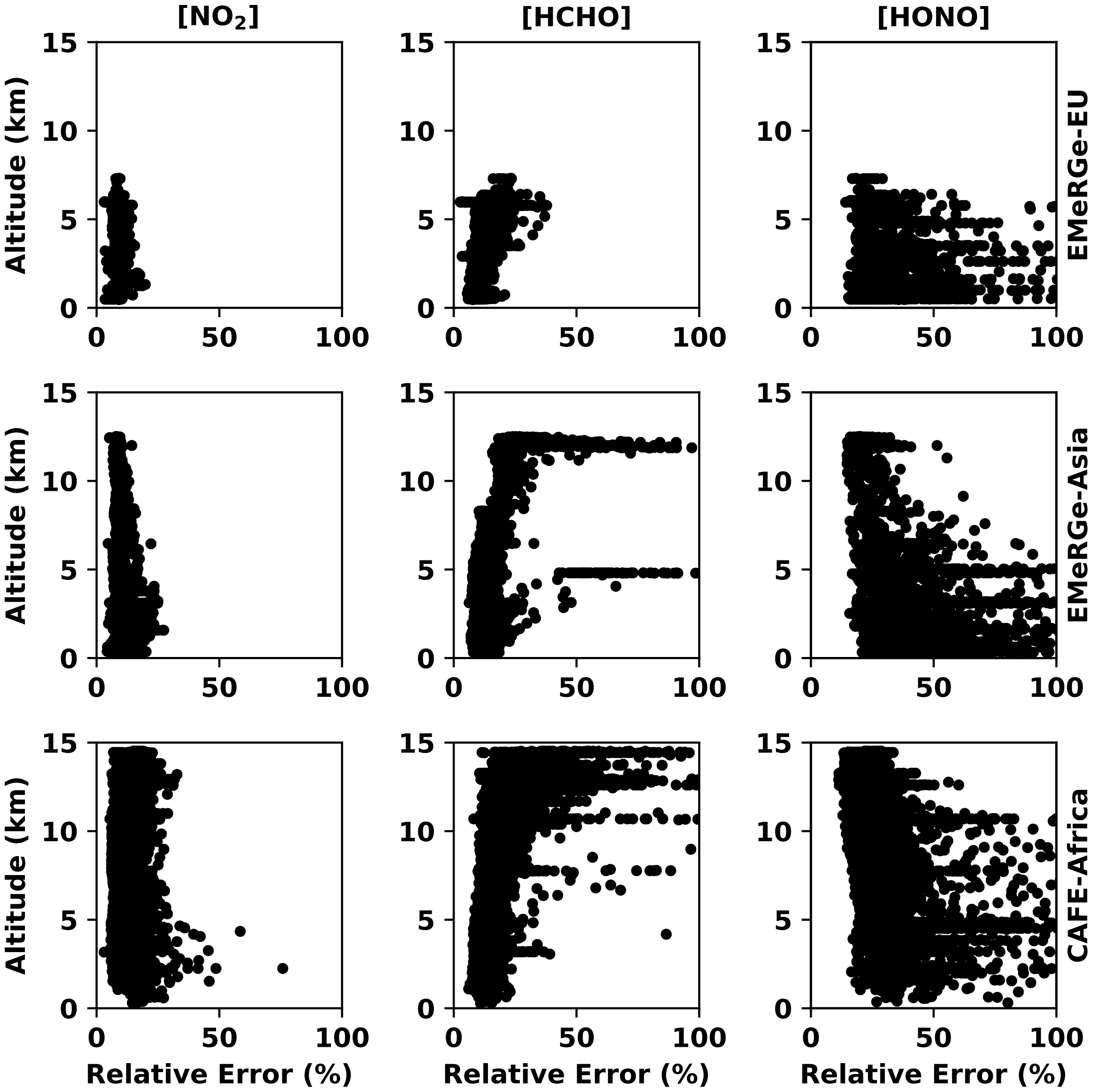

Figure 3.10: The relative errors for the three gases retrieved in the UV wavelength range (NO_2 (left), HCHO (middle) and HONO (right)), for the three missions (the two phases of EMeRGe and CAFE-Africa), for all flights as altitude profiles. Retrievals are discarded above 100 % error.

3.3.4 Comparison of measurements from the UV and visible spectral ranges

Light absorption by NO_2 molecules can be detected in both the UV and visible wavelength ranges with the DOAS technique (as can O_3 and O_4), and can therefore be retrieved independently with two spectrometers via the scaling method. Figure 3.11 shows the NO_2 VMRs retrieved in the UV and visible wavelength ranges (using O_4 as a scaling gas) for the data from all flights. The comparison demonstrates that the difference in radiative transfer between the UV and visible wavelength ranges effectively cancels out in the scaling retrieval in most cases. Distinctions exist primarily at lower altitudes; less spatial variability is expected at high altitudes.

Residual differences between the NO_2 retrievals are mostly due to the reference SCDs and arise from sampling biases between the UV and visible channels. The reference SCDs are determined by comparing the measured dSCDs to simulated SCDs, which are generated from the a priori profiles taken from the EMAC and MECO(n) models. Since the a priori profiles represent averages over several hours of flight time, the difference between measurements and simulations may be biased — especially within polluted air masses. Particularly, during the EMeRGe mission, frequent samples from low altitudes introduce a bias to the reference SCD of NO_2.

This bias is then an artifact of the high sampling frequency of visible spectra. Since HCHO and HONO can only be retrieved in the UV wavelength range, the UV retrievals of NO_2 are preferred, so that the three gases have coincident time series. A similar comparison for all flights using O_3 as a scaling gas can be found in appendix B.

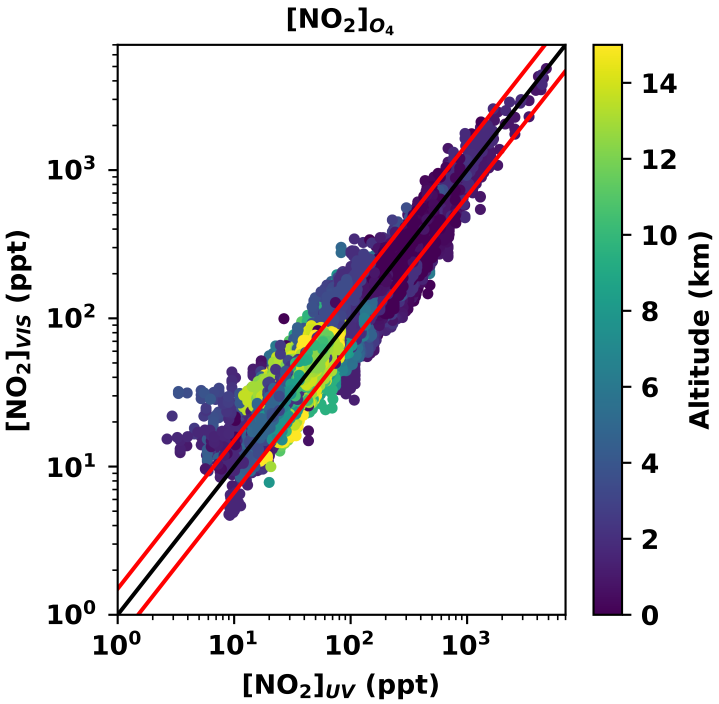

Figure 3.11: The NO_2 VMRs (ppt) as retrieved in the visible plotted against those retrieved in the UV wavelength range (using O_4 as a scaling gas). The color scale represents altitude. Note the logarithmic axes. The black line is a 1:1 line, the red lines are ± 50 %.

3.3.5 Using O_3 or O_4 as a scaling gas

To demonstrate the relative insensitivity of the scaling method with respect to the choice of scaling gas, the NO_2 retrievals in the UV wavelength range with O_3 as a scaling gas are compared with the results using O_4 as a scaling gas. The comparison is shown in figure 3.12, for data from all flights. Whether a target gas is scaled with O_3 or O_4, the retrieved VMRs compare well, indicating the robustness of scaling gas choice, although there are cases — especially at higher altitudes — where the O_3 scaling is biased high, likely as a result of the intrusion of stratospheric air. While the NO_2 scaled with O_3 and O_4 compare well, O_4 is preferred as a scaling gas hereafter, since 1) O_4 does not vary locally near boundaries such as intrusions of stratospheric air in the troposphere or crossing the tropopause, which results in large changes in O_3 and 2) scaling with O_4 does not rely on additional external data. Similar comparisons in the visible wavelength range, as well as for HCHO and HONO retrievals, can be found in appendix B.

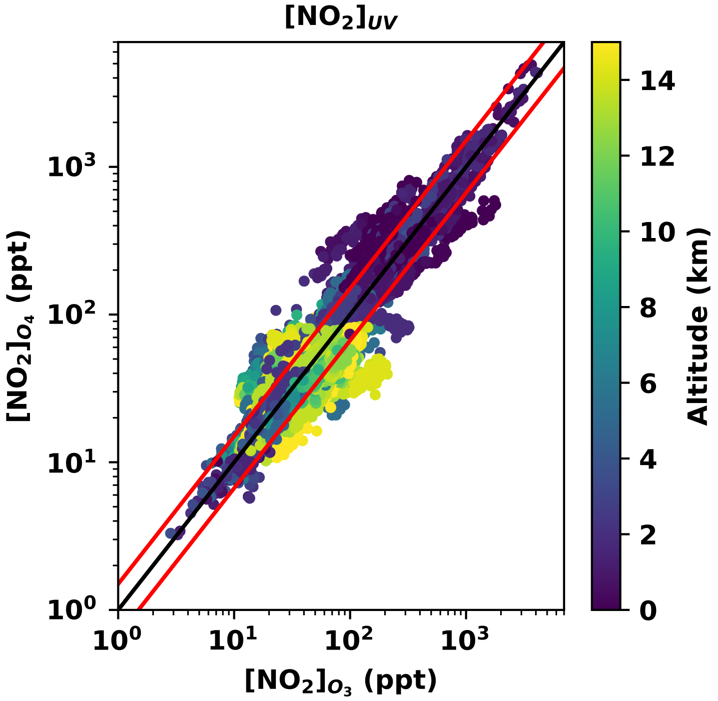

Figure 3.12: The NO_2 VMRs (ppt) retrieved using O_4 as a scaling gas plotted against those retrieved using O_3 as a scaling gas, all in the UV wavelength range. The color scale represents altitude. The black line is a 1:1 line, the red lines are ± 50 %. Note the logarithmic axes.

3.4 Additional instruments on board the HALO aircraft

The interpretation and contextualization of the measurements of the mini-DOAS instrument require observations of supplementary instrumentation on board the HALO aircraft. The instruments on board the HALO aircraft vary between missions. Those instruments which were present for the EMeRGe mission as well as the CAFE-Africa mission are enumerated below. Those which were present only for one mission or the other are described in the sections which detail those missions (see sections 4.1 & 4.2).

3.4.1 The BAHAMAS instrument

The Basic Halo Measurement and Sensor System (BAHAMAS) instrument [Mallaun et al., 2015] operated by the DLR provides onboard measurements of temperature [K], pressure [mbar], (relative) humidity [%], latitude, longitude, altitude [m], and water vapor [ppm], as well as roll, pitch, heading, velocity, etc. at 1 Hz (10 Hz during EMeRGe-EU). The BAHAMAS instrument provides the roll angle of the aircraft against which the mini-DOAS aligns the telescopes to the horizon during flight[1]. In this work, the measurements of the BAHAMAS instrument are used to

---

[1] During the SouthTRAC mission, a three second time delay was discovered between the ARINC roll angles and the roll angles provided to the mini-DOAS by the BAHAMAS instrument.

locate all other measurements in space and time, determine atmospheric density, and calculate reaction rate coefficients.

3.4.2 The C-ToF-AMS instrument

Mass concentrations [µg m^{-3}] of sub-micron aerosol components such as NO_3^-, SO_4^{2-}, NH_4^+, and organics are provided (with precision offsets) by the C-ToF-AMS instrument [Schulz et al., 2018] operated by the Max Planck Institute for Chemistry (MPIC). The instrument operates at a 30 second resolution during EMeRGe-EU and CAFE-Africa, and at a 15 second resolution during EMeRGe-Asia (since saturation takes less time in more polluted air). The C-ToF-AMS instrument measures aerosols of a sub-micron diameter only. The measurements of the Compact Time-of-Flight Aerosol Mass Spectrometer (C-ToF-AMS) are used to characterize the chemical composition of the sampled aerosol. For details on the chemical composition of the aerosols sampled during the EMeRGe and CAFE-Africa missions, see appendix C.

3.4.3 The HALO-SR-A instrument

Photolysis frequencies [s^{-1}] are measured by the HALO-SR-A instrument [Bohn and Lohse, 2017] operated by the Forschungszentrum Juelich (FZJ). Integrated flux densities are determined in the wavelength range 280 − 650 nm, with the spectral actinic radiation part of the HALO-SR instrument, which measures spectral solar radiance in the nadir geometry. In this work, the photolysis frequencies (with estimated errors) of HONO, NO_2, and HNO_3 are relevant.

3.4.4 The SKY-OPC instrument

Aerosol surface area [µm^2 cm^{-3}] and volume [cm^3 cm^{-3}] data are derived [Heintzenberg, 1994] for both coarse (d = 1 − 10 µm) and fine (d = 0.15 − 0.5 µm) aerosols from measurements of the Optical Particle Counter in C-ToF-AMS (SKY-OPC) instrument [Grimm, 2008] with a 60 second resolution. These measurements are also used as indicators for the presence of dust in the observed air masses.

3.4.5 The FAIRO instrument

In situ ozone measurements [ppb] are provided by the Fast AIRborne Ozone (FAIRO) instrument [Zahn et al., 2012] operated by the Institute for Meterology and Climate Research (IMK) using a dual-beam UV-photometer. Uncertainty is 2 % or at least 1 ppb. These in situ measurements are used in the scaling retrieval when O_3 is used as a scaling gas.

3.4.6 The SP2 instrument

The black carbon number concentration [cm^{-3}] and mass concentration [µg m^{-3}] are measured at 1 Hz using the Single Particle Soot Photometer (SP2) instrument [Holanda et al., 2020] operated by the MPIC.

3.5 Atmospheric chemistry models

In the absence of an in situ instrument which measures HONO, or satellite measurements thereof, the VMRs of HONO observed by the mini-DOAS instrument can only instead be compared to the simulations of global Chemical Transport Model (CTM)s. Model outputs are also compared to the HCHO and NO_2 retrievals, and used to construct a priori profiles of the target gases for the scaling method. The two models used in this study are the EMAC and MECO(n) CTM models. Neither model is suited for fine scale comparison with the VMRs retrieved by the scaling method. This is not due to a deficiency of either model per se, but rather that the concentrations of these gases may vary at timescales which neither model resolves. Generally, model comparisons should still be broadly representative of atmospheric chemistry, and capture the general profile shapes of the target gases.

3.5.1 The EMAC model

The EMAC model (ECMWF Hamburg (ECHAM) version 5.3.02) is a global atmospheric chemistry transport model [Jöckel et al., 2016]. Simulated data is provided at 90 pressure levels, with a time resolution of 10 minutes. EMAC model data is available for both phases of the EMeRGe mission as well as during the CAFE-Africa mission.

3.5.2 The MECO(n) model

The MECO(n) model (Consortium for Small-scale Modeling (COSMO) version 5.0) is a chemistry-climate model which calculates atmospheric dynamics. It is however nudged toward European Centre for Medium-Range Weather Forecasts (ECMWF) data at the synoptic scale [Mertens et al., 2016]. Simulated data is provided at 40 pressure levels during the -EU phase of the EMeRGe mission, and at 45 levels during the -Asia phase. The MECO(n) model has a time resolution of one minute and a horizontal resolution of 7 km. MECO(n) data is available for both phases of the EMeRGe mission but not for the CAFE-Africa mission.

Chapter 4

Research Missions

This chapter reports on the different airborne research missions conducted with the HALO[1] aircraft which are analyzed in this study. The mini-DOAS instrument was deployed on eight missions between 2014 and 2019. This thesis focuses on the analysis of data collected during three missions: EMeRGe-EU (July 2017), EMeRGe-Asia (March & April 2018) — which are two phases of the same broader mission (EMeRGe) — and CAFE-Africa (August & September 2018). The choice of missions is necessitated by the scheduled flight patterns, and the presence of additional instruments on board the HALO aircraft during those missions, which augment the study of the trace gases observed with the mini-DOAS instrument. The geographical areas and flight altitudes probed during these missions varies significantly, providing a broad overview of the concentrations of the trace gases studied in different seasons, layers of the troposphere and regions of the globe. The instrumentation on board the HALO aircraft during each mission is described in sections 4.1.2 and 4.2.1. Overview tables of flight parameters for all flights of each mission can be found in appendix D. Following the descriptions of the missions in sections 4.1 and 4.2, general features of the mini-DOAS field measurements are described in section 4.3.

4.1 The EMeRGe missions

The EMeRGe missions aimed at investigating the composition, transport and transformation of pollution plumes from megacities and MPCs. Within the two phases of the EMeRGe mission, airborne measurements of relevant atmospheric parameters, trace gases, and aerosols were performed on board the HALO aircraft at different altitudes over Europe in July 2017 and the east China Sea and south China Sea between the Philippines and Japan in spring 2018 (during the inter-monsoon period). These airborne observations were complemented by a suite of ground- and satellite-based measurements, as well as photochemical transport modeling (e.g. Hybrid Single-Particle Lagrangian Integrated Trajectory (HYSPLIT), FLEXible PARTicle (FLEXPART), EMAC, MECO(n), ...) [Andrés Hernández et al., 2022]. The field observations concentrated on the characterization of different air mass types downwind from a variety of emission sources (e.g., those of anthropogenic, biogenic, and biomass burning origin as well as background air). The transformation of the studied suite of trace gases and radicals as well as aerosol parameters (e.g., particle number, size distribution and chemical composition) has been used to provide some insights into chemical processing (and mixing) of these air masses during their atmospheric transport [Förster et al., 2023]. A detailed description of the objectives, instrument payload, and findings of the EMeRGe mission can be found in publications of the ACP/AMT inter-journal EMeRGe special issue `https://acp.copernicus.org/articles/special_issue1074.html`, specifically in the EMeRGe-EU overview paper by Andrés Hernández et al. [2022]. The result of an intercomparison exercise during the EMeRGe-EU mission have been published in Schumann [2021] and are partly reported on in chapter 5.

One of the EMeRGe objectives developed only after our observation of larger nitrous acid (HONO) concentrations — which were reported from the boundary layer and lower free troposphere — than gas phase chemistry may explain (see chapter 5). These observations are reported along with photochemical model simulations, to unravel its possible causes and poten-

---

[1] `https://halo-research.de/`

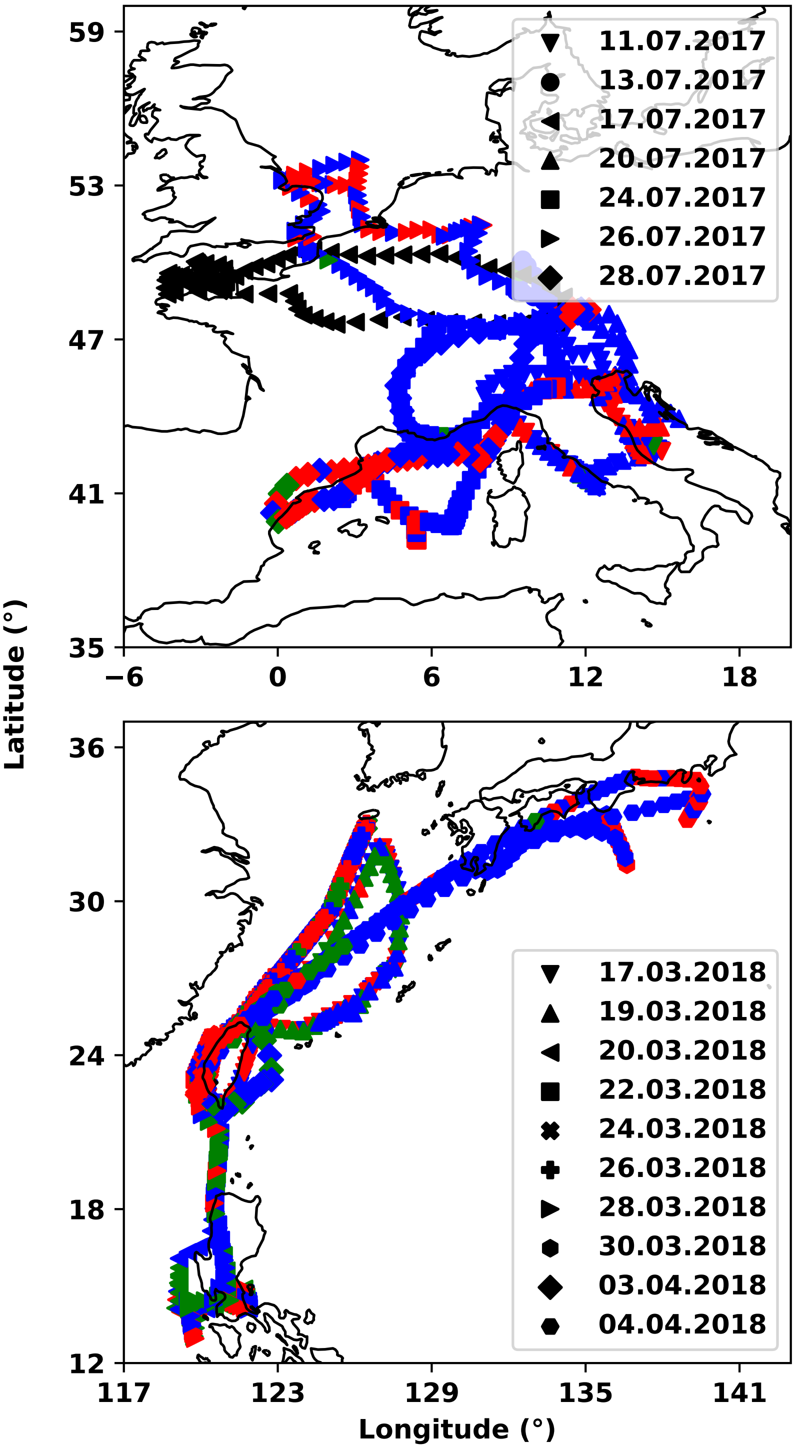

Figure 4.1: The flight tracks of the seventeen scientific flights of the two phases of the EMeRGe mission during July 2017 and March/April 2018. The latitude and longitude coordinates are colored by air mass tags from measurements of the HKMS instrument [Förster et al., 2023] (see text), except for the flight on 17.07.2017 due to an instrument failure (shown in black). Red coloring indicates primarily anthropogenic emissions (determined from measurements of benzene), green indicates biomass burning (determined from measurements of acetonitrile), while blue indicates neither, and is assumed to be background air. The operational base of EMeRGe-EU (upper panel) was Oberpfaffenhofen, Germany; EMeRGe-Asia was (lower panel) based out of Tainan. Transfer flights to and from Tainan during EMeRGe-Asia are excluded.

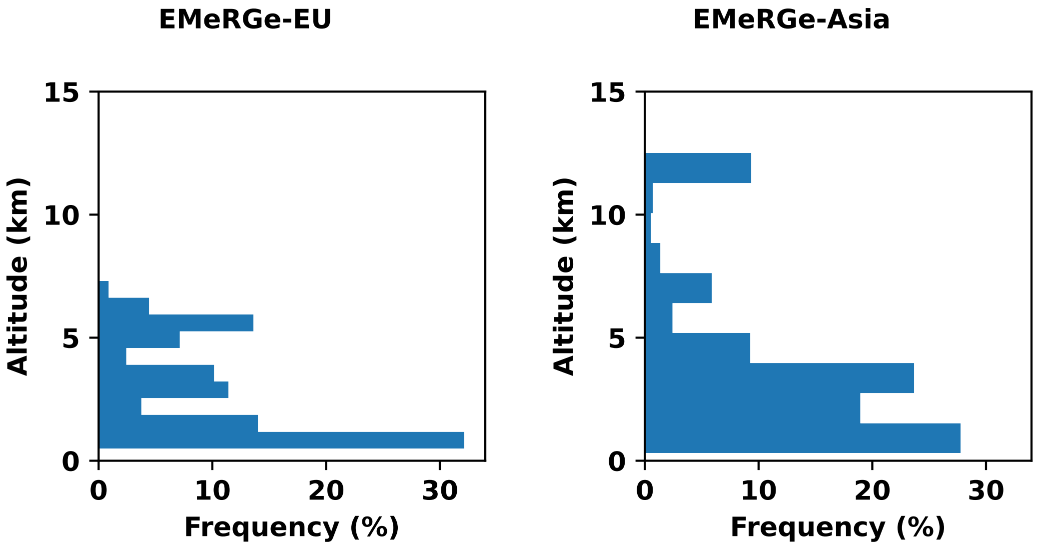

Figure 4.2: The frequency of measurements at flight altitudes during both phases of EMeRGe.

tial heterogeneous formation mechanism(s). In particular, since these mechanism(s) (see table 2.1) potentially involve a variety of different species and aerosol parameters (specifically surface area and volume, chemical composition, etc.), these measurements are included in our analysis when available. Parameters measured during the EMeRGe missions include (but are not limited to) basic aircraft data (e.g. pressure, temperature, humidity), black carbon number and mass concentrations, aerosol surface area and volume, major sub-micron aerosol composition ingredients (e.g. NO_3^-, SO_4^-, NH_4^+, organic substances), NO, NO_y, O_3, RO_2* (HO_2 + RO_2), SO_2, spectral actinic flux density derived photolysis frequencies, and finally HCHO, HONO and NO_2 measured as described above. Several of these species and parameters are used as proxies in investigating the potential HONO formation mechanism(s). A more complete analysis of the HONO budget would also require measurements of HNO_3 and OH, both of which are unfortunately not available during the EMeRGe missions.

During both EMeRGe phases (Europe and Asia) the measurement flights usually lasted eight hours on average with take off in the mornings and landings in the early afternoons, i.e. exclusively during daylight. While the flight levels spanned measurement altitudes from a few dozen meters above sea level to up to 12500 m, 72 % of the air masses analyzed were within the lowermost four kilometers of the atmosphere, i.e. in the boundary layer and lower free troposphere. As a consequence of the covered altitude range and season, the ambient temperatures were mostly above (water) freezing temperature; the high ambient temperatures limited the duration of thermal stability of the instrument during some flights. The measurement flights of the EMeRGe missions sampled large geographical areas, spanning continental Europe and east Asia. Various atmospheric conditions characterized each flight, such as the occurrence of thunderstorms in southern Europe, as well as the presence of anthropogenic pollution plumes (see figure 4.1). During the European deployments most of the flight time was spent over land, in contrast with deployments during the phase in Asia, where much of the flight time was spent over the East China Sea and South China Sea. Detailed flight tracks together with air mass tags (see below) are shown in figure 4.1. The air masses observed during the -Asia phase contained more signatures of biomass burning than the -EU phase [Förster et al., 2023].

4.1.1 The characterization of air masses

The origin and composition of an air mass may determine the concentrations of trace gases sampled from the HALO aircraft. In keeping with the scientific objectives of the EMeRGe missions, the air masses probed during the EMeRGe missions are characterized with plume tags, which are interpolated from the VOC measurements of the HKMS instrument [Förster et al., 2023]. Elevated VMRs of acetonitrile (above 145 ppt) are indicative of biomass burning influence, while elevated VMRs of benzene (above 19 ppt) are indicative of anthropogenic pollution. Across all flights, 34 % of air masses observed during the EMeRGe missions are tagged with anthropogenic influence, 14 % contain signatures of biomass burning, and the remaining 51 % are assumed to be otherwise background air. These percentages vary from flight to flight and across mission phases. As expected, less biomass burning influenced air was found during the deployments in Europe, compared to those probed over Asia [Förster et al., 2023]. The studies by Kluge et al. [2020, 2023] also associate enhanced glyoxal as measured by the mini-DOAS with the air masses influenced by biomass burning and anthropogenic pollution. Fine and coarse aerosol surface area and volume data calculated from the measurements of the SKY-OPC instrument may also be used to distinguish dust events.

4.1.2 Additional instruments on board HALO during EMeRGe

In addition to the instruments described above, in situ measurements from several other instruments on board the HALO aircraft complemented the measurements of the mini-DOAS instrument during the EMeRGe missions. Each is only briefly described below. More detailed descriptions can be found in the publications of the respective institutions.

The NO [ppb] (and NO_y [ppb]) measurements of the AtmosphEric Nitrogen oxides mEAsuring System (AENEAS) instrument [Ziereis et al., 2004] operated by the Institute of Atmospheric Physics (IPA) are made using a two channel chemiluminescence detector at 1 Hz. NO_y is detected with a gold converter in one channel.

The measurements of SO_2 [ppt] were performed with a Chemical Ionization Mass Spectrometer (CIMS) instrument operated by the IPA with an uncertainty of 7 % and a 20 ppt detection limit.

The HKMS instrument [Brito and Zahn, 2011; Warneke et al., 2011] operated by the Karlsruhe Institute of Technology (KIT)'s IMK measures several VOCs, including formaldehyde [ppt] above a 208 ppt detection limit and 18 % uncertainty. Acetonitrile and benzene concentrations measured by the HKMS instrument are interpolated to 1 Hz and used to identify emission outflows (see above). The measurements of the HKMS instrument are not available for the research flight on 17.07.2017.

The sum of peroxy radicals ($RO_2{}^* = HO_2 + RO_2$) [ppt] was measured by the Peroxy Radical Chemical Enhancement and Absorption Spectrometer (PeRCEAS) instrument [George et al., 2020, 2023] operated by the University of Bremen's Institut fur Umweltphysik (IUP) at a 60 second resolution. Precision is expressed by a standard deviation measured over two minutes. Measurements of $RO_2{}^*$ are not available for the research flight on 17.03.2018.

In addition to those provided by the FAIRO instrument, measurements of O_3 [ppb] are also provided by the AtMospheric Trace EXperiment (AMTEX) instrument [Gerbig et al., 1996] operated by the IPA at 1 Hz.

4.2 The CAFE-Africa mission

The CAFE-Africa[2] mission was headquartered in Sal, Cape Verde and took place in August and September of 2018. The area of study was the tropical troposphere over the Atlantic Ocean and western Africa. Of the fourteen scientific flights, 12 are analyzed here — the transfer flights are excluded. The scientific objectives of CAFE-Africa included the study of oxidation chemistry, thunderstorm effects, radiative forcing, long-distance transport, and biomass burning. The investigated region overlaps with the Intertropical Convergence Zone (ITCZ), while the maximum flight altitude was ≈ 15 km. The flight tracks are shown in figure 4.3, and an overview table of the dates and objectives of each flight is given in appendix D.

The measurement flights took off in the mornings, landed in the evenings and were primarily conducted during daylight (with the exception of the flight on 26.08.2018, which continued past sunset). Most flight time was spent at high altitudes, over the Atlantic Ocean. Ambient temperatures were therefore usually below (water) freezing temperature, enhancing the temperature stability of the mini-DOAS instrument. The flight on 02.09.2018 probed air of the recently formed tropical storm Florence.

---

[2] `https://mpic.de/4130589/cafe-africa`

Here, as in the EMeRGe mission, unexpectedly elevated VMRs of HONO were observed in the upper troposphere, relative to expectations from the known gas phase chemistry (see chapter 5). During the CAFE-Africa mission, simultaneous measurements of OH, NO, and J_{HONO} allow the quantification of gas phase HONO formation. Compared to the EMeRGe missions, less HONO was observed in the lower troposphere, though VMRs retrieved with the scaling method are still above what would be expected based only on gas-phase production.

Airborne measurements of HONO within the same region the following year, reported by Andersen et al. [2023], corroborate the HONO reported by this thesis (see section 6.1).

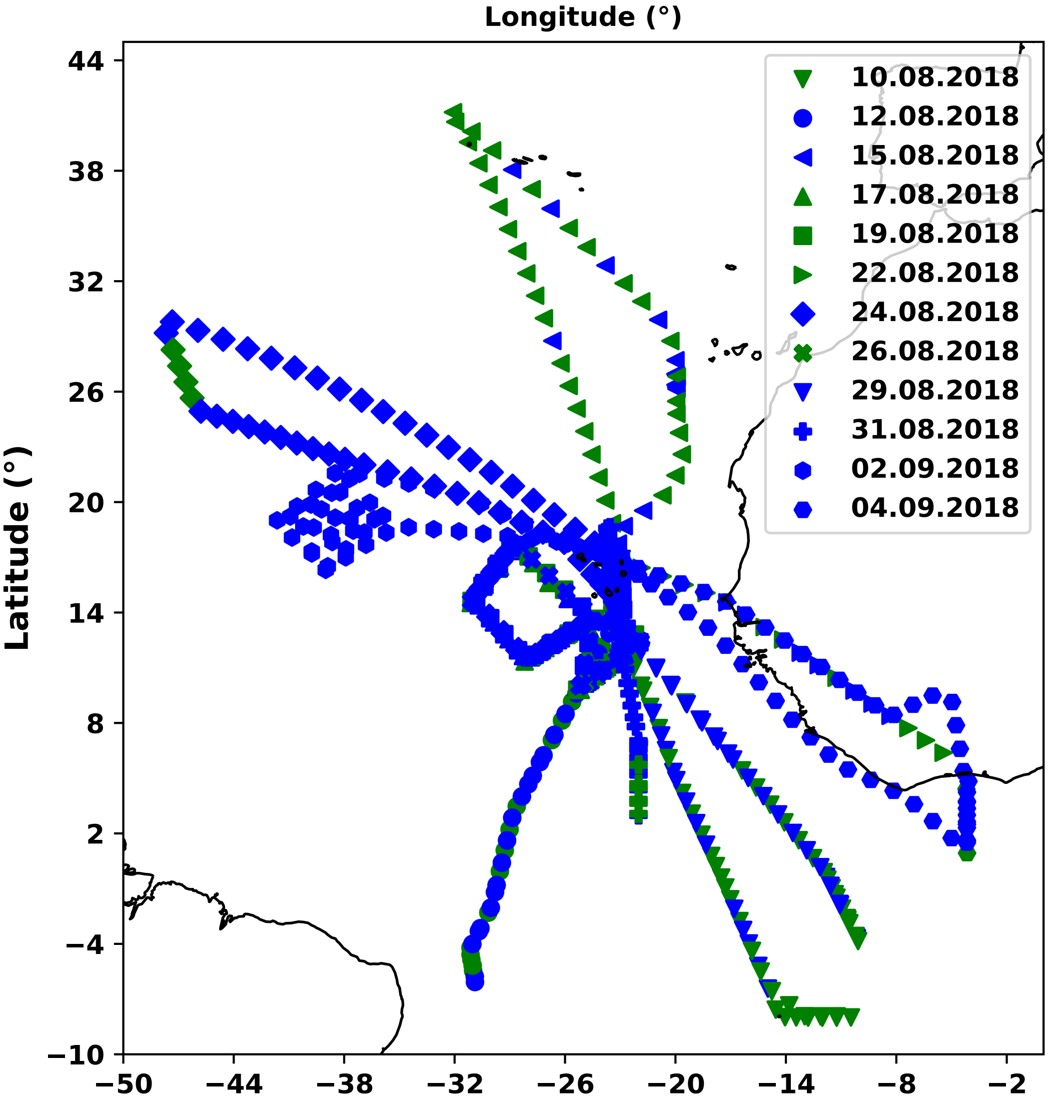

Figure 4.3: The flight tracks of the twelve scientific flights of the CAFE-Africa mission in August and September of 2018 (the transfer flights are excluded). The operational base of the CAFE-Africa mission was Sal, Cape Verde. As in figure 4.1, the longitude and latitude coordinates are colored according to the air mass tags described in the text. Green indicates biomass burning, here determined from acetonitrile measurements of the MMS instrument; blue indicates acetonitrile below the 145 ppt threshold and is assumed to be otherwise pristine air.

4.2.1 Additional instruments on board HALO during CAFE-Africa

In addition to those described in section 3.4, several other in situ instruments on board the HALO aircraft complement the study of the trace gases measured by the mini-DOAS instrument during

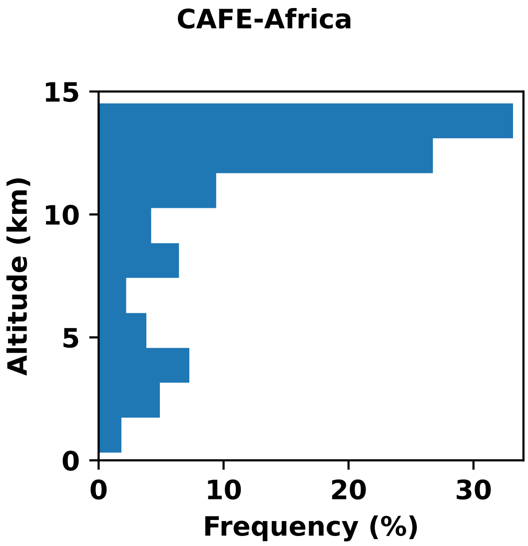

Figure 4.4: The frequency of measurements at flight altitudes during the CAFE-Africa mission.

the CAFE-Africa mission. Each is only briefly described below. More detailed descriptions can be found in the publications of the respective institutions.

The Nitrogen Oxides Analyser on HALO (NOAH) instrument [Tadic et al., 2020] operated by the MPIC provides measurements of NO [ppb] above a 16 ppt detection limit at 1 Hz with a total measurement uncertainty of 6 %. Measurements of the NOAH instrument are not available for the first flight of the CAFE-Africa mission on 10.08.2018.

The HydrOxyl Radical measurement Unit based on fluorescence Spectroscopy (HORUS) instrument [Marno et al., 2020; Marno, 2021] operated by the MPIC provides measurements of OH [ppt] and HO_2 [ppt]. Measurements of the HORUS instrument are not available on the first flight of the CAFE-Africa mission on 10.08.2018.

Measurements of HNO_3 [ppb] are provided by the CIMS instrument [Dörich et al., 2021] operated by the MPIC. HNO_3 measurements are not available for the first four flights of the CAFE-Africa mission (10.08.2018, 12.08.2018, 15.08.2018, 17.08.2018).

The Proton transfer reaction time-of-Flight mass spectrometer (MMS) instrument [Wang et al., 2020] is operated by the MPIC and measures acetonitrile in ppt, which is used to indicate biomass burning plumes as in the EMeRGe mission. Enhancements are determined relative to a 145 ppt background. Measurements are reported every 60 seconds.

4.3 Field measurements of the mini-DOAS instrument

The measurements reported here are derived from several thousand spectra successfully recorded with the mini-DOAS instrument.

Rarely, there are periods of time during some flights when skylight cannot be collected, or when measured skylight spectra cannot be analyzed. The former includes highly variable cloud conditions, when the aircraft flew inside or next to bright clouds, since then the spectrometers tend to become oversaturated (in the post-flight analysis such periods are identified by inspecting images captured with the IDS uEye camera described above). Otherwise, night flights do not provide sufficient light for the collection of spectra. The latter occurs when the detector and/or spectrometer temperature increase beyond ≈ 4 °C, since increasing detector temperatures increase the dark current and changing spectrometer temperatures degrade the imaging of the spectrometers (by broadening the instrument's spectral response function). Temperature stability for some flights lasted up to 9 hours, while when flying for longer periods at higher ambient temperatures (i.e. at low altitudes), the stable measurement interval lasted only 3 hours in some cases (particularly during the EMeRGe mission). Spectra recorded during turns of the aircraft are also discarded from analysis. Communication problems between the BA-

HAMAS and mini-DOAS instruments during four flights of the EMeRGe mission prevented the live alignment of the telescopes with the horizon, rendering the correct attribution of observed absorption to a particular layer in the atmosphere practically impossible. Therefore, the affected flights on 26.07.2017, 28.07.2017, 22.03.2018, and 03.04.2018 are excluded from analysis. These communication problems have been circumvented by the installation of an additional Aeronautical Radio, Incorporated (ARINC) port, which communicates the aircraft's data directly with the mini-DOAS instrument, preventing this problem in any future flights.

Unfortunately, not only failure or malfunctions of the mini-DOAS instrument restrict our analysis, but also the availability of the necessary data measured by the complementary instruments operated on board the HALO aircraft. For example, during the EMeRGe mission, measurements of VOCs made by the HKMS instrument (and consequently the air mass characterizing plume tags) are not available on 17.07.2017, while RO_2^* measured with the PeRCEAS instrument is not available on 17.03.2018.

During the CAFE-Africa mission, measurements of NO, OH, and HO_2 are unavailable on 10.08.2018, while measurements of HNO_3 with the CIMS instrument are not available for the first four flights of the mission on 10.08.2018, 12.08.2018, 15.08.2018, and 17.08.2018.

Chapter 5

Observations & Results

This chapter presents the retrieved NO_2, HCHO, and HONO from the EMeRGe and CAFE-Africa missions. An overview of the altitude profiles of NO_2, HCHO, and HONO is presented in section 5.1. The retrieved NO_2, HCHO, and HONO are compared with in situ measurements and with models where available in section 5.2, and while the NO_2 and HCHO measured by the mini-DOAS instrument compare well with in situ measurements, the HONO can only be compared with previously reported measurements, or with model simulations. The measured NO_2 and HCHO are in agreement with those models' predictions, but the measured HONO is often in excess of those predictions.

This excess HONO requires explanation. The necessary strength of the HONO source term in the observed air masses (and thereby the OH produced upon photolysis) is investigated in section 5.3. Meanwhile, the NO_2 observed by the mini-DOAS instrument is combined with measurements of auxiliary parameters by in situ instruments, and the observed and expected Leighton relationship (a proxy for oxidation capacity of the atmosphere, see section 3.4) within the observed air masses are presented in section 5.4. These observations present another line of evidence for a missing oxidant in those air masses. Section 5.5 briefly explains the collision frequency of air with measured aerosol surface area — according to kinetic gas theory — to motivate the invocation of possible heterogeneous phase HONO formation mechanisms within the lower troposphere, and a gas phase HONO formation mechanism in the upper troposphere. Respective heterogeneous and homogeneous potential sources of the excess HONO in three separate regimes of the troposphere are investigated in detail in chapter 6.

In the appendix, the NO_x- or VOC-limited nature of ozone production within the observed air masses is characterized (appendix E), and a combined coordinate system from the Leighton ratio and ozone production parameters can be found in appendix F.

5.1 Retrieved vertical profiles of NO_2, HCHO and HONO

Altitude profiles of NO_2, HCHO, and HONO VMRs retrieved in the UV wavelength range using O_4 as a scaling gas are shown in figure 5.1 for all 25 flights of the two EMeRGe missions and the CAFE-Africa mission. An overview of the general profiles of each gas for each mission is provided in the following subsections.

5.1.1 NO_2

NO_2 VMRs are generally elevated near the surface where most of the anthropogenic sources are located, decrease with altitude, and increase again into the upper troposphere because of the sources and sinks described in chapter 2. In the polluted air masses observed during the EMeRGe mission, NO_2 VMRs near the surface reach 1–4 ppb, decrease with altitude, reach a minimum in the free troposphere, and increase again into the upper troposphere during the two flights which probed those altitudes during the EMeRGe-Asia mission. During the CAFE-Africa mission, comparatively little NO_2 is observed, generally less than 100 ppt at all altitudes. The VMRs of NO_2 observed in the upper troposphere are typical for those altitudes (20–80 ppt) [Marais et al., 2018, 2021].

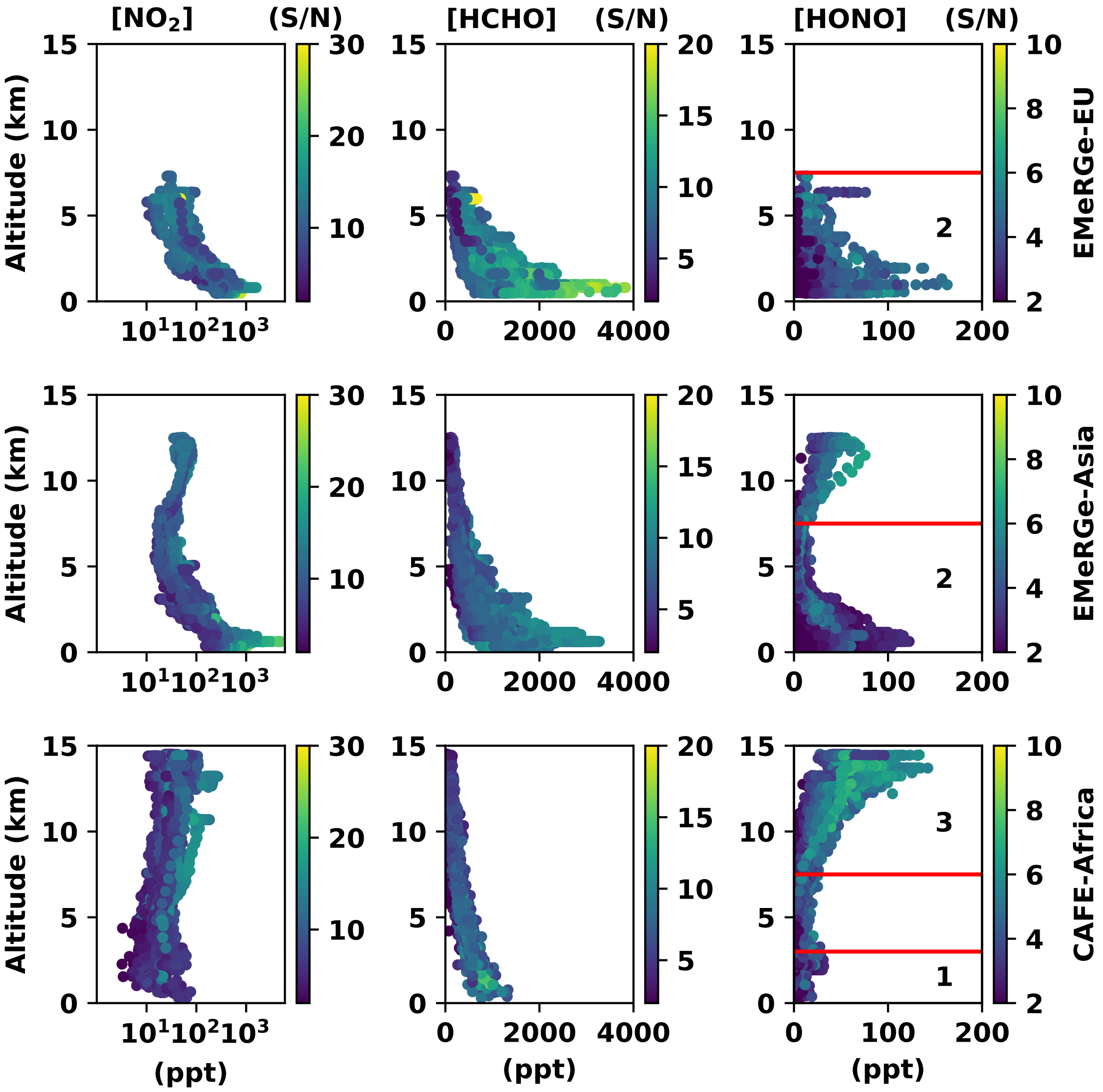

Figure 5.1: Altitude profiles of the VMRs (in ppt) for the three gases retrieved with the mini-DOAS instrument: NO_2 (left column), HCHO (middle column), and HONO (right column), each retrieved in the UV wavelength range using O_4 as a scaling gas. Each row displays all flights from each of the three missions: EMeRGe-EU (top row), EMeRGe-Asia (middle row) and CAFE-Africa (bottom row). Note the logarithmic x axes for NO_2. The red horizontal lines distinguish the MBL (regime 1) as well as the lower (regime 2) and upper (regime 3) tropospheres for the regimes where excess HONO is observed. The signal to noise ratio (S/N) is marked by the color scheme, with different ranges for the individual gases.

5.1.2 HCHO

The atmospheric concentration of species directly emitted or indirectly produced near the surface (such as formaldehyde) often decay exponentially with altitude unless they are produced in situ (see Kluge et al. [2020], figure 10 and references therein). In the polluted air masses sampled during both phases of the EMeRGe mission, HCHO reaches 3–4 ppb at the lowest altitudes sampled, and decreases with increasing altitude to less than 160 ppt in the upper troposphere. These VMRs are similar to those reported from Europe, measured with other DOAS instruments [Heckel et al., 2005]. Considerably less HCHO is observed in the lower troposphere during the CAFE-Africa mission, reaching only ≈ 1 ppb near the surface.

5.1.3 HONO

HONO VMRs are elevated in the lower troposphere (up to 150 ppt) for every flight of the EMeRGe mission (regime 2), as well as in the upper troposphere (up to 75 ppt) during the two flights which probed those altitudes during the EMeRGe-Asia mission. Comparatively little HONO is observed in the free troposphere. In comparison to the EMeRGe mission, during the CAFE-Africa mission, lower HONO VMRs are retrieved in the lower troposphere, though some tens of ppt are still observed within the MBL (regime 1). Meanwhile HONO VMRs are elevated in the upper troposphere (upwards of 100 ppt) during all flights of the CAFE-Africa mission (regime 3). HONO is consistently found in excess relative to expectations based on known gas phase formation mechanisms or model predictions (see below).

5.2 Validation of the measurements

In order to validate the measurements reported in section 5.1, the reported VMRs of NO_2, HCHO, and HONO are compared with in situ instruments where available, as well as with the EMAC and MECO(n) models' predictions.

Validation is only possible when other instruments on board HALO (or another aircraft) coincidentally measure the same gases in the same air masses. For NO_2, only the intercomparison exercise over Germany on 13.07.2017 during the EMeRGe-EU mission provides an opportunity for validation. NO_2 measured by the AQD instrument on board the FAAM aircraft is compared with the NO_2 measured by the mini-DOAS instrument (see below). NO_2 measured during the CAFE-Africa mission has also been compared with photolysis-chemiluminescence measurements [Nussbaumer et al., 2021a]. The comparison revealed problems with the employed photolytic converter (see figure 4a in Nussbaumer et al. [2021a]). During the same intercomparison exercise, HCHO measured by the HKMS instrument on board HALO is compared with HCHO measured by the mini-DOAS instrument (see figure 69 in Schumann [2021]). HCHO was measured by the HKMS instrument throughout both phases of the EMeRGe mission, and is additionally compared with the HCHO retrieved by the mini-DOAS instrument for all flights (see below). No in situ instruments on board either aircraft measured HONO. Therefore validation is only possible with other studies in the same regions as those investigated during the EMeRGe and CAFE-Africa missions. Otherwise, the observed NO_2, HCHO, and HONO can be compared with CTMs such as EMAC for all three missions and MECO(n) for the EMeRGe missions (see below).

5.2.1 Comparison and validation of NO_2 measurements

A comparison between the NO_2 measured by the remote sensing mini-DOAS instrument on board HALO and NO_2 measured in situ by the AQD instrument on board the FAAM aircraft during the EMeRGe mission's intercomparison flight is shown in figure 5.2. The NO_2 retrieved by the mini-DOAS instrument in the UV wavelength range and scaled with O_4 compares well with NO_2 measured using an in situ instrument on board another aircraft, although short temporal or spatial scale spikes detected by the in situ instrument are not resolved by the mini-DOAS instrument. Otherwise the NO_2 measured by the mini-DOAS instrument is robust with respect to choice of scaling gas and spectral range (see chapter 3).

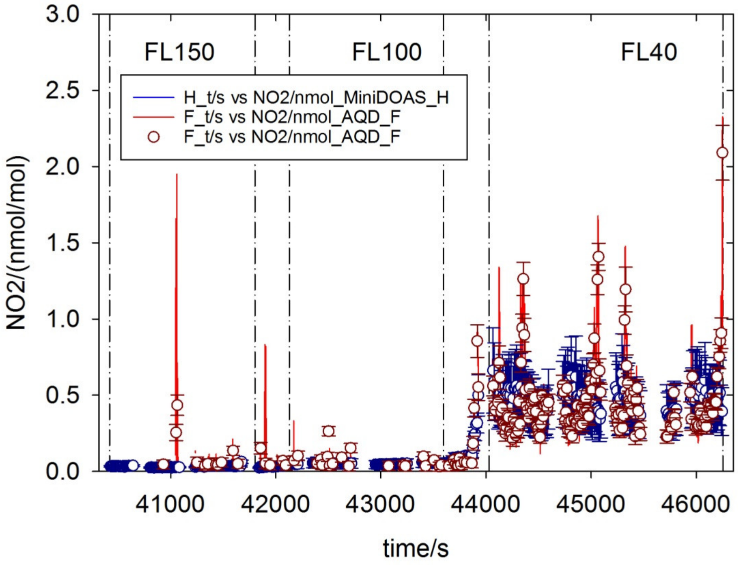

Figure 5.2: The time series of NO_2 measurements from the remote sensing mini-DOAS instrument on board HALO and the in situ AQD instrument on board the FAAM aircraft in blue and red, respectively. Data is from a segment of the intercomparison flight on 13.07.2017 during the EMeRGe-EU mission. The figure is taken from Schumann [2021]. Units of nmol/mol are synonymous with ppb.

5.2.2 Comparison and validation of HCHO measurements

A comparison between the HCHO measured by the remote sensing mini-DOAS instrument on board HALO and HCHO measured in situ by the HKMS instrument also on board the HALO aircraft during the EMeRGe mission's intercomparison flight is shown in figure 5.3.

Despite the inherent differences between in situ and remote sensing measurements, and the comparably large averaging kernel of the scaling method, HCHO VMRs retrieved with the scaling method compare well with HCHO retrieved in situ by the HKMS instrument during both EMeRGe missions. Figure 5.4 shows the HCHO VMRs retrieved by the mini-DOAS instrument (in the UV wavelength range using O_4 scaling) and the HCHO retrieved by the HKMS instrument for all flights of the EMeRGe missions, as functions of altitude. While local spikes in the VMRs detected by the in situ HKMS instrument are not resolved by the remote sensing mini-DOAS instrument, the background signal and general profile shapes generally agree within the reported margins of error (see Andrés Hernández et al. [2022], figure 16).

5.2.3 Comparison of HONO measured in the boundary layer and lower free troposphere with previous studies

Since no other measurements of HONO were available on HALO, we discuss how they compared with previously reported HONO measured under similar conditions (see figure 5.5). The measured HONO observed in the polluted lower troposphere exceeds expectations based on the known gas phase formation. This excess HONO has been reported previously [Zhang et al., 2009; Li et al., 2014; Heue et al., 2014; Ye et al., 2016b, 2018; Andersen et al., 2023], which are summarized below and shown in figure 5.5.

Zhang et al. [2009] and coworkers were the first to measure HONO vertical profiles from on board a small aircraft in the lower atmosphere, where HONO mixing ratios ranged from 4 – 17 ppt in the FT and from 8 – 74 ppt in the PBL over a forested region in northern Michigan and the neighboring Great Lakes in summer 2007. They argued that most (> 90 %) of the detected HONO in the upper part of the PBL and FT may have originated from in situ production (at local noon in total $\sim$ 57 ppt h^{-1} in the FT and $\sim$ 110 – 180 ppt h^{-1} in the upper part of the PBL) other than by the reactions 1.1 to 1.3, but they could not firmly conclude on the possible HONO formation mechanism(s).

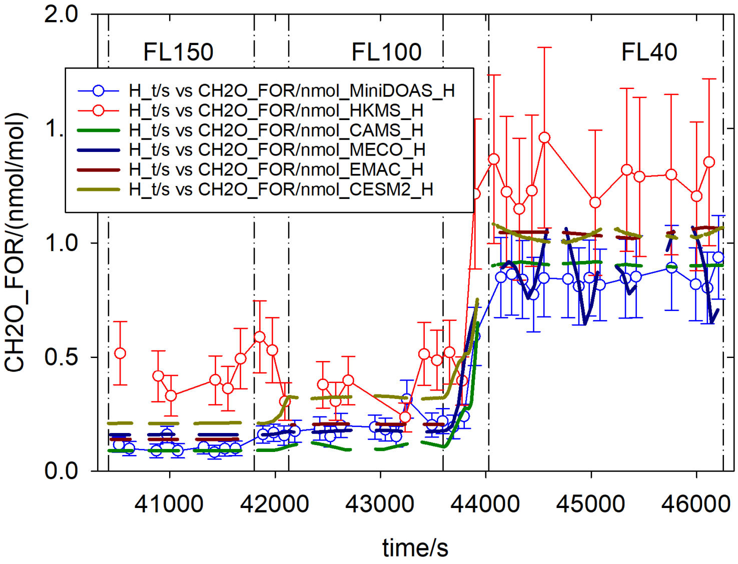

Figure 5.3: Time series of the HCHO measurements from the remote sensing mini-DOAS instrument on board HALO and the in situ HKMS instrument also on board HALO in blue and red, respectively. Data is from a segment of the intercomparison flight on 13.07.2017 during the EMeRGe-EU mission. The figure is taken from Schumann [2021]. Units of nmol/mol are synonymous with ppb.

Using an airship (a Zeppelin), Li et al. [2014] measured HONO mixing ratios of 100 – 150 ppt in the transitional layer at the top of the boundary layer (i.a. above 350 m) over the polluted Po valley during sunrise and well into the morning (4:00 – 8:30 UTC) in July 2012. They suggested the reaction $HO_2 \cdot H_2O\,(g) + NO_2\,(g) \longrightarrow HONO\,(g) + O_2 + H_2O\,(g)$ explains best their observations, but this explanation was later refuted by Ye et al. [2015] due to the small HONO yield of this reaction (< 0.03) (see mechanism 3 in table 2.1).

Heue et al. [2014] measured HONO within a large thunderstorm cloud from nearby with a DOAS instrument during the Civil Aircraft for the Regular Investigation of the atmosphere Based on an Instrument Container (CARIBIC) mission over the Caribbean Sea in August, 2011. They attributed their observations to updraft as well as HONO production initiated by lightning NO_x.

Next, using a novel chemical ionization mass spectrometer instrument, Neuman et al. [2016] measured HONO on the National Oceanic and Atmospheric Administration (NOAA) WP-3D aircraft over the Southeast U.S. during the Southeast Nexus Experiment in June and July 2013. During the night, HONO mixing ratios in excess of 4 ppb were found in the PBL, mostly due to emissions from agriculture as well as urban and power plant emissions. From the daytime measurement of HONO in plumes of power plants complemented by Lagrangian plume dispersion modeling, they concluded that the gas phase reactions 1.1 to 1.3 are sufficient to explain their observations. Further, the daytime HONO measurements were at or below the detection limit (~ 15 ppt) of the instrument in background air of the PBL (e.g., outside freshly emitted plumes); they concluded that their observations would not support the existence of a ubiquitous unknown HONO source that produces significant HONO concentrations in the lower troposphere.

During two research flights, Ye et al. [2016b] detected between 8.8 ± 2.3 ppt and 11.3 ± 1.6 ppt HONO in the marine PBL over the Northern Atlantic Ocean (around 32 – 33 ° N, and 71.6 ° E) in summer 2013. They explained their observations contending that pNO_3 photolysis (mechanism 13 in table 2.1) mainly sustained the observed levels of nitrous acid and nitrogen oxides at midday under typical marine boundary layer conditions (in agreement with Andersen et al. [2023], see below).

From the same mission, Ye et al. [2018] reported on HONO measured in background air of the PBL (5 – 15 ppt) and FT (low parts per billion) over the Southeastern US in summer 2013. From these measurements combined with actinic flux measurements and assuming a steady state, they calculated a mean HONO source strength of 53 ± 21 ppt h^{-1}, of which at most 10 ± 5 ppt h^{-1}

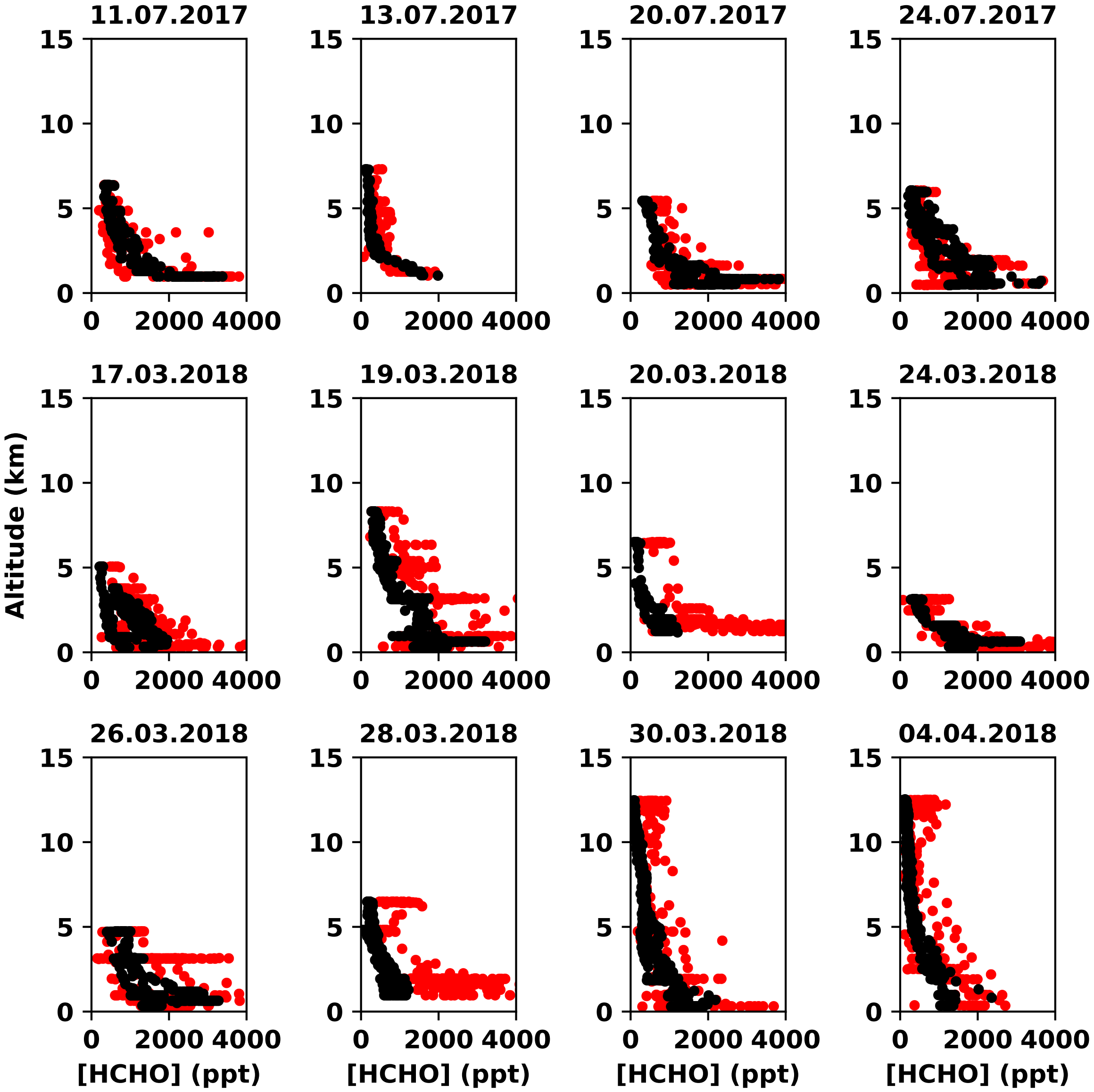

Figure 5.4: HCHO VMRs (ppt) measured by the remote sensing mini-DOAS instrument (black) and the in situ HKMS instrument (red) — both on board HALO — for all but one flight of the EMeRGe missions as altitude profiles. The flight on 17.07.2017 is excluded due to a failure of the HKMS instrument.

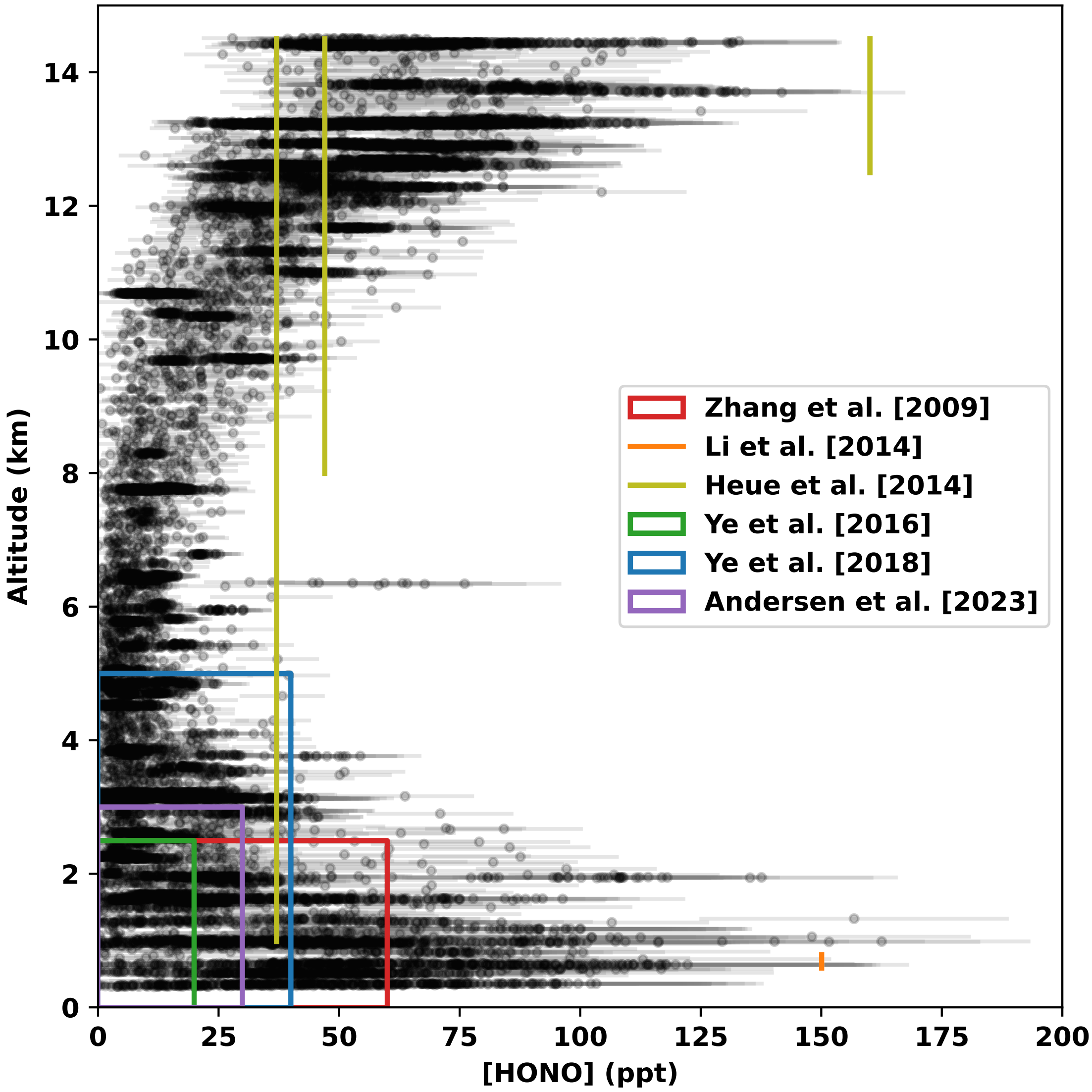

Figure 5.5: Comparison of airborne HONO altitude profiles reported here (gray), as well as regions representing the range of airborne HONO observations reported previously. Previously reported HONO observations from aircraft are limited to the lower troposphere with only one exception [Heue et al., 2014], the altitude of which is not precisely defined. The HONO VMRs reported by Heue et al. [2014] are converted from DOAS retrievals within a thunderstorm cloud and are sensitive to the assumed HONO profile shape.

were from NO_x-related sources and 38 ± 23 ppt h^{-1} from photolysis of pNO_3. In their study, the latter became evident from measured pNO_3 concentrations and the median pNO_3 photolysis rate constant of $2.0 \cdot 10^{-4}$ s^{-1} determined in the laboratory using ambient aerosol samples.

Recent aircraft observations of HONO in the MBL reported by Andersen et al. [2023] corroborate those reported here (see section 6.1). Andersen et al. [2023] measured HONO using differential photolysis, in the same region investigated by us during the CAFE-Africa mission (i.e. around Cape Verde up to 3 km altitude), in August 2019.

5.2.4 Comparison between modeled and measured NO_2, HCHO, and HONO

In the absence of other validation options, the retrieved VMRs of NO_2, HCHO, and HONO may also be compared with the EMAC and MECO(n) models' predictions. Given the relatively low temporal resolution of the EMAC and MECO(n) models, ten minutes and one minute, respectively, the model predictions and retrieved VMRs are best compared visually as altitude profiles (see figures 5.6, 5.7, and 5.8). Comparing the measured VMRs directly with the EMAC model predictions would require down-sampling the measured VMRs by a factor of at least twenty. During the EMeRGe missions, both the EMAC and MECO(n) models are available for comparison, while only EMAC model simulations are available for comparison during the CAFE-Africa mission. The comparison is performed separately for each of the three retrieved gases (see below).

NO_2

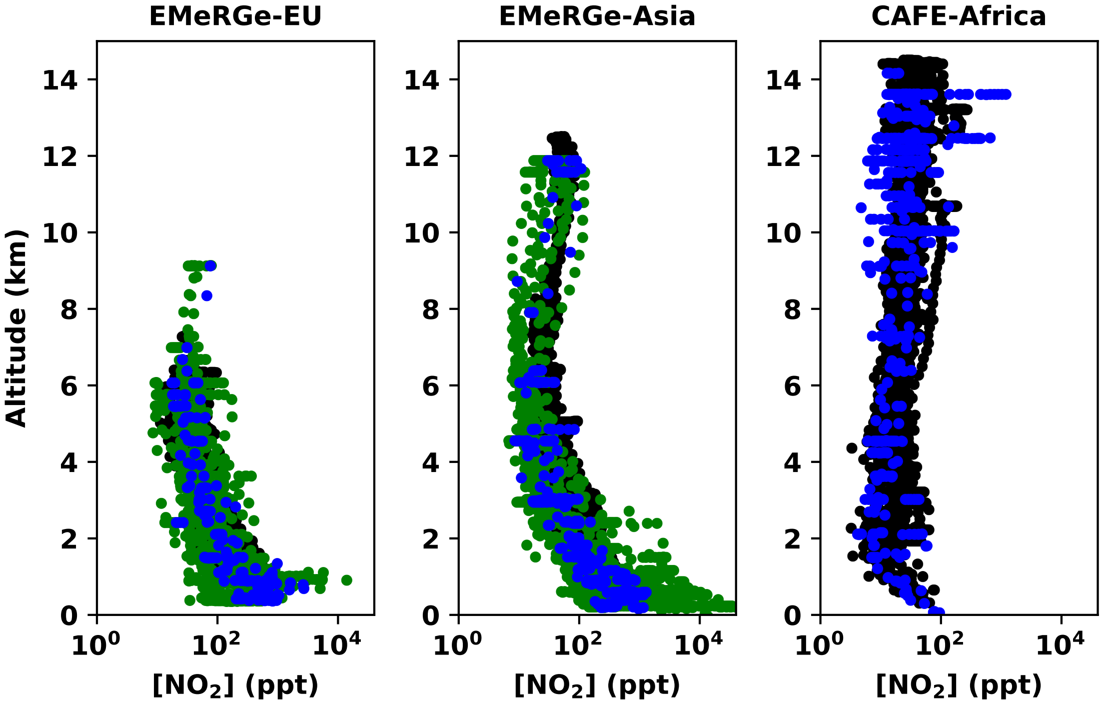

Figure 5.6: Altitude profiles of NO_2 as observed by the mini-DOAS instrument (black), as predicted by the EMAC model (blue), and as predicted by the MECO(n) model (green), for the three research missions: EMeRGe-EU (left), EMeRGe-Asia (center), and CAFE-Africa (right). MECO(n) data is not available for the CAFE-Africa mission. Note the logarithmic x axes.

Figure 5.6 shows the NO_2 retrieved with the mini-DOAS instrument together with the simulations of the EMAC and MECO(n) models. With respect to NO_2, the EMAC model predicts well the general shape and magnitude of the retrieved profiles. The MECO(n) model predicts more NO_2 than the EMAC model, and more than is observed by the mini-DOAS instrument within the PBL. During the CAFE-Africa mission, the EMAC model predicts the retrieved NO_2 profile well, including the increasing NO_2 into the upper troposphere.

HCHO

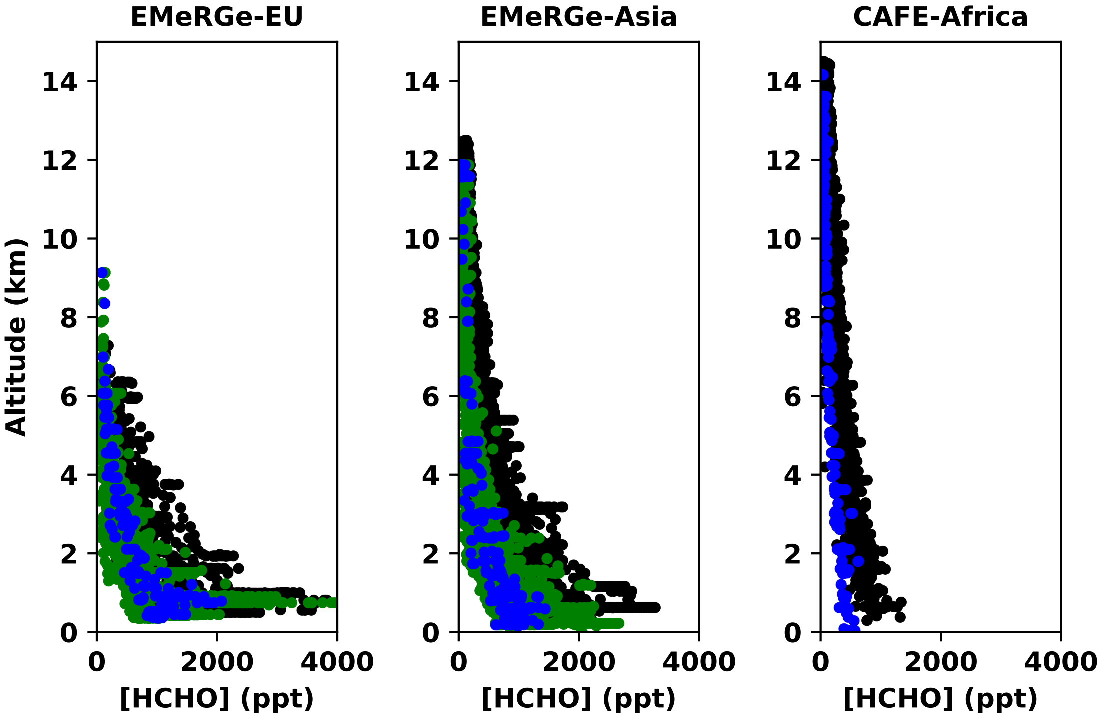

Figure 5.7: Altitude profiles of HCHO as observed by the mini-DOAS instrument (black), as predicted by the EMAC model (blue), and as predicted by the MECO(n) model (green), for the three research missions: EMeRGe-EU (left), EMeRGe-Asia (center), and CAFE-Africa (right). MECO(n) data is not available for the CAFE-Africa mission.

Figure 5.7 shows the HCHO retrieved by the mini-DOAS instrument together with the predictions of the EMAC and MECO(n) models. Regarding HCHO, the EMAC model reasonably predicts the general shape and magnitude of the retrieved profiles during both phases of the EMeRGe mission. The MECO(n) model better predicts the observed HCHO VMRs, which is to be expected given its superior temporal resolution. During the CAFE-Africa mission, the EMAC model generally predicts less HCHO than is observed.

HONO

Figure 5.8 shows the HONO observed by the mini-DOAS instrument together with the predictions of the EMAC and MECO(n) models, which only include the known gas phase formation mechanisms of HONO (see equation 1.1).

During the -EU phase of the EMeRGe mission, the EMAC model predicts at most 35 ppt of HONO along the flight track of the HALO aircraft in the boundary layer. The MECO(n) model, by comparison predicts up to 60 ppt of HONO along the HALO flight track. Neither model predicts appreciable concentrations of HONO in the free troposphere. During the -Asia phase of the EMeRGe mission, the EMAC model predicts at most 16 ppt HONO in the boundary layer along the flight track of the HALO aircraft. The MECO(n) model, by comparison predicts up to 127 ppt of HONO along the HALO flight track. While the MECO(n) model predicts only 2 ppt of HONO in the upper troposphere, the EMAC model predicts up to 10 ppt of HONO at 12 km altitude for the HALO flights towards Japan.

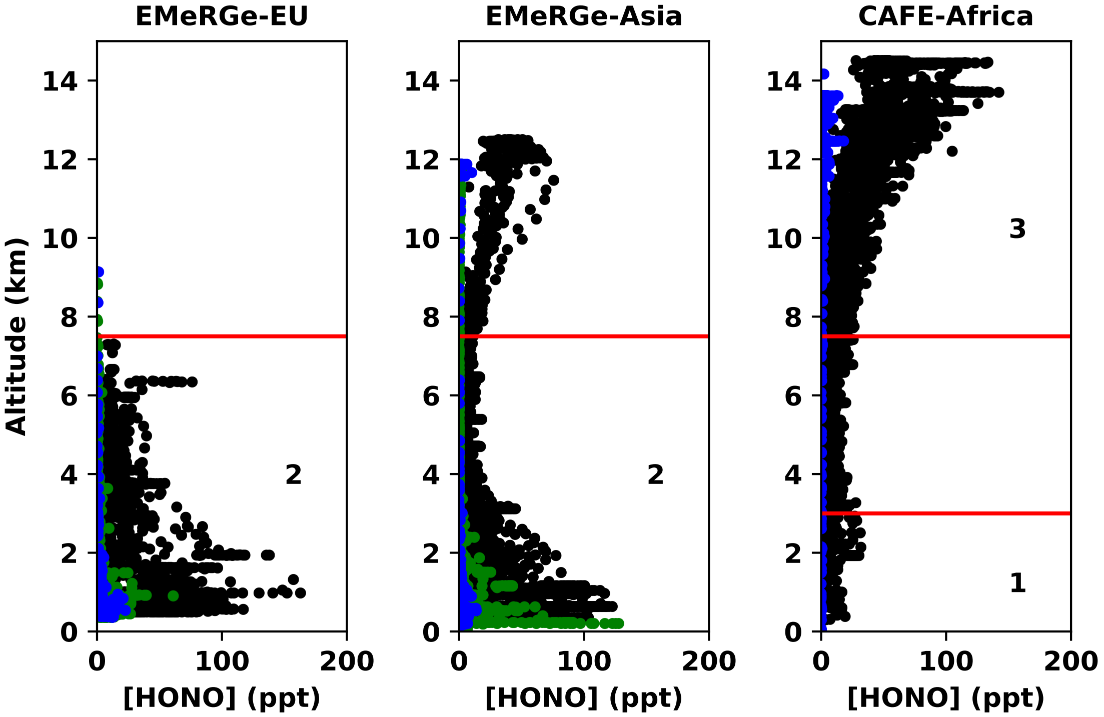

Figure 5.8: Altitude profiles of HONO as observed by the mini-DOAS instrument (black), as predicted by the EMAC model (blue), and as predicted by the MECO(n) model (green), for the three research missions: EMeRGe-EU (left), EMeRGe-Asia (center), and CAFE-Africa (right). MECO(n) data is not available for the CAFE-Africa mission. The red horizontal lines distinguish the MBL (regime 1), as well as lower (regime 2) and upper (regime 3) troposphere.

During both phases of the EMeRGe mission, the observed HONO VMRs exceed both models' predictions throughout the probed altitude ranges. During the -EU phase, the observations are in excess of model predictions by at least a factor of 2–5. During the -Asia phase, the excess relative to predictions is model and altitude dependent and may exceed an order of magnitude.

For the CAFE-Africa mission, only the EMAC model simulations are available for comparison. The retrieved HONO VMRs are here, again, much larger than the model predictions. The EMAC model correctly predicts the general shape of the retrieved HONO profiles, but on average predicts VMRs in the single digits (ppt), and never more than 18 ppt along the flight track of the HALO aircraft (at 12.5 km altitude).

Given the general agreement between model predictions and the observations of the mini-DOAS instrument for HCHO and NO_2 (see above), the discrepancies between model predicted HONO and the observations of the mini-DOAS instrument are unlikely to be due to model resolution, instrumental or methodological issues. Rather, HONO formation in the troposphere (especially the upper troposphere) may act via a mechanism (or mechanisms) which are altogether not represented in the models.

5.3 Required source strength to explain excess HONO

The excess HONO (relative to model predictions) described above requires an in situ source. Upon photolysis, the observed HONO represents a significant source of OH during both phases of the EMeRGe mission, necessitating a considerable source of HONO within the lower troposphere (see figure 5.9). The photolytic loss of HONO is described by the quantity $J_{\mathrm{HONO}} \cdot [\mathrm{HONO}]$, where J is the photolysis frequency of HONO (s^{-1}). This quantity represents the photolytic loss of HONO in ppt/s, and therefore the strength of the HONO source term necessary to sustain the HONO VMRs observed by the mini-DOAS instrument against said photolysis — assuming a PSS (see equation 1.4). During the CAFE-Africa mission, a less powerful HONO source term is necessary to sustain the observed HONO in the lower troposphere (see figure 5.9). Still, in neither context are the observations consistent with models based on gas phase formation. Moreover, the observed HONO in the upper troposphere during the CAFE-Africa mission requires a significant in situ source. Potential sources of HONO within these three regimes are investigated separately in chapter 6. For comparison, the OH production from the photolysis of ozone and formaldehyde depends on the concentrations of those gases, and varies with sunlight over the course of a day. Either one may exceed several ppb per day, especially in polluted air masses [Alicke et al., 2003].

5.4 Observed Leighton ratios as a proxy for the atmospheric oxidation capacity

An indicator that may corroborate the presence of additional oxidants (excess HONO) in the troposphere is the measurable ratio $[NO]/[NO_2]$. The Leighton ratio — a proxy for oxidation capacity (see chapter 2, sections 2.2 & 2.3) — is investigated using the NO_2 retrieved in the UV wavelength range with O_4 scaling, together with the NO measured by the AENEAS instrument during the EMeRGe mission and by the NOAH instrument during the CAFE-Africa mission. This observed $[NO]/[NO_2]$ ratio can be compared to the $[NO]/[NO_2]$ ratio expected from the measurements of O_3 from the FAIRO instrument and J_{NO_2} from the HALO-SR-A instrument. The addition of $RO_2{}^*$ (measured by the PeRCEAS instrument during the EMeRGe missions) or HO_2 (measured by the HORUS instrument during the CAFE-Africa mission) introduces an additional term to the expected $[NO]/[NO_2]$ ratio derived from the Leighton relationship (equation 2.53). In figure 5.10, the $[NO]/[NO_2]$ ratios as directly observed are plotted against calculations from measured quantities (see equation 2.53), and the two often differ significantly. While both are clearly altitude dependent, the scatter around the 1:1 line spans orders of magnitude. During the EMeRGe missions, data below the 1:1 line can be explained by fresh NO_x emissions at low altitudes. Especially during the CAFE-Africa mission, the observed ratio is generally less than what would be expected, across all altitudes, indicating that oxidants other than ozone or HO_2 must be present. While no measurements of RO_2 are available during the CAFE-Africa mission, the orders of magnitude difference requires further explanation. Previous studies have explained similar observations by invoking chemical interferences in the instruments which detect NO_2

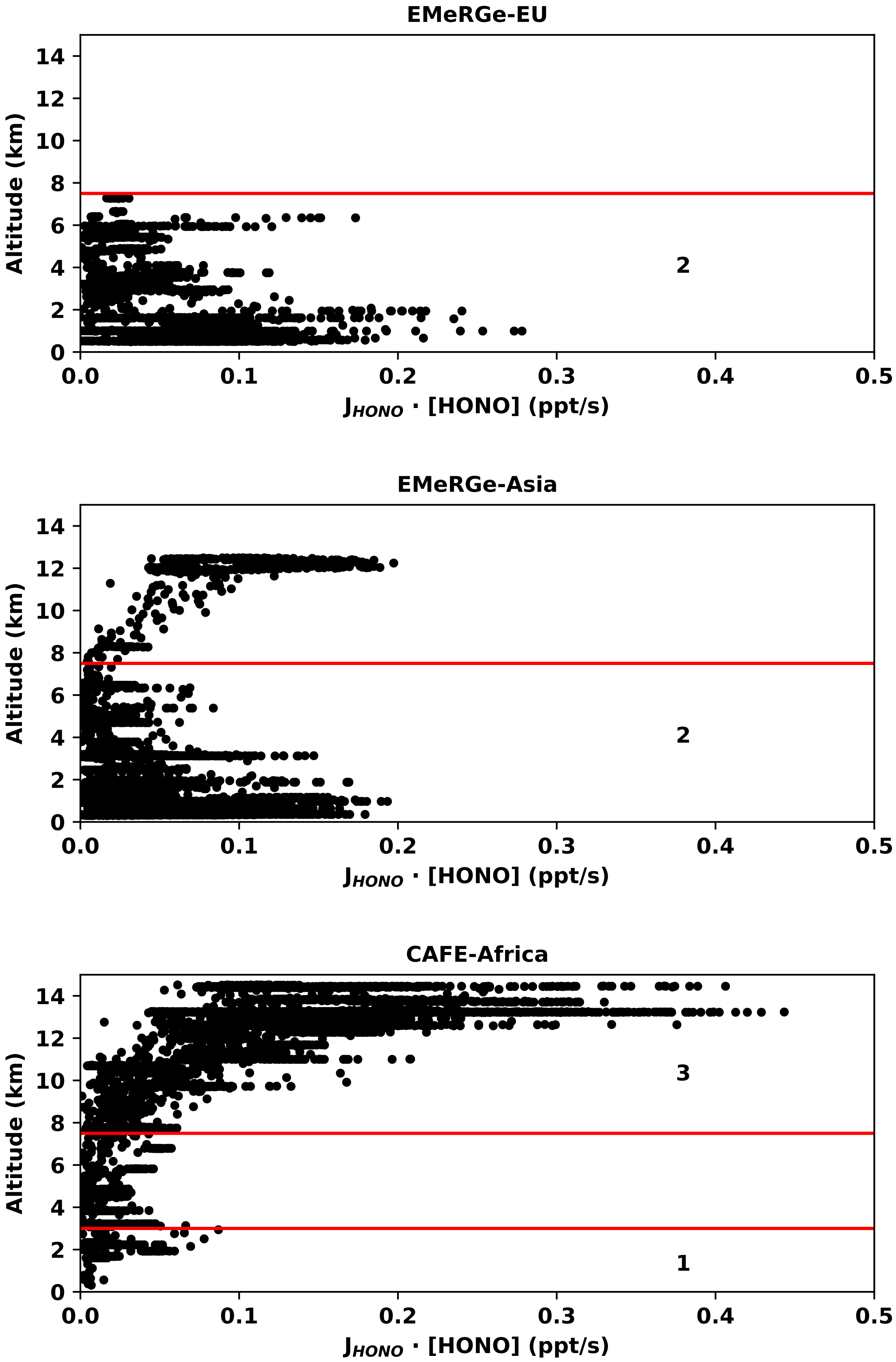

Figure 5.9: Altitude profiles of the HONO production/destruction rate $J_{HONO} \cdot$[HONO] (ppt/s) for all flights of the EMeRGe-EU, EMeRGe-Asia, and CAFE-Africa missions. This quantity simultaneously represents the OH produced upon photolysis of HONO, as well as the strength of the HONO source term necessary to sustain the observed HONO VMRs against said photolysis under the assumption of a photo-stationary state.

[Silvern et al., 2018; Nussbaumer et al., 2021a]; the mini-DOAS instrument has no such chemical interferences. It may be that the conversion of NO to NO_2 proceeds via a mechanism which is not included in this simple representation. Indeed, other radicals may react with NO to produce NO_2 without ozone, HO_2, or organic peroxides. In any case, the discrepancy between observed and expected Leighton ratios reveals that the oxidation capacity within the observed air masses is not well quantified.

5.5 The collision rate of air with measured aerosol surface

The feasibility of any hypothetical HONO formation mechanism depends on its phase and the relevant region of the atmosphere. In the lower troposphere, heterogeneous reactions are common due to the presence of high aerosol loading (and therefore plentiful aerosol surfaces), while the relative lack of aerosols in the upper troposphere makes heterogeneous reactions less efficient than gas phase reactions. This section quantifies that distinction.

During both the EMeRGe and CAFE-Africa missions, the fine and coarse aerosol surface area and volume are derived from the measurements of the SKY-OPC instrument. Total aerosol surface area, together with the thermal velocity of air, gives the collision frequency of any gas with the aerosol surface. According to kinetic gas theory [Finlayson-Pitts and Pitts Jr, 1999], the collision frequency of air with the aerosol surface is approximately given by

$$\nu_{\mathrm{aerosol}} = \frac{\mathrm{V} \cdot \mathrm{SA}}{4} \tag{5.1}$$

where SA is the measured aerosol surface area density, and V is the thermal velocity of air, given by

$$\mathrm{V} = \sqrt{\frac{8 \cdot \mathrm{R} \cdot \mathrm{T}}{\pi \cdot \mathrm{M}}}. \tag{5.2}$$

Here R is the gas constant, T the temperature, and M the mass of air (assumed to be 0.028 kg/mol, the molar mass of dry air). For atmospheric temperatures, V is several hundred meters per second. Meanwhile, the collision frequency of air with any gas — according to kinetic gas theory [Finlayson-Pitts and Pitts Jr, 1999] — is given by

$$\nu_{\mathrm{gas}} = \mathrm{n} \cdot \sigma \cdot \mathrm{V}. \tag{5.3}$$

Here V is again the thermal velocity of air, in this case of the reduced mass $\mu = \frac{m_a \cdot m_b}{m_a + m_b}$, n is the concentration of said gas, and σ is the collisional cross section between two hard-sphere molecules given by

$$\sigma = \pi \cdot (\mathrm{r_a} + \mathrm{r_b})^2, \tag{5.4}$$

where r is the radius of a molecule of gas. Here it is assumed that the molecular radius is 155 picometers, and that the masses and radii of gases a and b are equal.

In the upper troposphere, collisions of air with another gas are twelve orders of magnitude more rapid than collisions with the measured aerosol surface, with only some exceptions (see figure 5.11). Under the assumptions described, any gas phase reaction at higher altitudes may be more efficient than a heterogeneous phase reaction (not accounting for efficiencies in either case, i.e. a successful reaction for every collision). Modulating the assumed mass of air and particle radius does not considerably affect this conclusion. In the upper troposphere, then, heterogeneous sources of HONO can be ruled out on the basis of the measured aerosol surface area (10^{-7} $\mathrm{cm^2/cm^3}$) and thermal velocity of air ($4 \cdot 10^4$ cm/s), which even for γ=1 would lead to a collision rate of (ν = A*v/4 $\approx$ 10^{-3}/s) for any nitrogen species. Therefore, even for a measured HNO_3 of $\approx$ 1 ppb, heterogeneous reaction rates would likely be too small to balance the measured HONO photolysis rate of some tenths of ppt/s for any realistic value of γ (see section 5.3, figure 5.9).

This motivates heterogeneous phase explanations for sources of excess HONO only in the lower troposphere, and stipulates gas phase explanations of excess HONO in the upper troposphere. In chapter 6, the excess HONO observed in the lower and upper troposphere are investigated separately.

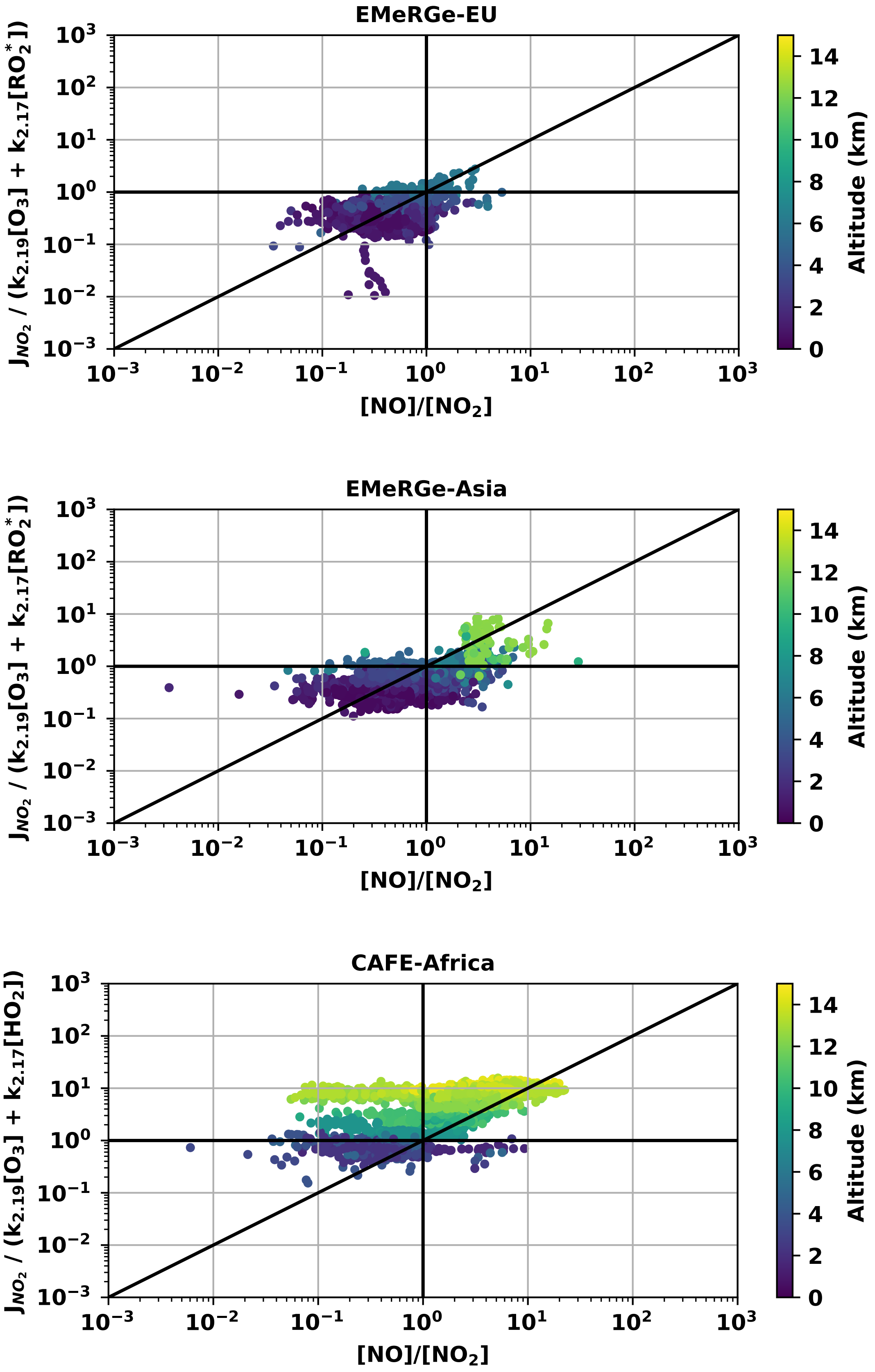

Figure 5.10: In each panel are the Leighton ratios (see section 2.2, equation 2.53) as modeled from measurements of J_{NO_2}, O_3, and HO_2 or RO_2^* plotted against those directly observed by [NO]/[NO_2] for each of the three missions, colored by altitude. Note the logarithmic axes. The black lines are 1:1 lines. Data above / to the left of the 1:1 line indicates the presence of additional oxidants converting NO to NO_2.

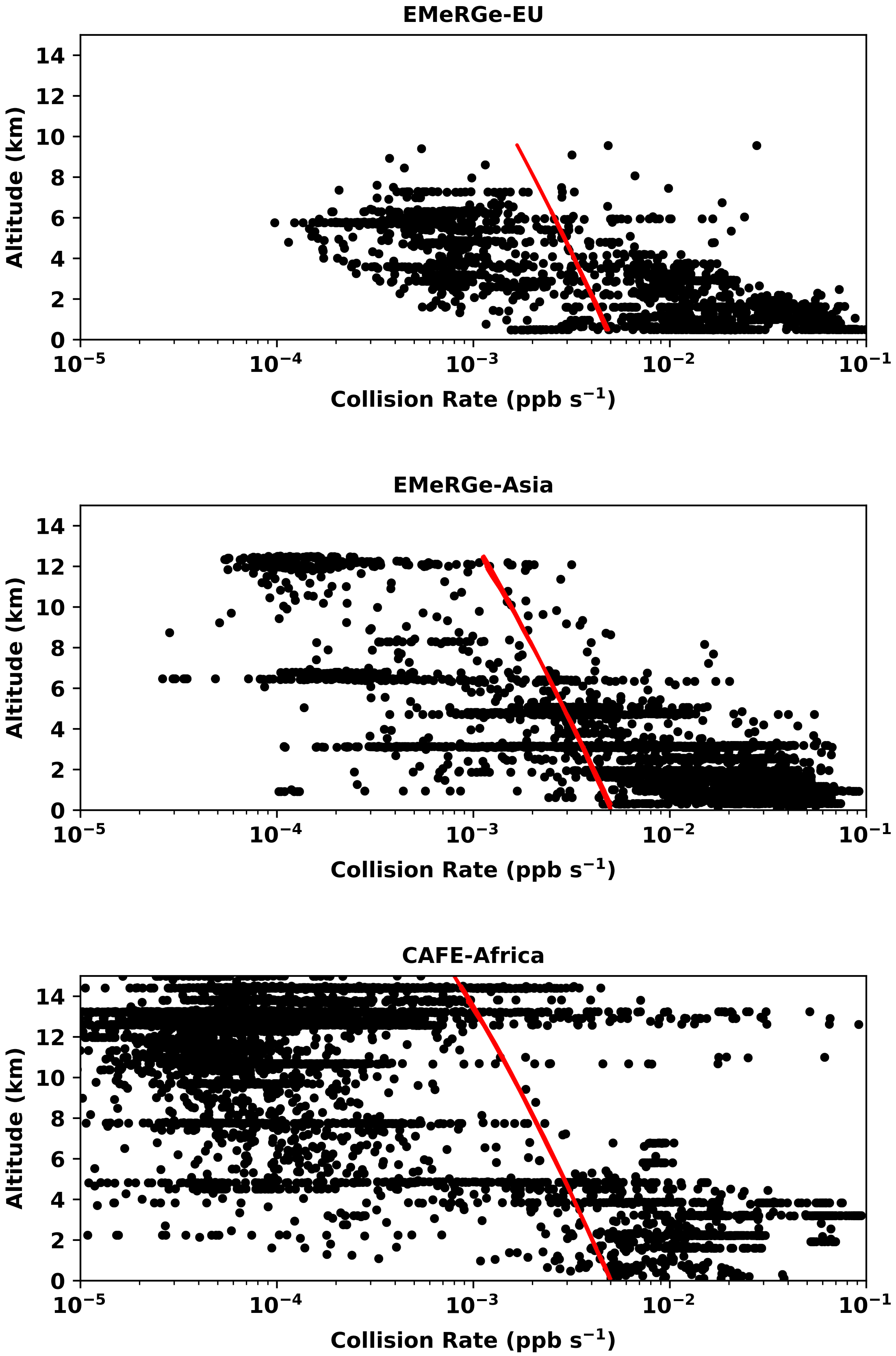

Figure 5.11: Altitude profiles of the assumed collision rate of 1 ppb of odd nitrogen with the measured aerosol surface area density, according to kinetic gas theory (equation 5.1), for both phases of the EMeRGe missions, and the CAFE-Africa mission. The solid red line in each panel represents the collision rate (equation 5.3) of 1 ppb of odd nitrogen with another gas found only in 1 part per trillion. Note the logarithmic x axes.

Chapter 6

Discussion

> If you don't control for confounding variables, they'll mask the real effect and mislead you. But if you control for too many variables, your choices will shape the data, and you'll mislead yourself. Somewhere in the middle is the sweet spot where you do both, making you doubly wrong.
>
> Randall Munroe

This chapter discusses the likely sources of the excess HONO observed by the mini-DOAS instrument within three regimes of the troposphere reported in chapter 5. The detection of HONO VMRs in excess of what would be expected from gas-phase formation or what is predicted by models requires explanation, particularly the HONO source term necessary to sustain the observed VMRs against photolysis under the assumption of a PSS (see figure 5.9). Here, we investigate the photolysis of particulate nitrate in the MBL, potential heterogeneous sources of HONO in the polluted lower troposphere, and a potential new gas phase source of HONO in the cold upper troposphere.

Section 6.2 examines potential heterogeneous sources of HONO in the polluted air masses observed during both EMeRGe missions (as well as the low-NO_x air masses observed during the CAFE-Africa mission), within the lower troposphere. Specific attention is given in subsection 6.1 to the HONO observations from the air masses observed during the CAFE-Africa mission in the low-NO_x MBL, where the photolysis of particulate nitrate may be a potential HONO source. A potential new gas phase source of HONO in the cold upper troposphere is discussed in section 6.3.

6.1 Evidence for HONO produced from the photolysis of particulate nitrate

Within the low-NO_x regime of the marine lower troposphere, a growing body of research explains observed HONO VMRs by invoking the photolysis of particulate nitrate [Ye et al., 2016b; Reed et al., 2017; Andersen et al., 2023]. While the photolysis frequency of particulate nitrate is not measured directly, it is argued that the photolysis frequency is up to two orders of magnitude greater than the photolysis frequency of gaseous nitric acid [Ye et al., 2016b, 2017]. However, enhancement factors derived from field measurements have been at odds with those determined in laboratories [Romer et al., 2018; Shi et al., 2021]. Recently, Andersen et al. [2023] speculated that this discrepancy may arise from a saturation effect, whereby the enhancement factor decreases with increasing particulate nitrate concentration. Here, we follow the approach of Andersen et al. [2023] and construct the photolysis enhancement factor necessary to explain our HONO observations using measured quantities from around the Cape Verde Islands during the CAFE-Africa mission in 2018.

Particulate nitrate as measured by the C-ToF-AMS instrument is generally an order of magni-

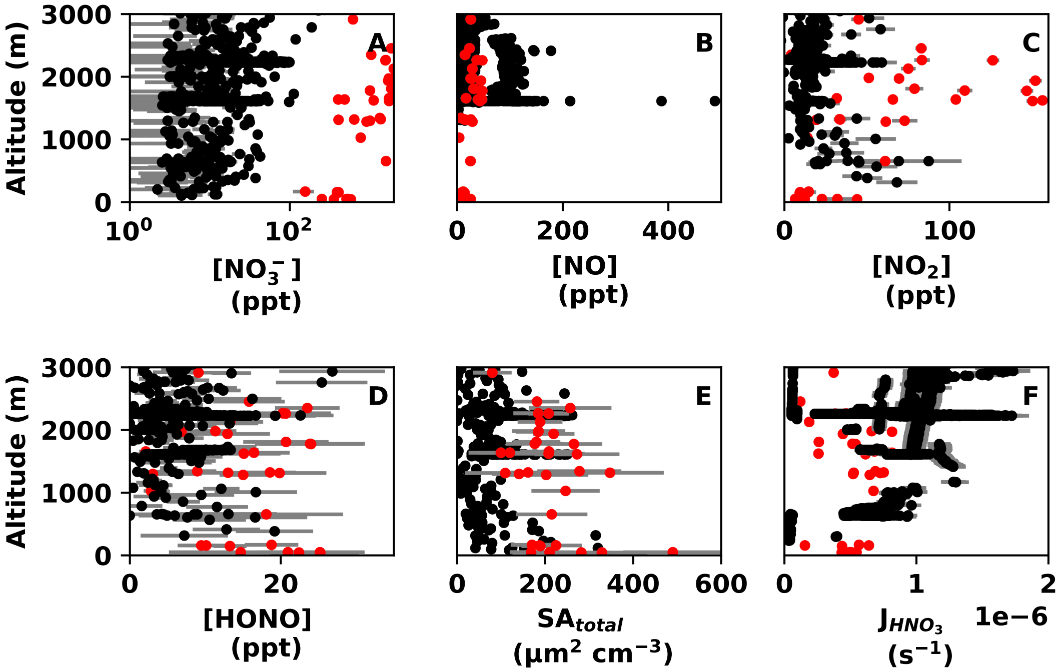

Figure 6.1: In each panel are from left to right, top to bottom: altitude profiles of the VMR of particulate nitrate, the VMR of NO, the VMR of NO_2, the VMR of HONO, the total aerosol surface area, and the photolysis frequency of HNO_3. Note that from on board the HALO aircraft, only sub-micron particulate nitrate was measured (the black points in panel A). In each panel, the black data is from the instruments on board the HALO aircraft during the CAFE-Africa mission, while the red color represents the data reported by Andersen et al. [2023]. Note the logarithmic x axis in the panel A. The investigated altitude range is limited to 3 km in order to compare the HALO measurements with those of Andersen et al. [2023].

tude less than those reported by Andersen et al. [2023] (see figure 6.1, panel A). The C-ToF-AMS instrument only measures sub-micron aerosol, which does not represent the whole aerosol load, and unfortunately the nitrate fraction across size regimes also cannot be assumed to be constant [Lee et al., 2008]. The other quantities (NO, NO_2, HONO, SA_{total}, and J_{HNO_3}) measured from the HALO aircraft during the CAFE-Africa mission are of the same magnitude and largely corroborate the measurements of Andersen et al. [2023].

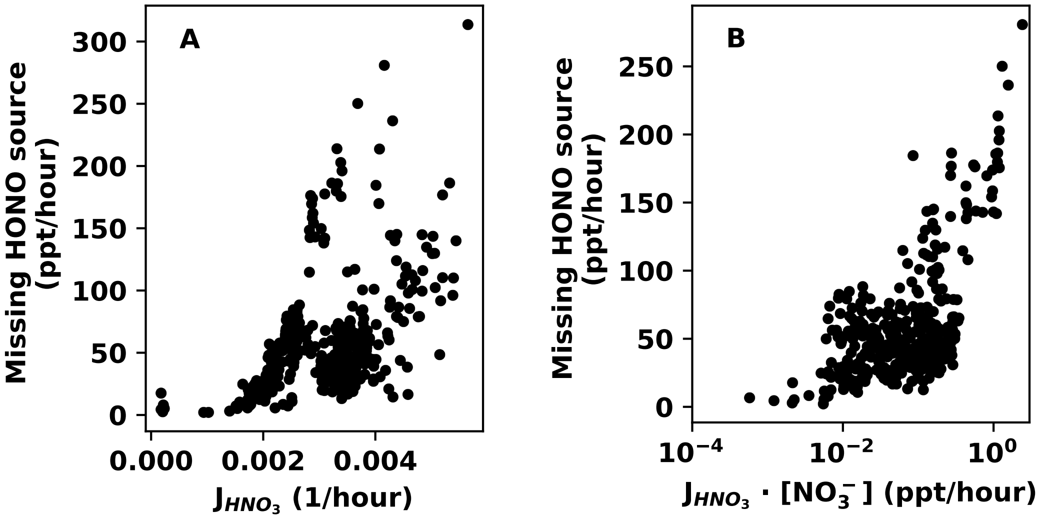

Figure 6.2: The missing HONO source (ppt/hour) plotted against the photolysis frequency of gaseous nitric acid (/hour) (panel A) and the product of the photolysis frequency of gaseous nitric acid times the VMR of particulate nitrate (ppt/hour) (panel B). Data are from the lowermost 3 km of the troposphere measured during the CAFE-Africa mission. Note the logarithmic x axis in panel B. The units are chosen to facilitate comparison with figures 2A and 3B in Andersen et al. [2023].

The photolysis frequency of HNO_3 is prohibitively slow (see figure 6.2, panel A). The photolysis rate — the product of the photolysis frequency of HNO_3 times the VMR of particulate nitrate — is several hundred times smaller than the HONO source term necessary to match the photolytic loss of HONO in a steady state. The enhancement in the photolysis frequency of particulate nitrate vs gaseous nitrate necessary for the quantities to be equal is defined by their quotient:

$$EF = \frac{J_{HONO} \cdot [HONO]}{J_{HNO_3} \cdot [NO_3^-]}.$$

We observe enhancement factors which decrease with the concentration of particulate nitrate, in agreement with the findings of Andersen et al. [2023] (see figure 6.3). The missing HONO source strength and rate of particulate nitrate photolysis reported in figure 6.2 also match those observed by Ye et al. [2016b] and Andersen et al. [2023]. The required enhancement factors needed to explain our observations however, exceed those reported by Andersen et al. [2023], likely due to the order of magnitude difference in reported particulate nitrate concentrations. According to Hrdina et al. [2021], much of the nitrate may be present in the coarse aerosol. Naively scaling the particulate nitrate measurements of the C-ToF-AMS instrument by the ratio of coarse mode aerosol volume to fine mode aerosol volume reduces the resultant enhancement factors (figure 6.3, panel B), and narrows — but does not fully close — the gap between the enhancement factors reported by Andersen et al. [2023] and those required to explain our observations.

Moreover, the photolysis rate of gaseous nitric acid — the product of the photolysis frequency of gaseous nitric acid as measured by the HALO-SR-A instrument and the VMR of HNO_3 as measured by the CIMS instrument — also correlates well with the necessary HONO source term (see figure 6.4). However, the quantum yield of the photolysis of HNO_3 which leads to HONO

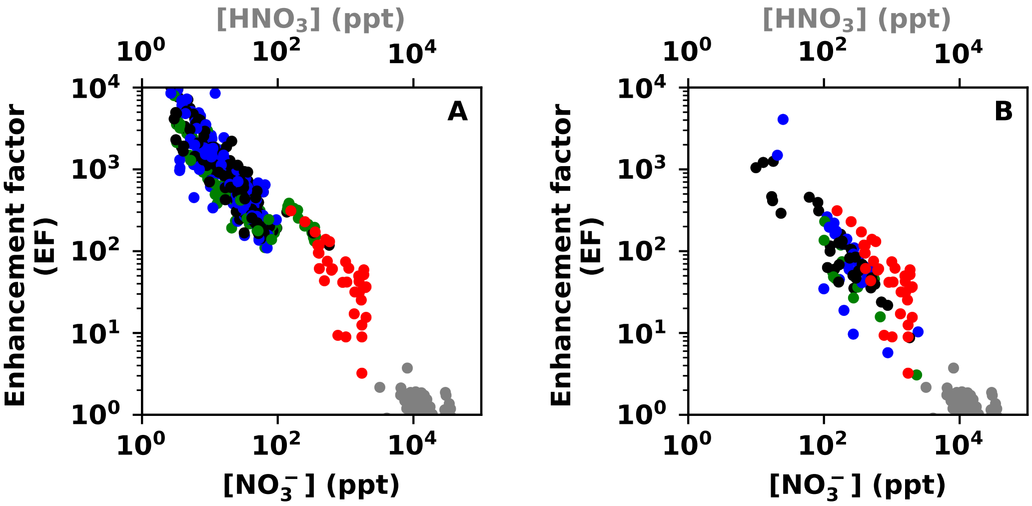

Figure 6.3: The enhancement factor in the photolysis frequency of particulate nitrate relative to gaseous nitric acid necessary to match the missing HONO source, plotted as a function of the (sub-micron) particulate nitrate VMR (ppt, panel A). The coloration is indicative of the influence of biomass burning, whereby acetonitrile above or below the 145 ppt threshold is shown in green (biomass influence) and blue (background air), respectively. Missing tags are shown in black. For comparison, the data from Andersen et al. [2023] are shown in red. In gray, the enhancement factors are calculated relative to the amount of HNO_3 observed by the CIMS instrument. In panel B, the observed sub-micron particulate nitrate concentration has been scaled by the ratio of coarse mode particle volume to fine mode particle volume, reducing the consequent enhancement factors. Data are from the lowermost 3 km of the troposphere from flights to and from the island of Sal, Cape Verde in August 2018 during the CAFE-Africa mission. Note the logarithmic axes.

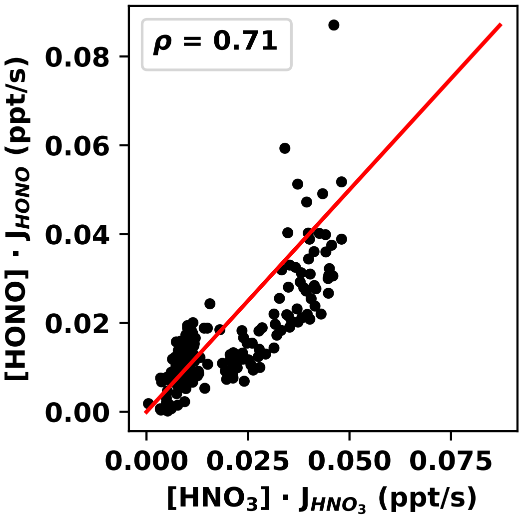

Figure 6.4: The HONO (ppt) observed by the mini-DOAS instrument, multiplied by its photolysis frequency measured by the HALO-SR-A instrument plotted against the HNO_3 (ppt) observed by the CIMS instrument, multiplied by its photolysis frequency measured by the HALO-SR-A instrument. The legend is the Spearman correlation coefficient ρ between the two products. The red line is a one to one line. Data included here is from the lowermost 3 km of the troposphere during the CAFE-Africa mission, i.e. within the MBL. The HNO_3 measured by the CIMS instrument is likely not exclusively gaseous nitric acid.

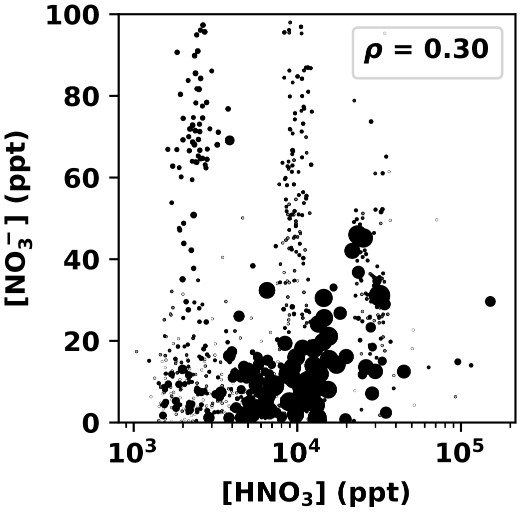

Figure 6.5: The atmospheric nitrate measured by the C-ToF-AMS instrument as particulate nitrate plotted against the atmospheric nitrate measured by the CIMS instrument as HNO_3. Data is from the lowermost 7.5 km of troposphere during the CAFE-Africa mission. The marker size parameter is indicative of the volume of large particles (µm^3 cm^{-3}, d > 500 nm) . The legend is the Spearman correlation coefficient ρ between the two quantities. Note the logarithmic x axis.

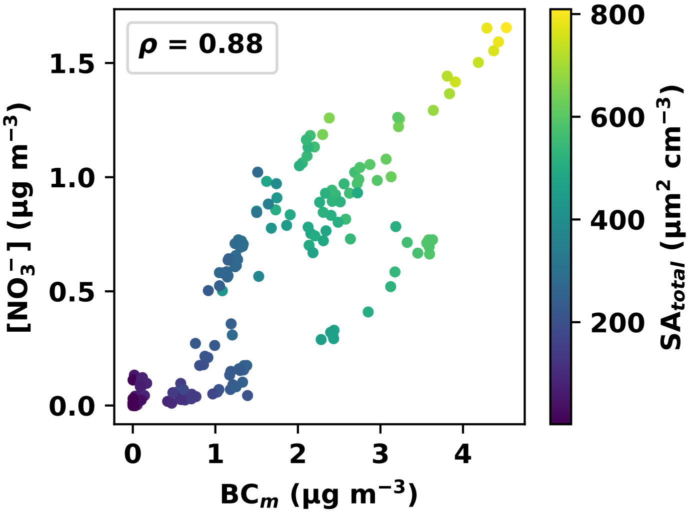

Figure 6.6: The nitrate measured by the C-ToF-AMS instrument (µg m^{-3}) is plotted against the black carbon mass (BC$_m$ [µg m^{-3}]) measured by the SP2 instrument, colored by the total aerosol surface area (SA$_{\text{total}}$ [µm^2 cm^{-3}]) measured by the SKY-OPC instrument. Data is only from biomass burning plumes within the lowermost 7.5 km of the troposphere during the CAFE-Africa mission. The legend is the Spearman correlation coefficient ρ between the black carbon and particle nitrate measurements.

(equation 2.27) is only 3 % [Burkholder et al., 2020], excluding the possibility of the photolysis of gaseous HNO_3 as a source of HONO.

However, the two instruments which detect atmospheric nitrate measure incomplete fractions of the total nitrate in the air. The CIMS instrument detects not only gaseous nitric acid, but also particulate nitrate as gaseous nitric acid, if the nitrate is in the form of ammonium nitrate or weakly bound on black carbon (Crowley, personal communication).

If all of the HNO_3 measured by the CIMS instrument is produced by particulate nitrate, no enhancement in the frequency of particulate nitrate photolysis (relative to the frequency of gaseous nitric acid photolysis) would be necessary to explain our HONO observations. However, this is unlikely, as the HNO_3 detected by the CIMS instrument exceeds the particulate nitrate measured by the C-ToF-AMS instrument by orders of magnitude (see figure 6.5), and the two are not strictly correlated.

Meanwhile, the C-ToF-AMS instrument observes particulate nitrate mostly tied to black carbon (see figure 6.6). As previously mentioned, the C-ToF-AMS instrument also only detects sub-micron particulate nitrate as a consequence of its operating temperature.

Given the ambiguity, the enhancement factor in the frequency of particulate nitrate photolysis relative to the photolysis frequency of gaseous nitric acid cannot be precisely determined, but the observed HONO provides further evidence on the potential relevance of particulate nitrate photolysis.

6.2 Evidence for heterogeneous HONO formation

6.2.1 HONO in high-NO_x air masses during the EMeRGe-EU mission

The air masses sampled during the EMeRGe-EU mission were primarily confined to the lower troposphere, particularly to less than 6 km altitude [Andrés Hernández et al., 2022]. Most of the air masses sampled were in high-NO_x environments (see figure 5.1). The EU phase of the EMeRGe mission is characterized by mostly continental background air, with some instances of anthropogenic influence [Förster et al., 2023]. The HONO VMRs observed in the lower troposphere during the EMeRGe-EU mission exceed predictions of the EMAC and MECO(n) models, which are based on gas phase production. Therefore we next consider possible heterogeneous sources of HONO.

In order to determine which of the many proposed formation mechanisms listed in table 2.1 correlates well with the observed HONO VMRs, the reactants from each formation mechanism are multiplied and their product is correlated with the observed HONO. Correlations are determined with the Spearman correlation coefficient rather than the Pearson coefficient, in case the relationship is non-linear (for example due to saturation effects). While the HONO formation rate necessary to match its loss via photolysis is what should be correlated with the reactants of these mechanisms, many include photolysis frequencies themselves. Therefore, the correlation analysis is performed against the retrieved HONO VMRs in order to avoid an auto-correlation with the photolysis frequencies measured by the HALO-SR-A instrument. Similarly, the correlations are determined between VMRs instead of concentrations to avoid auto-correlations as a function of atmospheric density. Several of the in situ instruments have time resolutions of only 15, 30, or 60 seconds, so for each spectrum recorded by the mini-DOAS instrument, all data reported by the in situ instruments is averaged over the integration time of the mini-DOAS spectra. This down-sampling avoids interpolation or repeated values which may lead to spurious or diluted correlations, respectively.

The observed HONO VMRs may however also be correlated directly with other gases and atmospheric parameters simultaneously observed on board the HALO aircraft (see figure 6.7). The trace gases retrieved with the mini-DOAS usually share a strong auto-correlation ($\rho > 0.7$). The correlation between HCHO and HONO is not necessitated by their photochemical relationship, but e.g. Hendrick et al. [2014] also observed a strong correlation of HONO with NO_2. Since most of the heterogeneous sources of HONO proposed in table 2.1 require NO_2 as a reactant, the correlation between HONO and NO_2 is to be expected. However, any correlation between the observed HONO and some other gas, parameter, or the product of the reactants of some hypothetical formation mechanism should ideally correlate more strongly than this threshold, i.e. the correlation with NO_2.

Not all species listed in table 2.1 were measured during the EMeRGe mission. Indeed, no nitrophenols were measured, so mechanism 2 is left out of this analysis entirely. Nitric acid was measured but is unavailable, therefore a proxy (NO_z) is constructed by subtracting NO_x ($NO + NO_2$) from the NO_y measured by the AENEAS instrument. OH also was not measured at all, precluding analysis of mechanism 1, while measured RO_2^* serves as a proxy for HO_2. Figure 6.8 shows the observed HONO as a function of the proposed formation mechanisms for the -EU phase of the EMeRGe mission. Unsurprisingly, the proposed formation mechanisms are correlated to varying strengths with the observed HONO. The strength of the Spearman correlation coefficient varies with air mass type (anthropogenic, biomass burning, background). Filtering the lower tropospheric EMeRGe-EU data further according to air mass type yields different correlations. Tables 6.1 and 6.2 show the correlation coefficients between HONO and the reactants and formation mechanisms for the subsets of data according to air mass type. Versions of figures 6.7 and 6.8 which have been filtered by air mass tags can be found in appendix G.

When including the spectra from the entire mission, the measurements of black carbon, nitric oxide, and particulate nitrate correlate strongly with the observed HONO ($\rho \approx 0.7$), while the products of the reactants of all the formation mechanisms listed in table 2.1 also correlate strongly with the observed HONO ($\rho \approx 0.7$).

Table 6.1: Spearman correlation coefficients ρ between HONO VMRs and eleven other reactants simultaneously measured on board the HALO aircraft, when the EMeRGe-EU data from the lower troposphere is filtered further by air mass tags. AG is anthropogenic, BG is background air.

	ORG	BC_m	NO_z	NO	NO_2	SA	HCHO	${NO_3}^-$	${NH_4}^+$	${SO_4}^{2-}$	RO_2^*
All	0.64	0.70	0.44	0.74	0.83	0.66	0.82	0.70	0.66	0.56	0.27
AG	0.29	0.04	0.22	0.66	0.64	0.00	0.52	0.40	0.25	0.08	-0.41
BG	0.46	0.51	0.32	0.58	0.71	0.52	0.76	0.53	0.51	0.42	0.31

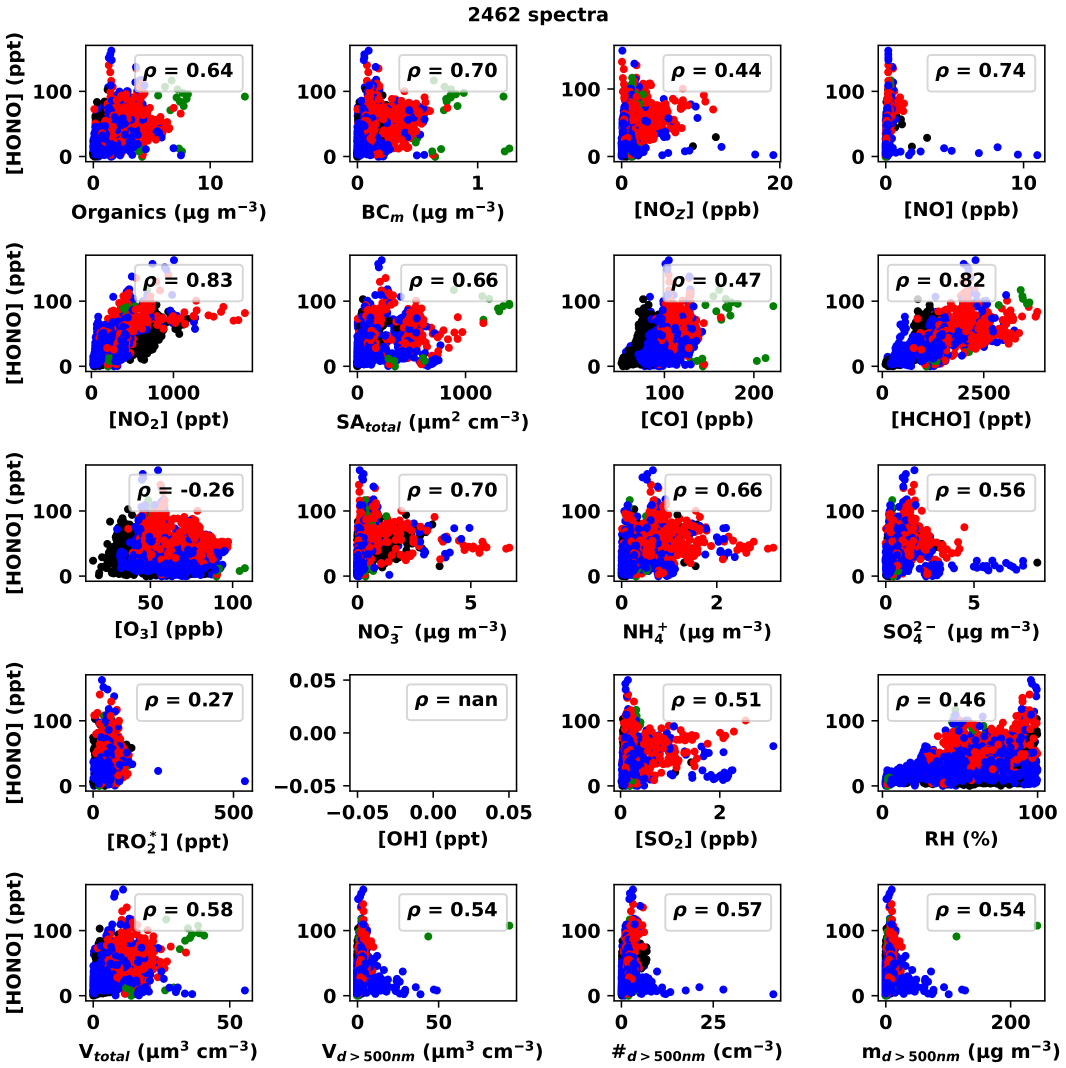

Figure 6.7: Each panel shows the observed HONO VMRs plotted against twenty other species and components simultaneously observed on board the HALO aircraft during the -EU phase of the EMeRGe mission in the lower troposphere. The legend is the Spearman correlation coefficient ρ. The coloration is representative of the air mass tags described in section 4.1.1. Red data represents anthropogenic influence determined from measurements of benzene, green data represents biomass burning influence detected via measurements of acetonitrile, blue data represents otherwise background air. Black data represents missing air mass tags. OH was not measured during the EMeRGe missions.

Table 6.2: Spearman correlation coefficients ρ between HONO VMRs and twelve formation mechanisms from table 2.1 when the EMeRGe-EU data from the lower troposphere is filtered further by air mass tags. AG stands for anthropogenic, BG for background air.

	1	3	4	5	6	7	8	9	10	11	12	13
All	N/A	0.77	0.81	0.82	0.80	0.79	0.69	0.74	0.79	0.75	0.83	0.74
AG	N/A	0.41	0.66	0.54	0.51	0.63	0.22	0.39	0.60	0.55	0.71	0.43
BG	N/A	0.70	0.73	0.69	0.68	0.65	0.57	0.67	0.69	0.68	0.72	0.67

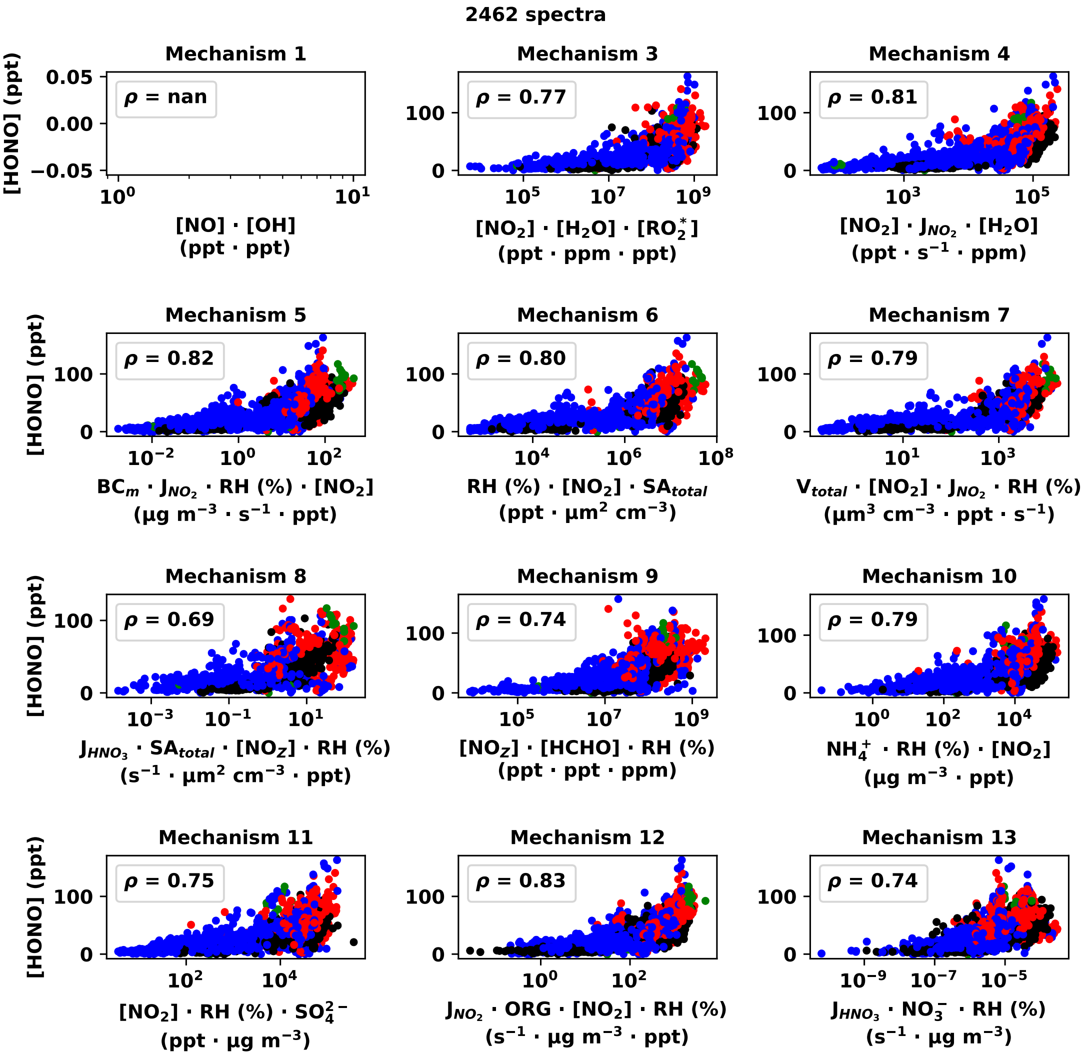

Figure 6.8: For twelve of the thirteen potential HONO formation mechanisms listed in table 2.1, the observed HONO VMRs are plotted against the product of any measured reactants (or proxies thereof), from the -EU phase of the EMeRGe mission, in the lower troposphere. In each panel, the legend is the Spearman correlation coefficient ρ. During the EMeRGe mission, no measurements or proxies for OH are available. Here, $RO_2{}^*$ acts as a proxy for HO_2, while NO_z ($NO_y - NO_x$) acts as a proxy for HNO_3. Data is colored by the tags described in section 4.1.1; red represents anthropogenic influence, green represents biomass burning influence, and the absence of either is indicated in blue and assumed to be background air. Missing tags are represented in black. Note the logarithmic x axes. Mechanism 2 is excluded because ortho-nitrophenols were not measured.

Anthropogenic air

Considering only the measurements tagged as having anthropogenic influence (determined from the presence of benzene), none of the reactants correlate with the observed HONO, not even the other gases measured with the mini-DOAS (see appendix G). Nor do any of the proposed formation mechanisms correlate, except for mechanism 12, the photo-sensitized reduction of NO_2 on organic surfaces / humic acid ($\rho \approx 0.7$).

Biomass burning influence

During the EMeRGe-EU mission, not enough coincident measurements were tagged with biomass burning influence to perform a correlation analysis.

Background air

Considering only the data which is tagged as background air, none of the individual reactants correlate strongly with the observed HONO (except for NO_2 and HCHO, $\rho \approx 0.7$). Mechanisms 3, 4, and 12 correlate strongly ($\rho > 0.7$), but as discussed in the introduction, the gas phase reactions 3 & 4 are not efficient enough to explain the observed HONO VMRs. Either the similar profile shapes of HONO and water vapor leads to these correlations, or some as yet undiscovered gas phase mechanism converts NO_2 to HONO, as suggested by Li et al. [2015]. Mechanism 12 represents the photo-sensitized reduction of NO_2 on organic surfaces / humid acid.

6.2.2 The high-NO_x air masses of the EMeRGe-Asia mission

Like the EMeRGe-EU mission, the -Asia mission was largely confined to the lower troposphere, with exceptions only during the final two flights towards Japan. The air masses sampled were high-NO_x environments, and there was regular detection of benzene from anthropogenic plumes. In addition, the air masses sampled during EMeRGe-Asia were often influenced by biomass burning [Lin et al., 2023]. Here, as before, HONO VMRs observed with the mini-DOAS instrument exceed model simulations. This excess HONO requires a heterogeneous source (see section 5.5).

The observed HONO is correlated against several other simultaneously measured species (see figure 6.9), as well as with the formation mechanisms proposed in table 2.1 (see figure 6.10). There is a clear distinction between background and anthropogenic air masses in figure 6.10. Filtering the EMeRGe-Asia data further according to the air mass tags modulates the resultant correlation coefficients. The correlation coefficient ρ between the observed HONO VMRs and several co-measured species as well as the formation mechanisms listed in table 2.1 are shown in tables 6.3 and 6.4 for the subsets of filtered data. Versions of figures 6.9 and 6.10 which have been filtered by air mass tags can be found in appendix G.

When including all measurements from the entire mission, only the HCHO and NO_2 also measured by the mini-DOAS instrument correlate with the observed HONO ($\rho > 0.7$). The products of the reactants of mechanisms 4, 5, 6, 7, 9, 10, and 11 correlate strongly with the observed HONO ($\rho \approx 0.7$).

Table 6.3: Spearman correlation coefficients ρ between HONO VMRs and eleven other reactants simultaneously measured on board the HALO aircraft, when the EMeRGe-Asia data from the lower troposphere is further filtered by air mass tags. AG is anthropogenic, BB is biomass burning, BG is background air.

	ORG	BC_m	NO_z	NO	NO_2	SA	HCHO	$NO_3{}^-$	$NH_4{}^+$	$SO_4{}^{2-}$	RO_2*
All	0.42	0.55	0.61	0.53	0.74	0.62	0.82	0.53	0.52	0.52	0.14
AG	0.46	0.59	0.61	0.60	0.75	0.63	0.81	0.55	0.57	0.56	0.15
BB	0.38	0.52	0.33	0.15	0.58	0.49	0.67	0.41	0.37	0.40	0.18
BG	0.39	0.48	0.55	0.44	0.64	0.51	0.73	0.45	0.37	0.34	0.30

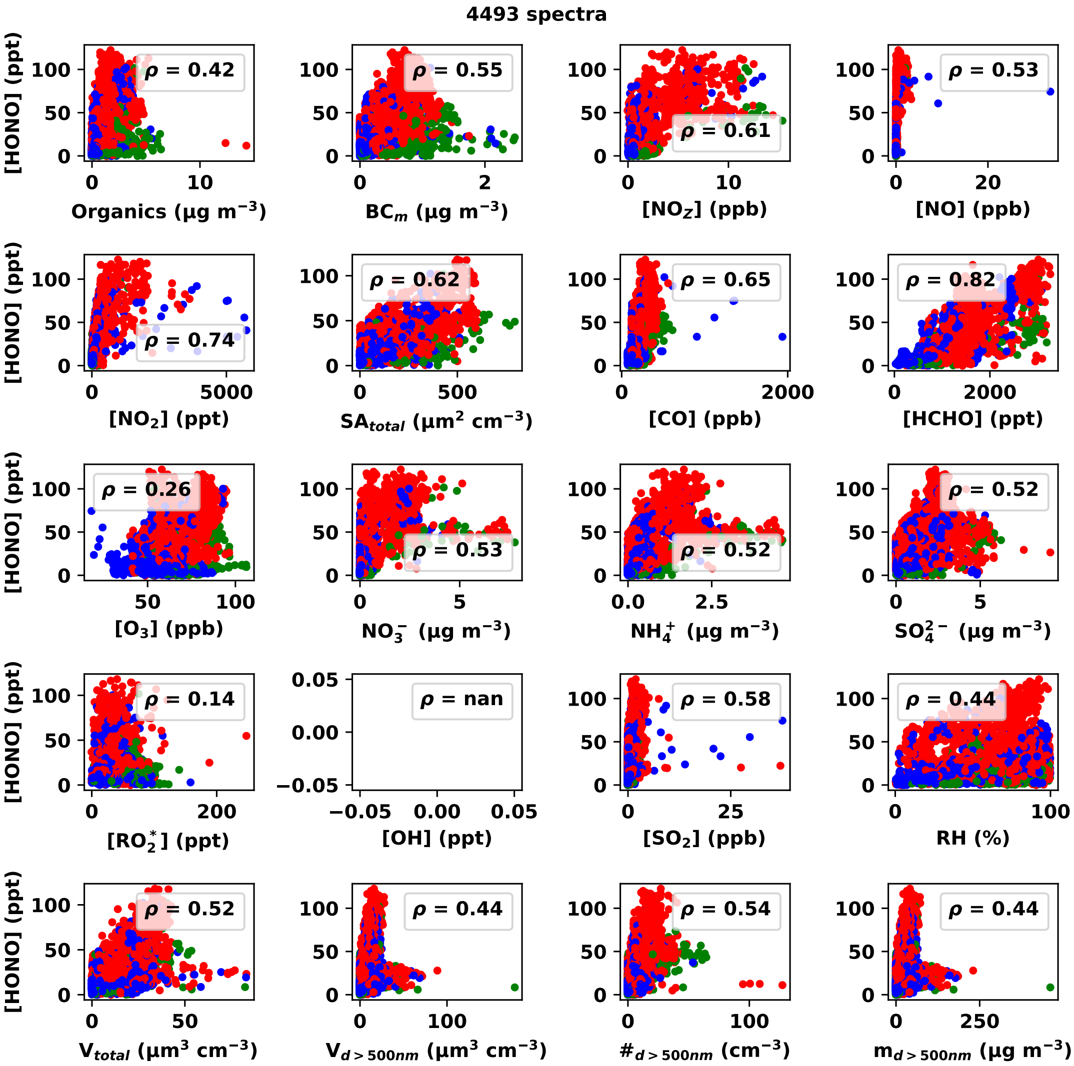

Figure 6.9: In each panel the observed HONO VMRs are plotted against twenty other species and components simultaneously observed on board the HALO aircraft in the lower troposphere during the -Asia phase of the EMeRGe mission. The legend is the Spearman correlation coefficient ρ. The coloration is representative of the air mass tags described in section 4.1.1. Red represents anthropogenic influence determined from measurements of benzene, green represents biomass burning influence detected via measurements of acetonitrile, blue represents otherwise presumably background air. Black represents missing air mass tag data. OH was not measured during the EMeRGe mission.

Table 6.4: Spearman correlation coefficients ρ between HONO VMRs and twelve formation mechanisms from table 2.1 when the EMeRGe-Asia data from the lower troposphere is further filtered by air mass tags. AG is anthropogenic, BB is biomass burning, BG is background air.

	1	3	4	5	6	7	8	9	10	11	12	13
All	N/A	0.62	0.71	0.74	0.75	0.75	0.67	0.73	0.74	0.74	0.68	0.57
AG	N/A	0.61	0.67	0.74	0.74	0.75	0.65	0.75	0.76	0.74	0.68	0.54
BB	N/A	0.49	0.54	0.58	0.54	0.48	0.42	0.57	0.49	0.51	0.49	0.39
BG	N/A	0.63	0.68	0.67	0.69	0.66	0.65	0.70	0.70	0.66	0.68	0.60

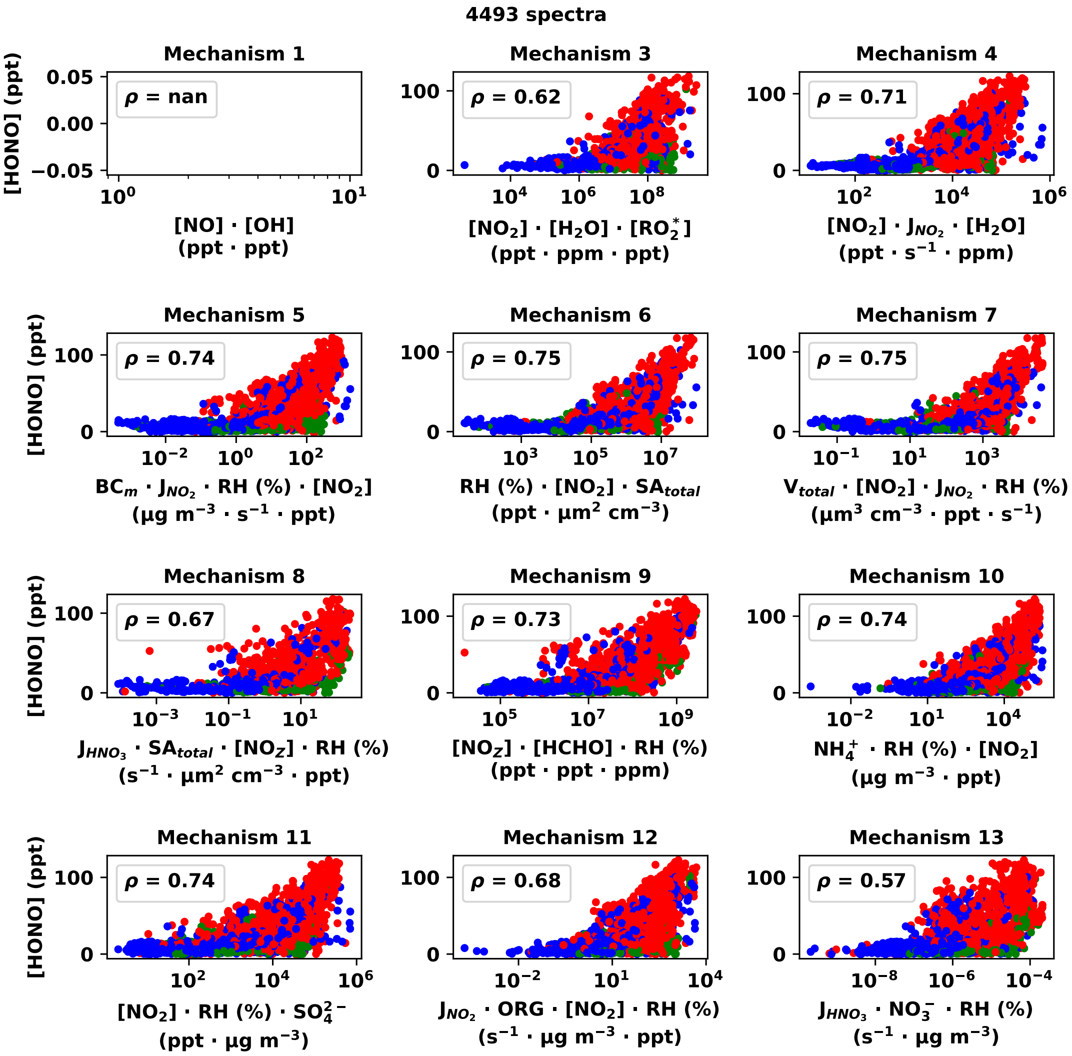

Figure 6.10: For twelve of the thirteen potential formation mechanisms listed in table 2.1, the observed HONO VMRs are plotted against the product of any measured reactants (or proxies thereof), from the lower troposphere during the -Asia phase of the EMeRGe mission. In each panel, the legend is the Spearman correlation coefficient ρ. During the EMeRGe mission, no measurements or proxies for OH are available. Here, RO_2* acts as a proxy for HO_2, while NO_z (NO_y − NO_x) acts as a proxy for HNO_3. Data is colored by the tags described in section 4.1.1; red represents anthropogenic influence, green represents biomass burning influence, and the absence of either is indicated in blue and assumed to be otherwise background air. Missing tags are represented in black. Note the logarithmic x axes. Mechanism 2 is excluded because ortho-nitrophenols were not measured.

Anthropogenic air

Considering only the spectra tagged as having anthropogenic influence (determined from the presence of benzene), the correlation with NO_2 and HCHO remains ($\rho > 0.7$). The products of the reactants of mechanisms 5, 6, 7, 9, 10, and 11 correlate strongly with the observed HONO ($\rho \approx 0.7$). Mechanisms 5, 6, 7, 9, 10 and 11 refer to the production of HONO on soot, the conversion of NO_2 on humid surfaces, the uptake of NO_2 on illuminated mineral dust, the reaction of nitric acid with VOCs, the ammonia-promoted hydrolysis of NO_2, and the oxidation of SO_2 by NO_2 in aerosol water, respectively. The correlations suggest that most likely, heterogeneous reactions or photo-sensitized reaction of NO_2 on surfaces leads to the production of HONO in polluted air masses, while HONO may also be formed during haze events.

Biomass burning influence

Considering only the data with elevated concentrations of acetonitrile (indicative of biomass burning influence), no co-measured species correlate strongly with the observed HONO, not even the coincident NO_2 and HCHO. None of the proposed formation mechanisms correlate strongly either. Considering in particular the biomass burning event from the flight on 19.03.2018 [Lin et al., 2023], the observed HONO is strongly correlated with NO_z ($\rho = 0.7$) and only mechanism 9 shows a strong correlation of the relevant parameters with HONO ($\rho = 0.8$).

Background air

Considering only the data which is tagged as otherwise background air, none of the individual reactants correlate strongly with the observed HONO, except for HCHO ($\rho \approx 0.7$). Only mechanisms 6, 9 and 10 correlate strongly in these air masses ($\rho \approx 0.7$).

6.2.3 The low-NO_x air masses of the CAFE-Africa mission

The VMRs of HONO observed by the mini-DOAS instrument in the lower troposphere during the CAFE-Africa mission require a weaker source of HONO than necessary to explain the observations from the EMeRGe mission (see figure 5.9). Still, the observed HONO VMRs require a source term stronger than the gas phase formation by OH + NO provides (see figure 6.11). Unlike during the EMeRGe mission, during the CAFE-Africa mission, the HORUS instrument on board the HALO aircraft provided measurements of OH, which complement the measurements of NO. Therefore, the observed HONO VMRs which are in excess of model predictions may also be compared against the gas phase formation of HONO from the reaction of OH and NO (see equation 2.46).

The observed HONO is in excess of calculations based on an assumed PSS between gas phase formation and photolytic destruction (see equations 1.1 & 1.2, and figure 6.11). Given the location of the CAFE-Africa measurements over the Atlantic Ocean, as well as the measurement altitudes, local emissions are unlikely sources. Therefore, we must again consider other sources of HONO to explain our observations. Since the NO_2 VMRs observed by the mini-DOAS instrument during the CAFE-Africa mission were generally less than 100 ppt (see figure 5.1), the air masses sampled during the CAFE-Africa mission can be described as low-NO_x environments. Accordingly, excess HONO observed during the CAFE-Africa mission is unlikely to be formed by any heterogeneous mechanism which requires NO_2 as a reactant (see table 2.1). We therefore assume that the observed HONO may be produced primarily by the photolysis of nitrates (in either the particulate or — less likely or to a lesser extent — the gaseous form, see subsection 6.1).

Moreover, the collision rate of measured aerosol with ambient air, together with the low-NO_x character of the air masses investigated during the CAFE-Africa mission, may preclude heterogeneous HONO sources that require NO_2 (see section 5.5). Still, it is worthwhile to correlate the observed HONO VMRs with all other quantities measured from on board the HALO aircraft as well as with the products of the reactants from the formation mechanisms listed in table 2.1.

In figure 6.12, the observed HONO VMRs are correlated with the Spearman correlation coefficient against twenty other species and parameters simultaneously measured on board the HALO aircraft. Taking the measurements from the entire mission, no single quantity correlates

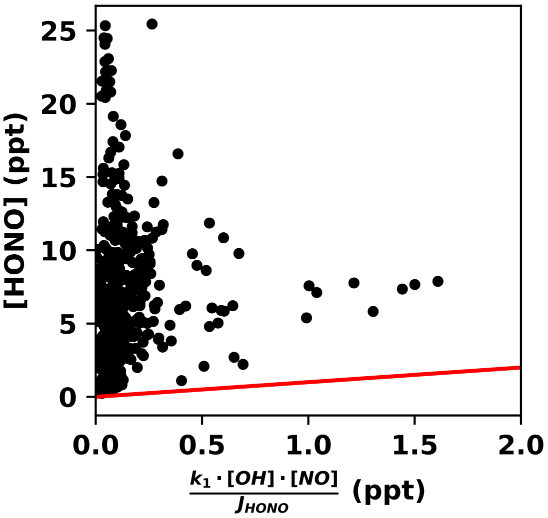

Figure 6.11: The HONO VMRs (ppt) measured by the mini-DOAS instrument plotted against the HONO VMRs (ppt) expected from the rates of gas phase formation (determined from measured quantities) and the measured photolysis rate during the CAFE-Africa mission within the lowermost 7.5 km of the troposphere. The red line is a 1:1 line. The slow destruction of HONO by reaction with OH (reaction 1.3) is neglected here and would further reduce the HONO expected.

strongly with the observed HONO VMRs, although organic aerosol mass, black carbon mass, nitrate aerosol mass, aerosol surface area, CO, O_3, sulfate aerosol mass, and ammonium aerosol mass are all clearly elevated within biomass burning plumes.

In figure 6.13, the observed HONO VMRs are correlated with the Spearman correlation coefficient against twelve of the thirteen HONO formation mechanisms described in table 2.1. The air masses tagged as biomass burning are visually distinguishable from the background air. Here, as before, filtering the data according to the air mass tags modulates the resultant correlation coefficients. The Spearman correlation coefficient between observed HONO VMRs and other co-measured species upon further filtration by air mass tags are shown in table 6.5, while correlation with the various formation mechanisms under the same filtering are shown in table 6.6. Versions of figures 6.12 and 6.13 filtered by air mass tags can be found in appendix G.

While no single mechanism correlates strongly with the observed HONO VMRs across the entire mission, mechanisms 5, 7, and 12 correlate weakly ($\rho \approx 0.5$).

Table 6.5: Spearman correlation coefficients, ρ, between the HONO VMRs and eleven other reactants simultaneously measured on board the HALO aircraft, when the CAFE-Africa data from the lower troposphere is further filtered by air mass tags. BB is biomass burning, BG is otherwise background air.

	ORG	BC_m	HNO_3	NO	NO_2	SA	HCHO	${NO_3}^-$	${NH_4}^+$	${SO_4}^{2-}$	HO_2
All	0.48	0.47	0.00	0.32	0.41	0.47	0.13	0.43	0.30	0.28	0.14
BB	0.54	0.52	-0.53	0.55	0.59	0.60	-0.04	0.47	0.37	0.34	0.33
BG	0.16	0.34	0.04	0.11	0.29	0.40	0.15	0.23	0.19	0.24	-0.06

Anthropogenic air

Without an instrument to measure benzene during the CAFE-Africa mission, measurements cannot be tagged as being influenced by anthropogenic pollution. Since the flight tracks were mostly in the upper troposphere and far away from sources of anthropogenic pollution, this influence is unlikely.

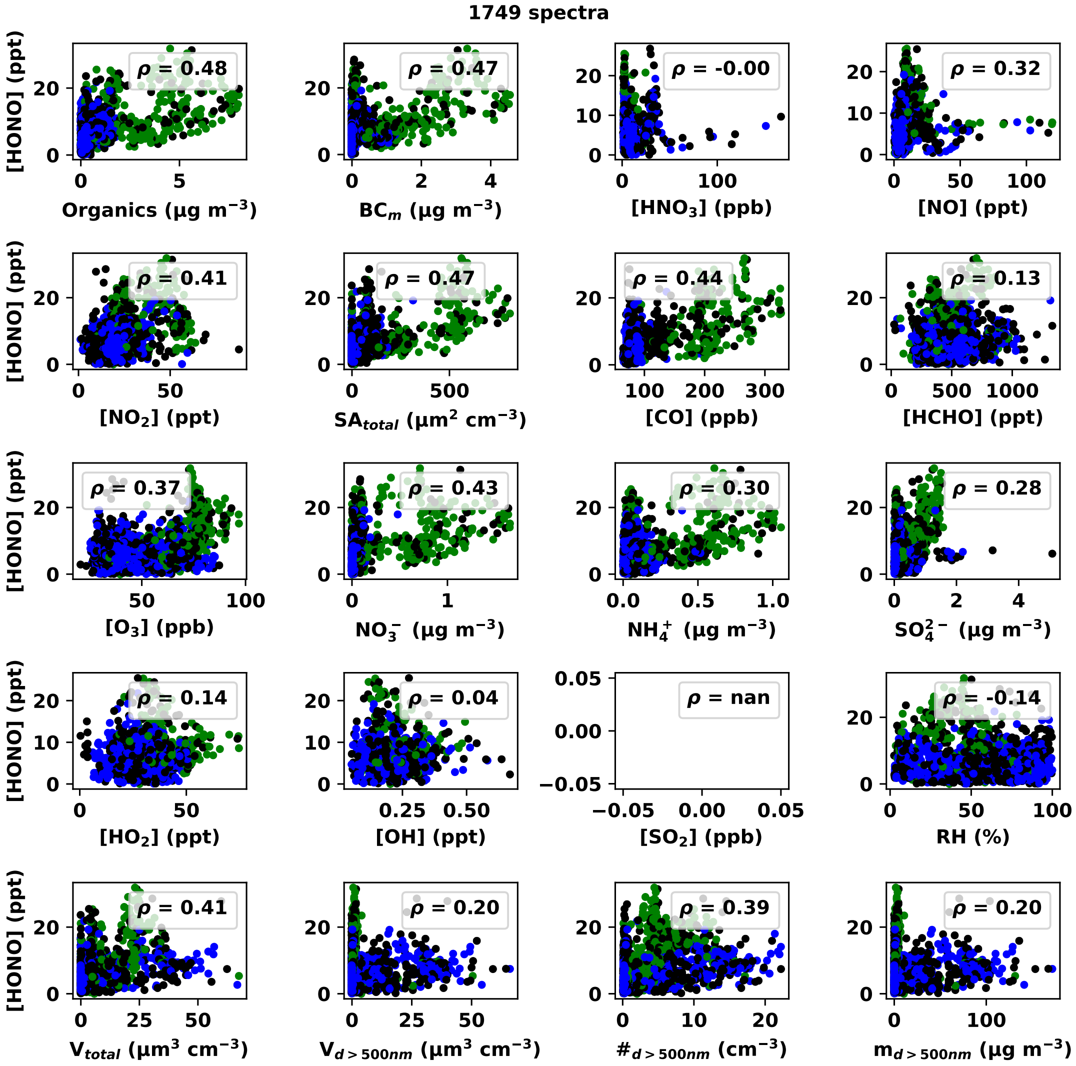

Figure 6.12: In each panel the HONO VMRs observed by the mini-DOAS instrument are plotted against twenty other trace gases or atmospheric parameters measured from the HALO aircraft during the CAFE-Africa mission. The legend is the Spearman correlation coefficient. Green markers represent the influence of biomass burning determined from elevated acetonitrile measured by the MMS instrument, blue data represents acetonitrile below threshold values, black markers represent missing acetonitrile measurements. Data is from the lowermost 7.5 km of the troposphere. SO_2 was not measured during the CAFE-Africa mission.

Table 6.6: Spearman correlation coefficients, ρ, between the HONO VMRs and twelve of the formation mechanisms in table 2.1 when the CAFE-Africa data from the lower troposphere is further filtered by air mass tags. BB is biomass burning, BG is otherwise background air.

	1	3	4	5	6	7	8	9	10	11	12	13
All	0.25	0.01	0.25	0.53	0.46	0.54	0.43	-0.03	0.30	0.29	0.51	0.47
BB	0.34	-0.24	0.15	0.48	0.55	0.49	-0.21	-0.60	0.31	0.30	0.47	0.36
BG	0.07	0.05	0.28	0.46	0.43	0.57	0.34	0.03	0.25	0.27	0.30	0.31

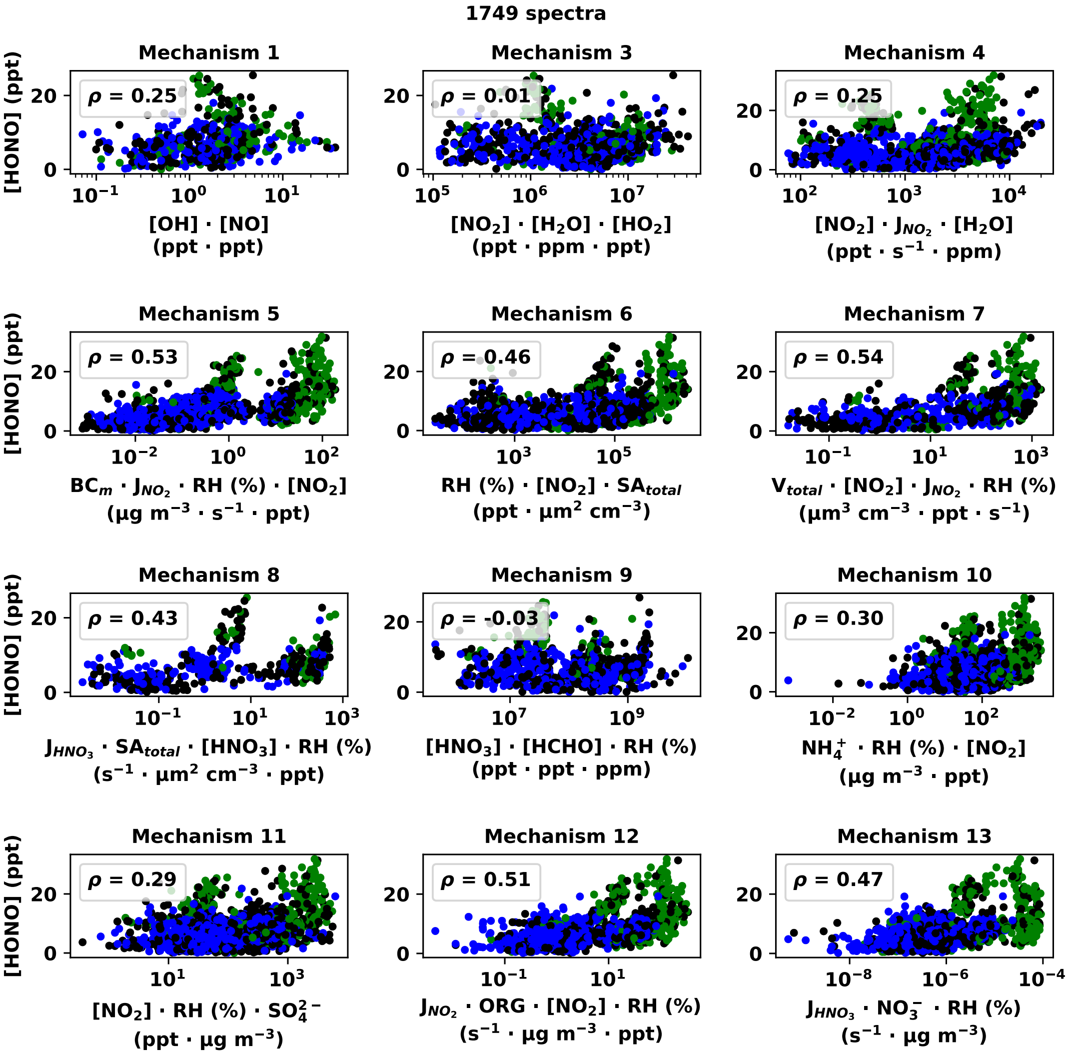

Figure 6.13: For twelve of the thirteen formation mechanisms listed in table 2.1, the HONO VMRs (ppt) are plotted against the product of the reactants observed during the CAFE-Africa mission, within the lower troposphere. The legend in each panel is the Spearman correlation coefficient ρ. The green, blue and black coloration indicates the presence of elevated, decreased, or missing acetonitrile measurements, respectively, as detected by the MMS instrument and should indicate the presence of biomass burning influence. Note the logarithmic x axes. Mechanism 2 is excluded because ortho-nitrophenols were not measured.

Biomass burning plumes

In the biomass burning tagged air masses, only ozone correlates strongly with the observed HONO ($\rho \approx 0.7$), and none of the formation mechanisms from table 2.1 correlate appreciably. Here the strongest correlations ($\rho \approx 0.5$) are with mechanisms 5, 6, 7, and 12, namely: the production of HONO on soot, the conversion of NO_2 on humid surfaces, the uptake of NO_2 on illuminated mineral dust, and the photo-sensitized reduction of NO_2 on organic surfaces / humic acid, respectively.

Background air

Considering only the air masses characterized as background air, no reactant correlates with the observed HONO VMRs. None of the formation mechanisms from table 2.1 correlate strongly either, only mechanism 7 correlates weakly ($\rho > 0.5$).

6.2.4 Discussion of HONO in the lower troposphere

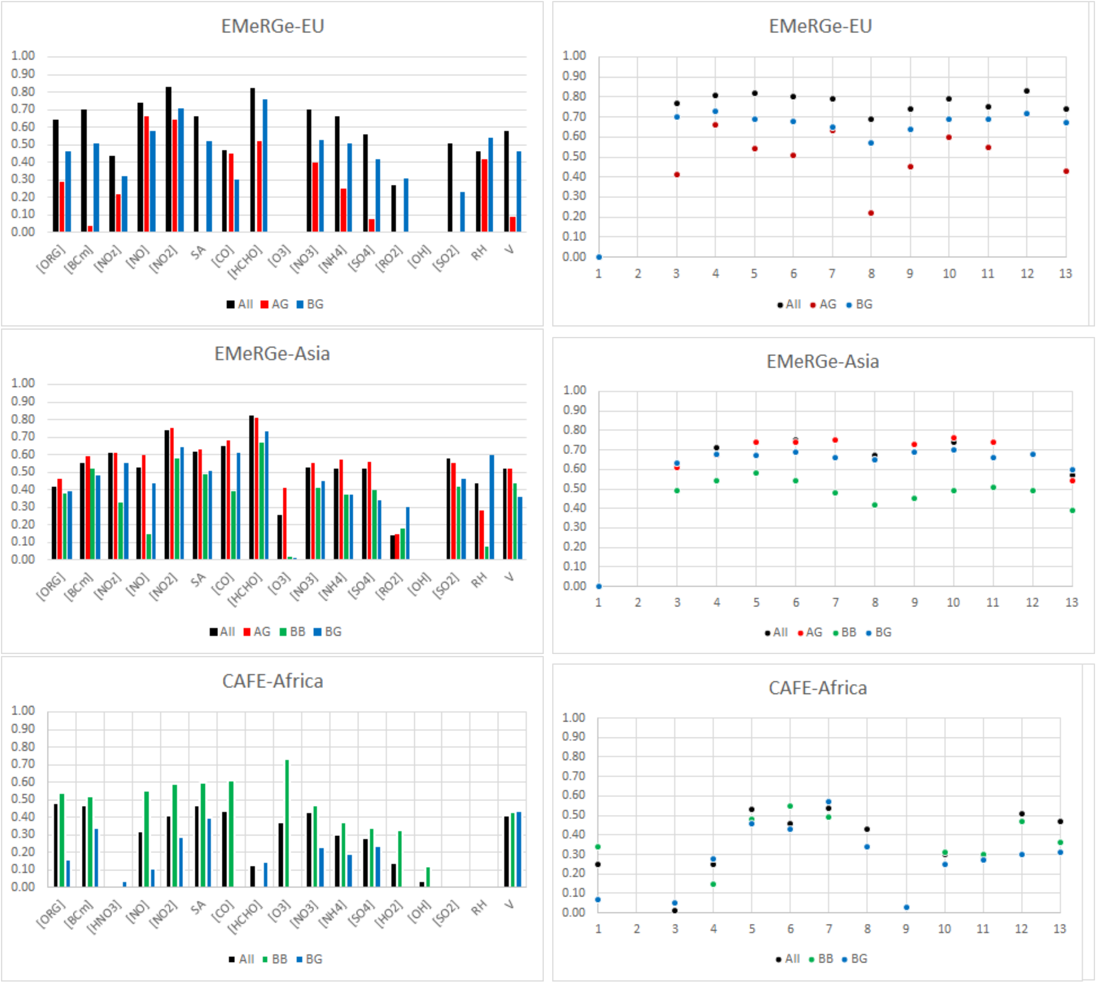

Figure 6.14: Spearman correlation coefficients ρ between the observed HONO VMRs and other parameters simultaneously measured on board the HALO aircraft (left) and the product of reactants of twelve of the thirteen heterogeneous HONO formation mechanisms listed in table 2.1 (right) for the EMeRGe-EU (upper), EMeRGe-Asia (middle), and CAFE-Africa (lower) missions. The data shown here is from the lower troposphere. The data in red, green, blue and black are those tagged as anthropogenic, biomass burning, background, or all data respectively.

During the CAFE-Africa mission, in low-NO_x air masses, only mechanisms 5, 7 and 12 reach a Spearman correlation coefficient of $\rho > 0.5$. Separating the air masses according to their tags does little to change this result, although mechanism 12 correlates in biomass burning plumes but not in background air. Across both phases of the EMeRGe mission, in high-NO_x air masses nearly every mechanism correlates with the observed HONO. Separating the observations according to their air mass tags reveals that some correlations are lost in the biomass burning plumes during EMeRGe-Asia and in anthropogenic air during EMeRGe-EU (see figure 6.14). The proposed formation mechanisms all have some described humidity dependence; water vapor is likely a necessary, but not sufficient component of the formation of HONO. Meanwhile, only mechanisms 1, 3, 6, 9, 10, and 11 do not involve photolysis.

Generally, mechanisms 5, 7 and 12 are correlated with the observed HONO in all probed environments, while mechanisms 9, 10 and 11 are only correlated with the observed HONO in the polluted high-NO_x air masses observed during the EMeRGe mission. The underwhelming correlation between the observed HONO and mechanisms 8 and 13 may arise from the undetermined phase of measured particulate nitrate and gaseous nitric acid. Otherwise the use of NO_z as a proxy for HNO_3 during the EMeRGe mission may obscure any correlation. The dependence of the enhancement factor for the photolysis of particulate nitrate on the nitrate load (see section 6.1) may also confound a simple monotonic relationship between the observed HONO and the components of mechanism 13. The observed HONO is correlated with the presence of NO_2, daylight, and some catalytic surface (i.e. soot, mineral dust, organics) in all air masses, as well as with haze aerosol water reactions in polluted air masses and to a lesser extent with the photolysis of nitrates in pristine air masses.

Previous studies have found similar relationships between NO_2, aerosol and HONO. In Xing et al. [2023], the heterogeneous reaction of NO_2 on aerosol was found to produce HONO. The photolytic nature of heterogeneous HONO production has also been reported previously: Lee et al. [2016] found a HONO source from NO_2 requiring sunlight. Zheng et al. [2020b], Jiang et al. [2020] and Yu et al. [2022] describe photo-enhanced heterogeneous conversion of NO_2 to HONO on aerosol surfaces. Singh et al. [2021] found during eclipse conditions that the HONO source must be photochemical. Hu et al. [2022] speculated that the conversion of NO_2 on BC enhanced by light may be a likely heterogeneous source of HONO, along with the photolysis of particulate nitrate.

This analysis is limited by the spatial and temporal resolutions of the mini-DOAS instrument, as well as those of the in situ instruments also on board the HALO aircraft: the necessary downsampling of parameters reported by in situ instruments may obscure correlations. Chemical interferences of the in situ instruments also obscure a precise attribution of observed HONO formation to a particular mechanism or even phase (mechanisms 8 and 13). The suitability of proxies also limits the scope of the analysis, e.g. whether black carbon mass (or number) is a suitable proxy for the presence of soot, particularly fresh soot (mechanism 5). NO_z is a poor proxy for HNO_3 (mechanisms 8 and 9), while HCHO does not represent total VOCs (mechanism 9). Moreover, volume, mass, and number of particles with a diameter larger than 500 nm are the only quantities available to determine the presence of dust (mechanism 7).

We also lack any measurements of aerosol pH, while the aerosol water content is represented only by relative humidity. These variables are not directly interchangeable, but instrumentation to observe aerosol water content and pH directly was not present, and attempts to model aerosol water content and pH failed. Moreover, particulate ammonium is not synonymous with gas phase ammonia (mechanism 10). Nor does aerosol sulfate equal gas phase SO_2 (mechanism 11). Indeed, the C-ToF-AMS instrument measures only sub-micron aerosol and thereby presents an incomplete picture of the aerosol composition; a more complete aerosol chemical composition would be necessary to investigate mechanisms 10, 11, 12, and especially 13 in more detail.

Moreover, the pH of haze is not well understood [Tao et al., 2020], though sub-micron aerosol is generally acidic [Weber et al., 2016]. Aerosol acidity is lower in China than in Europe [Ding et al., 2019], in large part due to the partitioning of gas phase ammonia and particulate ammonium [Zheng et al., 2020a]. Without measurements of these quantities (aerosol pH, gas phase ammonia), we can only observe the output of the aerosol water reactor. Further, the products of aerosol nitrate photolysis seem to also be pH dependent [Scharko et al., 2014; Benedict et al., 2017].

To summarize the proposed HONO formation mechanisms listed in table 2.1 which could be investigated with the available data and instrumentation:

- Mechanism 1 is the well known gas phase formation of HONO, and cannot explain the HONO VMRs observed by the mini-DOAS instrument. This mechanism cannot be investigated during the EMeRGe mission due to the lack of an instrument measuring OH on board the HALO aircraft.

- Mechanism 2, the photolysis of ortho-nitrophenols, cannot be investigated with the instrumentation on board the HALO aircraft for this study. It also is not sufficient to explain commonly observed HONO VMRs outside of urban environments [Bejan et al., 2006; Spataro and Ianniello, 2014].

- Mechanism 3, a gas phase mechanism proposed by Li et al. [2014], does not have sufficient yield to explain the observed HONO [Ye et al., 2015].

- Mechanism 4 is a gas phase mechanism describing the photo-excitation of NO_2, followed by its reaction with water vapor [Crowley and Carl, 1997]. The rate coefficient is not sufficient for mechanism 4 to explain the observed HONO [Amedro et al., 2011].

- Mechanism 5 describes the heterogeneous production of HONO on soot and may be relevant in polluted air masses [Monge et al., 2010]. Here we use black carbon mass as a proxy for the presence of soot.

- Mechanism 6 describes the conversion of NO_2 on humid surfaces and is not sufficient to explain observed HONO in the atmosphere [Spataro and Ianniello, 2014].

- Mechanism 7 describes the uptake of NO_2 on illuminated mineral dust which may be a source of HONO in the atmosphere [Ndour et al., 2008; Spataro and Ianniello, 2014]. Here we use the volume of large particles ($d > 500$ nm) as a proxy for the presence of dust.

- Mechanism 8 describes the photolysis of nitric acid adsorbed on surfaces. Correlation between mechanism 8 and the observed HONO is undermined by the use of NO_z as a proxy for HNO_3 measured during the EMeRGe mission.

- Mechanism 9 is the reaction of nitric acid with VOCs, the phase of which is undetermined. Correlations between mechanism 9 and the observed HONO is undermined by the use of NO_z as a proxy for HNO_3 during the EMeRGe mission, as well as the use of HCHO as a proxy for VOCs.

- Mechanisms 10 describes the ammonia promoted hydrolysis of NO_2 in haze. Here we use particulate ammonium as a proxy for gaseous ammonia.

- Mechanism 11 describes the oxidation of SO_2 by NO_2 in haze. Here, we use particulate sulfate as a proxy for gaseous SO_2, since measurements of gaseous SO_2 are only available during the EMeRGe mission.

- Mechanism 12 describes the photo-sensitized reduction of NO_2 on organic surfaces / humid acid. Here, the concentration of organic aerosols acts as a proxy for both.

- Mechanism 13 describes the photolysis of particulate nitrate. The process is pH dependent, and only sub-micron aerosol is measured by the C-ToF-AMS (see also mechanisms 10, 11, and 12).

Neglecting the mechanisms which have been found to be insufficient (mechanisms 1, 2, 3, 4, and 6), the remaining mechanisms can be categorized into distinct classes:

- The photolysis of nitrates, either gaseous or particulate, mechanisms 8 and 13, respectively.

- The formation of HONO within haze aerosol water, mechanisms 10 and 11.

- Heterogeneous reactions: mechanisms 5 and 9.

- Photo-catalytic or -sensitized reactions on surfaces: mechanisms 7 and 12, respectively.

6.2.5 Summary on HONO in the boundary layer and lower free troposphere

During both the EMeRGe and CAFE-Africa missions, HONO VMRs observed with the mini-DOAS instrument are in excess of predictions of the EMAC model, as well as of the MECO(n) model during the EMeRGe mission. During the CAFE-Africa mission, those observations are also in excess of gas phase predictions derived from measured quantities. Far enough away from the surface to disqualify emissions as an explanation (given the lifetime of HONO of only 10 minutes against photolysis), excess HONO observed by the mini-DOAS instrument in the lower troposphere may be better explained by in situ sources. Within the lower troposphere, heterogeneous phase sources of HONO are more efficient than gas phase sources (see section 5.5). Here we have correlated the observed HONO VMRs with several species simultaneously measured from the HALO aircraft, as well as with HONO formation mechanisms proposed in the literature, in particular with the photolysis of nitrates over the MBL during the CAFE-Africa mission.

Most of the heterogeneous sources described in the literature require NO_2 as a reactant. Therefore, in low-NO_x environments, such as the air masses investigated during the CAFE-Africa mission, only the photolysis of nitrates may offer a suitable explanation. The enhancement in the rate of particulate nitrate photolysis relative to gas phase nitric acid is found to depend on nitrate load and relative humidity, as reported by Andersen et al. [2023]. Furthermore, the product of gaseous nitric acid (as measured by the CIMS instrument) and its photolysis frequency correlates well with the observed HONO, although the quantum yield of this photolysis (equation 2.27) makes it unlikely [Burkholder et al., 2020]. Nitrate photolysis in one form or another then may provide a background HONO source which saturates under high nitrate loading [Ye et al., 2016a]. Distinguishing between the two phases would require more precise instrumentation which could e.g. differentiate gaseous nitric acid and particulate phase nitrate.

In high-NO_x environments, such as the air masses observed during both phases of the EMeRGe mission, several mechanisms may work in concert to produce HONO. Particularly, the photo-catalytic and photo-sensitized reaction of NO_2 on various surfaces (soot, dust, organics) is correlated with the observed HONO in most air masses, while haze aerosol water reactions are correlated with the observed HONO in polluted (high-NO_x) air masses. Distinguishing between various heterogeneous mechanisms may not be possible with the present composition of instruments on board the HALO aircraft. More precisely determining particular HONO formation mechanism(s) would require a more complete picture of the aerosol composition and size distribution, as well as measurements of the aerosol water content and pH. Attempts to model the aerosol water content and pH with the ISORROPIA model [Fountoukis and Nenes, 2007] failed to converge for the data measured during the EMeRGe missions.

Fu et al. [2019] describes Community Multiscale Air Quality (CMAQ) modeling of heterogeneous reactions on surfaces producing HONO, and reports improved model performance for O_3 and $PM_{2.5}$. In another modeling study, Zhang et al. [2021] found that HONO produced by heterogeneous reactions increased the concentration of OH by a factor of 2, increased aerosol nitrate via the conversion of NO_2, and increased SOA formation via reactions of OH with VOCs (see also Xing et al. [2019]). Heterogeneous HONO formation mechanisms have also been implemented in the chemistry-climate model CHASER [Ha et al., 2023], where the heterogeneous formation reactions were found to contribute more to HONO formation than direct emissions, particularly those on aerosol surfaces. Heterogeneous HONO formation mechanisms in the lower troposphere then represents a critical subject in the understanding of tropospheric oxidation capacity.

Within the lower troposphere, the photolysis rate of the observed HONO represents an OH source of up to 0.25 ppt/s (0.9 ppb/h). This represents a significant modification to the oxidation capacity of the lower troposphere. Previously reported daytime heterogeneous HONO sources in the NO_x polluted atmosphere include those reported by Li et al. [2012] (0.77 ppb/h), Ryan et al. [2018] (1 ppb/h), Jiang et al. [2020] (0.64 ppb/h), and Yu et al. [2022] (0.65 ppb/h), albeit at lower altitudes.

6.3 Excess HONO in the cold upper troposphere: HOONO as a potential new gas phase source of HONO

This section interprets the HONO VMRs reported in chapter 5, within the context of the cold upper troposphere, particularly during the CAFE-Africa mission. While there is data from the upper troposphere probed during two flights of the EMeRGe mission's -Asia phase, the lack of any instrument on board the HALO aircraft measuring OH during those flights precludes any investigation of the gas phase formation of HONO from in situ measured quantities at those altitudes.

HONO volume mixing ratios in the upper troposphere inferred from the mini-DOAS measurements during the CAFE-Africa mission are largely in excess of what may be expected according to the known gas phase formation mechanisms or is predicted by the EMAC model by a factor of at least five (see figure 6.15). While the presence of enhanced NO_x and HO_x from lightning are likely at these altitudes [Zhu et al., 2019; Mao et al., 2021; Brune et al., 2021; Wennberg et al., 1998; Tadic et al., 2021], in situ measurements of NO and OH by the MPIC from on board the HALO aircraft allow us to quantify the gas phase formation of HONO.

Unexpectedly high HONO mixing ratios have also previously been observed in the upper troposphere with balloon borne DOAS [Kritten, 2009] as well as in a thunderstorm cloud [Heue et al., 2014] at concentrations in excess of what would be expected from known gas phase formation. Since there may be an unaccounted thermally unstable NO_x reservoir in the upper troposphere, as evidenced by discrepancies between expected and observed $[NO]/[NO_2]$ ratios [Silvern et al., 2018; Shah et al., 2023], as well as an unknown source of HO_x in the same region [Wennberg et al., 1999], we investigate peroxynitrous acid (HOONO) as a potential gas phase source of HONO (B. Bohn, J. Crowley, private communications). As argued above (section 5.5), in the upper troposphere, heterogeneous formation of HONO can be excluded based on the low aerosol surface and the necessary HONO formation rates.

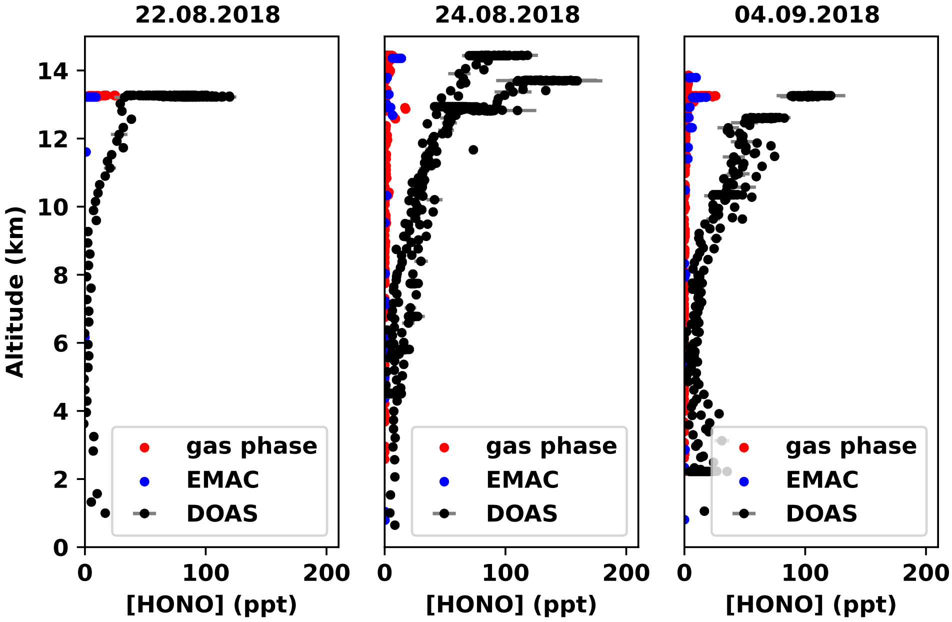

Figure 6.15: HONO VMRs retrieved from limb measurements of the mini-DOAS instrument using the scaling method (black), calculated according to known gas phase formation mechanisms (red), and predicted by the EMAC model (blue) for three selected CAFE-Africa flights, plotted as altitude profiles. The error bars of the mini-DOAS measurements are representative for their altitudes.

Here, we explore peroxynitrous acid as a potential HONO source in the upper troposphere. Amedro et al. [2020] suggests HOONO should be present in the upper troposphere. Unfortunately, to date there are no reported measurements of HOONO in the atmosphere, and several questions remain open:

- Which reactions produce HOONO, and how efficiently?
- How much HOONO can be expected to be found in the atmosphere?
- What loss processes remove HOONO from the atmosphere? Do they efficiently produce HONO? What is the temperature and pressure dependence?

Therefore in the following we briefly review several theoretical and experimental studies of HOONO to determine what is known or controversial about the formation of HOONO in the atmosphere (see figure 6.16). We address the distinct conformers of HOONO and their isomerization rates. We further discuss thermochemically favorable loss mechanisms of HOONO, specifically three reactions which potentially lead from HOONO to HONO. We use onboard measured photolysis frequencies and VMRs of OH, NO, HO_2, NO_2, HONO, and O_3 to make steady state arguments and quantify reaction rate coefficients for both the formation and destruction of HOONO.

By considering a PSS, we quantify how large reaction rate coefficients need to be for an efficient HOONO formation path leading to HONO at low temperatures. As a result of this work, we initiated ab-initio calculations at the Inorganic Chemistry Institute, University of Heidelberg, to assess the magnitude of the relevant reaction rate coefficients. This work is currently (December 4, 2023) ongoing (V. Gunasekaran, P. Comba, personal comm.). Finally, we summarize our findings and discuss the implications for the HO_x and NO_y budgets of the upper troposphere.

6.3.1 Formation of HOONO

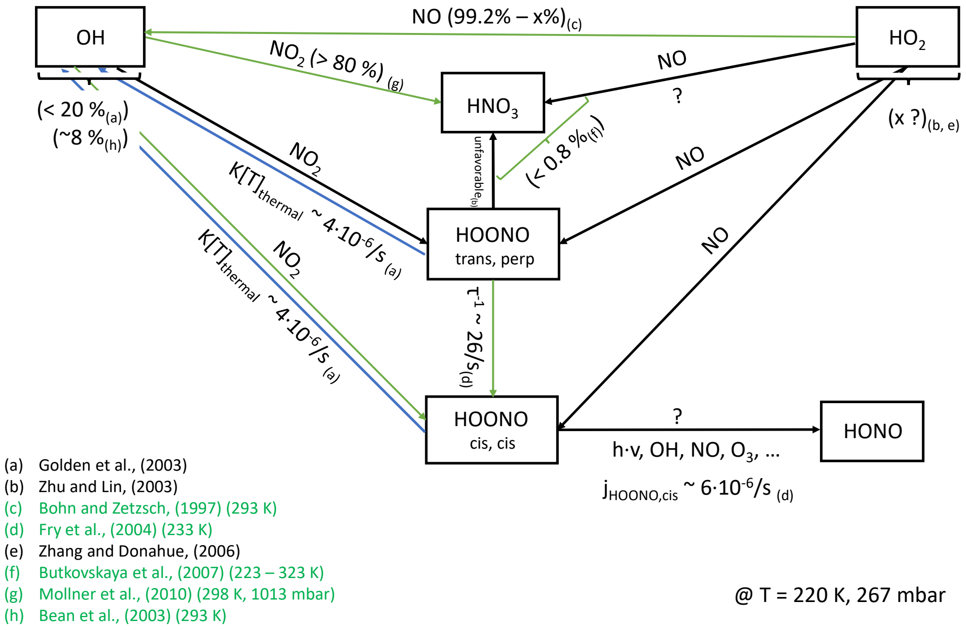

Figure 6.16: Possible reaction diagram leading to the formation and destruction of HOONO at temperature and pressure conditions of the upper troposphere based on a review of the available literature (studies (a) to (h)). Green arrows represent experimental measurements while black arrows represent master equation or ab initio studies. The blue arrows represent the thermal decomposition of HOONO, $k[T]_{thermal}$, see section 6.3.2.

HOONO is known to be formed in a side channel by the termolecular reaction of OH with

NO_2, a reaction which chiefly produces HNO_3 [Golden and Smith, 2000; Mollner et al., 2010].

$$\begin{aligned} OH + NO_2 + M &\longrightarrow HNO_3 + M \\ \Delta H &= -205 \text{ kJ/mol} \end{aligned} \tag{6.1}$$

$$\begin{aligned} OH + NO_2 + M &\longrightarrow HOONO + M \\ \Delta H &= -84 \text{ kJ/mol} \end{aligned} \tag{6.2}$$

(The M denotes any third body molecule in the air, and the enthalpy changes (H) are listed to emphasize that the reactions are exothermic.) The branching ratio β between the two reaction rate coefficients ($k_{6.2}/k_{6.1}$) is measured to be at least 8 % at room temperature and 27 mbar [Bean et al., 2003] and predicted to be up to 20 % for conditions prevailing in the upper troposphere [Golden et al., 2003]. Meanwhile, the reaction of HO_2 with NO has been measured to produce OH and NO_2, and to only a minor extent HNO_3 (if at all [Mertens et al., 2022]).

$$\begin{aligned} HO_2 + NO &\longrightarrow OH + NO_2 \\ \Delta H &= -32 \text{ kJ/mol} \end{aligned} \tag{6.3}$$

$$\begin{aligned} HO_2 + NO + M &\longrightarrow HNO_3 + M \\ \Delta H &= -237 \text{ kJ/mol} \end{aligned} \tag{6.4}$$

Figure 6.17 illustrates the known reaction rates as functions of altitude for eleven CAFE-Africa flights. Note that the reaction rate coefficients are calculated from temperature and pressure data according to the recommendations of the International Union for Pure and Applied Chemistry (IUPAC) (`https://iupac.aeris-data.fr`) data sheets I.A3.43 (NOx13) and I.A3.45 (NOx15) as of Nov. 2022.

However, the reaction of HO_2 with NO may also produce HOONO, as reaction 6.3 proceeds via HOONO as an intermediate [Zhu and Lin, 2003; Zhang and Donahue, 2006] before thermally decomposing (see section 6.3.2).

$$\begin{aligned} HO_2 + NO + M &\longrightarrow HOONO + M \\ \Delta H &= -116 \text{ kJ/mol} \end{aligned} \tag{6.5}$$

To what extent this two step process is mistaken for reaction 6.3 in experiments remains to be determined. The reaction rate coefficient $k_{6.5}$ and the branching ratio $k_{6.5}/k_{6.3}$ are unquantified. Butkovskaya et al. [2007] finds that $k_{6.4}/k_{6.3}$ is at most 0.8 % under temperature and pressure conditions of the upper troposphere, increasing from 0.5 % near the surface with altitude. Crucially, Butkovskaya et al. [2007] determined this ratio by measuring HNO_3 and NO_2, precluding the detection of HOONO as a possible intermediate.

Conformers of HOONO

Peroxynitrous acid has at least three conformers: “cis-cis”, “cis-perp”, and “trans-perp” where “cis”, “trans” and “perp” refer to molecular orientations. “Cis-cis” and “trans-perp” are known to be stable [Golden et al., 2003] and their orientations are shown in figure 6.18. Hereafter “cis-cis” will be referred to as “cis”, while “trans-perp” will be referred to as “trans” for brevity. Note that the ring shape of cis-HOONO may more easily allow for the formation of HONO, should the oxygen atom of the terminal OH group be removed by some reactant. However, this would require breaking two bonds. Alternatively, O-O bond cleavage (71 kJ/mol [Li and Francisco, 2000; Pollack et al., 2003; Zhao et al., 2004]) by NO in either conformer may allow for the formation of HONO (see reaction 6.11).

The literature on the fraction of the two stable conformers produced during reaction is inconsistent. Zhang and Donahue [2006] calculates that cis-HOONO forms 4 times faster than trans-HOONO, while Golden et al. [2003] finds nearly the inverse to be true, with trans-HOONO forming 2 times faster than cis-HOONO. In any case, trans-HOONO rapidly isomerizes, as measured by Fry et al. [2004], who assume the isomerization is to cis-HOONO. Zhang and Donahue [2006] argue that the trans-HOONO loss may be isomerization to HNO_3, but Zhu and Lin [2003] finds this energetically unfavorable. The controversy is driven by uncertainties in the energy barriers of the potential energy surface (see figure 6.19). Either way, of the two conformers, only cis-HOONO is expected to be found at appreciable concentrations in the atmosphere.

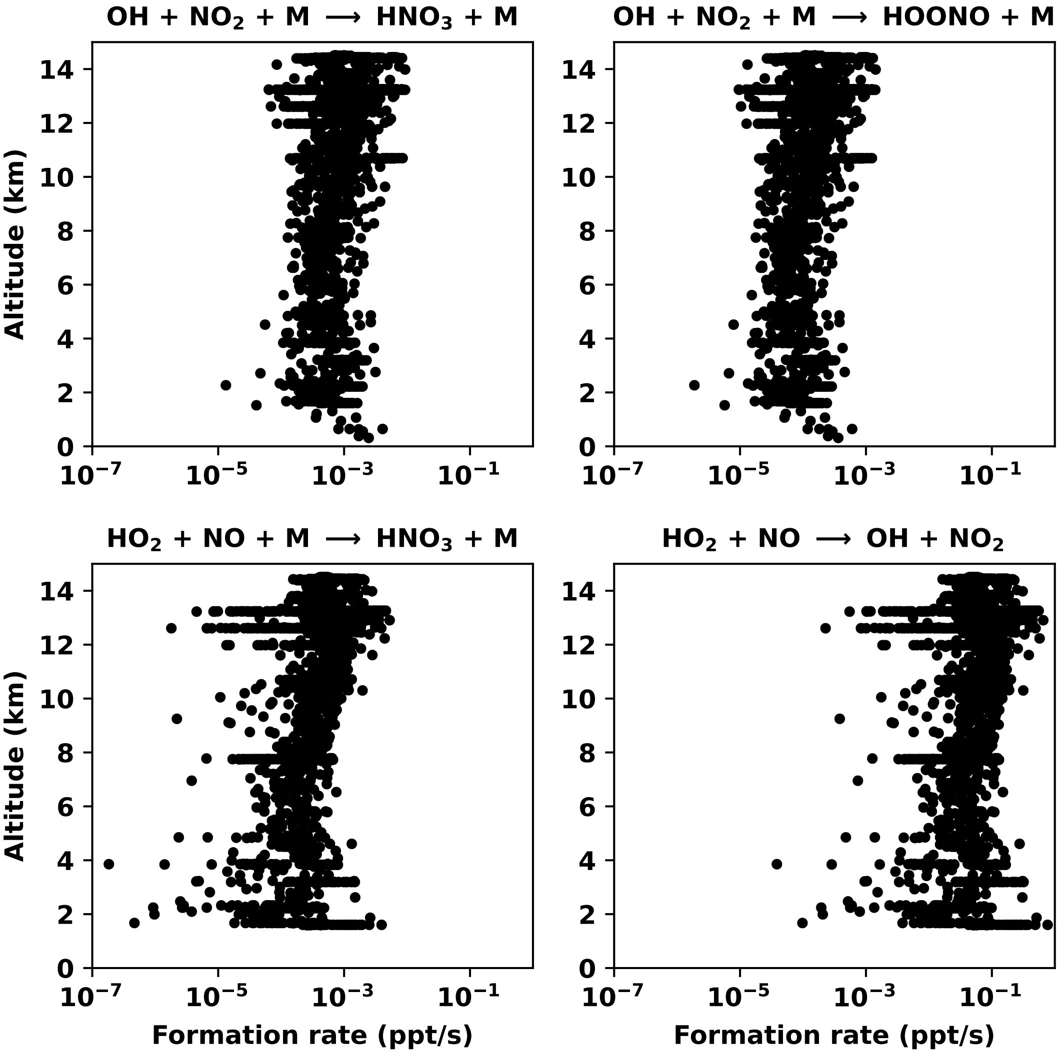

Figure 6.17: Reaction rates for reactions 6.1, 6.2, 6.3, and 6.4 plotted as altitude profiles, calculated from temperature and pressure data of eleven CAFE-Africa flights according to the recommendations of the IUPAC (`https://iupac.aeris-data.fr`), multiplied by the respective VMRs of the relevant reactants. Note the logarithmic x axes.

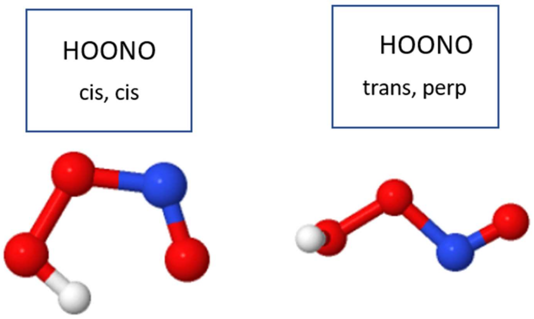

Figure 6.18: The arrangements of the two stable HOONO conformers. Oxygen atoms are shown in red, nitrogen atoms in blue, and hydrogen atoms in white. Visualizations from `https://atct.anl.gov`.

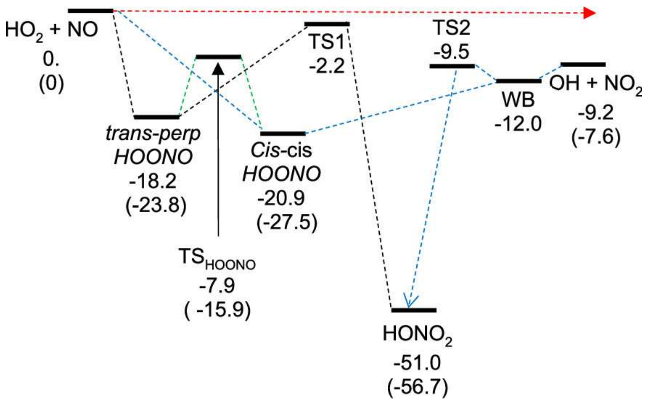

Figure 6.19: Potential energy surface of the HO_2 + NO reaction. Values from Butkovskaya et al. [2009]; figure adapted from Mertens et al. [2022]. Other studies have found similar but not identical energies [Golden and Smith, 2000; Pollack et al., 2003; Zhu and Lin, 2003; Butkovskaya et al., 2005; Zhang and Donahue, 2006].

6.3.2 Destruction of HOONO

Quantified loss processes

The rate of thermal decomposition of HOONO according to its chemical equilibrium with OH and NO_2

$$\begin{aligned} HOONO + M &\longrightarrow OH + NO_2 + M \\ \Delta H &= 84 \text{ kJ/mol} \end{aligned} \tag{6.6}$$

is given by $k_{6.6} = k_{6.2}/K_{eq}$, where $K_{eq} = 3.5 \times 10^{-27} \exp(10135/T)$ [Amedro et al., 2020]. Accordingly, the thermal decomposition rate should decease from $\approx 10^{-1}$ [s^{-1}] near the surface ($T = 298$ K) to $\approx 10^{-6}$ [s^{-1}] (more than 12 days) near the tropopause ($T = 210$ K) [Golden et al., 2003]. Lifetimes against thermal decomposition for the cis- and trans- conformers are reported to be similar [Golden et al., 2003]. Therefore cis-HOONO formed by reaction 6.2 (or 6.5) may accumulate in the upper troposphere [Amedro et al., 2020] (see figure 6.21), unless photolysis or reaction with some oxidant should reduce its lifetime there. Indeed, some loss mechanism must take place to prevent the buildup of all odd nitrogen in the upper troposphere as HOONO. If the loss mechanism produces NO_2 (c.f. reaction 6.11), this may offer an explanation for the yet unexplained [NO]/[NO_2] ratios observed in the upper troposphere by Silvern et al. [2018] and Shah et al. [2023]. Otherwise, if the reaction produces HONO, it may act as a reservoir of NO, and further reduce the observed Leighton ratio (Ibid).

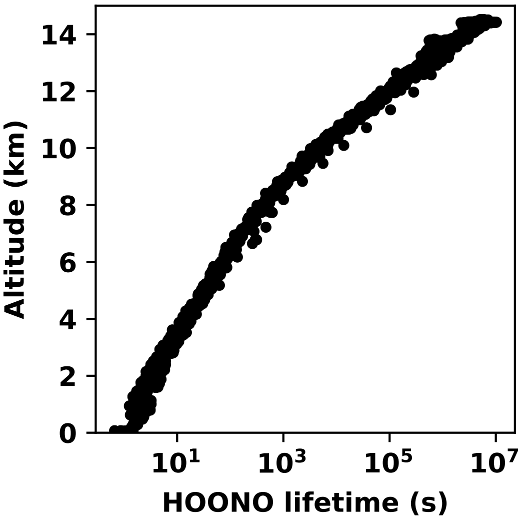

Figure 6.20: HOONO lifetime against thermal decomposition ($1/k_6$), plotted as an altitude profile, for eleven CAFE-Africa flights. Reaction rate coefficients are calculated from temperature and pressure data and according to the recommendations of the IUPAC (`https://iupac.aeris-data.fr`). Note the logarithmic x axis.

While reaction 6.2 may produce HOONO, it is likely not efficient enough to provide a source for the HONO we observe (see figure 6.21). Moreover, HOONO potentially formed by reaction 6.5 should not exceed the known NO_y budget in the upper troposphere. Therefore, either some other loss mechanism efficiently removes HOONO from the atmosphere (see below), or the reaction rate coefficient for reaction 6.5 is considerably less than the reaction rate coefficient for reaction 6.3, or both. In the following we will explore other processes which could remove HOONO from the atmosphere.

Speculative loss processes of HOONO

Photolysis: Measurements of photolysis frequencies of HOONO in the atmosphere are not available, but Fry et al. [2004] finds that near-IR photolysis of cis-HOONO should limit its lifetime during daylight to 45 hours. The products of the photolysis of HOONO given by

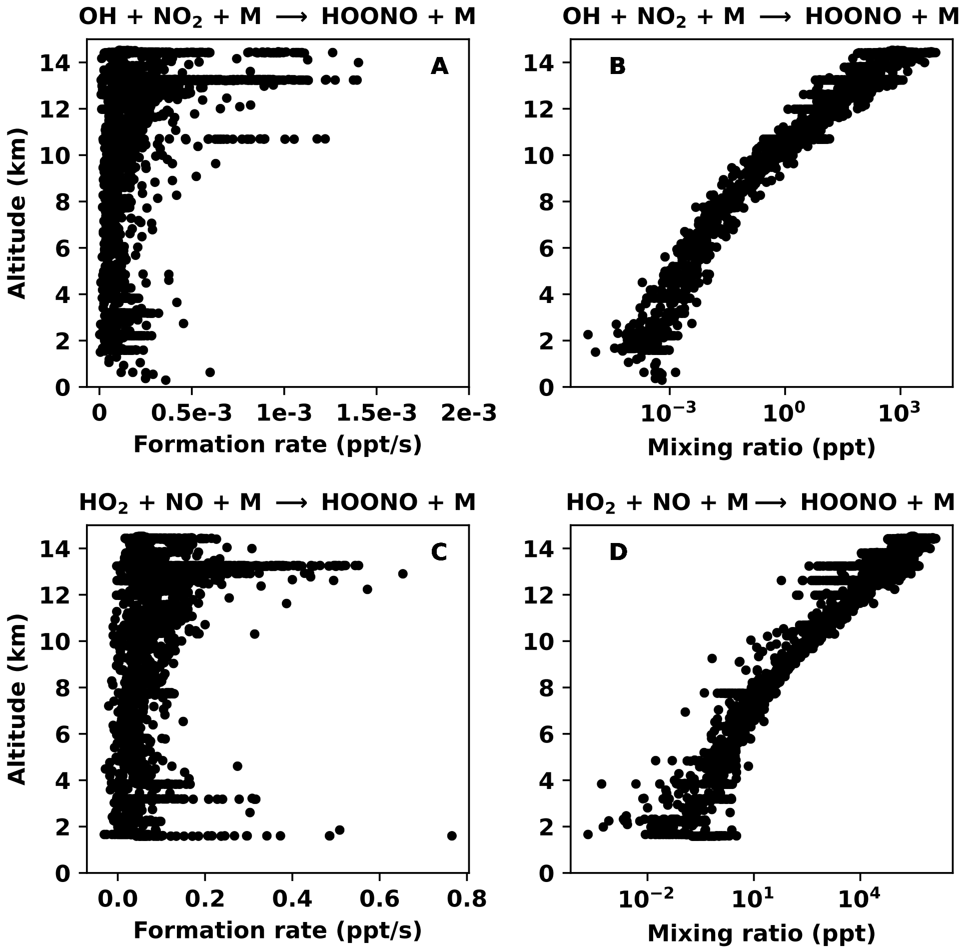

Figure 6.21: HOONO formation rates of reactions 6.2 and 6.5 in ppt/s (panels A and C, respectively), plotted as altitude profiles for eleven CAFE-Africa flights. Formation rates are products of the simultaneously measured volume mixing ratios of OH and NO_2 (or NO and HO_2) and the reaction rate coefficients calculated from temperature and pressure data according to the recommendations of the IUPAC (`https://iupac.aeris-data.fr`). For each formation reaction, the volume mixing ratio of HOONO predicted by assuming only loss via thermal decomposition (panels B and D), plotted as a function of altitude for eleven CAFE-Africa flights. Here $k_{6.5}$ is assumed to be equal to $k_{6.3}$, i.e. its maximum possible value. Note the logarithmic x axes.

Amedro et al. [2020] are based on the analysis of Golden and Smith [2000].

$$\begin{aligned} \mathrm{HOONO} + \mathrm{h}\nu(\lambda < 1424\ \mathrm{nm}) &\longrightarrow \mathrm{OH} + \mathrm{NO_2} \\ \Delta\mathrm{H} &= 84\ \mathrm{kJ/mol} \end{aligned} \tag{6.7}$$

Photolysis may also take the following forms at visible or UV wavelengths (Bohn, pers. comm.).

$$\begin{aligned} \mathrm{HOONO} + \mathrm{h}\nu(\lambda < 654\ \mathrm{nm}) &\longrightarrow \mathrm{HONO} + \mathrm{O(^3P)} \\ \Delta\mathrm{H} &= 183\ \mathrm{kJ/mol} \end{aligned} \tag{6.8}$$

$$\begin{aligned} \mathrm{HOONO} + \mathrm{h}\nu(\lambda < 320\ \mathrm{nm}) &\longrightarrow \mathrm{HONO} + \mathrm{O(^1D)} \\ \Delta\mathrm{H} &= 375\ \mathrm{kJ/mol} \end{aligned} \tag{6.9}$$

but the HOONO absorption cross section for photolysis in the UV/visible spectral range is not known. Furthermore, whether the hydrogen atom would “roam” to the terminal oxygen atom, as in aldehydes, is unknown. In either case, while photolysis should reduce the lifetime of HOONO in the atmosphere, unless it proceeds apace of the HONO photolysis rate, it cannot explain our HONO observations.

Other exothermic reactions potentially leading to HONO: We also hypothesize that destruction of HOONO and formation of HONO could proceed via other exothermic reactions (see the table in appendix H) if the reaction barriers aren't too large.

$$\begin{aligned} \mathrm{HOONO} + \mathrm{O_3} &\longrightarrow \mathrm{HONO} + 2\mathrm{O_2} \\ \Delta\mathrm{H} &= -208\ \mathrm{kJ/mol} \end{aligned} \tag{6.10}$$

$$\begin{aligned} \mathrm{HOONO} + \mathrm{NO} &\longrightarrow \mathrm{HONO} + \mathrm{NO_2} \\ \Delta\mathrm{H} &= -123\ \mathrm{kJ/mol} \end{aligned} \tag{6.11}$$

While kinetic data for reactions 6.10, 6.11 are unavailable (but presently being explored on a theoretical basis — ongoing work by our collaborators), we constrain their reaction rate coefficients using measurements of HONO and other quantities (see subsection 6.3.3). Other potential oxidation reactions involving HOONO may include reaction with $\mathrm{NO_2}$ or self reaction (Burrows, pers. comm.).

$$\begin{aligned} \mathrm{HOONO} + \mathrm{NO_2} &\longrightarrow \mathrm{HONO} + \mathrm{NO} + \mathrm{O_2} \\ \Delta\mathrm{H} &= -9\ \mathrm{kJ/mol} \end{aligned} \tag{6.12}$$

$$\begin{aligned} 2\mathrm{HOONO} &\longrightarrow 2\mathrm{HONO} + \mathrm{O_2} \\ \Delta\mathrm{H} &= -132\ \mathrm{kJ/mol} \end{aligned} \tag{6.13}$$

Neither reaction 6.12 nor reaction 6.13 are investigated further here given that reaction 6.12 would increase the $[\mathrm{NO}]/[\mathrm{NO_2}]$ ratio in the upper troposphere (contradicting the findings of Silvern et al. [2018] and Shah et al. [2023]), and the likely kinetic (and concentration) limitations of reaction 6.13.

Reaction with OH: Kinetic data concerning the reaction of HOONO with oxidants are not available, but Amedro et al. [2020] speculates that HOONO should react with OH.

$$\begin{aligned} \mathrm{HOONO} + \mathrm{OH} &\longrightarrow \mathrm{H_2O} + \mathrm{NO_3} \\ \Delta\mathrm{H} &= -192\ \mathrm{kJ/mol} \end{aligned} \tag{6.14}$$

We speculate that the reaction may also form HONO (though the reaction of HOONO with OH leading to HONO is later ruled out below for quantitative reasons).

$$\begin{aligned} \mathrm{HOONO} + \mathrm{OH} &\longrightarrow \mathrm{HONO} + \mathrm{HO_2} \\ \Delta\mathrm{H} &= -91\ \mathrm{kJ/mol} \end{aligned} \tag{6.15}$$

Due to its products, reaction 6.14 is not of further interest here.

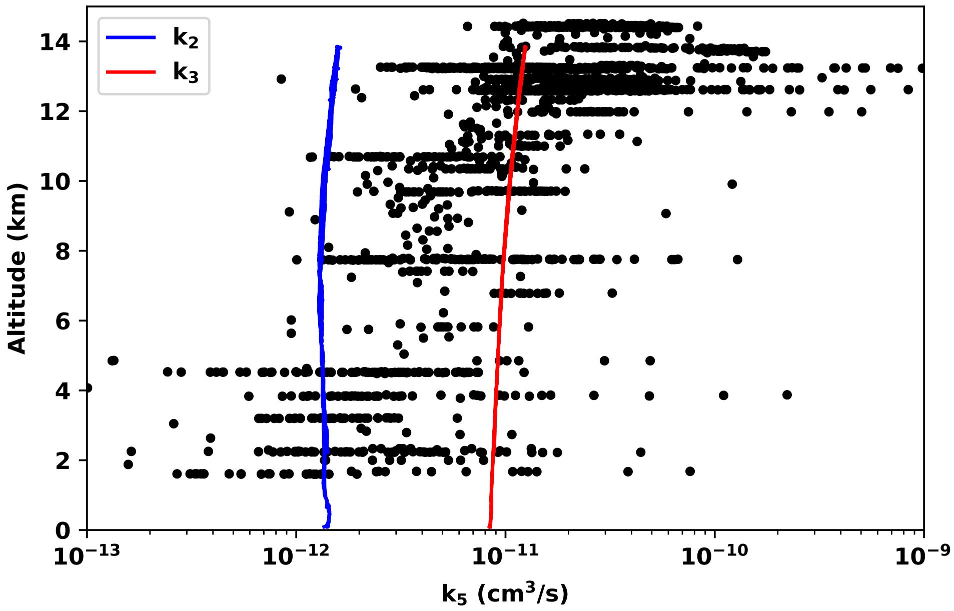

Figure 6.22: In a steady state, the reaction rate coefficient k$_{6.5}$ required to explain our HONO observations, as calculated from the ratio $\frac{J_{HONO}[HONO]}{[NO][HO_2]}$ using the simultaneously observed photolysis frequency J and volume mixing ratios of HONO, NO, and HO$_2$, plotted as altitude profiles for eleven CAFE-Africa flights. For comparison, the reaction rate coefficients k$_{6.2}$ and k$_{6.3}$, calculated according to the recommendations of the IUPAC (`https://iupac.aeris-data.fr`) are shown in blue and red, respectively. Note the logarithmic x axis.

6.3.3 Discussion

Estimating required k$_{6.5}$ from measured quantities

Since k$_{6.5}$ is not known from laboratory or theoretical studies, we infer its required magnitude from our observed HONO destruction rate and other measured quantities. If HOONO is a precursor for HONO, its loss could produce our missing HONO, and its formation needs to be in a steady state with the loss of HONO via photolysis. Under this assumption, the ratio $\frac{J_{HONO}[HONO]}{[NO][HO_2]}$ would approximately represent the reaction rate coefficient k$_{6.5}$ necessary to explain our HONO observations. Particularly at higher altitudes, k$_{6.5}$ necessary to explain our HONO observations would often exceed k$_{6.3}$ (see figure 6.22), which contradicts the measured decay of HO$_2$ and NO in the laboratory, and is therefore implausible. This inconsistency may also be due to spatial heterogeneities in the measured quantities, particularly the variability of HONO measured at high altitudes (see figure 6.15). Nevertheless, due to the larger HO$_2$ and NO concentrations as compared to OH and NO$_2$, k$_{6.5}$ is expected to be more efficient than k$_{6.2}$ in the upper troposphere.

Likely reactants according to measured quantities

In the absence of kinetic data regarding the reaction of HOONO with the aforementioned reactants, we estimate the necessary reaction rate coefficients using measured quantities. If the photolytic loss of HONO is in steady state with its production by some reaction of HOONO with a reactant, then for each proposed reactant X the ratio $\frac{J_{HONO}[HONO]}{[X]}$ derived from measurements should equal the product k_X [HOONO]. In this context, for each simultaneous observation of measured quantities, the necessary reaction rate coefficient between HOONO and the reactant X can be determined for any assumed HOONO volume mixing ratio (see figure 6.23).

O$_3$ is abundant enough to explain a potential HONO source term provided only that HOONO exists in the parts per trillion. Meanwhile, the reaction of HOONO with NO could explain a

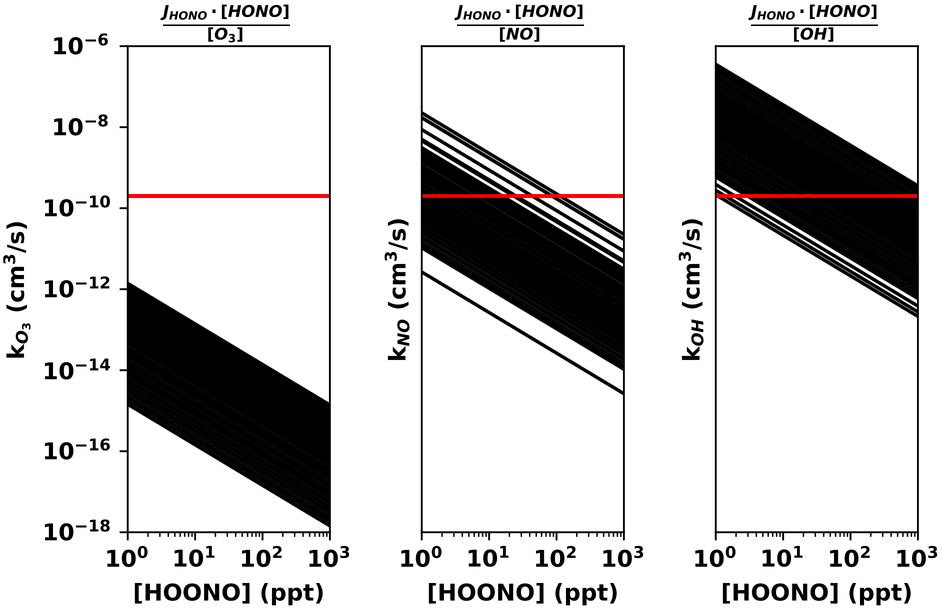

Figure 6.23: For each simultaneous observation of the photolysis frequency J_{HONO}, the concentration of HONO, and concentration of either O_3, NO, or OH, the necessary reaction rate coefficient k_X between HOONO and that oxidant for any assumed HOONO volume mixing ratio in the parts per trillion. Data from eleven CAFE-Africa flights visually overlap. The horizontal red line in each panel represents the maximum reaction rate coefficient possible if each collision of the reactants would be successful (see section 5.5). Steric effects and activation energy barriers would reduce the reaction rate in practice. Note the logarithmic axes.

HONO source term if HOONO is found in the tens of ppt, as is predicted by Amedro et al. [2020]. However, both reactions would have a significant effect on the nitrogen and ozone budgets of the upper troposphere, which for ozone is unlikely based on observations.

The reaction of HOONO with O_3 would create an unlikely several ppb per day loss term for ozone in the upper troposphere (0.2 ppt/s * 43200 s $\approx$ 9 ppb/day), which is not observed [Nussbaumer et al., 2023].

The proposed reaction of HOONO with NO would produce NO_2, creating a net zero effect on the nitrogen budget by substituting reactions 6.5 and 6.11 for reaction 6.3 , followed by the photolysis of HONO into OH and NO. HOONO would act as a reservoir of NO_2 in this way, confounding atmospheric measurements of NO_2 which use photolytic converters (see Silvern et al. [2018]; Nussbaumer et al. [2021a]; Shah et al. [2023]). Since OH would be recycled in the photolysis of HONO, the formation of HOONO and reaction with NO would also not have an impact on HO_x in the upper troposphere, but HOONO would simply serve as a temporary reservoir for OH. Potentially, both of these reactions take place, which would modulate the effect of either one in isolation.

It is unlikely that the reaction of HOONO with OH may explain our HONO observations (see figure 6.23), since the necessary reaction rate coefficient exceeds the maximum possible gas phase reaction rate coefficient for most observations, unless more than of 1 ppb HOONO is assumed.

Remaining open questions

Figure 6.23 indicates plausible pathways for the production of HONO from HOONO. However, there remain some open questions:

- If the reaction of HO_2 + NO proceeds via HOONO [Zhang and Donahue, 2006; Zhu and Lin, 2003], why should the produced HOONO have a different atmospheric fate than HOONO produced by reaction 6.2? Differences between the fates of HOONO formed via reactions 6.2 and 6.5 could arise from differences in the relative amounts of the produced conformers, although both should experience thermal decomposition at similar rates [Golden et al., 2003]. Since trans-HOONO isomerizes rapidly [Fry et al., 2004], only cis-HOONO is expected in the atmosphere. Alternatively, if trans-HOONO isomerizes to HNO_3 rather than cis-HOONO as Zhang and Donahue [2006] argues, why is the branching ratio $k_{6.4}/k_{6.3}$ measured by Butkovskaya et al. [2007] so small?

- Past laboratory studies of the HO_2 + NO reaction have been performed at or near room temperature [Bohn and Zetzsch, 1997; Mertens et al., 2022], where HOONO would thermally decompose within the time frame given by the experiment, which would preclude HOONO detection. Further, the presence of NO in the reaction would potentially destroy HOONO. Otherwise, Butkovskaya et al. [2005, 2007] only measure some of the relevant species, precluding the detection of intermediates entirely. To what extent could the formation/presence of HOONO have been overlooked in these experiments? To date only Butkovskaya et al. [2005, 2007] conducted experiments at the cold temperatures of the upper troposphere, and their results remain uncorroborated.

- The formation of HOONO via reaction 6.5 is potentially much more efficient than by reaction 6.2, while the reactants are also more abundant in the upper troposphere during the CAFE-Africa mission (OH $\approx$ 1 ppt, NO_2 < 100 ppt; NO >> 100 ppt, HO_2 $\approx$ 10 ppt). If reaction 6.2 produces HOONO at a sufficient rate to accumulate tens of ppt of HOONO in the upper troposphere against thermal decomposition or photolysis [Amedro et al., 2020], then even a minor branching ratio between reactions 6.5 and 6.3 would significantly increase the production (and therefore concentration) of HOONO (and potentially HONO) expected in the cold upper troposphere (see figure 6.21).

6.3.4 Summary

Our HONO measurements in the upper troposphere during CAFE-Africa offer a new line of evidence regarding necessary modifications of the NO_x and HO_x photochemistry in the cold upper troposphere. Peroxynitrous acid may become a precursor for HONO only if it is formed at a sufficient yield by reaction 6.5, survives thermal decomposition at the cold temperatures of the upper troposphere, and reacts with some reactant at a sufficient rate to sustain HONO formation against its loss via photolysis. Here we show that the reaction of HOONO with NO or O_3 is possible only on thermochemical grounds, and the abundances of O_3 and NO are sufficiently large, but information on the reaction barrier as well as kinetic data at low temperatures are still missing. Whether the potential formation of HOONO via reaction 6.5 is fast enough to sustain the reservoir is unclear. These hypotheses are currently (December 4, 2023) being investigated with transition state calculations of the relevant reaction rates, performed by our collaborators Dr. Velmurugan Gunasekaran and Prof. Peter Comba of the University of Heidelberg's Institute of Inorganic Chemistry.

Most necessary to investigate this subject further are measurements of HOONO and its photolysis frequency in the atmosphere. In the absence of HOONO measurements, the mechanism may be inferred by observing HONO formation, or OH-HO_2 cycle chain lengths under certain conditions. Otherwise, the reaction rate coefficient of reaction 6.5 needs to be quantified in the laboratory, especially at cold temperatures. Further studies on the kinetic data concerning the reaction of HOONO with oxidants such as NO and O_3 — especially at upper tropospheric temperatures and pressures — would be beneficial.

Chapter 7

Summary & Outlook

Summary

The present thesis reports on novel airborne remote sensing observations of nitrous acid in the troposphere from the HALO aircraft during twenty five scientific flights of the EMeRGe-EU, -Asia, and CAFE-Africa missions in summer 2017, spring 2018, and fall 2018, respectively. DOAS retrievals of slant column densities of O_3, O_4, NO_2, HCHO and HONO, in the UV-A and visible wavelength ranges are converted to VMRs using the O_3/O_4 scaling method. This work encompasses 200 retrievals — O_3 and O_4 scaled NO_2 (each retrieved in the UV-A and visible wavelength ranges), HONO, and HCHO across 25 flights each. The observations of nitrous acid are complemented by coincident measurements of HCHO and NO_2, as well as simultaneous measurements of a host of other trace gases and atmospheric parameters from a suite of in situ instruments on board the HALO aircraft. The atmospheric chemistry models EMAC and MECO(n) provide simulations for a priori information and post analysis comparison.

While the NO_2 and HCHO retrievals can be compared with in situ instruments on board the HALO aircraft or the FAAM aircraft during an intercomparison exercise [Schumann, 2021], the HONO retrievals can only be compared to model predictions. Both the EMAC and MECO(n) models predict less HONO than is observed during all missions. This excess HONO has been observed in previous studies in the boundary layer and lower free troposphere (e.g. Li et al. [2014]; Lee et al. [2016]; Jiang et al. [2020]; Zheng et al. [2020b]), but rarely from aircraft, especially in the upper troposphere. Elevated HONO is often observed near the surface and in the lower troposphere, and has only also previously been reported in the upper troposphere from balloon borne DOAS measurements [Kritten, 2009].

This thesis demonstrates that nitrous acid can be detected at all altitudes of the troposphere using the remote sensing mini-DOAS instrument and scaling method at relatively high precision for atmospheric measurements. While the HCHO and NO_2 measurements compare well to in situ measurements and model predictions, the observed HONO VMRs exceed model predictions by more than a factor of five and often up to an order of magnitude. Given the lifetime of HONO against photolysis (approximately ten minutes), the HONO measured outside the boundary layer cannot be explained by surface fluxes, especially the elevated HONO observed in the upper troposphere. This work therefore presents another line of evidence for missing HONO sources in the troposphere.

HONO observed in the low-NO_x MBL during the CAFE-Africa mission over the tropical Atlantic corroborates the findings of Andersen et al. [2023] in the same region. This further provides evidence that the excess HONO observed with the mini-DOAS instrument is not due to methodological issues related to the employed UV/visible limb spectroscopy. Here, the observed HONO may be explained primarily by the photolysis of nitrates, in agreement with previous studies [Ye et al., 2016b; Reed et al., 2017; Andersen et al., 2023]. In particular, the enhancement factor in the frequency of particulate nitrate photolysis (relative to the photolysis frequency of gaseous nitric acid) is found to depend on the nitrate load and relative humidity. However, the enhancement factor cannot be precisely determined with the instruments on board the HALO aircraft, since only a minor fraction of total particulate nitrate was measured.

Within more polluted air masses, observed HONO may not be explained by the photolysis of nitrates alone. Excess HONO observed during the EMeRGe missions is largely confined to the lower troposphere. Scaling method retrievals within the lower troposphere are shown to be robust and insensitive to a priori information, scaling gas, and spectrometer. Most species implicated in the literature as potential HONO sources also have elevated VMRs within the lower troposphere, especially in the high-NO_x polluted boundary layer probed during the EMeRGe missions. Determining a single potential HONO source in this context proves confounding. Several mechanisms may work in concert, depending on the chemical composition of the specific air mass being probed. In general, the reaction of NO_2 on humid aerosol surfaces are photosensitized or catalyzed and are likely to be relevant in the context of our measurements. This study joins several others which find that HONO is related to production from photo-sensitized reactions of NO_2 [Lee et al., 2016; Zheng et al., 2020b; Jiang et al., 2020; Singh et al., 2021; Yu et al., 2022; Hu et al., 2022; Xing et al., 2023]. More precisely determining a specific heterogeneous HONO formation mechanism would require additional instrumentation to quantify the pH of the aerosol, total nitrate load, mineral dust concentrations, et cetera.

While much of the excess HONO observed during the EMeRGe and CAFE-Africa missions in the lower troposphere can be attributed to formation mechanisms described as heterogeneous, excess HONO in the upper troposphere requires an alternative explanation given the time scale for uptake of HONO precursors on aerosol and the required rate of HONO formation. Gas phase explanations in the upper troposphere also require a quantification of the HO_x and NO_x budgets. During the EMeRGe missions, coincidentally measured species did not include OH (or HO_2, but RO_2*), precluding analysis of the HO_x budget in the upper troposphere. Furthermore, measurements of HNO_3 — which enable an analysis of the NO_y budget — are not available.

Excess HONO (relative to the PSS HONO from measured NO, OH, and J_{HONO}) was also observed during the CAFE-Africa mission within the cold upper troposphere. Here, measurements of OH, NO_2, NO, HO_2 and HNO_3 allow the analysis of the HO_x budget as well as an investigation of the NO_y budget. An investigation into the possibility of a gas phase HONO source, namely the oxidation of HOONO by OH, NO, or O_3, raises several hypotheses regarding the as yet largely unexplored photochemistry of HOONO. In the absence of HOONO measurements in the atmosphere, and lacking kinetic data on HOONO formation and destruction at cold temperatures, these hypotheses are largely speculative. In consequence, we initiated transition state calculations for the relevant reactions, results of which were not available by the submission of this thesis (December 4, 2023).

Further evidence for an additional missing oxidant in the upper troposphere comes from the Leighton ratio. The measured NO_2, together with NO, O_3, HO_2, RO_2*, and J_{NO_2} is used to quantify the Leighton ratio in the investigated air masses. The observed Leighton ratio, which serves as a proxy for oxidation capacity, is found to differ significantly from unity (especially in the upper troposphere), in agreement with recent reports [Silvern et al., 2018; Shah et al., 2023]. Formation of HOONO via the HO_2 and NO channel and further reaction of HOONO with NO into HONO and NO_2 would offer an explanation for the observed upper tropospheric Leighton ratios (see section 2.2).

The ubiquitous presence of HONO in the troposphere suggests that inconsistencies with models are not from a misunderstood emission strength but rather a lack of representation and quantification of some reactions which produce HONO [Akimoto et al., 2021]. Attempts to model heterogeneous HONO formation mechanisms [Fu et al., 2019; Zhang et al., 2021; Ha et al., 2023] narrow (but do not close) the gap between measurements and models. Meanwhile, unquantified NO_x reservoirs evidenced by observed Leighton ratios [Silvern et al., 2018], as well as sources of HO_x [Wennberg et al., 1999] in the upper troposphere may arise from the presence of HOONO and HONO at those altitudes.

The observed HONO, upon photolysis, represents an OH source term with a strength of up to 0.25 ppt/s or 0.9 ppb/h (see figure 5.9). This represents a significant source of OH in the troposphere, thereby affecting the atmospheric lifetime (and consequent radiative forcing) of greenhouse gases such as methane. The presence and source of HONO in the troposphere thereby affects our understanding of climate change, the fate of most air pollutants, and consequently, human health.

Outlook

This work joins a very limited set of airborne HONO observations in the upper boundary layer, free and upper troposphere under different photochemical conditions [Zhang et al., 2009; Heue et al., 2014; Li et al., 2014; Neuman et al., 2016; Ye et al., 2016b, 2018; Andersen et al., 2023].

To the author's knowledge, the observations reported here represent the most extensive measurements of HONO in the atmosphere to date. The mini-DOAS instrument has been deployed on several other missions of the HALO aircraft around the globe in the last several years, the analysis of which may complement the present thesis, to illuminate the presence and formation mechanism(s) of HONO in the troposphere.

Recent upgrades to the mini-DOAS computer enable collection of more spectra, while the inclusion of an ARINC board allows a tighter live alignment of the telescopes to the horizon. This reduces pointing error, one of the larger sources of systematic error in the scaling retrieval. Improvements to the DOAS retrieval, such as parameterizing the Instrumental Spectral Response Function (ISRF) as a super Gaussian, or including Taylor terms in the DOAS retrievals may also reduce fit errors in future missions.

The findings of this thesis urge further investigation of the presence and formation mechanism(s) of HONO in the troposphere. These airborne observations of excess HONO in the upper troposphere urgently require corroborating studies in the laboratory and field. For an improved understanding of excess HONO in the lower troposphere, instruments which provide a more complete picture of the aerosol chemical composition and pH would behoove any further analysis. Indeed, it is likely that HONO is formed via multiple mechanisms, depending on the chemical composition of the air mass.

Future missions of the HALO aircraft which investigate troposphere photochemistry should include measurements of HONO, since it is central to understand the HO_x budget and the oxidation capacity of the troposphere. Within the present thesis the HONO budget could not be closed, therefore further study would require simultaneous airborne measurements of all species relevant to potential HONO formation mechanisms, in particular OH, NO, NO_2, HNO_3, HO_2 and HOONO, as well as relevant aerosol parameters (e.g. chemical composition, pH, water content). Otherwise, the remote sensing observations of NO_2 and HCHO by the mini-DOAS instrument can complement studies of the atmosphere's oxidation capacity, as well as investigations of the NO_x- or VOC-limited nature of ozone production.

Appendix A

Sample DOAS Retrievals in the Visible Wavelength Range

In addition to the exemplary DOAS retrievals from the UV wavelength range shown in chapter 3, this appendix includes exemplary DOAS retrievals of O_3, O_4, and NO_2 from the visible wavelength range.

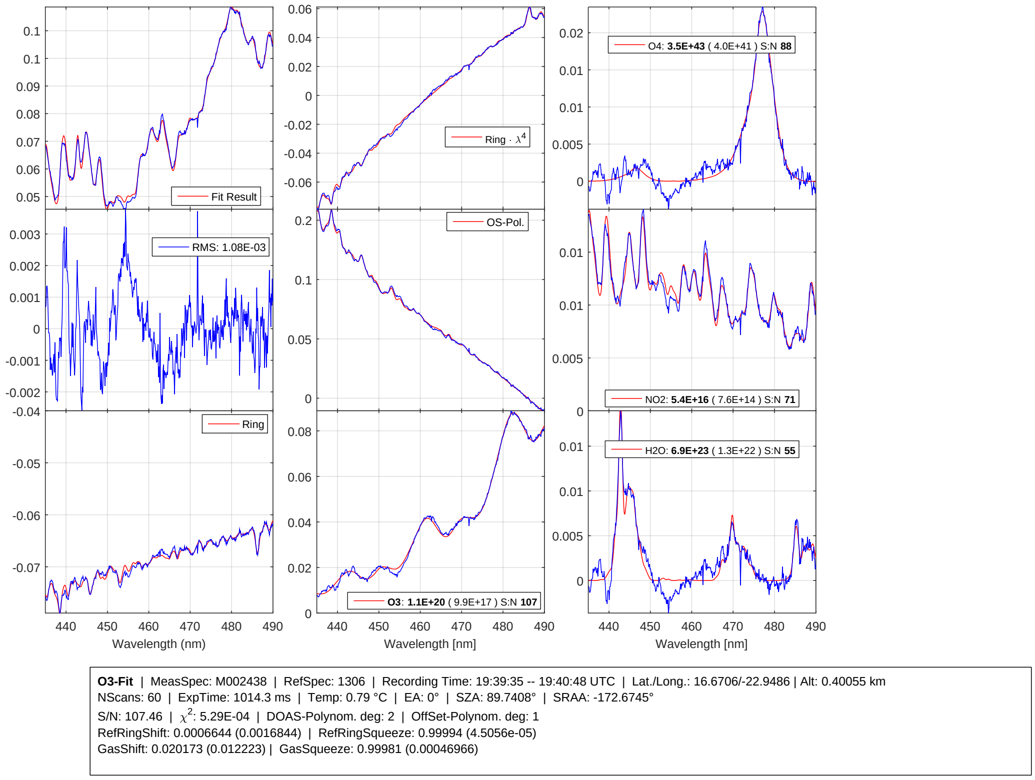

O3-Fit | MeasSpec: M002438 | RefSpec: 1306 | Recording Time: 19:39:35 -- 19:40:48 UTC | Lat./Long.: 16.6706/-22.9486 | Alt: 0.40055 km
NScans: 60 | ExpTime: 1014.3 ms | Temp: 0.79 °C | EA: 0° | SZA: 89.7408° | SRAA: -172.6745°
S/N: 107.46 | χ^2: 5.29E-04 | DOAS-Polynom. deg: 2 | OffSet-Polynom. deg: 1
RefRingShift: 0.0006644 (0.0016844) | RefRingSqueeze: 0.99994 (4.5056e-05)
GasShift: 0.020173 (0.012223) | GasSqueeze: 0.99981 (0.00046966)

Figure A.1: An exemplary O_3 spectral retrieval in the visible wavelength range. From top to bottom, left to right, the panels show: the optical depth τ in blue with the fit result overlaid in red, the fit residual with the RMS in the legend, the fitted parameters for the Ring effect, the wavelength dependent Ring effect, the offset polynomial, and the included absorbing trace gas species. For each absorbing trace gas the legend contains the retrieved SCD, the associated error, and the consequent signal to noise ratio. The text box lists associated information such as the spectrum number, reference spectrum number, integration time, latitude, longitude, altitude, number of scans, exposure time, detector temperature, elevation angle, solar zenith angle, solar relative azimuth angle, signal to noise ratio, cost parameter, DOAS polynomial order, offset polynomial order, ring shift and squeeze, and gas shift and squeeze.

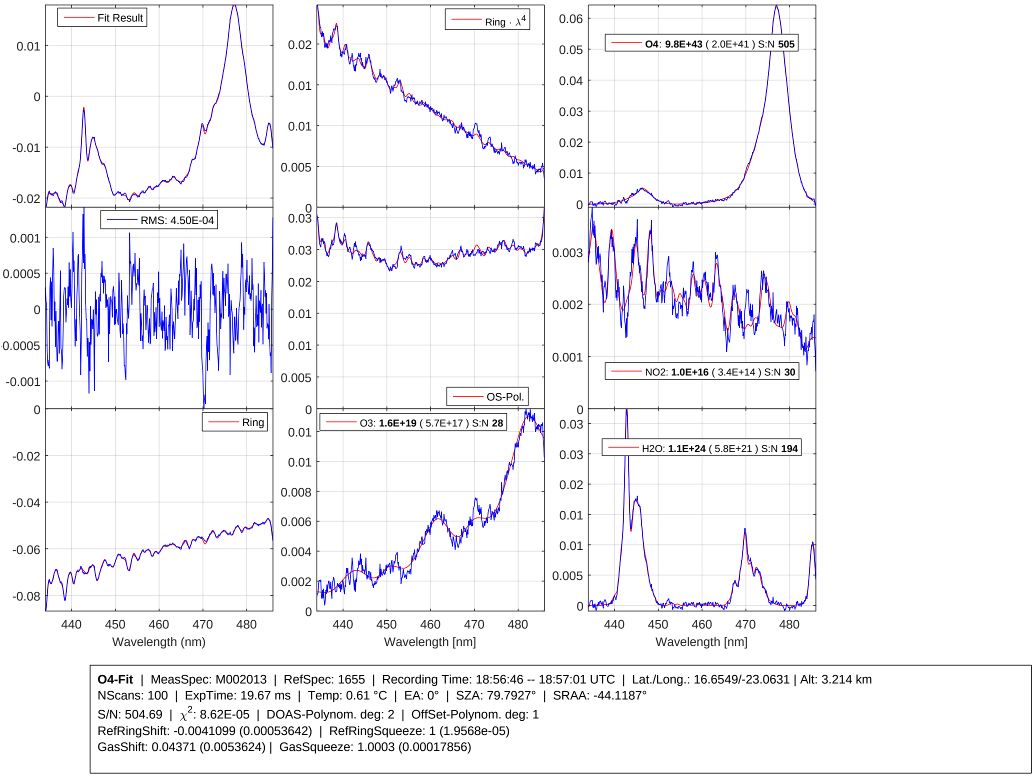

O4-Fit | MeasSpec: M002013 | RefSpec: 1655 | Recording Time: 18:56:46 -- 18:57:01 UTC | Lat./Long.: 16.6549/-23.0631 | Alt: 3.214 km
NScans: 100 | ExpTime: 19.67 ms | Temp: 0.61 °C | EA: 0° | SZA: 79.7927° | SRAA: -44.1187°
S/N: 504.69 | χ^2: 8.62E-05 | DOAS-Polynom. deg: 2 | OffSet-Polynom. deg: 1
RefRingShift: -0.0041099 (0.00053642) | RefRingSqueeze: 1 (1.9568e-05)
GasShift: 0.04371 (0.0053624) | GasSqueeze: 1.0003 (0.00017856)

Figure A.2: An exemplary O_4 spectral retrieval in the visible wavelength range. The panels are as described in figure A.1.

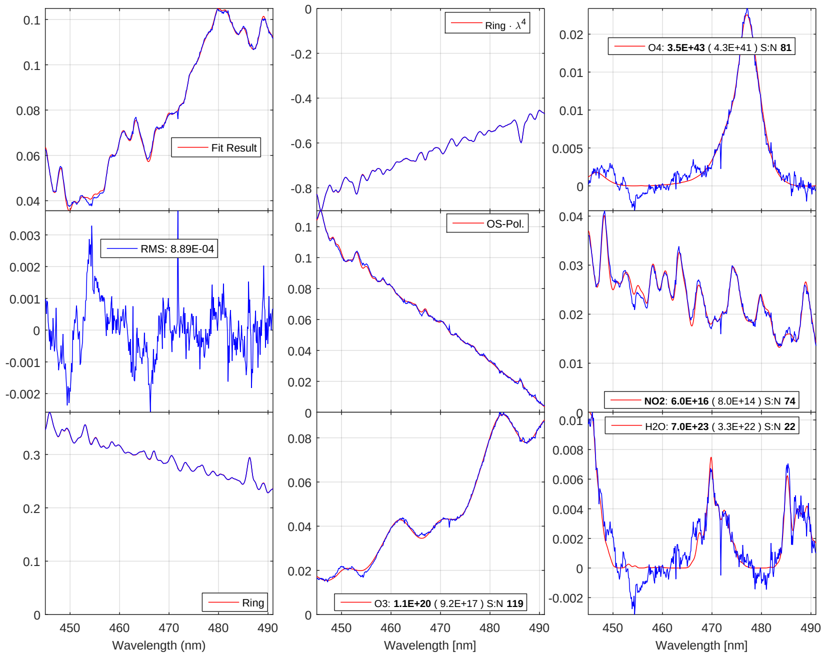

NO2-Fit | MeasSpec: M002438 | RefSpec: 1306 | Recording Time: 19:39:35 -- 19:40:48 UTC | Lat./Long.: 16.6706/-22.9486 | Alt: 0.40055 km
NScans: 60 | ExpTime: 1014.3 ms | Temp: 0.79 °C | EA: 0° | SZA: 89.7408° | SRAA: -172.6745°
S/N: 74.46 | χ^2: 3.02E-04 | DOAS-Polynom. deg: 2 | OffSet-Polynom. deg: 1
RefRingShift: -0.0048579 (0.0018323) | RefRingSqueeze: 1.0001 (5.5143e-05)
GasShift: -0.071287 (0.013054) | GasSqueeze: 1.0026 (0.0005301)

Figure A.3: An exemplary NO_2 spectral retrieval in the visible wavelength range. The panels are as described in figure A.1.

Appendix B

UV/visible & O_3/O_4 Scaling Comparisons

Discrepancies between UV and visible retrievals, or between retrievals scaled with O_3 or O_4 have several possible causes. Differences between retrievals from different spectral intervals may arise from incoherent sampling of the spectrometers, as well as from different temporal and spatial averaging of the spectra. Heterogeneity in local gas concentrations, combined with different averaging volumes (kernels) between the UV and visible spectra may also cause differences. The latter may become smaller with increasing distance from sources of the pollutants and with altitude. The discrepancies between O_3 and O_4 scaling for NO_2, HCHO, and HONO may arise at high altitudes due to intrusions of stratospheric air. See subsections 3.3.4 and 3.3.5.

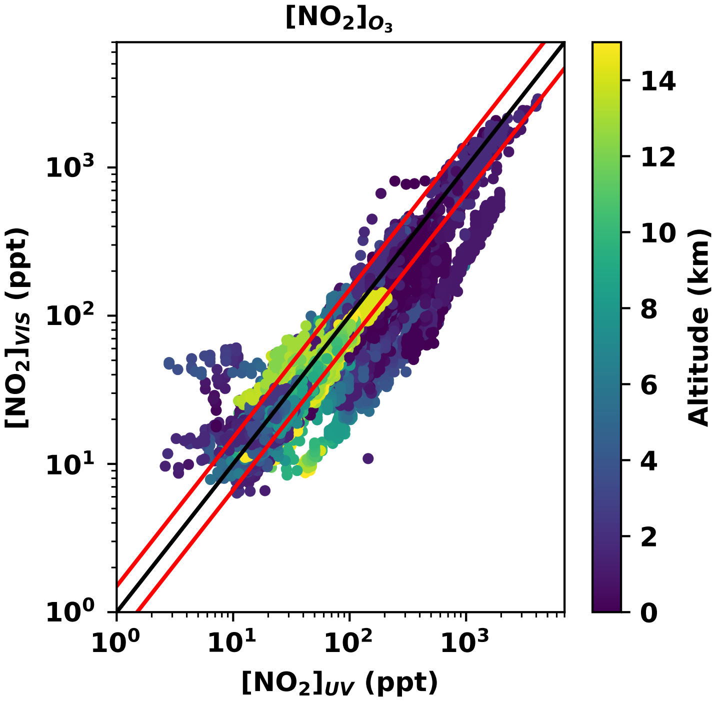

Figure B.1: The NO_2 VMRs (ppt) as retrieved in the visible wavelength range plotted against those from the UV (using O_3 as a scaling gas), for all 25 analyzed flights of the EMeRGe and CAFE-Africa missions, colored by altitude. Note the logarithmic axes. The black lines are 1:1 lines, the red lines are ±50 %.

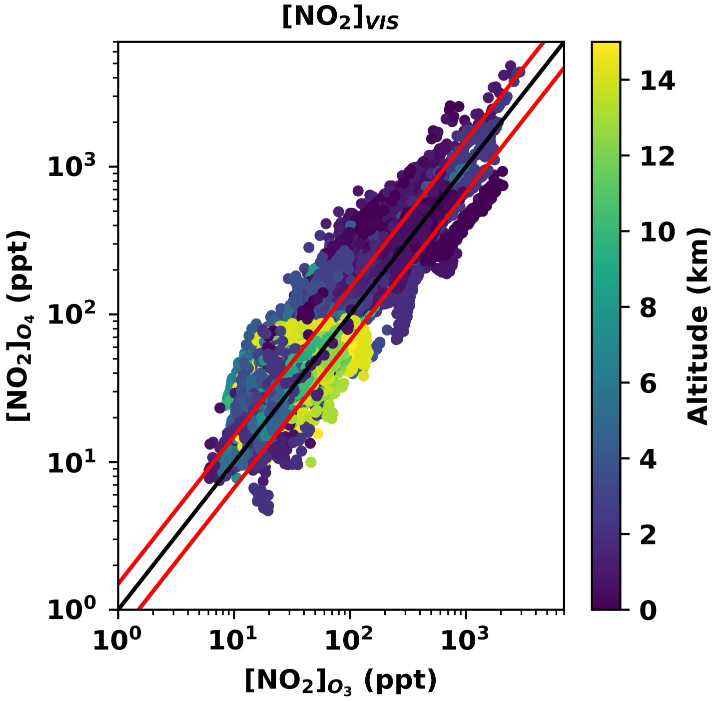

Figure B.2: The NO_2 VMRs (ppt) retrieved using O_4 as a scaling gas plotted against those retrieved using O_3 as a scaling gas, all in the visible wavelength range, for all 25 flights of the EMeRGe and CAFE-Africa missions, colored by altitude. Note the logarithmic axes. The black lines are 1:1 lines, the red lines are ±50 %.

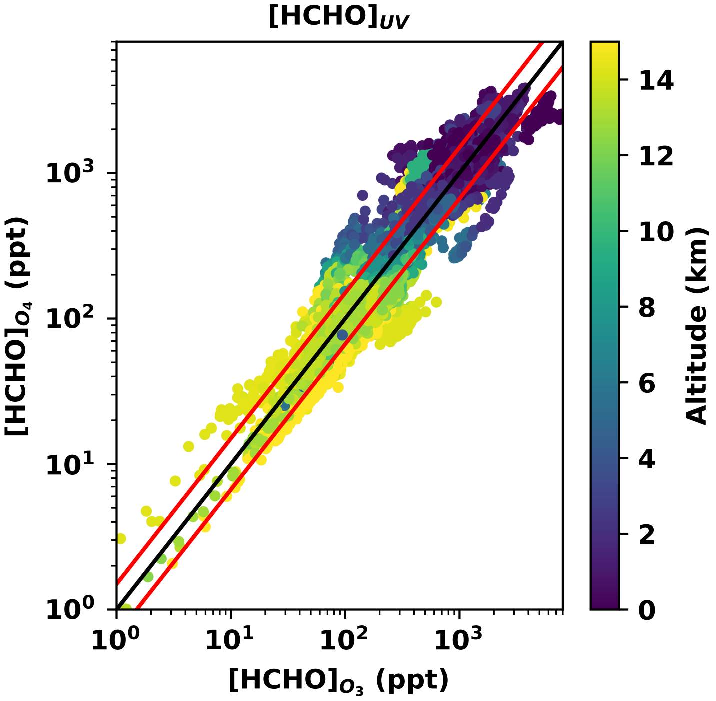

Figure B.3: The HCHO VMRs (ppt) retrieved using O_4 as a scaling gas plotted against those retrieved using O_3 as a scaling gas, all in the UV wavelength range, for all 25 flights of the EMeRGe and CAFE-Africa missions, colored by altitude. Note the logarithmic axes. The black lines are 1:1 lines, the red lines are ±50 %.

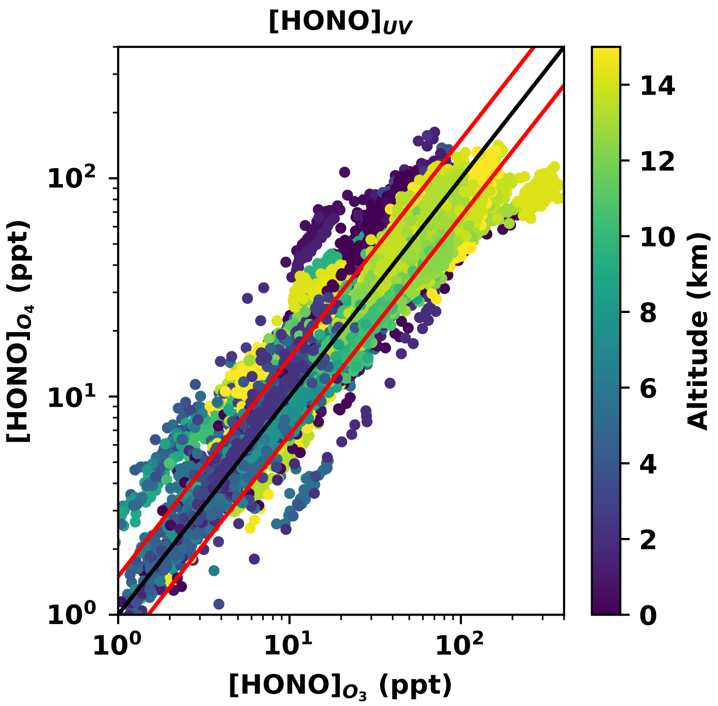

Figure B.4: The HONO VMRs (ppt) retrieved using O_4 as a scaling gas plotted against those retrieved using O_3 as a scaling gas, all in the UV wavelength range, for all 25 flights of the EMeRGe and CAFE-Africa missions, colored by altitude. Note the logarithmic axes. The black lines are 1:1 lines, the red lines are ±50 %.

Appendix C

Sub-Micron Aerosol Composition

To better understand the character of the atmospheric aerosol within the observed air masses, the chemical composition of the sub-micron aerosol as measured by the C-ToF-AMS instrument is shown in figures C.1, C.2 and C.3.

During the EMeRGe-EU mission, the inorganic aerosol is typically composed of some combination of ammonium nitrate (NH_4NO_3) and ammonium sulfate ($(NH_4)_2SO_4$), whereby ammonium makes up $\approx 25\%$ of the inorganic aerosol by weight in most cases. Deviation from the stoichiometric line between the two salts is associated with an increased organic fraction of the aerosol by weight. Moreover, more ammonium is present in the aerosol than the salt mass balance would suggest. There may be anions (e.g. chlorine) in the aerosol which are not measured by the C-ToF-AMS instrument.

By contrast, during the EMeRGe-Asia phase the aerosol is more inorganic, while there is more sulfate (characterizing haze events) associated with the organic aerosol. According to Becker et al. [1998], the presence of ammonium sulfate should drive HONO formed in the aerosol into the gas phase. The composition also suggests the presence of ammonium bisulfate (NH_4HSO_4).

During the CAFE-Africa mission, the observed aerosol is generally more organic by comparison, and does not fall neatly onto the stiochiometric line between ammonium nitrate and ammonium sulfate salts. The aerosol composition is very scattered; there are also organic nitrate aerosols.

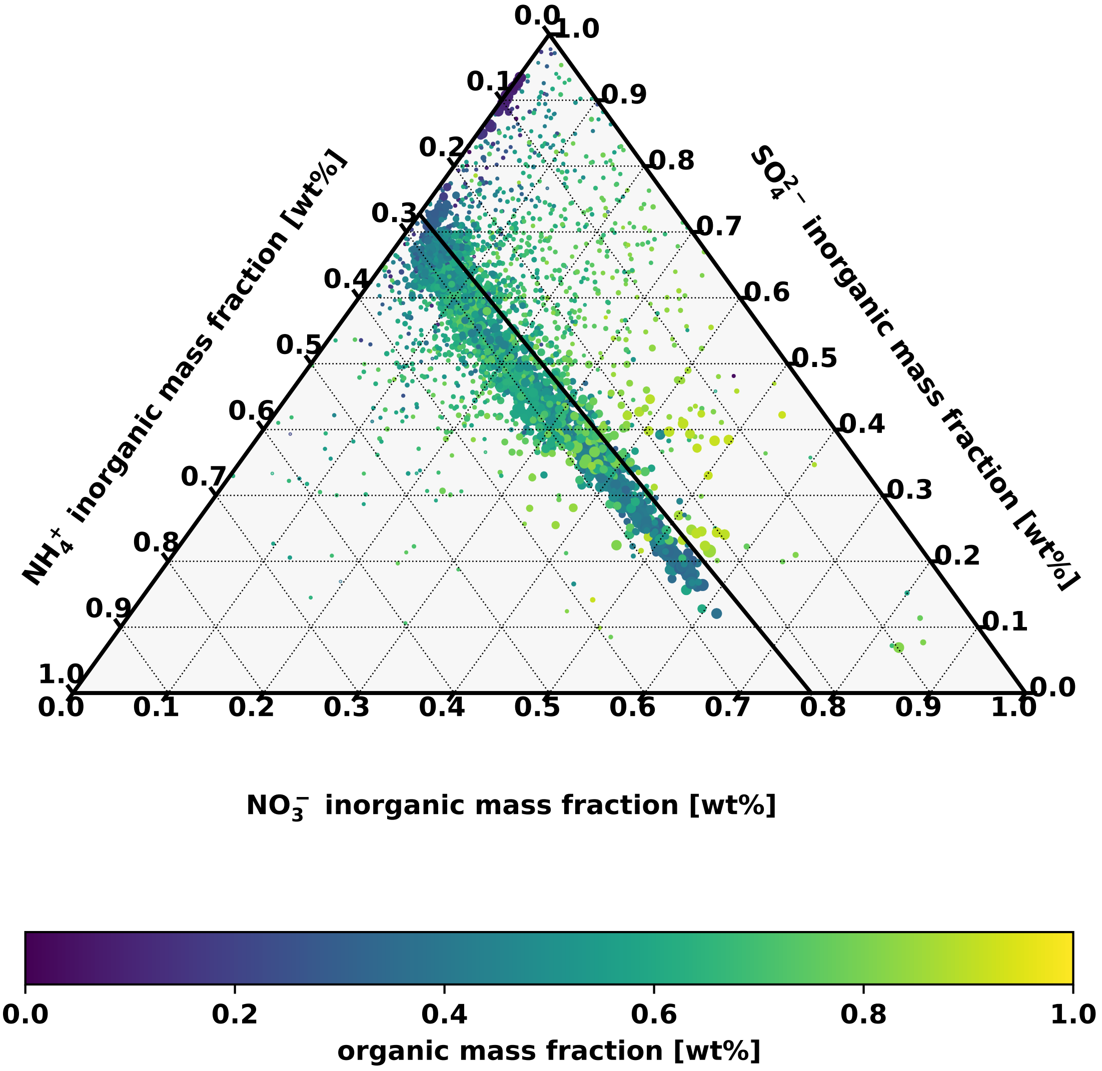

Figure C.1: A ternary plot of the sub-micron inorganic aerosol chemical composition during the EMeRGe-EU mission as measured by the C-ToF-AMS instrument. Note the stoichiometric line between ammonium sulfate and ammonium nitrate. The color scale indicates the organic mass fraction, while the marker size is indicative of the aerosol mass.

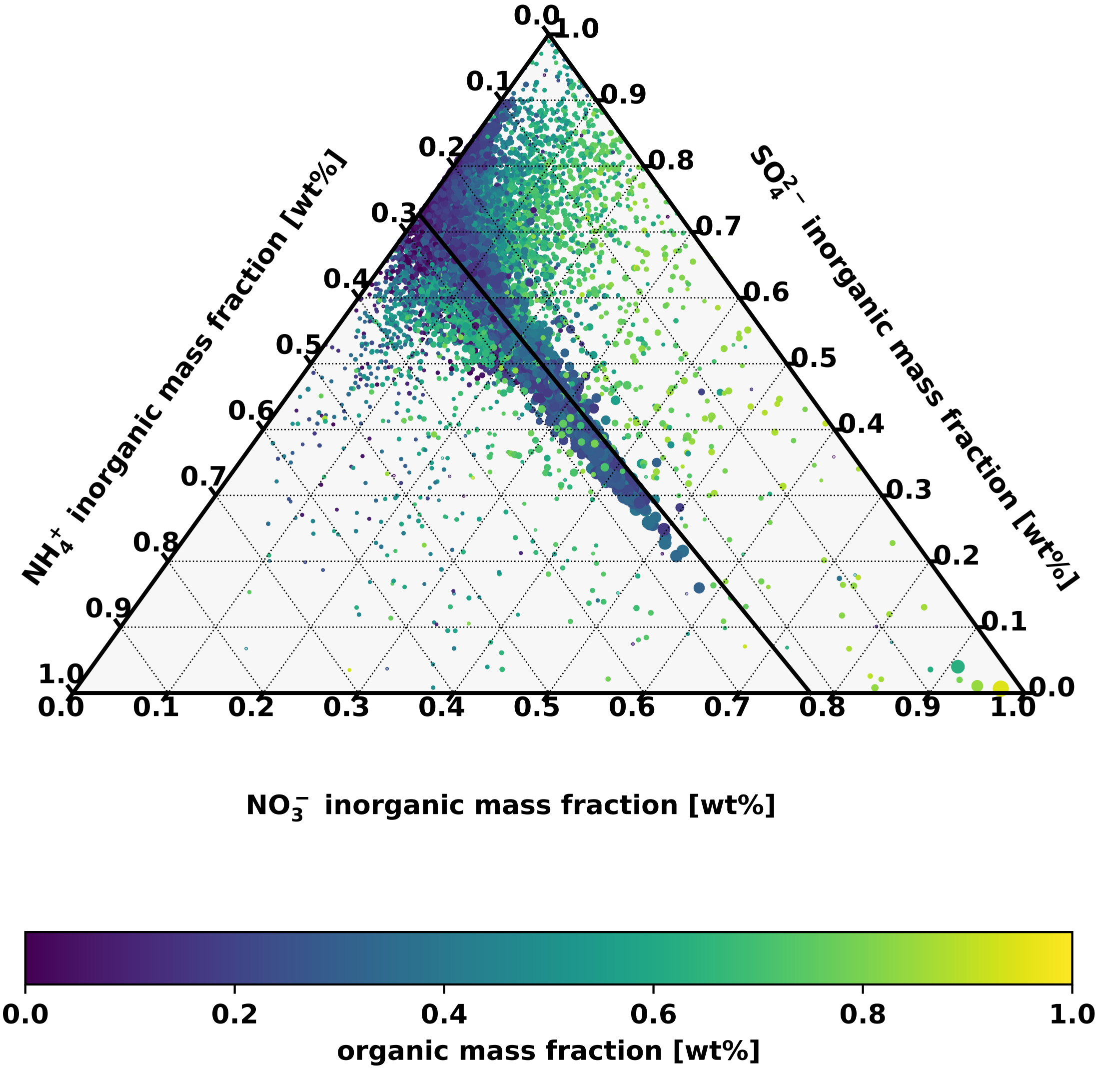

Figure C.2: A ternary plot of the sub-micron inorganic aerosol chemical composition during the EMeRGe-Asia mission as measured by the C-ToF-AMS instrument. Note the stoichiometric line between ammonium sulfate and ammonium nitrate. The color scale indicates the organic mass fraction, while the marker size is indicative of the aerosol mass.

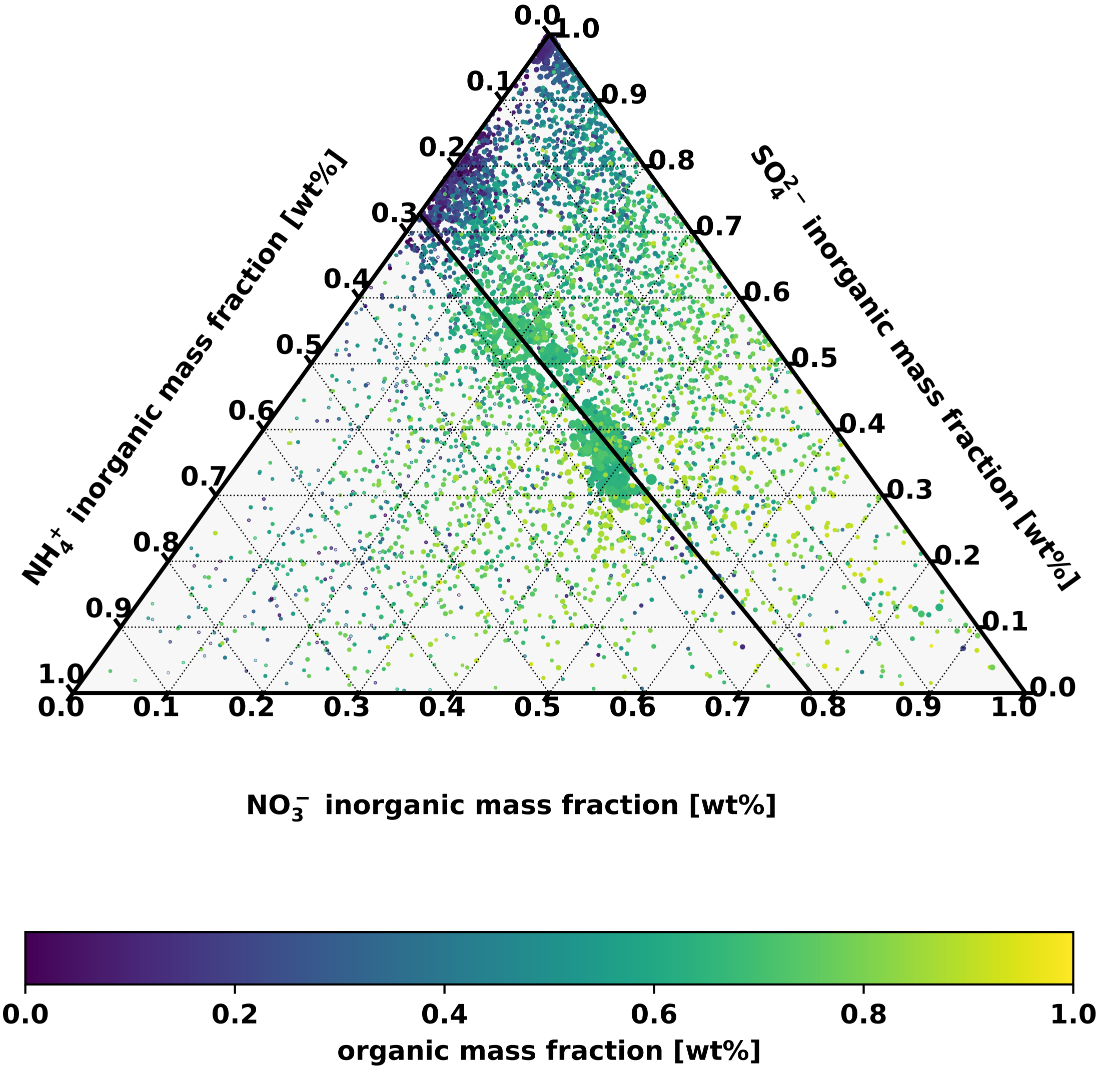

Figure C.3: A ternary plot of the sub-micron inorganic aerosol chemical composition during the CAFE-Africa mission as measured by the C-ToF-AMS instrument. Note the stoichiometric line between ammonium sulfate and ammonium nitrate. The color scale indicates the organic mass fraction, while the marker size is indicative of the aerosol mass.

Appendix D

Research Mission Overview Tables

This appendix details the instrumentation and parameters of the flights of the EMeRGe and CAFE-Africa missions. Table D.1 lists the instruments installed on board the HALO aircraft for each mission. Table D.2 enumerates the flights of the EMeRGe mission while table D.3 enumerates the flights of the CAFE-Africa mission.

Table D.1: The instrument payload on board the HALO aircraft during the EMeRGe and CAFE-Africa missions and the species/parameters they measured.

Species/quantity	EMeRGe	CAFE-Africa
A (km), T (K), P (mbar), RH (%), $[H_2O]$	BAHAMAS	BAHAMAS
J (s^{-1})	HALO-SR-A	HALO-SR-A
SA_{fine},SA_{coarse}, V_{fine}, V_{coarse}	SKY-OPC	SKY-OPC
$[NO_3{}^-]$, $[SO_4{}^{2-}]$, $[NH_4{}^+]$, [ORG]	C-ToF-AMS	C-ToF-AMS
$[BC_m]$, $[BC_n]$	SP2	SP2
$[O_3]$	AMTEX/FAIRO	FAIRO
[NO]	AENEAS	NOAH
$[NO_y]$	AENEAS	
$[HNO_3]$		CIMS
[OH]		HORUS
$[HO_2]$		HORUS
$[RO_2{}^*]$	PeRCEAS	
[HCHO], benzene	HKMS	
acetonitrile	HKMS	MMS
$[SO_2]$	CIMS	

Table D.2: The flight number, date, time (Coordinated Universal Time (UTC)), and targets of the flights of the EMeRGe mission's two phases.

Flight	Date	Start Time (UTC)	Stop Time (UTC)	Target(s)
3	11.07.2017	10:00	16:34	Italy
4	13.07.2017	10:40	15:03	Intercomparison
5	17.07.2017	10:28	18:27	English Channel
6	20.07.2017	09:00	17:29	Italy
7	24.07.2017	09:43	18:18	France
8	26.07.2017	07:47	15:19	English Channel
9	28.07.2017	09:55	18:30	France
1	10.03.2018	07:38	15:33	Transfer
3	12.03.2018	04:51	11:20	Transfer
4	17.03.2018	01:09	09:45	China Sea
5	19.03.2018	00:19	08:24	China Sea
6	20.03.2018	23:48*	06:37	Philippines
7	22.03.2018	03:48	09:31	Taiwan
8	24.03.2018	01:01	09:52	Korea
9	26.03.2018	00:24	09:26	Korea
10	28.03.2018	23:53*	08:33	Philippines
11	30.03.2018	00:03	09:26	Japan
12	03.04.2018	00:25	06:26	Taiwan
13	04.04.2018	00:27	09:25	Japan
14	07.04.2018	01:03	08:42	Transfer
16	09.04.2018	06:01	14:44	Transfer

Table D.3: The flight number, date, time, and features of each flight of the CAFE-Africa mission.

Flight	Date	Start Time (UTC)	Stop Time (UTC)	Feature(s)
3	07.08.2018	08:29	14:50	Transfer
4	10.08.2018	10:02	19:36	BB Fresh
5	12.08.2018	10:06	19:04	BB Aged
6	15.08.2018	10:11	19:00	Dust Layer
7	17.08.2018	10:18	19:17	Stack 1
8	19.08.2018	03:59	13:13	Stack 2
9	22.08.2018	09:42	12:52	Ghana
10	24.08.2018	09:52	18:41	Euro Africa
11	26.08.2018	15:56	01:40*	Stack 3
12	29.08.2018	10:00	19:05	Biomass
13	31.08.2018	09:57	19:34	ITCZ
14	02.09.2018	10:34	19:42	Storm Chaser
15	04.09.2018	09:58	19:07	ITCZ 2
16	07.09.2018	09:55	16:23	Transfer

Appendix E

VOC- or NO_x-Limited O_3 Production

Using the HCHO and NO_2 retrieved in the UV wavelength range with O_4 scaling, together with NO measured by the AENEAS instrument during the EMeRGe mission and the NOAH instrument during the CAFE-Africa mission, the photochemistry of the observed air masses can be characterized according to whether the ozone production therein is VOC- or NO_x-limited (see section 2.3).

In figure E.1, most of the air masses observed during the EMeRGe mission fall onto the 4:1 line, with exceptions to the trend indicating fresh NO_x emissions. While in the air masses observed during the CAFE-Africa mission, much lower VMRs of either species are observed, they can still be characterized as either NO_x- or VOC-limited. Here, again, the ratio is clearly altitude dependent, with NO_x-limited ozone production at lower altitudes and VOC-limited ozone production in the upper troposphere. Across the EMeRGe-Asia and CAFE-Africa missions, the ozone production in air masses at high altitudes is exclusively VOC-limited, in agreement with the more detailed study by Nussbaumer et al. [2023].

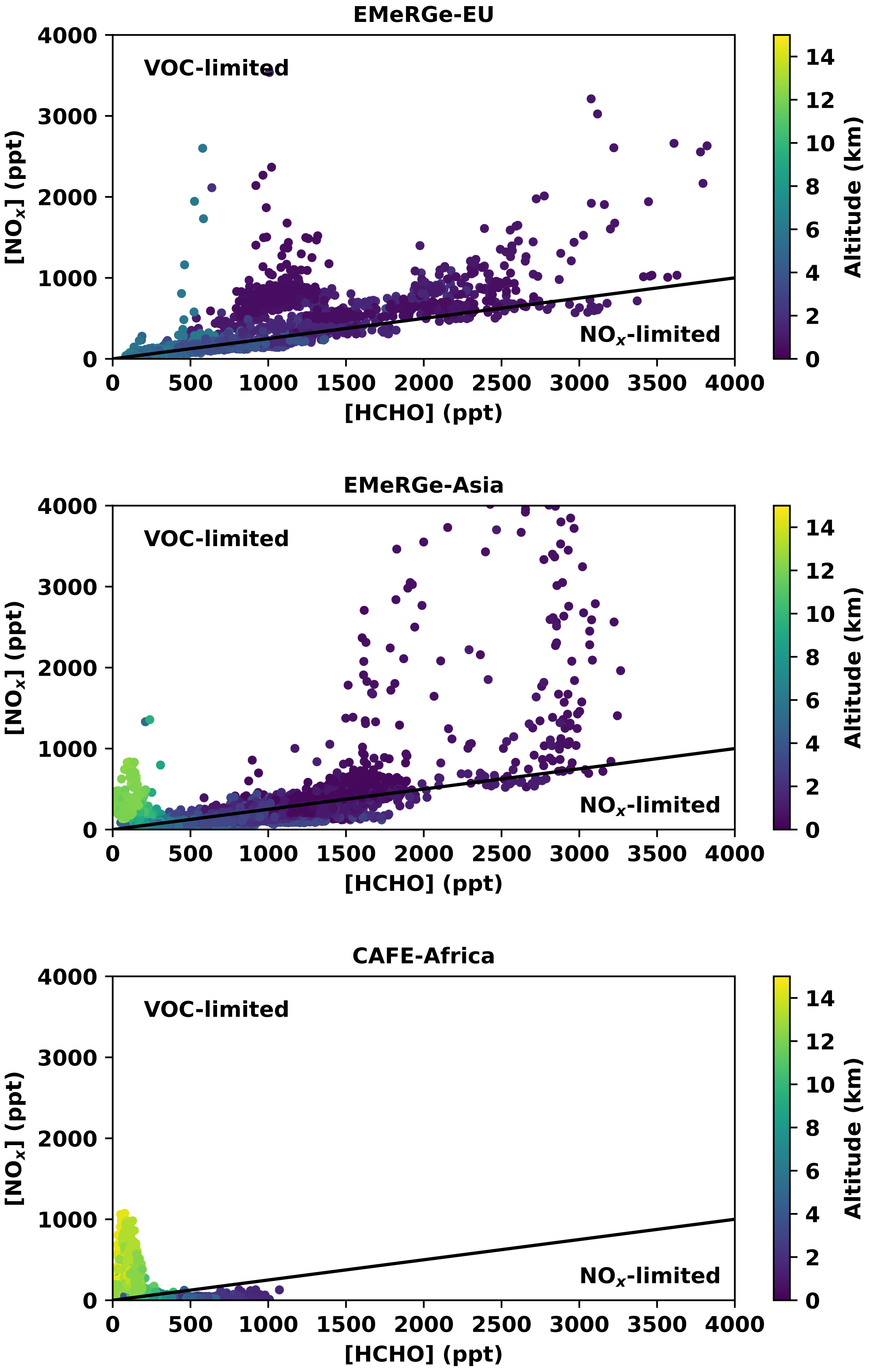

Figure E.1: Measured NO$_x$ VMRs (ppt) plotted against HCHO VMRs (ppt); the ratio characterizes whether the production of ozone in an observed air mass is NO$_x$- or VOC-limited (see figure 2.3). The black lines are 4:1 lines. The color scheme represents altitude.

Appendix F

A [VOC]/[NO_x] and Leighton Ratio Coordinate System

These two characterizations — the Leighton ratio (see section 2.2) and the [VOC]/[NO_x] ratio (see figure 2.3) — are combined into a single coordinate system. In figure F.1, the observed air masses are positioned on a grid, whereby the position on the x-axis reveals whether ozone production is VOC- or NO_x-limited (left or right respectively), and the position on the y-axis reveals whether the observed Leighton ratio Φ is above or below unity (see equation 2.52). During the EMeRGe-Asia mission, there is more scatter in the Leighton ratio Φ when the ozone production is NO_x-limited. During the CAFE-Africa mission, nearly all investigated air masses are below the unity line, indicating missing oxidants converting NO to NO_2. Especially at high altitudes during the CAFE-Africa mission, the Leighton relationships do not capture the photochemistry of nitrogen oxides in the troposphere. The ozone production in low altitude air masses is also NO_x-limited in this context, and only here is Φ above unity. During the flight near the recently formed tropical storm Florence, the Leighton ratio is significantly less than unity — by two orders of magnitude — indicating missing oxidants which convert NO to NO_2.

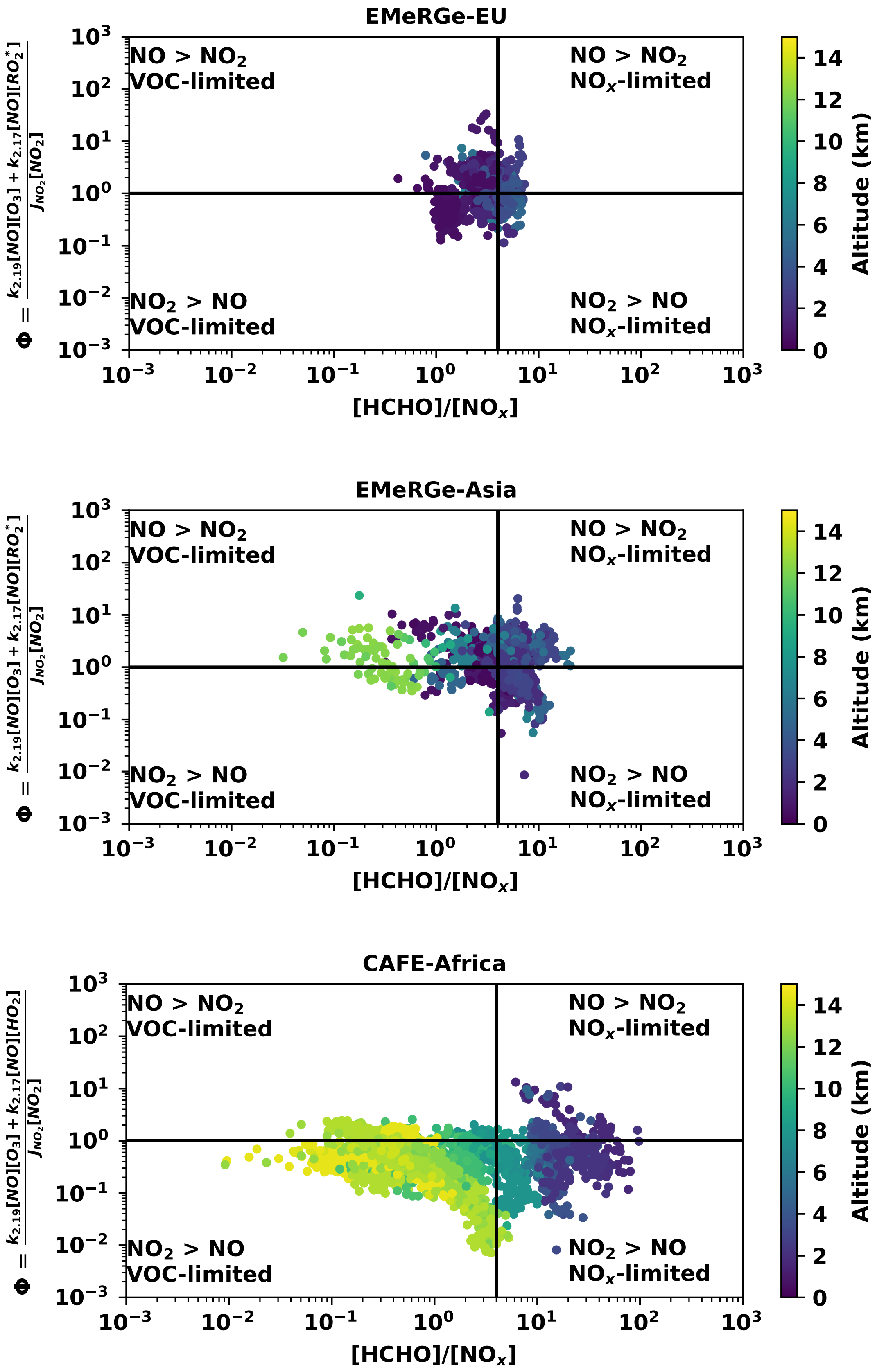

Figure F.1: The Leighton ratio Φ (see section 2.2, equation 2.52) plotted against the ratio [HCHO]/[NO$_x$] (which reveals the limiting factor in ozone production, see figure 2.3), colored by altitude. The black horizontal line represents unity. The black vertical line represents 4:1. Note the logarithmic axes.

Appendix G

Measured HONO as a Function of Measured Gas Phase and Aerosol Parameters and the Products Thereof, Sorted by Air Mass Tags

The Spearman correlation coefficient between the HONO observed by the mini-DOAS instrument and 1) various other trace gases and atmospheric parameters or 2) the product of the reactants of the various proposed heterogeneous HONO formation mechanisms depends on which air masses are included in the calculation. Here, the correlation analysis is performed on subsets of data, according to the air mass tags described in section 4.1.1.

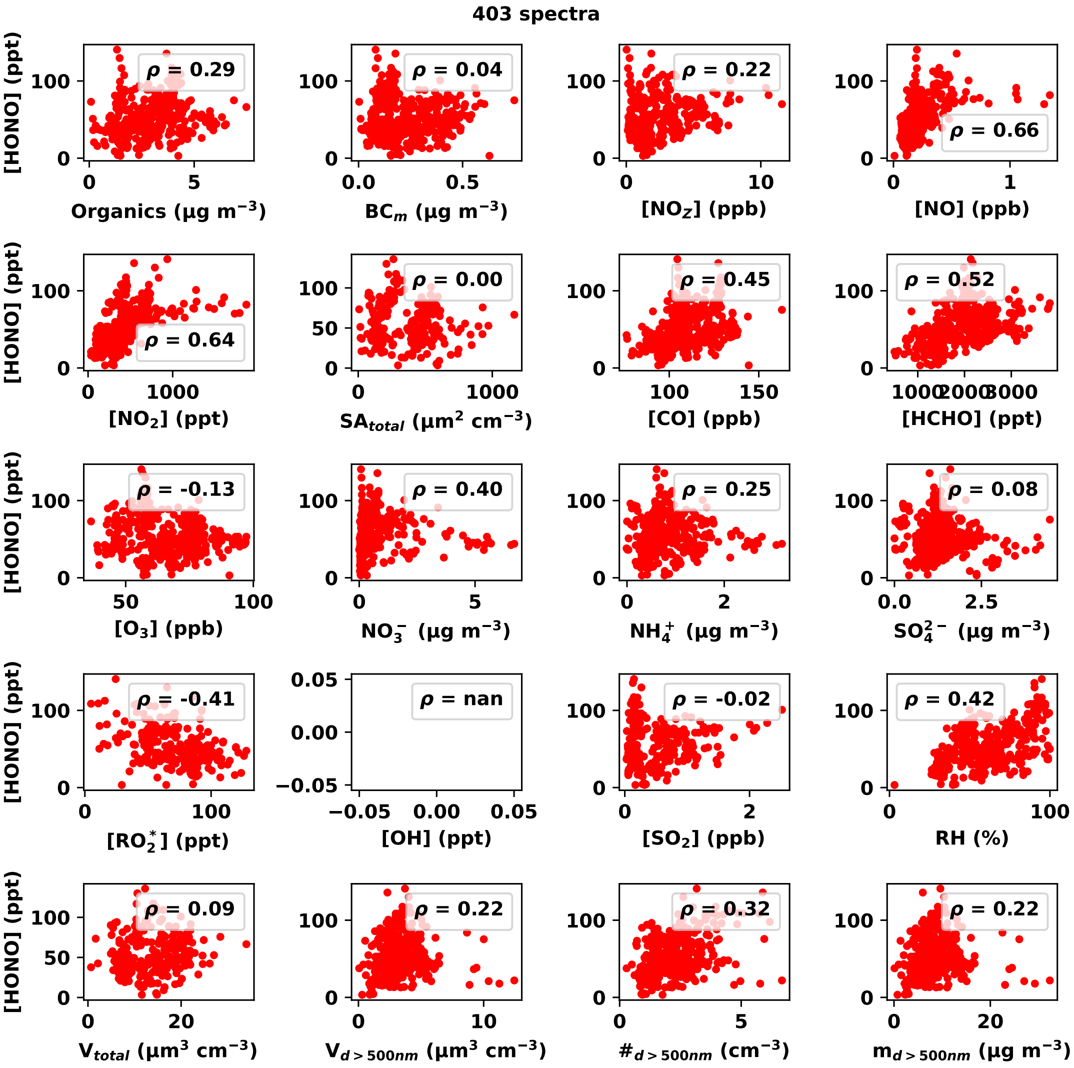

Figure G.1: In each panel the observed HONO VMRs are plotted against twenty other species and components simultaneously observed on board the HALO aircraft in the lower troposphere during the -EU phase of the EMeRGe mission. The legend is the Spearman correlation coefficient ρ. The coloration is representative of the air mass tags described in section 4.1.1. Red represents anthropogenic influence determined from measurements of benzene, green represents biomass burning influence detected via measurements of acetonitrile, blue represents otherwise presumably pristine air. Black represents missing air mass tag data. OH was not measured during the EMeRGe mission.

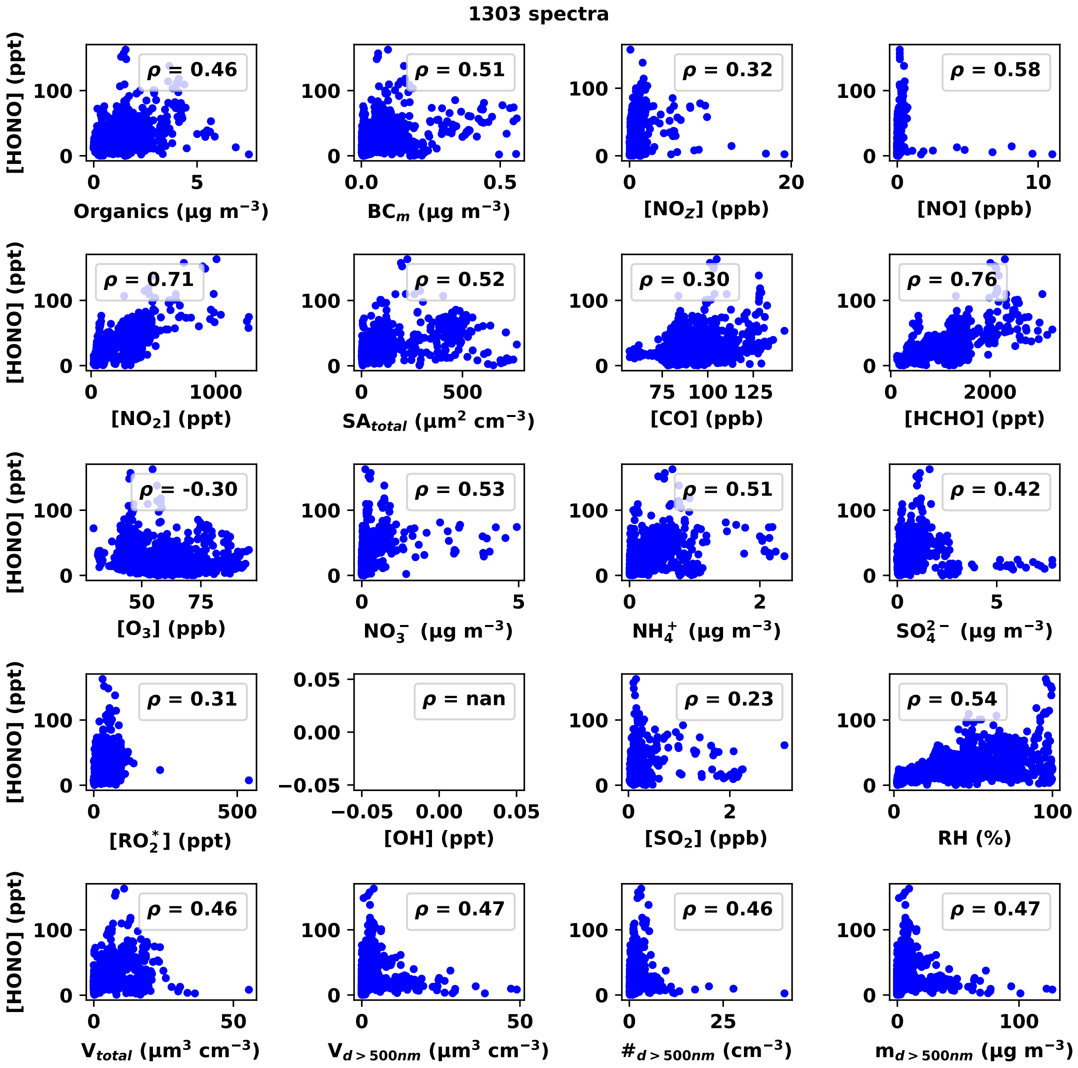

Figure G.2: In each panel the observed HONO VMRs are plotted against twenty other species and components simultaneously observed on board the HALO aircraft in the lower troposphere during the -EU phase of the EMeRGe mission. The legend is the Spearman correlation coefficient ρ. The coloration is representative of the air mass tags described in section 4.1.1. Red represents anthropogenic influence determined from measurements of benzene, green represents biomass burning influence detected via measurements of acetonitrile, blue represents otherwise presumably pristine air. Black represents missing air mass tag data. OH was not measured during the EMeRGe mission.

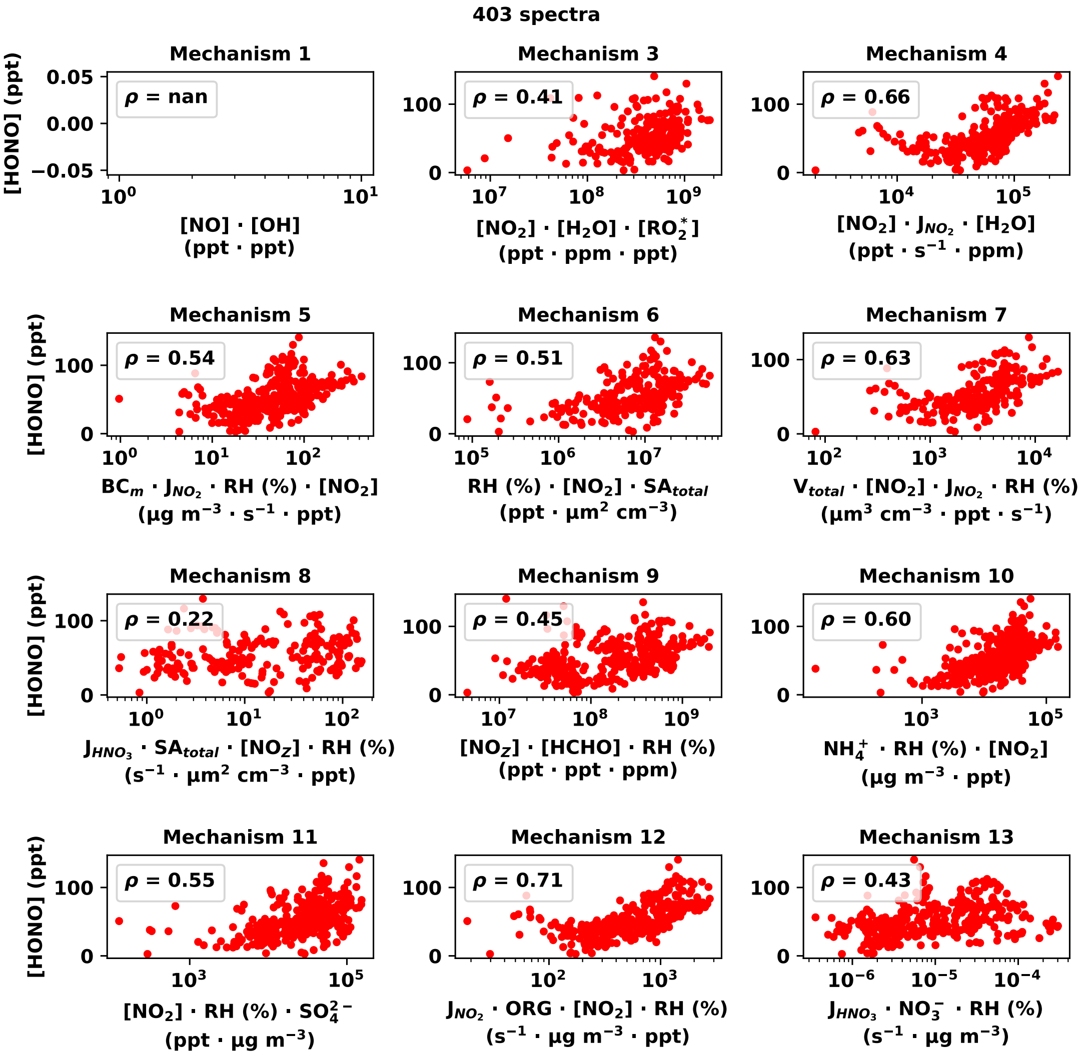

Figure G.3: For twelve of the thirteen potential formation mechanisms listed in table 2.1, the observed HONO VMRs plotted against the product of any measured reactants (or proxies thereof) from the lower troposphere during the -EU phase of the EMeRGe mission. In each panel, the legend is the Spearman correlation coefficient ρ. During the EMeRGe mission, no measurements or proxies for OH are available. Here, $RO_2{}^*$ acts as a proxy for HO_2, while NO_z ($NO_y - NO_x$) acts as a proxy for HNO_3. Data is colored by the tags described in section 4.1.1; red represents anthropogenic influence, green represents biomass burning influence, and the absence of either is indicated in blue and assumed to be otherwise pristine air. Missing tags are represented in black. Note the logarithmic x axes. Mechanism 2 is excluded because ortho-nitrophenols were not measured.

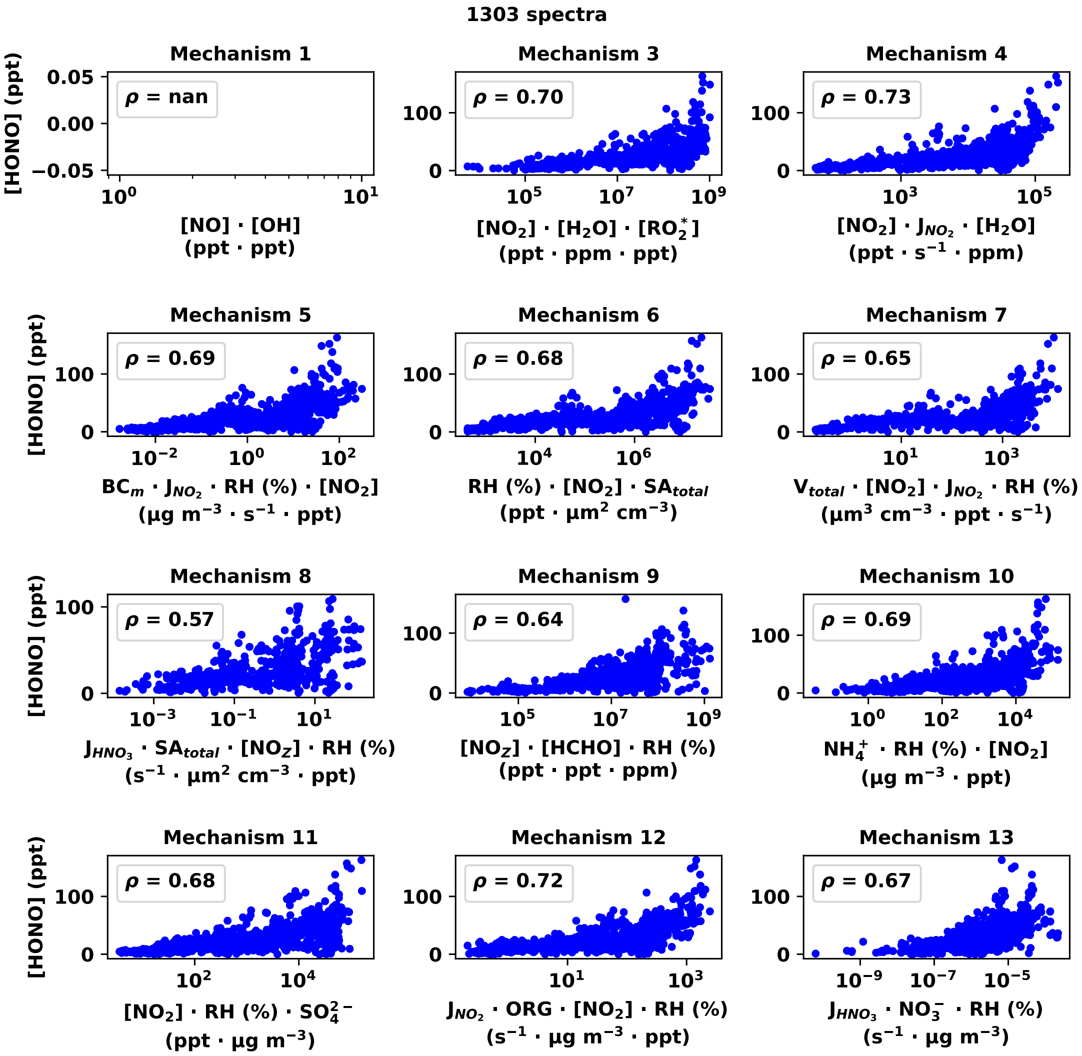

Figure G.4: For twelve of the thirteen potential formation mechanisms listed in table 2.1, the observed HONO VMRs plotted against the product of any measured reactants (or proxies thereof) from the lower troposphere during the -EU phase of the EMeRGe mission. In each panel, the legend is the Spearman correlation coefficient ρ. During the EMeRGe mission, no measurements or proxies for OH are available. Here, $RO_2{}^*$ acts as a proxy for HO_2, while NO_z ($NO_y - NO_x$) acts as a proxy for HNO_3. Data is colored by the tags described in section 4.1.1; red represents anthropogenic influence, green represents biomass burning influence, and the absence of either is indicated in blue and assumed to be otherwise pristine air. Missing tags are represented in black. Note the logarithmic x axes. Mechanism 2 is excluded because ortho-nitrophenols were not measured.

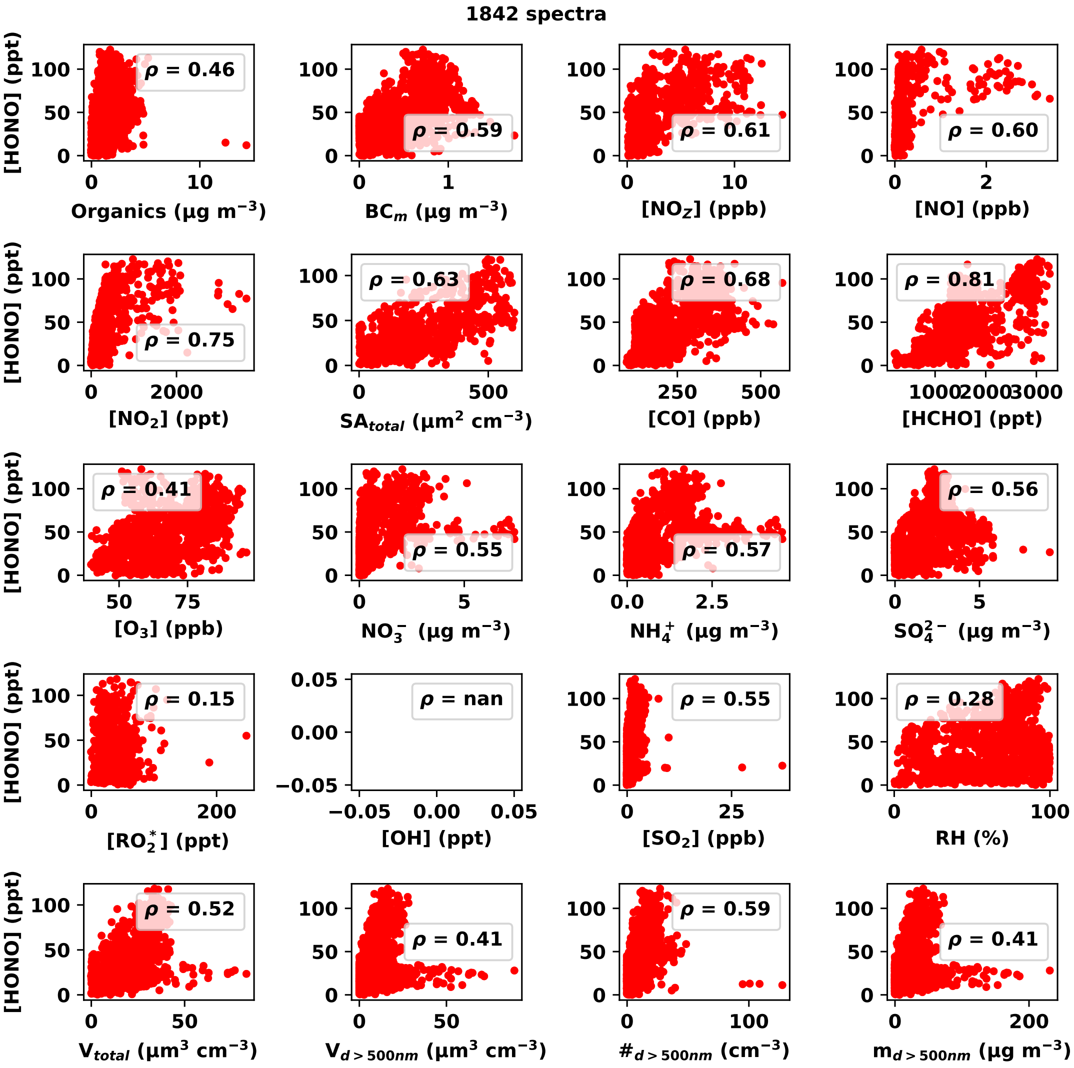

Figure G.5: In each panel the observed HONO VMRs are plotted against twenty other species and components simultaneously observed on board the HALO aircraft in the lower troposphere during the -Asia phase of the EMeRGe mission. The legend is the Spearman correlation coefficient ρ. The coloration is representative of the air mass tags described in section 4.1.1. Red represents anthropogenic influence determined from measurements of benzene, green represents biomass burning influence detected via measurements of acetonitrile, blue represents otherwise presumably pristine air. Black represents missing air mass tag data. OH was not measured during the EMeRGe mission.

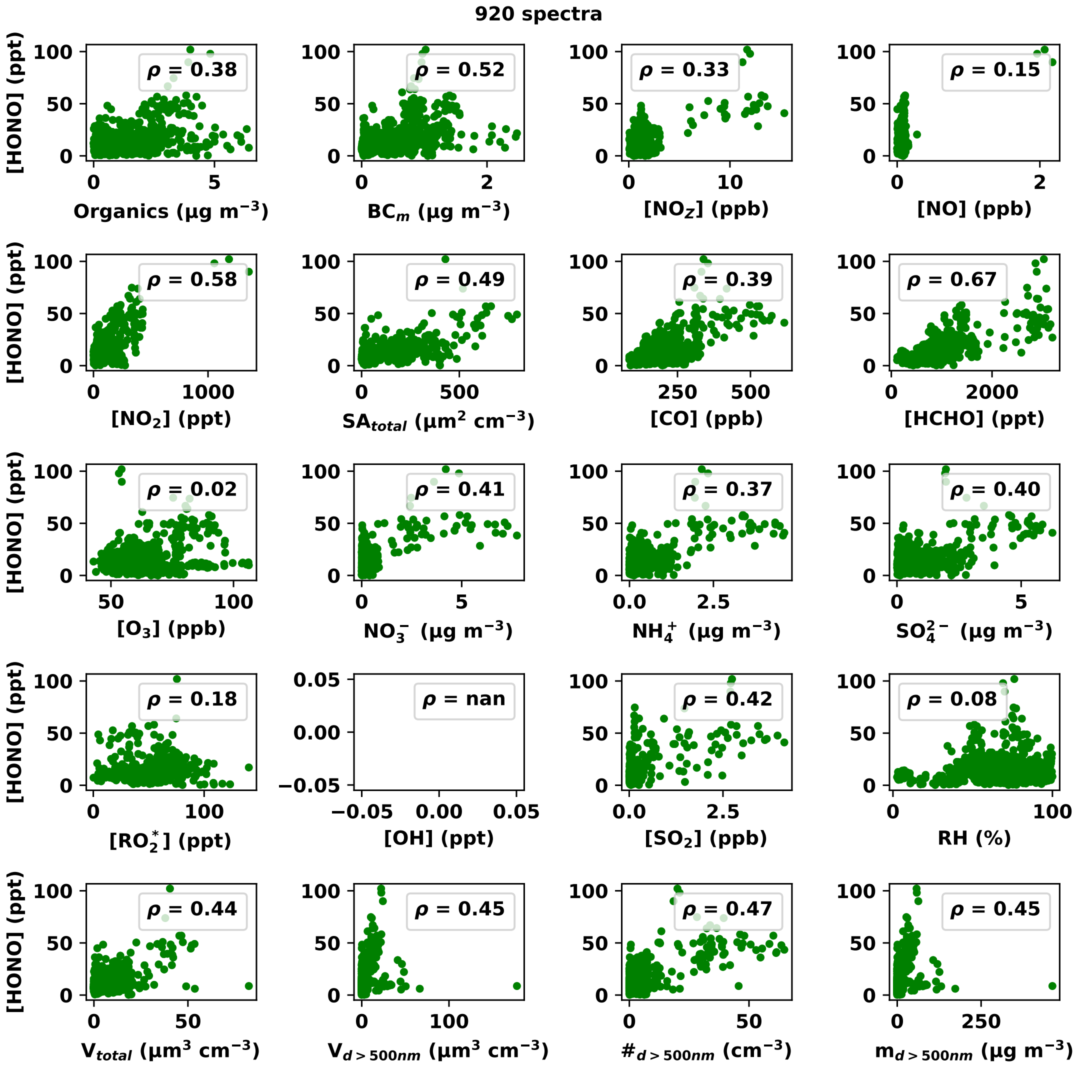

Figure G.6: In each panel the observed HONO VMRs are plotted against twenty other species and components simultaneously observed on board the HALO aircraft in the lower troposphere during the -Asia phase of the EMeRGe mission. The legend is the Spearman correlation coefficient ρ. The coloration is representative of the air mass tags described in section 4.1.1. Red represents anthropogenic influence determined from measurements of benzene, green represents biomass burning influence detected via measurements of acetonitrile, blue represents otherwise presumably pristine air. Black represents missing air mass tag data. OH was not measured during the EMeRGe mission.

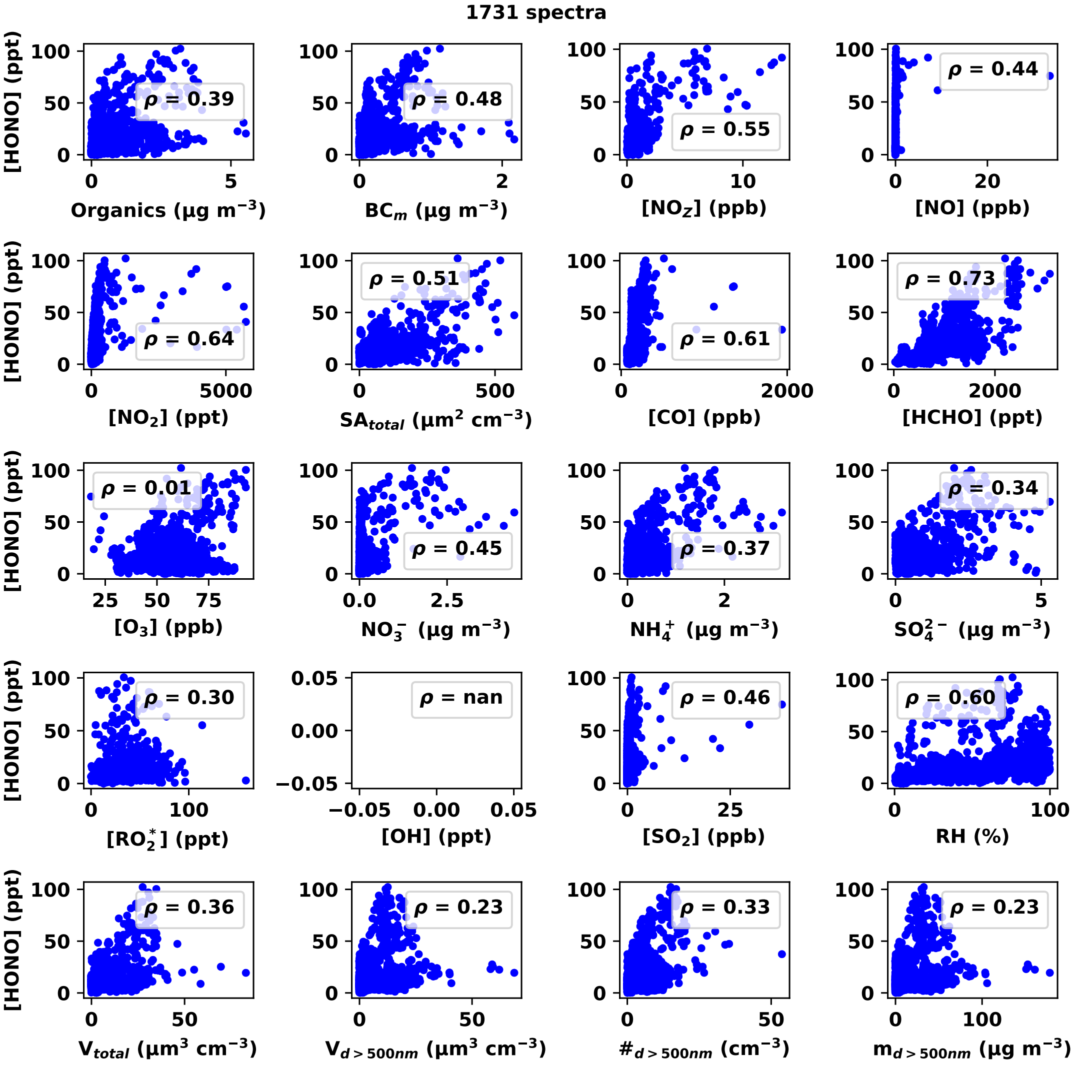

Figure G.7: In each panel the observed HONO VMRs are plotted against twenty other species and components simultaneously observed on board the HALO aircraft in the lower troposphere during the -Asia phase of the EMeRGe mission. The legend is the Spearman correlation coefficient ρ. The coloration is representative of the air mass tags described in section 4.1.1. Red represents anthropogenic influence determined from measurements of benzene, green represents biomass burning influence detected via measurements of acetonitrile, blue represents otherwise presumably pristine air. Black represents missing air mass tag data. OH was not measured during the EMeRGe mission.

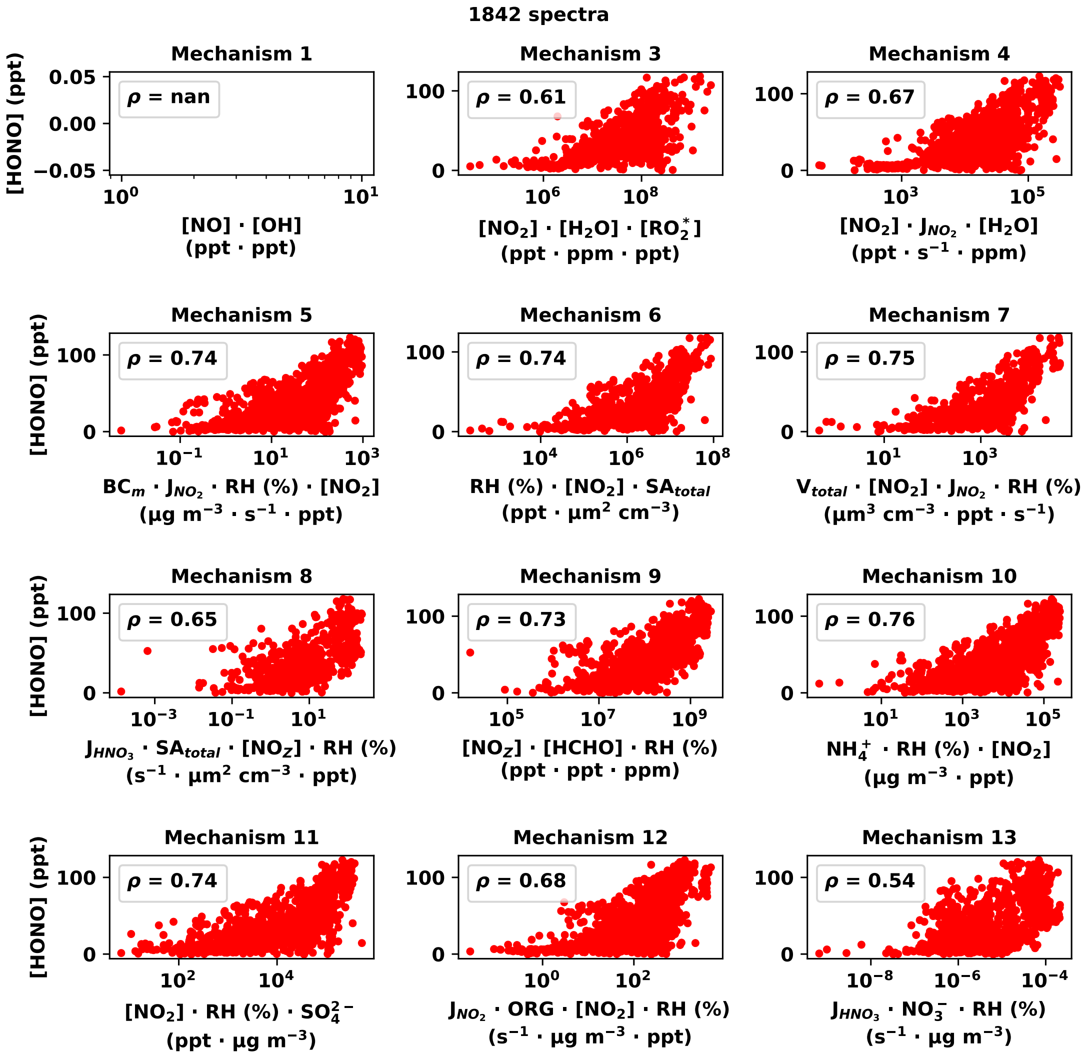

Figure G.8: For twelve of the thirteen potential formation mechanisms listed in table 2.1, the observed HONO VMRs plotted against the product of any measured reactants (or proxies thereof) from the lower troposphere during the -Asia phase of the EMeRGe mission. In each panel, the legend is the Spearman correlation coefficient ρ. During the EMeRGe mission, no measurements or proxies for OH are available. Here, $RO_2{}^*$ acts as a proxy for HO_2, while NO_z ($NO_y - NO_x$) acts as a proxy for HNO_3. Data is colored by the tags described in section 4.1.1; red represents anthropogenic influence, green represents biomass burning influence, and the absence of either is indicated in blue and assumed to be otherwise pristine air. Missing tags are represented in black. Note the logarithmic x axes. Mechanism 2 is excluded because ortho-nitrophenols were not measured.

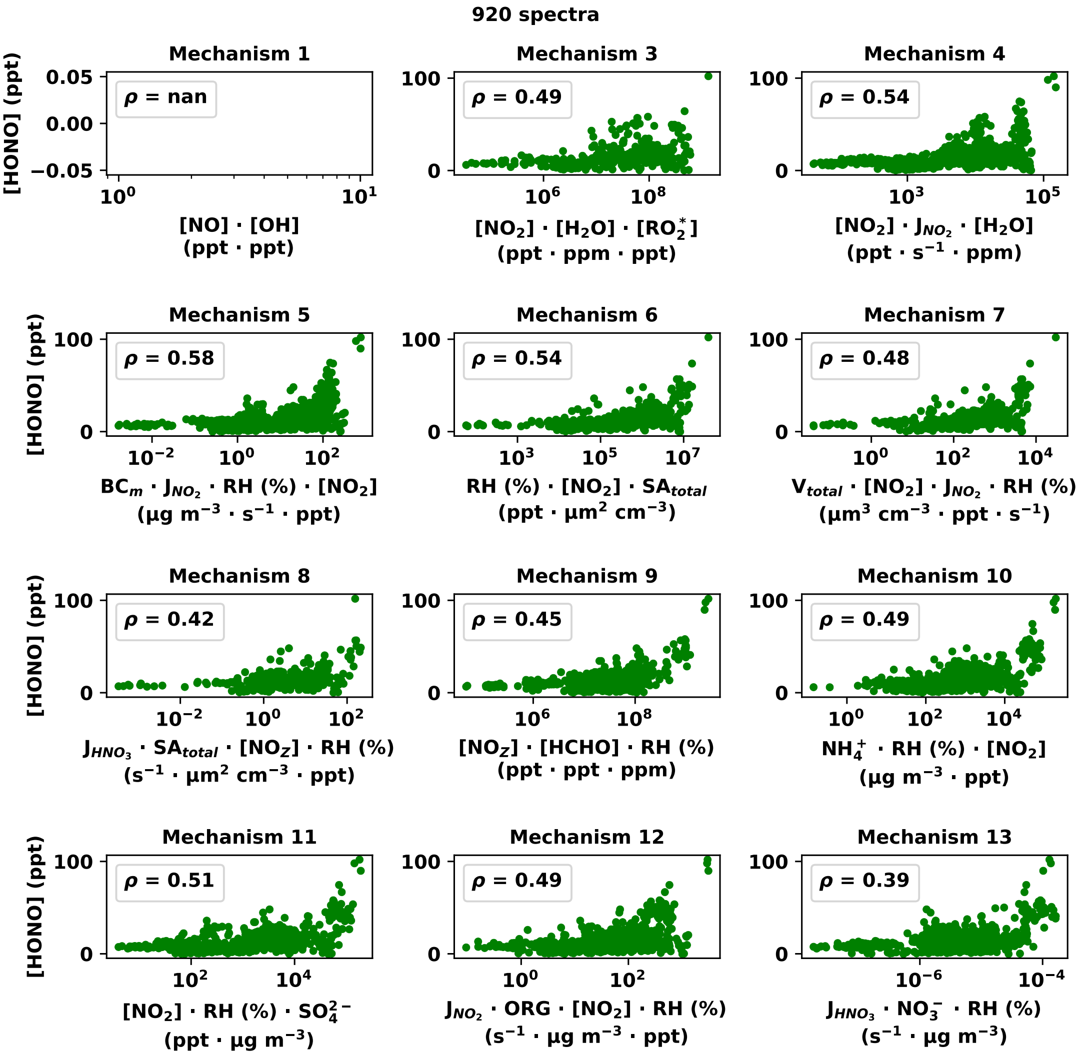

Figure G.9: For twelve of the thirteen potential formation mechanisms listed in table 2.1, the observed HONO VMRs plotted against the product of any measured reactants (or proxies thereof) from the lower troposphere during the -Asia phase of the EMeRGe mission. In each panel, the legend is the Spearman correlation coefficient ρ. During the EMeRGe mission, no measurements or proxies for OH are available. Here, $RO_2{}^*$ acts as a proxy for HO_2, while NO_z $(NO_y - NO_x)$ acts as a proxy for HNO_3. Data is colored by the tags described in section 4.1.1; red represents anthropogenic influence, green represents biomass burning influence, and the absence of either is indicated in blue and assumed to be otherwise pristine air. Missing tags are represented in black. Note the logarithmic x axes. Mechanism 2 is excluded because ortho-nitrophenols were not measured.

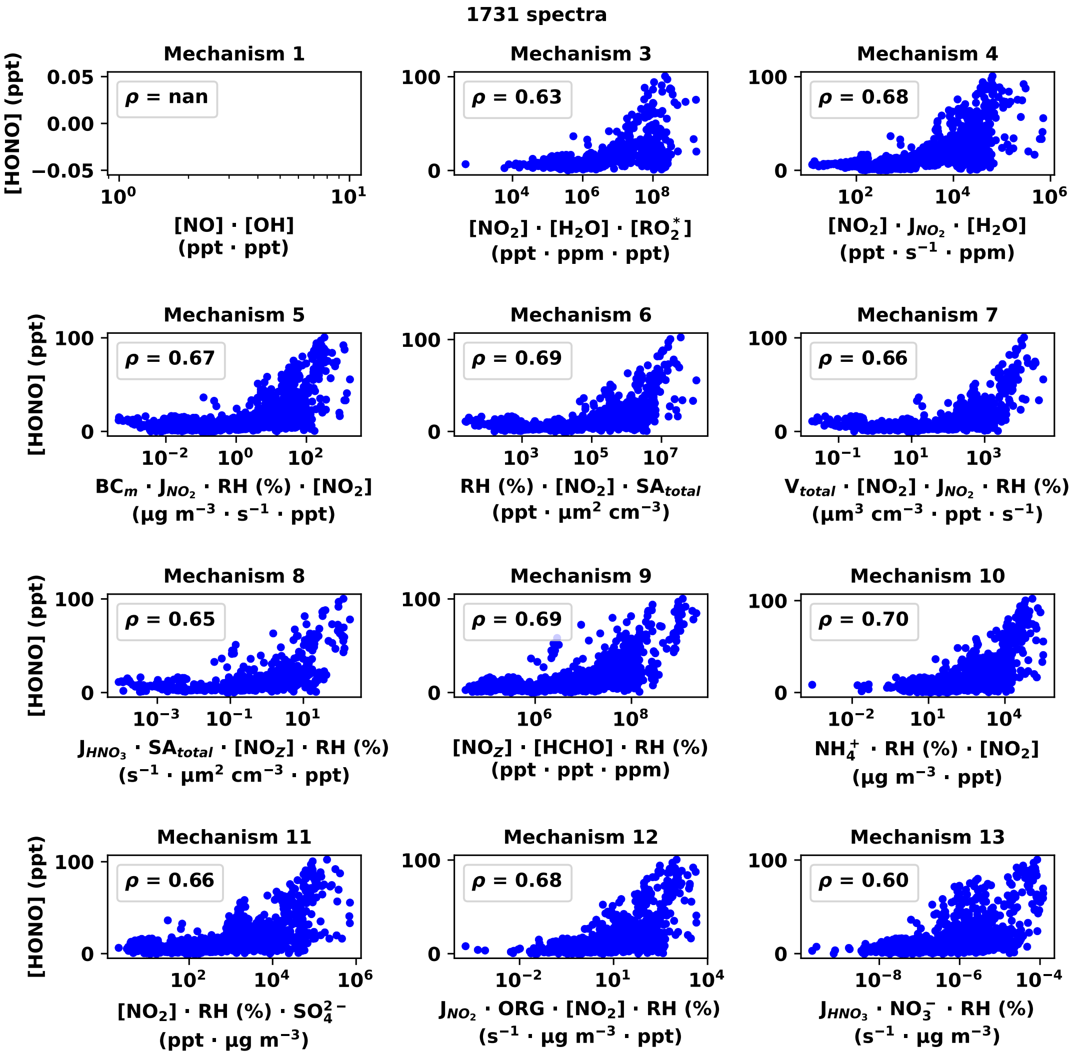

Figure G.10: For twelve of the thirteen potential formation mechanisms listed in table 2.1, the observed HONO VMRs plotted against the product of any measured reactants (or proxies thereof), from the lower troposphere during the -Asia phase of the EMeRGe mission. In each panel, the legend is the Spearman correlation coefficient ρ. During the EMeRGe mission, no measurements or proxies for OH are available. Here, RO_2* acts as a proxy for HO_2, while NO_z ($NO_y - NO_x$) acts as a proxy for HNO_3. Data is colored by the tags described in section 4.1.1; red represents anthropogenic influence, green represents biomass burning influence, and the absence of either is indicated in blue and assumed to be otherwise pristine air. Missing tags are represented in black. Note the logarithmic x axes. Mechanism 2 is excluded because ortho-nitrophenols were not measured.

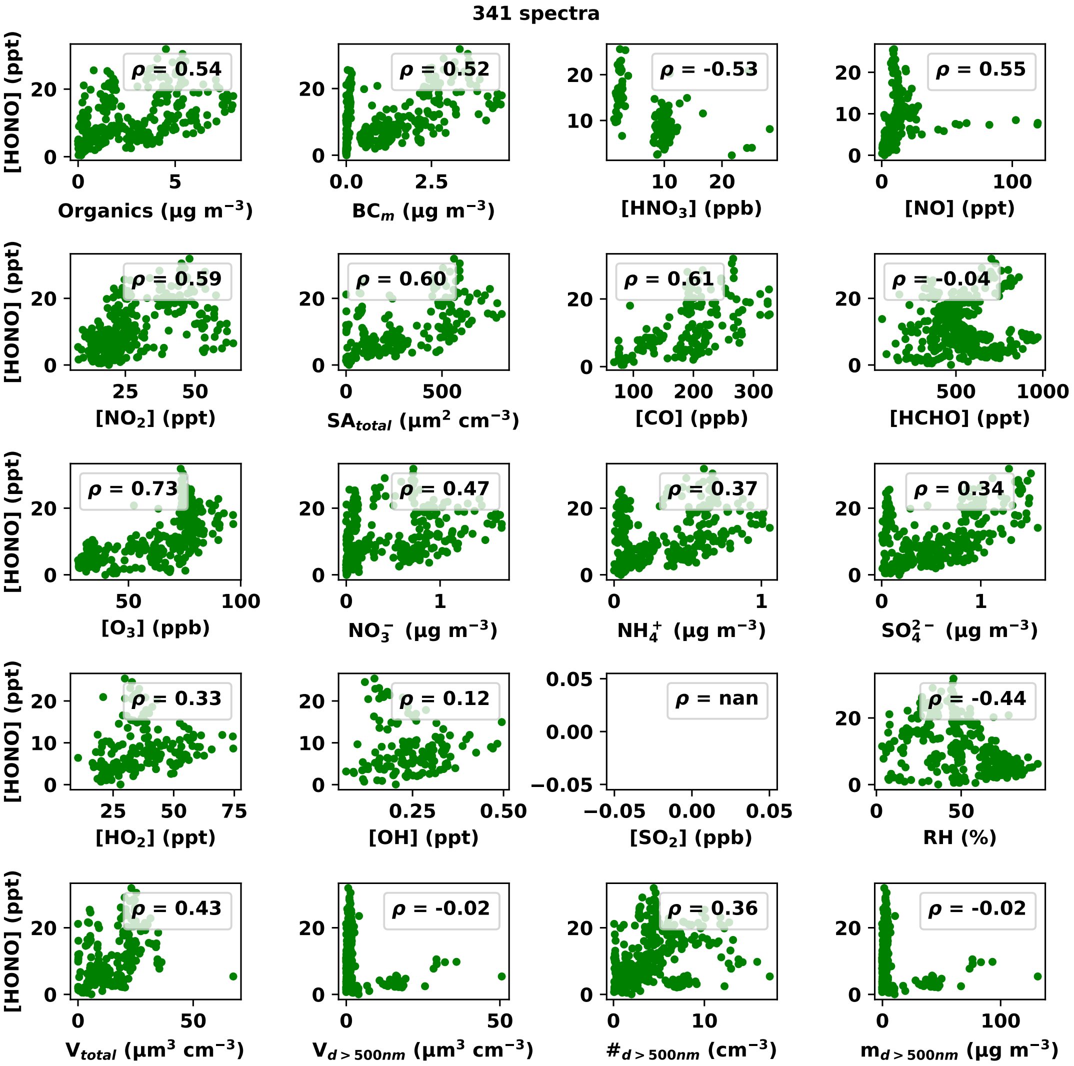

Figure G.11: In each panel the HONO VMRs observed by the mini-DOAS instrument are plotted against twenty other trace gases or atmospheric parameters measured from the HALO aircraft during the CAFE-Africa mission. The legend is the Spearman correlation coefficient. Green markers represent the influence of biomass burning determined from elevated acetonitrile measured by the MMS instrument, blue data represents acetonitrile below threshold values, black markers represent missing acetonitrile measurements. Data is from the lowermost 7.5 km of the troposphere. SO_2 was not measured during the CAFE-Africa mission.

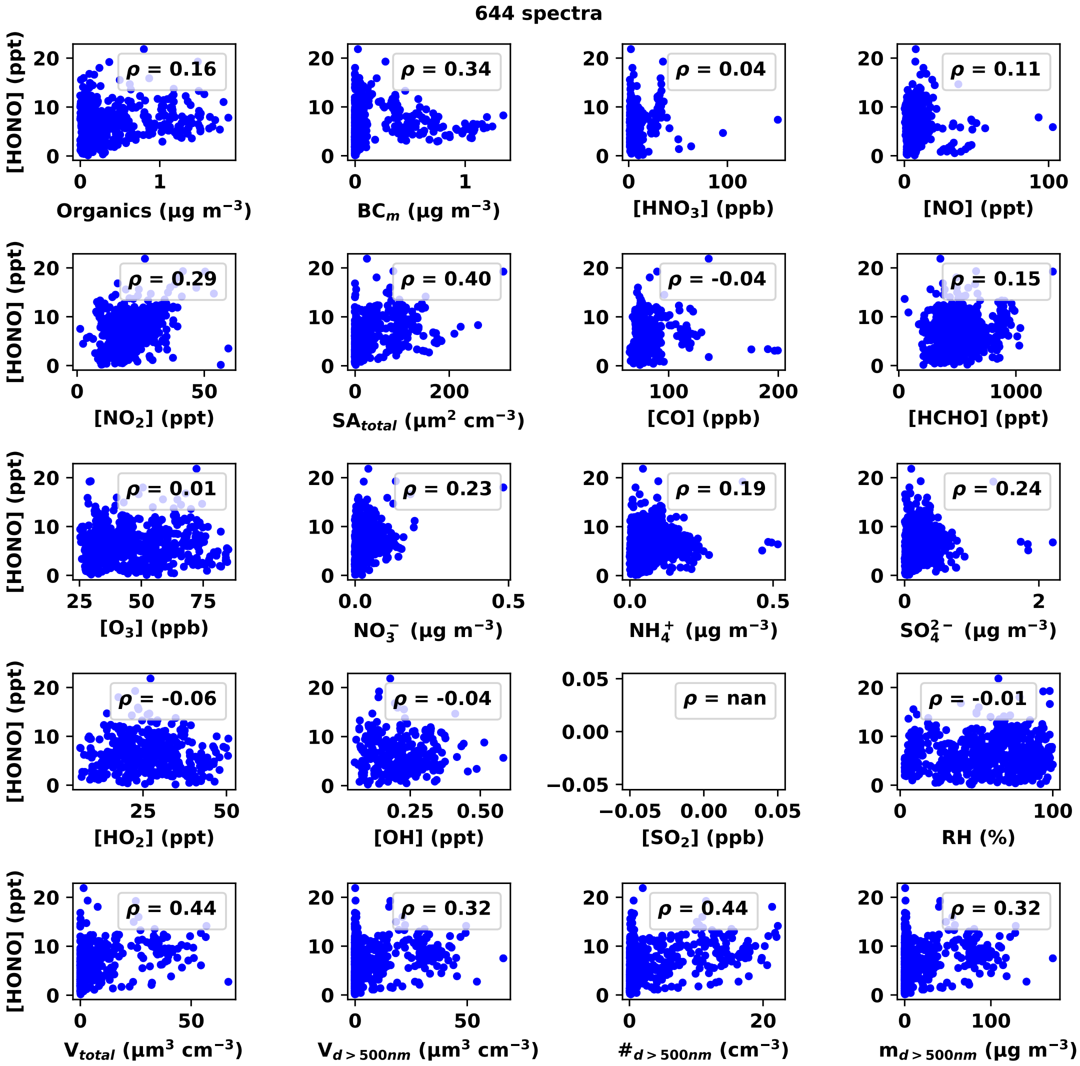

Figure G.12: In each panel the HONO VMRs observed by the mini-DOAS instrument are plotted against twenty other trace gases or atmospheric parameters measured from the HALO aircraft during the CAFE-Africa mission. The legend is the Spearman correlation coefficient. Green markers represent the influence of biomass burning determined from elevated acetonitrile measured by the MMS instrument, blue data represents acetonitrile below threshold values, black markers represent missing acetonitrile measurements. Data is from the lowermost 7.5 km of the troposphere. SO_2 was not measured during the CAFE-Africa mission.

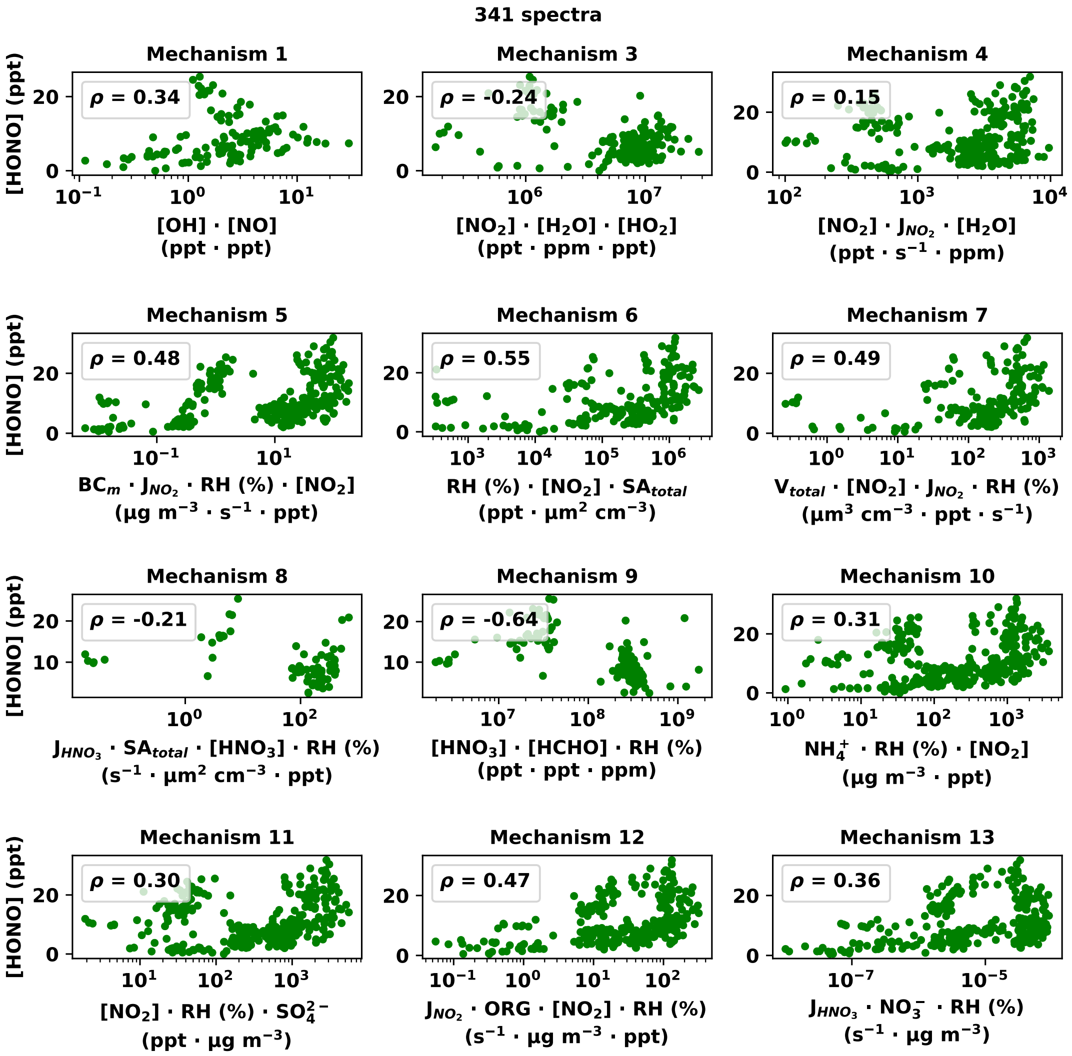

Figure G.13: For twelve of the thirteen formation mechanisms listed in table 2.1, the HONO VMRs (ppt) plotted against the product of the reactants observed during the CAFE-Africa mission, within the lower troposphere. The legend in each panel is the Spearman correlation coefficient ρ. The green, blue and black coloration indicates the presence of elevated, decreased, or missing acetonitrile measurements, respectively, as detected by the MMS instrument and should indicate the presence of biomass burning influence. Mechanism 2 is excluded because ortho-nitrophenols were not measured.

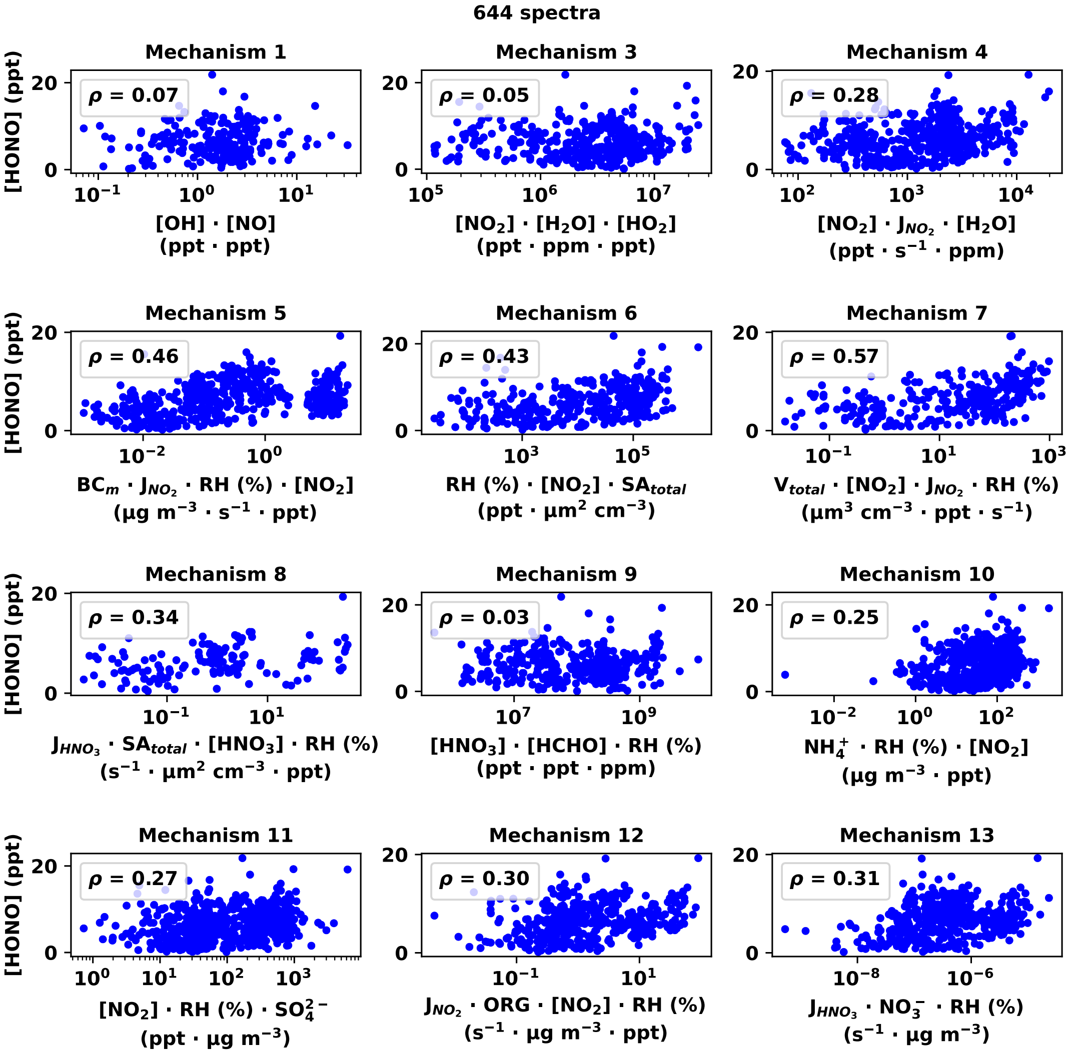

Figure G.14: For twelve of the thirteen formation mechanisms listed in table 2.1, the HONO VMRs (ppt) plotted against the product of the reactants observed during the CAFE-Africa mission, within the lower troposphere. The legend in each panel is the Spearman correlation coefficient ρ. The green, blue and black coloration indicates the presence of elevated, decreased, or missing acetonitrile measurements, respectively, as detected by the MMS instrument and should indicate the presence of biomass burning influence. Mechanism 2 is excluded because ortho-nitrophenols were not measured.

Appendix H

Thermochemistry of the Reactions Investigated in Chapter 6

The reactions investigated in chapter 6 must be exothermic. Table H.1 explores the thermodynamic variables of the investigated reactions.

Table H.1: Thermochemistry of the reactions discussed. For each species and reaction, the enthalpy (H), entropy (S) * temperature (T = 220 K), and corresponding Gibbs free energy (G) in kJ/mol. The color coding is only generally indicative of positive and negative. Negative enthalpy changes characterize exothermic reactions, negative free energy changes characterize exergonic reactions. Of the reactions listed here, only the thermal decomposition and photolysis of HOONO are endothermic/endergonic. Entropy and enthalpy data is from `https://webbook.nist.gov` and `https://atct.anl.gov`, except for HOONO, which is from Szakács et al. [2011]. Gibbs free energy is calculated according to ΔG = ΔH − TΔS.

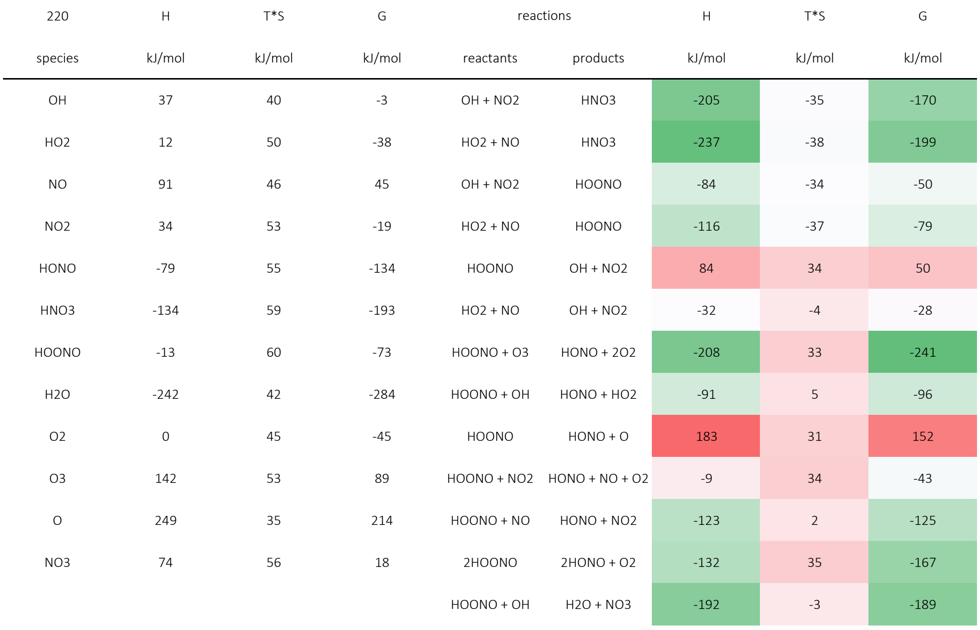

220	H	T*S	G	reactions		H	T*S	G
species	kJ/mol	kJ/mol	kJ/mol	reactants	products	kJ/mol	kJ/mol	kJ/mol
OH	37	40	-3	OH + NO2	HNO3	-205	-35	-170
HO2	12	50	-38	HO2 + NO	HNO3	-237	-38	-199
NO	91	46	45	OH + NO2	HOONO	-84	-34	-50
NO2	34	53	-19	HO2 + NO	HOONO	-116	-37	-79
HONO	-79	55	-134	HOONO	OH + NO2	84	34	50
HNO3	-134	59	-193	HO2 + NO	OH + NO2	-32	-4	-28
HOONO	-13	60	-73	HOONO + O3	HONO + 2O2	-208	33	-241
H2O	-242	42	-284	HOONO + OH	HONO + HO2	-91	5	-96
O2	0	45	-45	HOONO	HONO + O	183	31	152
O3	142	53	89	HOONO + NO2	HONO + NO + O2	-9	34	-43
O	249	35	214	HOONO + NO	HONO + NO2	-123	2	-125
NO3	74	56	18	2HOONO	2HONO + O2	-132	35	-167
				HOONO + OH	H2O + NO3	-192	-3	-189

Co-Authored Publications

Kluge, F., Hüneke, T., Knecht, M., Lichtenstern, M., Rotermund, M., Schlager, H., Schreiner, B., and Pfeilsticker, K.: Profiling of formaldehyde, glyoxal, methylglyoxal, and CO over the Amazon: normalized excess mixing ratios and related emission factors in biomass burning plumes, Atmos. Chem. Phys., 20, 12363–12389, https://doi.org/10.5194/acp-20-12363-2020, 2020.

Rotermund, M. K., Bense, V., Chipperfield, M. P., Engel, A., Grooß, J.-U., Hoor, P., Hüneke, T., Keber, T., Kluge, F., Schreiner, B., Schuck, T., Vogel, B., Zahn, A., and Pfeilsticker, K.: Organic and inorganic bromine measurements around the extratropical tropopause and lowermost stratosphere: insights into the transport pathways and total bromine, Atmos. Chem. Phys., 21, 15375–15407, https://doi.org/10.5194/acp-21-15375-2021, 2021.

Andrés Hernández, M. D., Hilboll, A., Ziereis, H., Förster, E., Krüger, O. O., Kaiser, K., Schneider, J., Barnaba, F., Vrekoussis, M., Schmidt, J., Huntrieser, H., Blechschmidt, A.-M., George, M., Nenakhov, V., Harlass, T., Holanda, B. A., Wolf, J., Eirenschmalz, L., Krebsbach, M., Pöhlker, M. L., Kalisz Hedegaard, A. B., Mei, L., Pfeilsticker, K., Liu, Y., Koppmann, R., Schlager, H., Bohn, B., Schumann, U., Richter, A., Schreiner, B., Sauer, D., Baumann, R., Mertens, M., Jöckel, P., Kilian, M., Stratmann, G., Pöhlker, C., Campanelli, M., Pandolfi, M., Sicard, M., Gómez-Amo, J. L., Pujadas, M., Bigge, K., Kluge, F., Schwarz, A., Daskalakis, N., Walter, D., Zahn, A., Pöschl, U., Bönisch, H., Borrmann, S., Platt, U., and Burrows, J. P.: Overview: On the transport and transformation of pollutants in the outflow of major population centres – observational data from the EMeRGe European intensive operational period in summer 2017, Atmos. Chem. Phys., 22, 5877–5924, https://doi.org/10.5194/acp-22-5877-2022, 2022.

Kluge, F., Hüneke, T., Lerot, C., Rosanka, S., Rotermund, M. K., Taraborrelli, D., Weyland, B., and Pfeilsticker, K.: Airborne glyoxal measurements in the marine and continental atmosphere: comparison with TROPOMI observations and EMAC simulations, Atmos. Chem. Phys., 23, 1369–1401, https://doi.org/10.5194/acp-23-1369-2023, 2023.

Ha, P. T. M., Kanaya, Y., Taketani, F., Andrés Hernández, M. D., Schreiner, B., Pfeilsticker, K., and Sudo, K.: Implementation of HONO into the chemistry–climate model CHASER (V4.0): roles in tropospheric chemistry, Geosci. Model Dev., 16, 927–960, https://doi.org/10.5194/gmd-16-927-2023, 2023.

Lin, C.-Y., Chen, W.-C., Chien, Y.-Y., Chou, C. C. K., Liu, C.-Y., Ziereis, H., Schlager, H., Förster, E., Obersteiner, F., Krüger, O. O., Holanda, B. A., Pöhlker, M. L., Kaiser, K., Schneider, J., Bohn, B., Pfeilsticker, K., Weyland, B., Andrés Hernández, M. D., and Burrows, J. P.: Effects of transport on a biomass burning plume from Indochina during EMeRGe-Asia identified by WRF-Chem, Atmos. Chem. Phys., 23, 2627–2647, https://doi.org/10.5194/acp-23-2627-2023, 2023.

George, M., Andrés Hernández, M. D., Nenakhov, V., Liu, Y., Burrows, J. P., Bohn, B., Förster, E., Obersteiner, F., Zahn, A., Harlaß, T., Ziereis, H., Schlager, H., Schreiner, B., Kluge, F., Bigge, K., and Pfeilsticker, K.: Airborne observations of peroxy radicals during the EMeRGe campaign in Europe, Atmos. Chem. Phys., 23, 7799–7822, https://doi.org/10.5194/acp-23-7799-2023, 2023.

Acknowledgments

I would also like to personally thank, in no particular order:

- Klaus Pfeilsticker, for his guidance and patience.
- The DLR, for organizing these missions.
- The EMeRGe and CAFE-Africa communities, for their cooperation and data.
- Katharina Kaiser of the MPIC, for the C-ToF-AMS data.
- Eric Förster of KIT's IMK, for the HKMS data.
- Tilman Hüneke, whose work made this analysis feasible in the first place.
- Flora Kluge and Meike Rotermund, for their encouragement and companionship.
- Birger Bohn and Jörg Kleffmann, for their thorough proofreading.
- Karl Heinz Schmidt, who kept the instrument working.
- My wife Kathrin, without whom none of this would be possible.

Bibliography

Acker, K., Möller, D., Wieprecht, W., Meixner, F. X., Bohn, B., Gilge, S., Plass-Dülmer, C., and Berresheim, H.: Strong daytime production of OH from HNO_2 at a rural mountain site, Geophysical Research Letters, 33, https://doi.org/10.1029/2005GL024643, 2006.

Akimoto, H., Tanimoto, H., et al.: Review of comprehensive measurements of speciated NO_y and its chemistry: need for quantifying the role of heterogeneous processes of HNO_3 and HONO, Aerosol and Air Quality Research, 21, 200 395, 2021.

Alicke, B., Geyer, A., Hofzumahaus, A., Holland, F., Konrad, S., Pätz, H. W., Schäfer, J., Stutz, J., Volz-Thomas, A., and Platt, U.: OH formation by HONO photolysis during the BERLIOZ experiment, Journal of Geophysical Research: Atmospheres, 108, PHO 3–1–PHO 3–17, https://doi.org/10.1029/2001JD000579, 2003.

Aliwell, S. R., Van Roozendael, M., Johnston, P. V., Richter, A., Wagner, T., Arlander, D. W., Burrows, J. P., Fish, D. J., Jones, R. L., Tørnkvist, K. K., Lambert, J.-C., Pfeilsticker, K., and Pundt, I.: Analysis for BrO in zenith-sky spectra: An intercomparison exercise for analysis improvement, J. Geophys. Res.-Atmos., 107, ACH 10–1–ACH 10–20, https://doi.org/10.1029/2001JD000329, 2002.

Amedro, D., Parker, A. E., Schoemaecker, C., and Fittschen, C.: Direct observation of OH radicals after 565nm multi-photon excitation of NO_2 in the presence of H_2O, Chemical Physics Letters, 513, 12–16, https://doi.org/10.1016/j.cplett.2011.07.062, 2011.

Amedro, D., Berasategui, M., Bunkan, A. J., Pozzer, A., Lelieveld, J., and Crowley, J. N.: Kinetics of the OH+ NO_2 reaction: effect of water vapour and new parameterization for global modelling, Atmospheric Chemistry and Physics, 20, 3091–3105, 2020.

Ammann, M., Kalberer, M., Jost, D., Tobler, L., Rössler, E., Piguet, D., Gäggeler, H., and Baltensperger, U.: Heterogeneous production of nitrous acid on soot in polluted air masses, Nature, 395, 157–160, 1998.

Andersen, S. T., Carpenter, L. J., Reed, C., Lee, J. D., Chance, R., Sherwen, T., Vaughan, A. R., Stewart, J., Edwards, P. M., Bloss, W. J., Sommariva, R., Crilley, L. R., Nott, G. J., Neves, L., Read, K., Heard, D. E., Seakins, P. W., Whalley, L. K., Boustead, G. A., Fleming, L. T., Stone, D., and Fomba, K. W.: Extensive field evidence for the release of HONO from the photolysis of nitrate aerosols, Science Advances, 9, eadd6266, https://doi.org/10.1126/sciadv.add6266, 2023.

Andrés Hernández, M. D., Hilboll, A., Ziereis, H., Förster, E., Krüger, O. O., Kaiser, K., Schneider, J., Barnaba, F., Vrekoussis, M., Schmidt, J., et al.: Overview: On the transport and transformation of pollutants in the outflow of major population centres–observational data from the EMeRGe European intensive operational period in summer 2017, Atmospheric Chemistry and Physics, 22, 5877–5924, 2022.

Bean, B. D., Mollner, A. K., Nizkorodov, S. A., Nair, G., Okumura, M., Sander, S. P., Peterson, K. A., and Francisco, J. S.: Cavity Ringdown Spectroscopy of cis-cis HOONO and the HOONO/$HONO_2$ Branching Ratio in the Reaction OH+ NO_2+ M, The Journal of Physical Chemistry A, 107, 6974–6985, 2003.

Becker, K. H., Kleffmann, J., Negri, R. M., and Wiesen, P.: Solubility of nitrous acid (HONO) in ammonium sulfate solutions, Journal of the Chemical Society, Faraday Transactions, 94, 1583–1586, 1998.

Beirle, S., Platt, U., Wenig, M., and Wagner, T.: Highly resolved global distribution of tropospheric NO 2 using GOME narrow swath mode data, Atmospheric Chemistry and Physics, 4, 1913–1924, 2004.

Beirle, S., Boersma, K. F., Platt, U., Lawrence, M. G., and Wagner, T.: Megacity emissions and lifetimes of nitrogen oxides probed from space, Science, 333, 1737–1739, 2011.

Beirle, S., Lampel, J., Lerot, C., Sihler, H., and Wagner, T.: Parameterizing the instrumental spectral response function and its changes by a super-Gaussian and its derivatives, Atmospheric Measurement Techniques, 10, 581–598, 2017.

Bejan, I., Abd El Aal, Y., Barnes, I., Benter, T., Bohn, B., Wiesen, P., and Kleffmann, J.: The photolysis of ortho-nitrophenols: a new gas phase source of HONO, Physical Chemistry Chemical Physics, 8, 2028–2035, 2006.

Benedict, K. B., McFall, A. S., and Anastasio, C.: Quantum Yield of Nitrite from the Photolysis of Aqueous Nitrate above 300 nm, Environmental Science & Technology, 51, 4387–4395, https://doi.org/10.1021/acs.est.6b06370, pMID: 28340298, 2017.

Bogumil, K., Orphal, J., Homann, T., Voigt, S., Spietz, P., Fleischmann, O. C., Vogel, A., Hartmann, M., Kromminga, H., Bovensmann, H., Frerick, J., and Burrows, J. P.: Measurements of molecular absorption spectra with the SCIAMACHY pre-flight model: instrument characterization and reference data for atmospheric remote-sensing in the 230–2380 nm region, J. Photochem. Photobiol. A.: Chem., 157, 167–184, https://doi.org/10.1016/S1010-6030(03)00062-5, 2003.

Bohn, B. and Lohse, I.: Calibration and evaluation of CCD spectroradiometers for ground-based and airborne measurements of spectral actinic flux densities, Atmospheric measurement techniques, 10, 3151–3174, 2017.

Bohn, B. and Zetzsch, C.: Rate constants of HO_2+ NO covering atmospheric conditions. 1. HO_2 formed by OH+ H_2O_2, The Journal of Physical Chemistry A, 101, 1488–1493, 1997.

Brasseur, G. P. and Solomon, S.: Aeronomy of the middle atmosphere: Chemistry and physics of the stratosphere and mesosphere, vol. 32, Springer Science & Business Media, 2005.

Brito, J. and Zahn, A.: An unheated permeation device for calibrating atmospheric VOC measurements, Atmospheric Measurement Techniques, 4, 2143–2152, https://doi.org/10.5194/amt-4-2143-2011, 2011.

Brune, W., McFarland, P., Bruning, E., Waugh, S., MacGorman, D., Miller, D., Jenkins, J., Ren, X., Mao, J., and Peischl, J.: Extreme oxidant amounts produced by lightning in storm clouds, Science, 372, 711–715, 2021.

Brust, A., Becker, K., Kleffmann, J., and Wiesen, P.: UV absorption cross sections of nitrous acid, Atmospheric Environment, 34, 13–19, 2000.

Burkholder, J., Sander, S., Abbatt, J., Barker, J., Cappa, C., Crounse, J., Dibble, T., Huie, R., Kolb, C., Kurylo, M., et al.: Chemical kinetics and photochemical data for use in atmospheric studies; evaluation number 19, Tech. rep., Pasadena, CA: Jet Propulsion Laboratory, National Aeronautics and Space . . . , 2020.

Butkovskaya, N., Kukui, A., Pouvesle, N., and Le Bras, G.: Formation of nitric acid in the gas-phase HO_2+ NO reaction: Effects of temperature and water vapor, The Journal of Physical Chemistry A, 109, 6509–6520, 2005.

Butkovskaya, N., Kukui, A., and Le Bras, G.: HNO_3 Forming Channel of the HO_2+ NO Reaction as a Function of Pressure and Temperature in the Ranges of 72- 600 Torr and 223- 323 K, The Journal of Physical Chemistry A, 111, 9047–9053, 2007.

Butkovskaya, N., Rayez, M.-T., Rayez, J.-C., Kukui, A., and Le Bras, G.: Water vapor effect on the HNO_3 yield in the HO_2+ NO reaction: experimental and theoretical evidence, The Journal of Physical Chemistry A, 113, 11 327–11 342, 2009.

Chance, K. and Kurucz, R. L.: An improved high-resolution solar reference spectrum for earth's atmosphere measurements in the ultraviolet, visible, and near infrared, Journal of quantitative spectroscopy and radiative transfer, 111, 1289–1295, 2010.

Chance, K. and Orphal, J.: Revised ultraviolet absorption cross sections of H_2CO for the HITRAN database, Journal of Quantitative Spectroscopy and Radiative Transfer, 112, 1509–1510, https://doi.org/10.1016/j.jqsrt.2011.02.002, 2011.

Cheng, Y., Zheng, G., Wei, C., Mu, Q., Zheng, B., Wang, Z., Gao, M., Zhang, Q., He, K., Carmichael, G., Pöschl, U., and Su, H.: Reactive nitrogen chemistry in aerosol water as a source of sulfate during haze events in China, Science Advances, 2, e1601 530, https://doi.org/10.1126/sciadv.1601530, 2016.

Council, N. R. et al.: VOCs and Nox: Relationship to Ozone and Associated Pollutants, Rethinking the Ozone Problem in Urban and Regional Air Pollution, pp. 163–186, 1991.

Crilley, L. R., Kramer, L. J., Ouyang, B., Duan, J., Zhang, W., Tong, S., Ge, M., Tang, K., Qin, M., Xie, P., Shaw, M. D., Lewis, A. C., Mehra, A., Bannan, T. J., Worrall, S. D., Priestley, M., Bacak, A., Coe, H., Allan, J., Percival, C. J., Popoola, O. A. M., Jones, R. L., and Bloss, W. J.: Intercomparison of nitrous acid (HONO) measurement techniques in a megacity (Beijing), Atmospheric Measurement Techniques, 12, 6449–6463, https://doi.org/10.5194/amt-12-6449-2019, 2019.

Crowley, J. N. and Carl, S. A.: OH Formation in the Photoexcitation of NO_2 beyond the Dissociation Threshold in the Presence of Water Vapor, The Journal of Physical Chemistry A, 101, 4178–4184, https://doi.org/10.1021/jp970319e, 1997.

Crutzen, P. J.: Tropospheric ozone: An overview, Tropospheric ozone: regional and global scale interactions, pp. 3–32, 1988.

De Smedt, I., Müller, J.-F., Stavrakou, T., Van Der A, R., Eskes, H., and Van Roozendael, M.: Twelve years of global observations of formaldehyde in the troposphere using GOME and SCIAMACHY sensors, Atmospheric Chemistry and Physics, 8, 4947–4963, 2008.

Delmas, R., Serça, D., and Jambert, C.: Global inventory of NO_x sources, Nutrient cycling in agroecosystems, 48, 51–60, 1997.

Deutschmann, T., Beirle, S., Frieß, U., Grzegorski, M., Kern, C., Kritten, L., Platt, U., Prados-Román, C., Puķīte, J., Wagner, T., Werner, B., and Pfeilsticker, K.: The Monte Carlo Atmospheric Radiative Transfer Model McArtim: Introduction and Validation of Jacobians and 3D Features, J. Quant. Spectrosc. Radiat. Transfer, 112, 1119–1137, https://doi.org/10.1016/j.jqsrt.2010.12.009, 2011.

Ding, J., Zhao, P., Su, J., Dong, Q., Du, X., and Zhang, Y.: Aerosol pH and its driving factors in Beijing, Atmospheric Chemistry and Physics, 19, 7939–7954, 2019.

Dörich, R., Eger, P., Lelieveld, J., and Crowley, J. N.: Iodide CIMS and m/ z 62: the detection of HNO 3 as NO 3- in the presence of PAN, peroxyacetic acid and ozone, Atmospheric Measurement Techniques, 14, 5319–5332, 2021.

Dupart, Y., Fine, L., D'Anna, B., and George, C.: Heterogeneous uptake of NO_2 on Arizona Test Dust under UV-A irradiation: An aerosol flow tube study, Aeolian Research, 15, 45–51, https://doi.org/10.1016/j.aeolia.2013.10.001, 2014.

Dyson, J. E., Boustead, G. A., Fleming, L. T., Blitz, M., Stone, D., Arnold, S. R., Whalley, L. K., and Heard, D. E.: Production of HONO from NO_2 uptake on illuminated TiO_2 aerosol particles and following the illumination of mixed TiO_2/ammonium nitrate particles, Atmospheric Chemistry and Physics, 21, 5755–5775, https://doi.org/10.5194/acp-21-5755-2021, 2021.

Elshorbany, Y. F., Kurtenbach, R., Wiesen, P., Lissi, E., Rubio, M., Villena, G., Gramsch, E., Rickard, A., Pilling, M., and Kleffmann, J.: Oxidation capacity of the city air of Santiago, Chile, Atmospheric Chemistry and Physics, 9, 2257–2273, 2009.

Finlayson-Pitts, B., Wingen, L., Sumner, A., Syomin, D., and Ramazan, K.: The heterogeneous hydrolysis of NO 2 in laboratory systems and in outdoor and indoor atmospheres: An integrated mechanism, Physical Chemistry Chemical Physics, 5, 223–242, 2003.

Finlayson-Pitts, B. J. and Pitts Jr, J. N.: Chemistry of the upper and lower atmosphere: theory, experiments, and applications, Elsevier, 1999.

Förster, E., Bönisch, H., Neumaier, M., Obersteiner, F., Zahn, A., Hilboll, A., Kalisz Hedegaard, A. B., Daskalakis, N., Poulidis, A. P., Vrekoussis, M., Lichtenstern, M., and Braesicke, P.: Chemical and dynamical identification of emission outflows during the HALO campaign EMeRGe in Europe and Asia, Atmospheric Chemistry and Physics, 23, 1893–1918, https://doi.org/10.5194/acp-23-1893-2023, 2023.

Fountoukis, C. and Nenes, A.: ISORROPIA II: a computationally efficient thermodynamic equilibrium model for K+–Ca 2+–Mg 2+–NH 4+–Na+–SO 4 2—NO 3—Cl—H 2 O aerosols, Atmospheric Chemistry and Physics, 7, 4639–4659, 2007.

Fry, J. L., Nizkorodov, S. A., Okumura, M., Roehl, C. M., Francisco, J. S., and Wennberg, P. O.: Cis-cis and trans-perp HOONO: Action spectroscopy and isomerization kinetics, The Journal of Chemical Physics, 121, 1432–1448, 2004.

Fu, X., Wang, T., Zhang, L., Li, Q., Wang, Z., Xia, M., Yun, H., Wang, W., Yu, C., Yue, D., Zhou, Y., Zheng, J., and Han, R.: The significant contribution of HONO to secondary pollutants during a severe winter pollution event in southern China, Atmospheric Chemistry and Physics, 19, 1–14, https://doi.org/10.5194/acp-19-1-2019, 2019.

George, C., Strekowski, R., Kleffmann, J., Stemmler, K., and Ammann, M.: Photoenhanced uptake of gaseous NO_2 on solid organic compounds: a photochemical source of HONO?, Faraday discussions, 130, 195–210, 2005.

George, M., Andrés Hernández, M. D., Nenakhov, V., Liu, Y., and Burrows, J. P.: Airborne measurement of peroxy radicals using chemical amplification coupled with cavity ring-down spectroscopy: the PeRCEAS instrument, Atmospheric Measurement Techniques, 13, 2577–2600, 2020.

George, M., Andrés Hernández, M. D., Nenakhov, V., Liu, Y., Burrows, J. P., Bohn, B., Förster, E., Obersteiner, F., Zahn, A., Harlaß, T., Ziereis, H., Schlager, H., Schreiner, B., Kluge, F., Bigge, K., and Pfeilsticker, K.: Airborne observations of peroxy radicals during the EMeRGe campaign in Europe, Atmospheric Chemistry and Physics, 23, 7799–7822, https://doi.org/10.5194/acp-23-7799-2023, 2023.

Gerbig, C., Kley, D., Volz-Thomas, A., Kent, J., Dewey, K., and McKenna, D. S.: Fast response resonance fluorescence CO measurements aboard the C-130: Instrument characterization and measurements made during North Atlantic Regional Experiment 1993, Journal of Geophysical Research: Atmospheres, 101, 29 229–29 238, 1996.

Gettelman, A., Hoor, P., Pan, L. L., Randel, W. J., Hegglin, M. I., and Birner, T.: The extratropical upper troposphere and lower stratosphere, Rev. Geophys., 49, RG3003, https://doi.org/10.1029/2011RG000355, 2011.

Golden, D. M. and Smith, G. P.: Reaction of $OH+ NO_2+ M$: A new view, The Journal of Physical Chemistry A, 104, 3991–3997, 2000.

Golden, D. M., Barker, J. R., and Lohr, L. L.: Master equation models for the pressure-and temperature-dependent reactions $HO+ NO_2\rightarrow HONO_2$ and $HO+ NO_2\rightarrow HOONO$, The Journal of Physical Chemistry A, 107, 11 057–11 071, 2003.

Goodman, A., Underwood, G., and Grassian, V.: Heterogeneous reaction of NO_2: characterization of gas-phase and adsorbed products from the reaction, $2\ NO_2\ (g)+ H_2O\ (a)\rightarrow HONO\ (g)+ HNO_3\ (a)$ on hydrated silica particles, The Journal of Physical Chemistry A, 103, 7217–7223, 1999.

Greenblatt, G. D., Orlando, J. J., Burkholder, J. B., and Ravishankara, A. R.: Absorption measurements of oxygen between 330 and 1140 nm, J. Geophys. Res., 95, 18 577–18 582, 1990.

Grimm: Aerosol spectrometer Series 1.129 "SKY-OPC", Grimm Aerosol Technik, manual edn., 2008.

Großmann, K.: Aircraft-borne DOAS limb observations of UV/visible absorbing trace gas species over Borneo: Implications for the photochemistry of iodine, volatile organic oxide degradation, and lightning-produced radicals, Phd, University of Heidelberg, Heidelberg, Germany, URL `https://archiv.ub.uni-heidelberg.de/volltextserver/17874/`, 2014.

Ha, P. T. M., Kanaya, Y., Taketani, F., Andrés Hernández, M. D., Schreiner, B., Pfeilsticker, K., and Sudo, K.: Implementation of HONO into the chemistry–climate model CHASER (V4.0): roles in tropospheric chemistry, Geoscientific Model Development, 16, 927–960, https://doi.org/10.5194/gmd-16-927-2023, 2023.

Hamryszczak, Z., Dienhart, D., Brendel, B., Rohloff, R., Marno, D., Martinez, M., Harder, H., Pozzer, A., Bohn, B., Zöger, M., Lelieveld, J., and Fischer, H.: Measurement report: Hydrogen peroxide in the upper tropical troposphere over the Atlantic Ocean and western Africa during the CAFE-Africa aircraft campaign, Atmospheric Chemistry and Physics, 23, 5929–5943, https://doi.org/10.5194/acp-23-5929-2023, 2023.

Heckel, A., Richter, A., Tarsu, T., Wittrock, F., Hak, C., Pundt, I., Junkermann, W., and Burrows, J. P.: MAX-DOAS measurements of formaldehyde in the Po-Valley, Atmospheric Chemistry and Physics, 5, 909–918, https://doi.org/10.5194/acp-5-909-2005, 2005.

Heintzenberg, J.: Properties of the log-normal particle size distribution, Aerosol Science and Technology, 21, 46–48, 1994.

Heintzenberg, J., Charlson, R., Clarke, A., Liousse, C., Ramaswamy, V., Shine, K., Wendisch, M., and Helas, G.: Measurements and modelling of aerosol single-scattering albedo: Progress, problems and prospects, Contributions to atmospheric physics, 70, 249–263, 1997.

Heland, J., Kleffmann, J., Kurtenbach, R., and Wiesen, P.: A New Instrument To Measure Gaseous Nitrous Acid (HONO) in the Atmosphere, Environmental Science & Technology, 35, 3207–3212, https://doi.org/10.1021/es000303t, pMID: 11506004, 2001.

Hendrick, F., Müller, J.-F., Clémer, K., Wang, P., De Mazière, M., Fayt, C., Gielen, C., Hermans, C., Ma, J. Z., Pinardi, G., Stavrakou, T., Vlemmix, T., and Van Roozendael, M.: Four years of ground-based MAX-DOAS observations of HONO and NO_2 in the Beijing area, Atmospheric Chemistry and Physics, 14, 765–781, https://doi.org/10.5194/acp-14-765-2014, 2014.

Heue, K.-P., Riede, H., Walter, D., Brenninkmeijer, C. A. M., Wagner, T., Frieß, U., Platt, U., Zahn, A., Stratmann, G., and Ziereis, H.: CARIBIC DOAS observations of nitrous acid and formaldehyde in a large convective cloud, Atmospheric Chemistry and Physics, 14, 6621–6642, https://doi.org/10.5194/acp-14-6621-2014, 2014.

Holanda, B. A., Pöhlker, M. L., Walter, D., Saturno, J., Sörgel, M., Ditas, J., Ditas, F., Schulz, C., Franco, M. A., Wang, Q., et al.: Influx of African biomass burning aerosol during the Amazonian dry season through layered transatlantic transport of black carbon-rich smoke, Atmospheric Chemistry and Physics, 20, 4757–4785, 2020.

Hrdina, A., Murphy, J. G., Hallar, A. G., Lin, J. C., Moravek, A., Bares, R., Petersen, R. C., Franchin, A., Middlebrook, A. M., Goldberger, L., et al.: The role of coarse aerosol particles as a sink of HNO 3 in wintertime pollution events in the Salt Lake Valley, Atmospheric Chemistry and Physics, 21, 8111–8126, 2021.

Hu, B., Duan, J., Hong, Y., Xu, L., Li, M., Bian, Y., Qin, M., Fang, W., Xie, P., and Chen, J.: Exploration of the atmospheric chemistry of nitrous acid in a coastal city of southeastern China: results from measurements across four seasons, Atmospheric Chemistry and Physics, 22, 371–393, https://doi.org/10.5194/acp-22-371-2022, 2022.

Huang, G., Zhou, X., Deng, G., Qiao, H., and Civerolo, K.: Measurements of atmospheric nitrous acid and nitric acid, Atmospheric Environment, 36, 2225–2235, https://doi.org/10.1016/S1352-2310(02)00170-X, 2002.

Hüneke, T.: The scaling method applied to HALO measurements: Inferring absolute trace gas concentrations from airborne limb spectroscopy under all sky conditions, Phd thesis, Universität Heidelberg, URL `https://www.ub.uni-heidelberg.de/archiv/22573`, 2016.

Hüneke, T., Aderhold, O.-A., Bounin, J., Dorf, M., Gentry, E., Grossmann, K., Grooß, J.-U., Hoor, P., Jöckel, P., Kenntner, M., Knapp, M., Knecht, M., Lörks, D., Ludmann, S., Matthes, S., Raecke, R., Reichert, M., Weimar, J., Werner, B., Zahn, A., Ziereis, H., and Pfeilsticker, K.: The novel HALO mini-DOAS instrument: inferring trace gas concentrations from airborne UV/visible limb spectroscopy under all skies using the scaling method, Atmos. Meas. Tech., 10, 4209–4234, https://doi.org/10.5194/amt-10-4209-2017, 2017.

Irvine, W. M.: The formation of absorption bands and the distribution of photon optical paths in a scattering atmosphere, Bull. Astron. Inst. Neth., 17, 266–279, 1964.

Jacob, D. J.: Heterogeneous chemistry and tropospheric ozone, Atmospheric Environment, 34, 2131–2159, https://doi.org/10.1016/S1352-2310(99)00462-8, 2000.

Jaeglé, L., Jacob, D. J., Brune, W. H., and Wennberg, P. O.: Chemistry of HOx radicals in the upper troposphere, Atmospheric Environment, 35, 469–489, 2001.

Jiang, Y., Xue, L., Gu, R., Jia, M., Zhang, Y., Wen, L., Zheng, P., Chen, T., Li, H., Shan, Y., Zhao, Y., Guo, Z., Bi, Y., Liu, H., Ding, A., Zhang, Q., and Wang, W.: Sources of nitrous acid (HONO) in the upper boundary layer and lower free troposphere of the North China Plain: insights from the Mount Tai Observatory, Atmospheric Chemistry and Physics, 20, 12 115–12 131, https://doi.org/10.5194/acp-20-12115-2020, 2020.

Jöckel, P., Tost, H., Pozzer, A., Kunze, M., Kirner, O., Brenninkmeijer, C. A., Brinkop, S., Cai, D. S., Dyroff, C., Eckstein, J., et al.: Earth system chemistry integrated modelling (ESCiMo) with the modular earth submodel system (MESSy) version 2.51, Geoscientific Model Development, 9, 1153–1200, 2016.

Kalberer, M., Ammann, M., Arens, F., Gäggeler, H. W., and Baltensperger, U.: Heterogeneous formation of nitrous acid (HONO) on soot aerosol particles, Journal of Geophysical Research: Atmospheres, 104, 13 825–13 832, https://doi.org/10.1029/1999JD900141, 1999.

Kirchner, U., Scheer, V., and Vogt, R.: FTIR Spectroscopic Investigation of the Mechanism and Kinetics of the Heterogeneous Reactions of NO_2 and HNO_3 with Soot, The Journal of Physical Chemistry A, 104, 8908–8915, https://doi.org/10.1021/jp0005322, 2000.

Kleffmann, J.: Daytime sources of nitrous acid (HONO) in the atmospheric boundary layer, ChemPhysChem, 8, 1137–1144, 2007.

Kleffmann, J., Kurtenbach, R., Lörzer, J., Wiesen, P., Kalthoff, N., Vogel, B., and Vogel, H.: Measured and simulated vertical profiles of nitrous acid—Part I: Field measurements, Atmospheric Environment, 37, 2949–2955, https://doi.org/10.1016/S1352-2310(03)00242-5, 2003.

Kleffmann, J., Gavriloaiei, T., Hofzumahaus, A., Holland, F., Koppmann, R., Rupp, L., Schlosser, E., Siese, M., and Wahner, A.: Daytime formation of nitrous acid: A major source of OH radicals in a forest, Geophysical Research Letters, 32, https://doi.org/10.1029/2005GL022524, 2005.

Kluge, F.: Airborne glyoxal measurements in different regions of the globe: Its atmospheric fate, comparison with TROPOMI observations and EMAC simulations, and inferred biomass burning emission factors for glyoxal and methylglyoxal, Ph.D. thesis, URL https://archiv.ub.uni-heidelberg.de/volltextserver/32874/, 2023.

Kluge, F., Hüneke, T., Knecht, M., Lichtenstern, M., Rotermund, M., Schlager, H., Schreiner, B., and Pfeilsticker, K.: Profiling of formaldehyde, glyoxal, methylglyoxal, and CO over the Amazon: normalized excess mixing ratios and related emission factors in biomass burning plumes, Atmospheric Chemistry and Physics, 20, 12 363–12 389, https://doi.org/10.5194/acp-20-12363-2020, 2020.

Kluge, F., Hüneke, T., Lerot, C., Rosanka, S., Rotermund, M. K., Taraborrelli, D., Weyland, B., and Pfeilsticker, K.: Airborne glyoxal measurements in the marine and continental atmosphere: comparison with TROPOMI observations and EMAC simulations, Atmospheric Chemistry and Physics, 23, 1369–1401, 2023.

Knecht, M.: Simulation of radiative field modification due to tropical clouds, Master's thesis, University of Heidelberg, Heidelberg, Germany, (last access: 29 January 2021), 2015.

Kraus, S.: DOASIS - A Framework Design for DOAS, Phd thesis, Heidelberg University, Germany, 2006.

Kritten, L.: Time dependent profiling of UV/vis absorbing radicals by balloon-borne spectroscopic limb measurements and implications for stratospheric photochemistry, Phd thesis, Universität Heidelberg, URL https://www.ub.uni-heidelberg.de/archiv/10461, 2009.

Lammel, G. and Cape, J. N.: Nitrous acid and nitrite in the atmosphere, Chem. Soc. Rev., 25, 361–369, https://doi.org/10.1039/CS9962500361, 1996.

Lampel, J., Frieß, U., and Platt, U.: The impact of vibrational Raman scattering of air on DOAS measurements of atmospheric trace gases, Atmospheric Measurement Techniques, 8, 3767–3787, 2015.

Lampel, J., Pöhler, D., Polyansky, O. L., Kyuberis, A. A., Zobov, N. F., Tennyson, J., Lodi, L., Frieß, U., Wang, Y., Beirle, S., et al.: Detection of water vapour absorption around 363 nm in measured atmospheric absorption spectra and its effect on DOAS evaluations, Atmospheric Chemistry and Physics, 17, 1271–1295, 2017a.

Lampel, J., Wang, Y., Hilboll, A., Beirle, S., Sihler, H., Puķīte, J., Platt, U., and Wagner, T.: The tilt effect in DOAS observations, Atmospheric Measurement Techniques, 10, 4819–4831, 2017b.

Lamsal, L., Janz, S., Krotkov, N., Pickering, K., Spurr, R., Kowalewski, M., Loughner, C., Crawford, J., Swartz, W., and Herman, J.: High-resolution NO2 observations from the Airborne Compact Atmospheric Mapper: Retrieval and validation, Journal of Geophysical Research: Atmospheres, 122, 1953–1970, 2017.

Laufs, S. and Kleffmann, J.: Investigations on HONO formation from photolysis of adsorbed HNO_3 on quartz glass surfaces, Physical Chemistry Chemical Physics, 18, 9616–9625, 2016.

Lee, J. D., Whalley, L. K., Heard, D. E., Stone, D., Dunmore, R. E., Hamilton, J. F., Young, D. E., Allan, J. D., Laufs, S., and Kleffmann, J.: Detailed budget analysis of HONO in central London reveals a missing daytime source, Atmospheric Chemistry and Physics, 16, 2747–2764, https://doi.org/10.5194/acp-16-2747-2016, 2016.

Lee, T., Yu, X.-Y., Ayres, B., Kreidenweis, S. M., Malm, W. C., and Collett Jr, J. L.: Observations of fine and coarse particle nitrate at several rural locations in the United States, Atmospheric Environment, 42, 2720–2732, 2008.

Lelieveld, J., Evans, J. S., Fnais, M., Giannadaki, D., and Pozzer, A.: The contribution of outdoor air pollution sources to premature mortality on a global scale, Nature, 525, 367–371, 2015.

Li, L., Duan, Z., Li, H., Zhu, C., Henkelman, G., Francisco, J. S., and Zeng, X. C.: Formation of HONO from the NH_3-promoted hydrolysis of NO_2 dimers in the atmosphere, Proceedings of the National Academy of Sciences, 115, 7236–7241, https://doi.org/10.1073/pnas.1807719115, 2018a.

Li, L., Hoffmann, M. R., and Colussi, A. J.: Role of Nitrogen Dioxide in the Production of Sulfate during Chinese Haze-Aerosol Episodes, Environmental Science & Technology, 52, 2686–2693, https://doi.org/10.1021/acs.est.7b05222, pMID: 29378118, 2018b.

Li, S., Matthews, J., and Sinha, A.: Atmospheric hydroxyl radical production from electronically excited NO2 and H2O, Science, 319, 1657–1660, 2008.

Li, X., Brauers, T., Häseler, R., Bohn, B., Fuchs, H., Hofzumahaus, A., Holland, F., Lou, S., Lu, K. D., Rohrer, F., Hu, M., Zeng, L. M., Zhang, Y. H., Garland, R. M., Su, H., Nowak, A., Wiedensohler, A., Takegawa, N., Shao, M., and Wahner, A.: Exploring the atmospheric chemistry of nitrous acid (HONO) at a rural site in Southern China, Atmospheric Chemistry and Physics, 12, 1497–1513, https://doi.org/10.5194/acp-12-1497-2012, 2012.

Li, X., Rohrer, F., Hofzumahaus, A., Brauers, T., Häseler, R., Bohn, B., Broch, S., Fuchs, H., Gomm, S., Holland, F., Jäger, J., Kaiser, J., Keutsch, F. N., Lohse, I., Lu, K., Tillmann, R., Wegener, R., Wolfe, G. M., Mentel, T. F., Kiendler-Scharr, A., and Wahner, A.: Missing Gas-Phase Source of HONO Inferred from Zeppelin Measurements in the Troposphere, Science, 344, 292–296, https://doi.org/10.1126/science.1248999, 2014.

Li, X., Rohrer, F., Hofzumahaus, A., Brauers, T., Häseler, R., Bohn, B., Broch, S., Fuchs, H., Gomm, S., Holland, F., Jäger, J., Kaiser, J., Keutsch, F. N., Lohse, I., Lu, K., Tillmann, R., Wegener, R., Wolfe, G. M., Mentel, T. F., Kiendler-Scharr, A., and Wahner, A.: Response to 'Comment on "Missing gas-phase source of HONO inferred from Zeppelin measurements in the troposphere"', Science, 348, 1326–1326, https://doi.org/10.1126/science.aaa3777, 2015.

Li, Y. and Francisco, J. S.: High level ab initio molecular orbital theory study of the structure, vibrational spectrum, stability, and low-lying excited states of HOONO, The Journal of Chemical Physics, 113, 7976–7981, 2000.

Lin, C.-Y., Chen, W.-C., Chien, Y.-Y., Chou, C. C. K., Liu, C.-Y., Ziereis, H., Schlager, H., Förster, E., Obersteiner, F., Krüger, O. O., Holanda, B. A., Pöhlker, M. L., Kaiser, K., Schneider, J., Bohn, B., Pfeilsticker, K., Weyland, B., Andrés Hernández, M. D., and Burrows, J. P.: Effects of transport on a biomass burning plume from Indochina during EMeRGe-Asia identified by WRF-Chem, Atmospheric Chemistry and Physics, 23, 2627–2647, https://doi.org/10.5194/acp-23-2627-2023, 2023.

Logan, J. A., Prather, M. J., Wofsy, S. C., and McElroy, M. B.: Tropospheric chemistry: A global perspective, Journal of Geophysical Research: Oceans, 86, 7210–7254, 1981.

Lu, X., Wang, Y., Li, J., Shen, L., and Fung, J. C. H.: Evidence of heterogeneous HONO formation from aerosols and the regional photochemical impact of this HONO source, Environmental Research Letters, 13, 114 002, https://doi.org/10.1088/1748-9326/aae492, 2018.

Ma, J., Beirle, S., Jin, J., Shaiganfar, R., Yan, P., and Wagner, T.: Tropospheric NO 2 vertical column densities over Beijing: results of the first three years of ground-based MAX-DOAS measurements (2008–2011) and satellite validation, Atmospheric Chemistry and Physics, 13, 1547–1567, 2013a.

Ma, J., Liu, Y., Han, C., Ma, Q., Liu, C., and He, H.: Review of heterogeneous photochemical reactions of NO_y on aerosol — A possible daytime source of nitrous acid (HONO) in the atmosphere, Journal of Environmental Sciences, 25, 326–334, https://doi.org/10.1016/S1001-0742(12)60093-X, 2013b.

Mallaun, C., Giez, A., and Baumann, R.: Calibration of 3-D wind measurements on a single-engine research aircraft, Atmospheric Measurement Techniques, 8, 3177–3196, 2015.

Mao, J., Zhao, T., Keller, C. A., Wang, X., McFarland, P. J., Jenkins, J. M., and Brune, W. H.: Global Impact of Lightning-Produced Oxidants, Geophysical Research Letters, 48, e2021GL095 740, 2021.

Marais, E. A., Jacob, D. J., Choi, S., Joiner, J., Belmonte-Rivas, M., Cohen, R. C., Beirle, S., Murray, L. T., Schiferl, L. D., Shah, V., and Jaeglé, L.: Nitrogen oxides in the global upper troposphere: interpreting cloud-sliced NO_2 observations from the OMI satellite instrument, Atmospheric Chemistry and Physics, 18, 17 017–17 027, https://doi.org/10.5194/acp-18-17017-2018, 2018.

Marais, E. A., Roberts, J. F., Ryan, R. G., Eskes, H., Boersma, K. F., Choi, S., Joiner, J., Abuhassan, N., Redondas, A., Grutter, M., Cede, A., Gomez, L., and Navarro-Comas, M.: New observations of NO_2 in the upper troposphere from TROPOMI, Atmospheric Measurement Techniques, 14, 2389–2408, https://doi.org/10.5194/amt-14-2389-2021, 2021.

Mark, G., Korth, H.-G., Schuchmann, H.-P., and von Sonntag, C.: The photochemistry of aqueous nitrate ion revisited, Journal of Photochemistry and Photobiology A: Chemistry, 101, 89–103, https://doi.org/10.1016/S1010-6030(96)04391-2, 1996.

Marno, D., Ernest, C., Hens, K., Javed, U., Klimach, T., Martinez, M., Rudolf, M., Lelieveld, J., and Harder, H.: Calibration of an airborne HO x instrument using the All Pressure Altitude-based Calibrator for HO x Experimentation (APACHE), Atmospheric measurement techniques, 13, 2711–2731, 2020.

Marno, D. R.: The Oxidation Capacity of the Summertime Asian Monsoon Anticyclone-Airborne measurements of OH and HO2 radicals in the Upper Troposphere using Laser Induced Fluorescence Spectroscopy, Ph.D. thesis, Universität Mainz, URL `https://hdl.handle.net/21.11116/0000-0008-F89B-2`, 2021.

Martins-Costa, M. T., Anglada, J. M., Francisco, J. S., and Ruiz-Loopez, M. F.: The aqueous surface as an efficient transient stop for the reactivity of gaseous NO2 in liquid water, Journal of the American Chemical Society, 142, 20 937–20 941, 2020.

Mertens, L. A., Winiberg, F. A., Allen, H. M., Sander, S. P., and Okumura, M.: Yields of $HONO_2$ and HOONO Products from the Reaction of HO_2 and NO Using Pulsed Laser Photolysis and Mid-Infrared Cavity-Ringdown Spectroscopy, The Journal of Physical Chemistry A, 126, 7342–7360, 2022.

Mertens, M., Kerkweg, A., Jöckel, P., Tost, H., and Hofmann, C.: The 1-way on-line coupled model system MECO (n)–Part 4: Chemical evaluation (based on MESSy v2. 52), Geoscientific Model Development, 9, 3545–3567, 2016.

Mollner, A. K., Valluvadasan, S., Feng, L., Sprague, M. K., Okumura, M., Milligan, D. B., Bloss, W. J., Sander, S. P., Martien, P. T., Harley, R. A., et al.: Rate of gas phase association of hydroxyl radical and nitrogen dioxide, Science, 330, 646–649, 2010.

Monge, M. E., D'Anna, B., Mazri, L., Giroir-Fendler, A., Ammann, M., Donaldson, D. J., and George, C.: Light changes the atmospheric reactivity of soot, Proceedings of the National Academy of Sciences, 107, 6605–6609, https://doi.org/10.1073/pnas.0908341107, 2010.

Ndour, M., D'Anna, B., George, C., Ka, O., Balkanski, Y., Kleffmann, J., Stemmler, K., and Ammann, M.: Photoenhanced uptake of NO_2 on mineral dust: Laboratory experiments and model simulations, Geophysical Research Letters, 35, https://doi.org/10.1029/2007GL032006, 2008.

Neuman, J. A., Trainer, M., Brown, S. S., Min, K.-E., Nowak, J. B., Parrish, D. D., Peischl, J., Pollack, I. B., Roberts, J. M., Ryerson, T. B., and Veres, P. R.: HONO emission and production determined from airborne measurements over the Southeast U.S., Journal of Geophysical Research: Atmospheres, 121, 9237–9250, https://doi.org/10.1002/2016JD025197, 2016.

Noxon, J. F.: Stratospheric NO_2: global behaviour, J. Geophys. Res., 84, 1979.

Nussbaumer, C. M., Parchatka, U., Tadic, I., Bohn, B., Marno, D., Martinez, M., Rohloff, R., Harder, H., Kluge, F., Pfeilsticker, K., et al.: Modification of a conventional photolytic converter for improving aircraft measurements of NO_2 via chemiluminescence, Atmospheric Measurement Techniques, 14, 6759–6776, 2021a.

Nussbaumer, C. M., Tadic, I., Dienhart, D., Wang, N., Edtbauer, A., Ernle, L., Williams, J., Obersteiner, F., Gutiérrez-Álvarez, I., Harder, H., Lelieveld, J., and Fischer, H.: Measurement report: In situ observations of deep convection without lightning during the tropical cyclone Florence 2018, Atmospheric Chemistry and Physics, 21, 7933–7945, https://doi.org/10.5194/acp-21-7933-2021, 2021b.

Nussbaumer, C. M., Fischer, H., Lelieveld, J., and Pozzer, A.: What controls ozone sensitivity in the upper tropical troposphere?, Atmospheric Chemistry and Physics, 23, 12 651–12 669, https://doi.org/10.5194/acp-23-12651-2023, 2023.

Oswald, R., Behrendt, T., Ermel, M., Wu, D., Su, H., Cheng, Y., Breuninger, C., Moravek, A., Mougin, E., Delon, C., Loubet, B., Pommerening-Röser, A., Sörgel, M., Pöschl, U., Hoffmann, T., Andreae, M., Meixner, F., and Trebs, I.: HONO Emissions from Soil Bacteria as a Major Source of Atmospheric Reactive Nitrogen, Science, 341, 1233–1235, https://doi.org/10.1126/science.1242266, 2013.

Partain, P. T., Heidinger, A. K., and Stephens, G. L.: High spectral resolution atmospheric radiative transfer: Application of the equivalence theorem, Journal of Geophysical Research: Atmospheres, 105, 2163–2177, 2000.

Perliski, L. M. and Solomon, S.: On the evaluation of air mass factors for atmospheric near-ultraviolett and visible absorption spectroscopy, J. Geophys. Res., 98, 10 363–10 374, 1993.

Perner, D. and Platt, U.: Detection of nitrous acid in the atmosphere by differential optical absorption, Geophysical Research Letters, 6, 917–920, https://doi.org/10.1029/GL006i012p00917, 1979.

Peters, E., Pinardi, G., Seyler, A., Richter, A., Wittrock, F., Bösch, T., Van Roozendael, M., Hendrick, F., Drosoglou, T., Bais, A. F., et al.: Investigating differences in DOAS retrieval codes using MAD-CAT campaign data, Atmospheric Measurement Techniques, 10, 955–978, 2017.

Pfeilsticker, K., Bösch, H., Camy-Peyret, C., Fitzenberger, R., Harder, H., and Osterkamp, H.: First atmospheric profile measurements of the atmospheric UV/vis O_4 absorption bands strength: Implications for the spectroscopy and the formation enthalpy of the O_2-O_2 dimer, Geophys. Res. Lett., 28, 4595–4598, https://doi.org/10.1029/2001GL013734, 2001.

Platt, U. and Stutz, J.: Differential absorption spectroscopy, in: Differential optical absorption spectroscopy, pp. 135–174, Springer, 2008.

Platt, U., Perner, D., Harris, G., Winer, A., and Pitts, J. j.: Observations of nitrous acid in an urban atmosphere by differential optical absorption, Nature, 285, 312–314, 1980.

Pollack, I. B., Konen, I. M., Li, E. X., and Lester, M. I.: Spectroscopic characterization of HOONO and its binding energy via infrared action spectroscopy, The Journal of Chemical Physics, 119, 9981–9984, 2003.

Polyansky, O. L., Kyuberis, A. A., Zobov, N. F., Tennyson, J., Yurchenko, S. N., and Lodi, L.: ExoMol molecular line lists XXX: a complete high-accuracy line list for water, Monthly Notices of the Royal Astronomical Society, 480, 2597–2608, https://doi.org/10.1093/mnras/sty1877, 2018.

Puķīte, J., Kühl, S., Deutschmann, T., Platt, U., and Wagner, T.: Extending differential optical absorption spectroscopy for limb measurements in the UV, Atmospheric Measurement Techniques, 3, 631–653, 2010.

Reed, C., Evans, M. J., Crilley, L. R., Bloss, W. J., Sherwen, T., Read, K. A., Lee, J. D., and Carpenter, L. J.: Evidence for renoxification in the tropical marine boundary layer, Atmospheric Chemistry and Physics, 17, 4081–4092, https://doi.org/10.5194/acp-17-4081-2017, 2017.

Reisinger, A. R.: Observations of HNO_2 in the polluted winter atmosphere: possible heterogeneous production on aerosols, Atmospheric Environment, 34, 3865–3874, https://doi.org/10.1016/S1352-2310(00)00179-5, 2000.

Roland, R.: Konvektiver Einfluss auf das OH-Oxidationspotential der oberen tropischen Troposphäre, Ph.D. thesis, Dissertation, Mainz, Johannes Gutenberg-Universität Mainz, 2022, URL `http://doi.org/10.25358/openscience-6844`, 2022.

Romer, P. S., Wooldridge, P. J., Crounse, J. D., Kim, M. J., Wennberg, P. O., Dibb, J. E., Scheuer, E., Blake, D. R., Meinardi, S., Brosius, A. L., Thames, A. B., Miller, D. O., Brune, W. H., Hall, S. R., Ryerson, T. B., and Cohen, R. C.: Constraints on Aerosol Nitrate Photolysis as a Potential Source of HONO and NO_x, Environmental Science & Technology, 52, 13 738–13 746, https://doi.org/10.1021/acs.est.8b03861, pMID: 30407797, 2018.

Rotermund, M. K.: Organic, inorganic and total bromine in the extratropical tropopause and lowermost stratosphere in fall 2017: Origins, transport pathways and consequences for ozone, Phd thesis, Universität Heidelberg, URL `https://www.ub.uni-heidelberg.de/archiv/30093`, 2021.

Rotermund, M. K., Bense, V., Chipperfield, M. P., Engel, A., Grooß, J.-U., Hoor, P., Hüneke, T., Keber, T., Kluge, F., Schreiner, B., Schuck, T., Vogel, B., Zahn, A., and Pfeilsticker, K.: Organic and inorganic bromine measurements around the extratropical tropopause and lowermost stratosphere: insights into the transport pathways and total bromine, Atmos. Chem. Phys., 21, 15 375–15 407, https://doi.org/10.5194/acp-21-15375-2021, 2021.

Rothman, L., Barbe, A., Benner, D., Brown, L., Camy-Peyret, C., Carleer, M., Chance, K., Clerbaux, C., Dana, V., Devi, V., Fayt, A., Flaud, J.-M., Gamache, R., Goldman, A., Jacquemart, D., Jucks, K., Lafferty, W., Mandin, J.-Y., Massie, S., Nemtchinov, V., Newnham, D., Perrin, A., Rinsland, C., Schroeder, J., Smith, K., Smith, M., Tang, K., Toth, R., Vander Auwera, J., Varanasi, P., and Yoshino, K.: The HITRAN Molecular Spectroscopic Database: Edition of 2000 Including Updates through, J. Quant. Spec. and Rad. Transf., 82, 1–4, 2003.

Rothman, L. S., Gordon, I. E., Barbe, A., Benner, D. C., Bernath, P. F., Birk, M., Boudon, V., Brown, L. R., Campargue, A., Champion, J.-P., Chance, K., Coudert, L. H., Dana, V., Devi, V. M., Fally, S., Flaud, J.-M., Gamache, R. R., Goldman, A., Jacquemart, D., Kleiner, I., Lacome, N., Lafferty, W. J., Mandin, J.-Y., Massie, S. T., Mikhailenko, S. N., Miller, C. E., Moazzen-Ahmadi, N., Naumenko, O. V., Nikitin, A. V., Orphal, J., Perevalov, V. I., Perrin, A., Predoi-Cross, A., Rinsland, C. P., Rotger, M., Šimečková, M., Smith, M. A. H., Sung, K., Tashkun, S. A., Tennyson, J., Toth, R. A., Vandaele, A. C., and Vander Auwera, J.: The HITRAN 2008 molecular spectroscopic database, J. Quant. Spectrosc. Ra., 110, 533–572, https://doi.org/10.1016/j.jqsrt.2009.02.013, 2009.

Rutter, A., Malloy, Q., Leong, Y., Gutierrez, C., Calzada, M., Scheuer, E., Dibb, J., and Griffin, R.: The reduction of HNO3 by volatile organic compounds emitted by motor vehicles, Atmospheric Environment, 87, 200–206, https://doi.org/10.1016/j.atmosenv.2014.01.056, 2014.

Ryan, R. G., Rhodes, S., Tully, M., Wilson, S., Jones, N., Frieß, U., and Schofield, R.: Daytime HONO, NO_2 and aerosol distributions from MAX-DOAS observations in Melbourne, Atmospheric Chemistry and Physics, 18, 13 969–13 985, https://doi.org/10.5194/acp-18-13969-2018, 2018.

Salawitch, R. J., Fahey, D. W., Hegglin, M. I., McBride, L. A., Tribett, W. R., and Doherty, S. J.: Twenty questions and answers about the ozone layer: 2018 Update, World Meteorological Organization, 2019.

Sander, S., Friedl, R. R., Barker, J., Golden, D., Kurylo, M., Wine, P., Abbat, J., Burkholder, J., Kolb, C. E., Moortgat, G. K., Huie, R., and Orkin, V.: Chemical kinetics and photochemical data for use in atmospheric studies: Evaluation Number 17, Technical Report, NASA/JPL Publication, 17, 2011.

Scharko, N. K., Berke, A. E., and Raff, J. D.: Release of Nitrous Acid and Nitrogen Dioxide from Nitrate Photolysis in Acidic Aqueous Solutions, Environmental Science & Technology, 48, 11 991–12 001, https://doi.org/10.1021/es503088x, pMID: 25271384, 2014.

Schulz, C., Schneider, J., Amorim Holanda, B., Appel, O., Costa, A., de Sá, S. S., Dreiling, V., Fütterer, D., Jurkat-Witschas, T., Klimach, T., et al.: Aircraft-based observations of isoprene-epoxydiol-derived secondary organic aerosol (IEPOX-SOA) in the tropical upper troposphere over the Amazon region, Atmospheric chemistry and physics, 18, 14 979–15 001, 2018.

Schumann, U.: Measurement and model data comparisons for the HALO-FAAM formation flight during EMeRGe on 13 July 2017, https://doi.org/10.5281/zenodo.4427965, (last access: 6 January 2022), 2021.

Seinfeld, J. H. and Pandis, S. N.: From air pollution to climate change, Atmospheric chemistry and physics, 1326, 1998.

Seinfeld, J. H. and Pandis, S. N.: Atmospheric chemistry and physics: from air pollution to climate change, John Wiley & Sons, 2016.

Serdyuchenko, A., Gorshelev, V., Weber, M., Chehade, W., and Burrows, J. P.: High spectral resolution ozone absorption cross-sections – Part 2: Temperature dependence, Atmos. Meas. Tech., 7, 625–636, https://doi.org/10.5194/amt-7-625-2014, 2014.

Shah, V., Jacob, D. J., Dang, R., Lamsal, L. N., Strode, S. A., Steenrod, S. D., Boersma, K. F., Eastham, S. D., Fritz, T. M., Thompson, C., et al.: Nitrogen oxides in the free troposphere: implications for tropospheric oxidants and the interpretation of satellite NO_2 measurements, Atmospheric Chemistry and Physics, 23, 1227–1257, 2023.

Shi, Q., Tao, Y., Krechmer, J. E., Heald, C. L., Murphy, J. G., Kroll, J. H., and Ye, Q.: Laboratory investigation of renoxification from the photolysis of inorganic particulate nitrate, Environmental Science & Technology, 55, 854–861, 2021.

Silvern, R., Jacob, D., Travis, K., Sherwen, T., Evans, M., Cohen, R., Laughner, J., Hall, S., Ullmann, K., Crounse, J., et al.: Observed NO/NO_2 ratios in the upper troposphere imply errors in NO-NO_2-O_3 cycling kinetics or an unaccounted NO_X reservoir, Geophysical Research Letters, 45, 4466–4474, 2018.

Singh, A., Crilley, L. R., Pope, F. D., and Bloss, W. J.: Insights into HONO sources from observations during a solar eclipse, Environmental Science: Atmospheres, 1, 395–405, 2021.

Spataro, F. and Ianniello, A.: Sources of atmospheric nitrous acid: State of the science, current research needs, and future prospects, Journal of the Air & Waste Management Association, 64, 1232–1250, https://doi.org/10.1080/10962247.2014.952846, 2014.

Stemmler, K., Ammann, M., Donders, C., Kleffmann, J., and George, C.: Photosensitized reduction of nitrogen dioxide on humic acid as a source of nitrous acid, Nature, 440, 195–198, 2006.

Stemmler, K., Ndour, M., Elshorbany, Y., Kleffmann, J., D'anna, B., George, C., Bohn, B., and Ammann, M.: Light induced conversion of nitrogen dioxide into nitrous acid on submicron humic acid aerosol, Atmospheric Chemistry and Physics, 7, 4237–4248, 2007.

Stutz, J., Kim, E., Platt, U., Bruno, P., Perrino, C., and Febo, A.: UV-visible absorption cross-sections of nitrous acid, J. Geophys. Res., 105, 14,585–14,592, 2000.

Stutz, J., Werner, B., Spolaor, M., Scalone, L., Festa, J., Tsai, C., Cheung, R., Colosimo, S. F., Tricoli, U., Raecke, R., Hossaini, R., Chipperfield, M. P., Feng, W., Gao, R.-S., Hintsa, E. J., Elkins, J. W., Moore, F. L., Daube, B., Pittman, J., Wofsy, S., and Pfeilsticker, K.: A new Differential Optical Absorption Spectroscopy instrument to study atmospheric chemistry from a high-altitude unmanned aircraft, Atmos. Meas. Tech., 10, 1017 – 1042, https://doi.org/10.5194/amt-10-1017-2017, 2017.

Su, H., Cheng, Y., Oswald, R., Behrendt, T., Trebs, I., Meixner, F. X., Andreae, M. O., Cheng, P., Zhang, Y., and Pöschl, U.: Soil Nitrite as a Source of Atmospheric HONO and OH Radicals, Science, 333, 1616–1618, https://doi.org/10.1126/science.1207687, 2011.

Sullivan, M. N., Chu, L. T., and Zhu, L.: Comment on "Investigations on HONO formation from photolysis of adsorbed HNO_3 on quartz glass surfaces" by S. Laufs and J. Kleffmann, Phys. Chem. Chem. Phys., 2016, 18, 9616, Physical Chemistry Chemical Physics, 20, 30 537–30 539, 2018.

Szakács, P., Csontos, J., Das, S., and Kállay, M.: High-accuracy theoretical thermochemistry of atmospherically important nitrogen oxide derivatives, The Journal of Physical Chemistry A, 115, 3144–3153, 2011.

Tadic, I., Crowley, J. N., Dienhart, D., Eger, P., Harder, H., Hottmann, B., Martinez, M., Parchatka, U., Paris, J.-D., Pozzer, A., et al.: Net ozone production and its relationship to nitrogen oxides and volatile organic compounds in the marine boundary layer around the Arabian Peninsula, Atmospheric Chemistry and Physics, 20, 6769–6787, 2020.

Tadic, I., Nussbaumer, C. M., Bohn, B., Harder, H., Marno, D., Martinez, M., Obersteiner, F., Parchatka, U., Pozzer, A., Rohloff, R., et al.: Central role of nitric oxide in ozone production in the upper tropical troposphere over the Atlantic Ocean and western Africa, Atmospheric Chemistry and Physics, 21, 8195–8211, 2021.

Tao, W., Su, H., Zheng, G., Wang, J., Wei, C., Liu, L., Ma, N., Li, M., Zhang, Q., Pöschl, U., et al.: Aerosol pH and chemical regimes of sulfate formation in aerosol water during winter haze in the North China Plain, Atmospheric Chemistry and Physics, 20, 11 729–11 746, 2020.

Thalman, R. and Volkamer, R.: Temperature dependent absorption cross-sections of O_2–O_2 collision pairs between 340 and 630 nm and at atmospherically relevant pressure, Phys. Chem. Chem. Phys., 15, 15 371–15 381, https://doi.org/10.1039/C3CP50968K, 2013.

Tong, S., Hou, S., Zhang, Y., Chu, B., Liu, Y., He, H., Zhao, P., and Ge, M.: Exploring the nitrous acid (HONO) formation mechanism in winter Beijing: direct emissions and heterogeneous production in urban and suburban areas, Faraday discussions, 189, 213–230, 2016.

Toublanc, D.: Henyey–Greenstein and Mie phase functions in Monte Carlo radiative transfer computations, Applied optics, 35, 3270–3274, 1996.

Villena, G., Kleffmann, J., Kurtenbach, R., Wiesen, P., Lissi, E., Rubio, M. A., Croxatto, G., and Rappenglück, B.: Vertical gradients of HONO, NO_x and O_3 in Santiago de Chile, Atmospheric Environment, 45, 3867–3873, https://doi.org/10.1016/j.atmosenv.2011.01.073, 2011.

Vountas, M., Rozanov, V., and Burrows, J.: Ring effect: Impact of rotational Raman scattering on radiative transfer in Earth's atmosphere, Journal of Quantitative Spectroscopy and Radiative Transfer, 60, 943–961, 1998.

Wang, L., Wen, L., Xu, C., Chen, J., Wang, X., Yang, L., Wang, W., Yang, X., Sui, X., Yao, L., and Zhang, Q.: HONO and its potential source particulate nitrite at an urban site in North China during the cold season, Science of The Total Environment, 538, 93–101, https://doi.org/10.1016/j.scitotenv.2015.08.032, 2015.

Wang, N., Edtbauer, A., Stönner, C., Pozzer, A., Bourtsoukidis, E., Ernle, L., Dienhart, D., Hottmann, B., Fischer, H., Schuladen, J., et al.: Measurements of carbonyl compounds around the Arabian Peninsula: overview and model comparison, Atmospheric Chemistry and Physics, 20, 10 807–10 829, 2020.

Wang, Y., Beirle, S., Hendrick, F., Hilboll, A., Jin, J., Kyuberis, A. A., Lampel, J., Li, A., Luo, Y., Lodi, L., Ma, J., Navarro, M., Ortega, I., Peters, E., Polyansky, O. L., Remmers, J., Richter, A., Puentedura, O., Van Roozendael, M., Seyler, A., Tennyson, J., Volkamer, R., Xie, P., Zobov, N. F., and Wagner, T.: MAX-DOAS measurements of HONO slant column densities during the MAD-CAT campaign: inter-comparison, sensitivity studies on spectral analysis settings, and error budget, Atmospheric Measurement Techniques, 10, 3719–3742, https://doi.org/10.5194/amt-10-3719-2017, 2017.

Wang, Y., Dörner, S., Donner, S., Böhnke, S., De Smedt, I., Dickerson, R. R., Dong, Z., He, H., Li, Z., Li, Z., Li, D., Liu, D., Ren, X., Theys, N., Wang, Y., Wang, Y., Wang, Z., Xu, H., Xu, J., and Wagner, T.: Vertical profiles of NO_2, SO_2, HONO, HCHO, CHOCHO and aerosols derived from MAX-DOAS measurements at a rural site in the central western North China Plain and their relation to emission sources and effects of regional transport, Atmospheric Chemistry and Physics, 19, 5417–5449, https://doi.org/10.5194/acp-19-5417-2019, 2019.

Warneck, P. and Wurzinger, C.: Product quantum yields for the 305-nm photodecomposition of nitrate in aqueous solution, The Journal of Physical Chemistry, 92, 6278–6283, 1988.

Warneke, C., Veres, P., Holloway, J., Stutz, J., Tsai, C., Alvarez, S., Rappenglueck, B., Fehsenfeld, F., Graus, M., Gilman, J., et al.: Airborne formaldehyde measurements using PTR-MS: calibration, humidity dependence, inter-comparison and initial results, Atmospheric Measurement Techniques, 4, 2345–2358, 2011.

Weber, R. J., Guo, H., Russell, A. G., and Nenes, A.: High aerosol acidity despite declining atmospheric sulfate concentrations over the past 15 years, Nature Geoscience, 9, 282–285, 2016.

Wennberg, P., Hanisco, T., Jaegle, L., Jacob, D., Hintsa, E., Lanzendorf, E., Anderson, J., Gao, R.-S., Keim, E., Donnelly, S., et al.: Hydrogen radicals, nitrogen radicals, and the production of O3 in the upper troposphere, science, 279, 49–53, 1998.

Wennberg, P., Salawitch, R., Donaldson, D., Hanisco, T., Lanzendorf, E., Perkins, K., Lloyd, S., Vaida, V., Gao, R., Hintsa, E., et al.: Twilight observations suggest unknown sources of HOx, Geophysical Research Letters, 26, 1373–1376, 1999.

Werner, B., Stutz, J., Spolaor, M., Scalone, L., Raecke, R., Festa, J., Colosimo, S. F., Cheung, R., Tsai, C., Hossaini, R., Chipperfield, M. P., Taverna, G. S., Feng, W., Elkins, J. W., Fahey, D. W., Gao, R.-S., Hintsa, E. J., Thornberry, T. D., Moore, F. L., Navarro, M. A., Atlas, E., Daube, B. C., Pittman, J., Wofsy, S., and Pfeilsticker, K.: Probing the subtropical lowermost stratosphere and the tropical upper troposphere and tropopause layer for inorganic bromine, Atmos. Chem. Phys., 17, 1161–1186, https://doi.org/10.5194/acp-17-1161-2017, 2017.

Wittrock, F., Richter, A., Oetjen, H., Burrows, J. P., Kanakidou, M., Myriokefalitakis, S., Volkamer, R., Beirle, S., Platt, U., and Wagner, T.: Simultaneous global observations of glyoxal and formaldehyde from space, Geophysical Research Letters, 33, 2006.

WMO, G. and OMM, G.: International meteorological vocabulary, 1966.

Wu, D., Horn, M. A., Behrendt, T., Müller, S., Li, J., Cole, J. A., Xie, B., Ju, X., Li, G., Ermel, M., et al.: Soil HONO emissions at high moisture content are driven by microbial nitrate reduction to nitrite: tackling the HONO puzzle, The ISME journal, 13, 1688–1699, 2019.

Xing, C., Xu, S., Song, Y., Liu, C., Liu, Y., Lu, K., Tan, W., Zhang, C., Hu, Q., Wang, S., Wu, H., and Lin, H.: A new insight into the vertical differences in NO_2 heterogeneous reaction to produce HONO over inland and marginal seas, Atmospheric Chemistry and Physics, 23, 5815–5834, https://doi.org/10.5194/acp-23-5815-2023, 2023.

Xing, L., Wu, J., Elser, M., Tong, S., Liu, S., Li, X., Liu, L., Cao, J., Zhou, J., El-Haddad, I., Huang, R., Ge, M., Tie, X., Prévôt, A. S. H., and Li, G.: Wintertime secondary organic aerosol formation in Beijing–Tianjin–Hebei (BTH): contributions of HONO sources and heterogeneous reactions, Atmospheric Chemistry and Physics, 19, 2343–2359, https://doi.org/10.5194/acp-19-2343-2019, 2019.

Xu, W., Kuang, Y., Zhao, C., Tao, J., Zhao, G., Bian, Y., Yang, W., Yu, Y., Shen, C., Liang, L., Zhang, G., Lin, W., and Xu, X.: NH_3-promoted hydrolysis of NO_2 induces explosive growth in HONO, Atmospheric Chemistry and Physics, 19, 10 557–10 570, https://doi.org/10.5194/acp-19-10557-2019, 2019.

Yabushita, A., Enami, S., Sakamoto, Y., Kawasaki, M., Hoffmann, M. R., and Colussi, A. J.: Anion-Catalyzed Dissolution of NO_2 on Aqueous Microdroplets, The Journal of Physical Chemistry A, 113, 4844–4848, https://doi.org/10.1021/jp900685f, pMID: 19331373, 2009.

Yang, W., Han, C., Yang, H., and Xue, X.: Significant HONO formation by the photolysis of nitrates in the presence of humic acids, Environmental Pollution, 243, 679–686, https://doi.org/10.1016/j.envpol.2018.09.039, 2018.

Ye, C., Zhou, X., Pu, D., Stutz, J., Festa, J., Spolaor, M., Cantrell, C., Mauldin, R. L., Weinheimer, A., and Haggerty, J.: Comment on "Missing gas-phase source of HONO inferred from Zeppelin measurements in the troposphere", Science, 348, 1326–1326, https://doi.org/10.1126/science.aaa1992, 2015.

Ye, C., Gao, H., Zhang, N., and Zhou, X.: Photolysis of nitric acid and nitrate on natural and artificial surfaces, Environmental science & technology, 50, 3530–3536, 2016a.

Ye, C., Zhou, X., Pu, D., Stutz, J., Festa, J., Spolaor, M., Tsai, C., Cantrell, C., Mauldin, R. L., Campos, T., et al.: Rapid cycling of reactive nitrogen in the marine boundary layer, Nature, 532, 489–491, 2016b.

Ye, C., Zhang, N., Gao, H., and Zhou, X.: Photolysis of Particulate Nitrate as a Source of HONO and NO_x, Environmental Science & Technology, 51, 6849–6856, https://doi.org/10.1021/acs.est.7b00387, pMID: 28505434, 2017.

Ye, C., Zhou, X., Pu, D., Stutz, J., Festa, J., Spolaor, M., Tsai, C., Cantrell, C., Mauldin III, R. L., Weinheimer, A., Hornbrook, R. S., Apel, E. C., Guenther, A., Kaser, L., Yuan, B., Karl, T., Haggerty, J., Hall, S., Ullmann, K., Smith, J., and Ortega, J.: Tropospheric HONO distribution and chemistry in the southeastern US, Atmospheric Chemistry and Physics, 18, 9107–9120, https://doi.org/10.5194/acp-18-9107-2018, 2018.

Yu, Y., Cheng, P., Li, H., Yang, W., Han, B., Song, W., Hu, W., Wang, X., Yuan, B., Shao, M., et al.: Budget of nitrous acid (HONO) at an urban site in the fall season of Guangzhou, China, Atmospheric Chemistry and Physics, 22, 8951–8971, 2022.

Zahn, A., Weppner, J., Widmann, H., Schlote-Holubek, K., Burger, B., Kühner, T., and Franke, H.: A fast and precise chemiluminescence ozone detector for eddy flux and airborne application, Atmos. Meas. Tech., 5, 363–375, https://doi.org/10.5194/amt-5-363-2012, 2012.

Zhang, J. and Donahue, N. M.: Constraining the mechanism and kinetics of $OH+ NO_2$ and $HO_2+ NO$ using the multiple-well master equation, The Journal of Physical Chemistry A, 110, 6898–6911, 2006.

Zhang, N., Zhou, X., Shepson, P. B., Gao, H., Alaghmand, M., and Stirm, B.: Aircraft measurement of HONO vertical profiles over a forested region, Geophysical Research Letters, 36, https://doi.org/10.1029/2009GL038999, 2009.

Zhang, S., Sarwar, G., Xing, J., Chu, B., Xue, C., Sarav, A., Ding, D., Zheng, H., Mu, Y., Duan, F., et al.: Improving the representation of HONO chemistry in CMAQ and examining its impact on haze over China, Atmospheric Chemistry and Physics, 21, 15 809–15 826, 2021.

Zhao, Y., Houk, K., and Olson, L. P.: Mechanisms of peroxynitrous acid and methyl peroxynitrite, ROONO (R = H, Me), rearrangements: A conformation-dependent homolytic dissociation, The Journal of Physical Chemistry A, 108, 5864–5871, 2004.

Zheng, G., Su, H., Wang, S., Andreae, M. O., Pöschl, U., and Cheng, Y.: Multiphase buffer theory explains contrasts in atmospheric aerosol acidity, Science, 369, 1374–1377, 2020a.

Zheng, H., Song, S., Sarwar, G., Gen, M., Wang, S., Ding, D., Chang, X., Zhang, S., Xing, J., Sun, Y., Ji, D., Chan, C. K., Gao, J., and McElroy, M. B.: Contribution of Particulate Nitrate Photolysis to Heterogeneous Sulfate Formation for Winter Haze in China, Environmental Science & Technology Letters, 7, 632–638, https://doi.org/10.1021/acs.estlett.0c00368, 2020b.

Zhou, X., Beine, H. J., Honrath, R. E., Fuentes, J. D., Simpson, W., Shepson, P. B., and Bottenheim, J. W.: Snowpack photochemical production of HONO: A major source of OH in the Arctic boundary layer in springtime, Geophysical Research Letters, 28, 4087–4090, https://doi.org/10.1029/2001GL013531, 2001.

Zhou, X., Gao, H., He, Y., Huang, G., Bertman, S. B., Civerolo, K., and Schwab, J.: Nitric acid photolysis on surfaces in low-NO_x environments: Significant atmospheric implications, Geophysical Research Letters, 30, https://doi.org/10.1029/2003GL018620, 2003.

Zhou, X., Huang, G., Civerolo, K., Roychowdhury, U., and Demerjian, K. L.: Summertime observations of HONO, HCHO, and O_3 at the summit of Whiteface Mountain, New York, Journal of Geophysical Research: Atmospheres, 112, https://doi.org/10.1029/2006JD007256, 2007.

Zhu, Q., Laughner, J. L., and Cohen, R. C.: Lightning NO_2 simulation over the contiguous US and its effects on satellite NO_2 retrievals, Atmospheric Chemistry and Physics, 19, 13 067–13 078, 2019.

Zhu, R. and Lin, M.-C.: Ab initio study of the HO_2+ NO reaction: Prediction of the total rate constant and product branching ratios for the forward and reverse processes, The Journal of Chemical Physics, 119, 10 667–10 677, 2003.

Ziemba, L. D., Dibb, J. E., Griffin, R. J., Anderson, C. H., Whitlow, S. I., Lefer, B. L., Rappenglück, B., and Flynn, J.: Heterogeneous conversion of nitric acid to nitrous acid on the surface of primary organic aerosol in an urban atmosphere, Atmospheric Environment, 44, 4081–4089, https://doi.org/10.1016/j.atmosenv.2008.12.024, 2010.

Ziereis, H., Minikin, A., Schlager, H., Gayet, J., Auriol, F., Stock, P., Baehr, J., Petzold, A., Schumann, U., Weinheimer, A., et al.: Uptake of reactive nitrogen on cirrus cloud particles during INCA, Geophysical research letters, 31, 2004.